

Alma Mater Studiorum – Università di Bologna

DOTTORATO DI RICERCA IN

CHIMICA

Ciclo XXXI

Settore Concorsuale: 03/B1

Settore Scientifico Disciplinare: CHIM/03

**SUPPORTED GOLD NANOPARTICLES
CATALYSTS FOR ORGANIC
TRANSFORMATIONS**

Presentata da: Chiara Parise

Coordinatore Dottorato

Prof. Aldo Roda

Supervisore

Prof. Maria Cristina Cassani

Co-Supervisori

Prof. Barbara Ballarin

Prof. Daniele Nanni

Esame finale anno 2019

Abstract

The research work described in this thesis concerns the synthesis, characterisation and study of the catalytic activity of supported gold nanoparticles (AuNPs) immobilised on various oxide supports, i.e. silica (SiO_2), alumina (Al_2O_3), titania (TiO_2) and magnetite (Fe_3O_4), previously functionalised with [3-(2-propynylcarbamate)propyl]triethoxysilane (PTEOS). The alkynyl-carbamate moieties anchored on the support were capable of straightforwardly reducing the gold precursor chloroauric acid (HAuCl_4) to afford **Au/OS@Yne** (OS = Oxide Support, Yne = organic functionalisation), without the need of additional reducing or stabilising agents.

The resulting materials were characterised by means of several complementary techniques, such as thermogravimetric analysis (TGA), atomic absorption spectroscopy (AAS), transmission electron microscopy (TEM), solid state NMR spectroscopy (SS NMR) and x-rays photoelectron spectroscopy (XPS), in order to investigate their structural and chemical properties.

Furthermore, the catalytic activity of the obtained **Au/OS@Yne** was evaluated first in the oxidation of alcohols and then in the hydroamination of alkynes.

Finally, during a six months stay at the Karl-Franzens University of Graz, a second research work was carried out, concerning the study of metal organic frameworks biocomposites.

The thesis organisation and the content of each chapter can be summarised as follows:

Chapter 1. General introduction on the topic of nanocatalysis, followed by an overview on the synthesis and properties of gold nanoparticles, with a special focus on their application as catalysts. Moreover, a brief discussion on the main advantages of flow chemistry and the exploitation of this technology in heterogeneous catalysis is reported.

Chapter 2. The **Au/SiO₂@Yne**, **Au/Al₂O₃@Yne** and **Au/TiO₂@Yne** systems were prepared by *in situ* reduction of a gold precursor in the presence of the alkynyl carbamate moieties grafted on the support surface. The physical and chemical characterisation of the obtained materials was then carried out, alongside an investigation on the mechanism of formation/stabilisation of AuNPs on the functionalised supports.

Chapter 3. The catalytic activity of **Au/SiO₂@Yne**, **Au/Al₂O₃@Yne** and **Au/TiO₂@Yne** in the oxidation of benzyl alcohol was first evaluated in batch conditions, with the aim of tuning the reaction selectivity by employing different oxidising agents and solvent media. Furthermore, the oxidation of a variety of primary and secondary alcohols catalysed by **Au/SiO₂@Yne** was performed, both in batch and in continuous-flow conditions. Finally, the effect of the oxide support on the catalytic properties of the system was studied in the oxidation of 1-phenylethanol.

Chapter 4. A further functionalisation of the silica supported catalyst was carried out following two approaches: grafting with ethoxytrimethylsilane (**Au/SiO₂@Yne-TMS**) and impregnation with triethylamine (**Au/SiO₂@Yne-NEt₃**). The new synthesized materials were thoroughly characterised and employed as catalysts in the hydroamination of phenylacetylene with aniline.

Chapter 5. The synthesis of nanomagnetite supports was performed by co-precipitation of iron salts in alkaline media (NH₃ and NaOH), then the obtained magnetic nanoparticles were functionalised with PPTEOS and decorated with AuNPs. Furthermore the characterisation of these magnetic systems was carried out and compared with the analogues materials formed by immobilising AuNPs on bare magnetite.

Chapter 6. Synthesis and characterisation of zeolitic imidazolate framework-8 biocomposites containing bovine serum albumin (**BSA@ZIF-8**). The possibility of tuning the ZIF-8 topology by varying the reaction conditions was first investigated in batch conditions, then the synthesis was carried out in a continuous-flow system with a special focus on the control of particle size.

Table of contents

1. GENERAL INTRODUCTION	1
1.1 Nanoscience and nanotechnologies	1
1.2 Nanocatalysis	2
1.2.1 Catalysis by metal nanoparticles	4
1.3 An overview on gold nanoparticles	6
1.3.1 Optical properties of gold nanoparticles	6
1.3.2 Synthesis of gold nanoparticles	8
1.4 Catalysis by supported gold nanoparticles	10
1.4.1 Preparation of heterogeneous catalysts based on gold nanoparticles	10
1.4.2 Characterisation of gold catalysts	13
1.4.3. The importance of the support	14
1.4.4 Supported gold nanoparticles catalysts for organic reactions	15
1.5 Flow chemistry	17
1.5.1 An introduction to flow chemistry	17
1.5.2 Nanocatalysis in continuous-flow systems	20
<i>References</i>	23
2. SYNTHESIS AND CHARACTERISATION OF GOLD NANOPARTICLES SUPPORTED ON FUNCTIONALISED OXIDES	28
2.1 Introduction	28
2.1.1 Previous work of the research group	28
2.1.2 Principles of Solid State NMR spectroscopy	35
2.1.3 Aim of the chapter	37
2.2 Results and discussion	38
2.2.1 Preparation of OS@Yne and Au/OS@Yne	38
2.2.2 Characterisation of OS@Yne and Au/OS@Yne	40

2.2.3 Investigation of the gold reduction/immobilisation mechanism by Solid State NMR spectroscopy	48
2.2.4 XPS analysis of Au/OS@Yne	51
2.3 Conclusions	55
2.4 Experimental section	56
2.4.1 Materials	56
2.4.2 Synthesis of PPTEOS	56
2.4.3 Preparation of OS@Yne	57
2.4.4 Preparation of Au/OS@Yne	58
2.4.5 Instruments and methods	59
<i>References</i>	61
3. ALCOHOL OXIDATION CATALYSED BY GOLD NANOPARTICLES SUPPORTED ON FUNCTIONALISED OXIDES	64
3.1 Introduction	64
3.1.1 Oxidation of alcohols: sustainability and selectivity issues	64
3.1.2 Supported gold nanoparticles as catalysts for alcohol oxidation	66
3.1.3 Mechanism of alcohol oxidation over AuNPs catalysts	69
3.1.4 Gold-catalysed alcohol oxidation in continuous-flow systems	70
3.1.5 Aim of the chapter	71
3.2 Results and discussion	72
3.2.1 Oxidation of benzyl alcohol with Au/OS@Yne in batch conditions	72
3.2.2 Oxidation of primary and secondary alcohols with Au/SiO₂@Yne in batch conditions	75
3.2.3 Oxidation of primary and secondary alcohols with Au/SiO₂@Yne in continuous-flow conditions	80
3.2.4 Oxidation of 1-phenylethanol with Au/OS@Yne in continuous-flow conditions	82
3.3 Conclusions	84

3.4 Experimental section	85
3.4.1 Materials	85
3.4.2 Catalytic tests	85
3.4.3 Instruments	86
<i>References</i>	88
4. GOLD NANOPARTICLES SUPPORTED ON FUNCTIONALISED SILICA AS CATALYSTS FOR ALKYNES HYDROAMINATION	90
4.1 Introduction	90
4.1.1 Hydroamination of alkynes	90
4.1.2 Supported gold nanoparticles as catalysts for hydroamination of alkynes	93
4.1.3 Aim of the chapter	95
4.2 Results and discussion	96
4.2.1 Preparation of Au/SiO₂@Yne-TMS and Au/SiO₂@Yne-NEt₃	96
4.2.2 Characterisation of Au/SiO₂@Yne-TMS and Au/SiO₂@Yne-NEt₃	99
4.2.3 Solid State NMR characterisation	104
4.2.4 Hydroamination of alkynes	107
4.3 Conclusions	114
4.4 Experimental section	115
4.4.1 Materials	115
4.4.2 Preparation of Au/SiO₂@Yne-TMS	115
4.4.3 Preparation of SiO₂-NEt₃	116
4.4.4 Preparation of Au/SiO₂@Yne-NEt₃ and Au/SiO₂@Yne-NEt₃*	116
4.4.6 Catalytic tests	117
4.4.7 Instruments and methods	117
<i>References</i>	119
5. SYNTHESIS AND CHARACTERISATION OF Au/Fe₃O₄ NANOCOMPOSITES	121
5.1 Introduction	121

5.1.1 Magnetism in materials	121
5.1.2 Magnetite nanoparticles	124
5.1.3 Functionalisation of magnetic nanoparticles	126
5.1.4 Aim of the chapter	127
5.2 Results and discussion	128
5.2.1 Synthesis of Au/Fe₃O₄@Yne and Au/Fe₃O₄ nanocomposites	128
5.2.2 Characterisation of Fe ₃ O ₄ and Fe₃O₄@Yne	129
5.2.3. Characterisation of Au/Fe₃O₄@Yne and Au/Fe₃O₄	134
5.2.4 Magnetic properties	140
5.3 Conclusions	143
5.4 Experimental section	144
5.4.1 Materials	144
5.4.2 Synthesis of Fe₃O₄-NH₃ and Fe₃O₄-NaOH	144
5.4.3 Synthesis of Fe₃O₄-NH₃@Yne and Fe₃O₄-NaOH@Yne	144
5.4.4 Synthesis of Au/Fe₃O₄-NH₃@Yne and Au/Fe₃O₄-NaOH@Yne	145
5.4.5 Instruments and methods	145
<i>References</i>	148
6. SYNTHESIS AND CHARACTERISATION OF ZEOLITIC IMIDAZOLATE FRAMEWORK-8 BICOMPOSITES	151
6.1 Introduction	151
6.1.1 An overview on metal organic frameworks	151
6.1.2 Biomimetic mineralisation of zeolitic imidazolate framework-8	153
6.1.3 The importance of size control	156
6.1.4 Synthesis of BSA@ZIF-8 biocomposites in continuous-flow conditions	157
6.1.5 Aim of the chapter	159
6.2 Results and discussion	160
6.2.1 Influence of reaction conditions on the BSA@ZIF-8 topology	160

6.2.2 Size-controlled synthesis of BSA@ZIF-8 in continuous-flow conditions	164
6.3 Conclusions	171
6.4 Experimental section	172
6.4.1 Materials	172
6.4.2 Synthesis of BSA@ZIF-8	172
6.4.3 Synthesis of BSA@ZIF-8 biocomposites for BSA/Zn/2-MIM ternary plot	172
6.4.4 Synthesis of BSA@ZIF-8 in continuous-flow conditions	174
6.4.5 Instruments and methods	175
<i>References</i>	176

1. GENERAL INTRODUCTION

1.1 Nanoscience and nanotechnologies

Nanoscience is defined as the study of phenomena and manipulation of materials at atomic, molecular and macromolecular scales, where properties differ significantly from those at a larger scale. The design, production, characterisation and application of structures, devices and systems with at least one size at nanometric scale (1 - 100 nm) constitute the wide world of *nanotechnologies*.¹

Contrary to what one might believe, nanoscience and nanotechnologies are not new, since the first examples of the production of nanostructured materials can be dated back to ancient history, when for example gold, silver and copper nanoparticles were used as coloured pigments in stained glass and ceramics.² The natural world also presents many examples of nanoscale structures, from milk (a nanoscale colloid) to more sophisticated nanostructured proteins.¹

However, the ideas and concepts at the base of nowadays nanotechnologies were first discussed in 1959 by the physicist Richard Feynman during the famous talk entitled “*There’s plenty of room at the bottom*”, in which the possibility to manipulate and control individual atoms and molecules was described, though the term “*nanotechnology*” was coined by Prof. Norio Taniguchi only several years later.

One of the most important developments that gave a boost to the studies in this field was the invention of the scanning tunnelling microscope by Gerd Binnig and Heinrich Rohrer in 1981, which allowed scientists to “see” individual atoms for the first time. Afterwards, with the discovery and synthesis of new materials and the development of new characterisation techniques, nanotechnology has been exploited in a large variety of fields, such as chemistry, engineering, medicine, biotechnology, etc. (Figure 1.1).

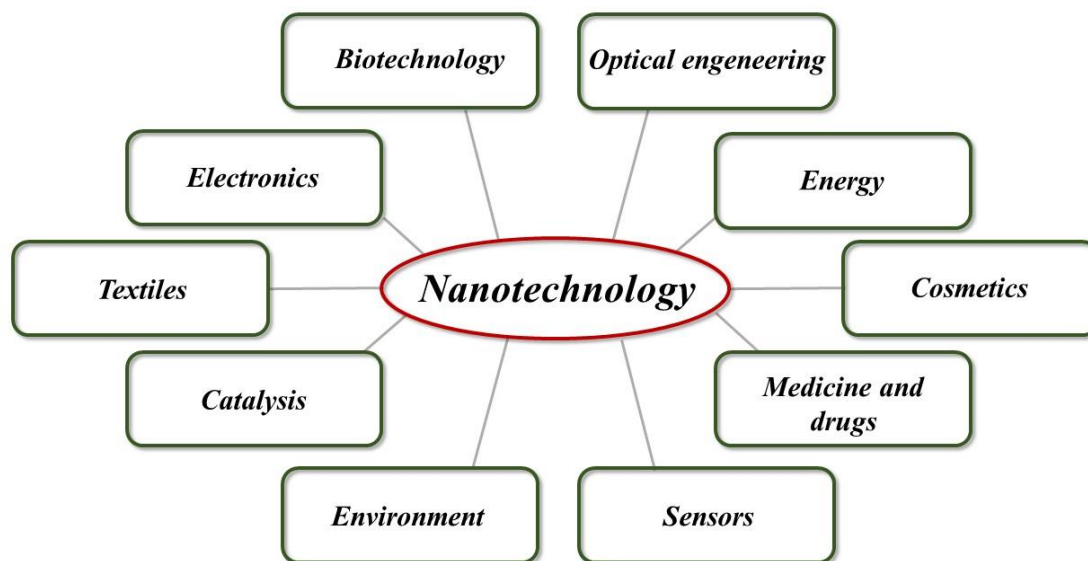


Figure 1.1. Applications of nanotechnology.

1.2 Nanocatalysis

The development of efficient catalysts is currently one of the main topic of research in chemistry, since the majority of chemicals industrial manufacturing involves one or more catalytic stages.

In general, catalysis can be *homogenous*, when the catalyst is in the same phase of the reactants, or *heterogeneous*, when the catalyst is in a different phase, namely solid. The main advantage of a heterogeneous catalyst is the easy recovery at the end of the process, but the drawbacks are related to the mass transfer problems and the harsh conditions often required to obtain good performances. On the other hand, homogeneous catalysts present higher activity and selectivity, but their separation from the reaction environment is still a key issue for industrial applications.³

The distinction between the two approaches is usually well defined, but with the growing interest in the study of nanotechnologies, a new domain of catalysts has emerged at the interphase amid homogenous and heterogeneous catalysis. *Nanocatalysis*, indeed, represents the bridging between the benefits of the two, i.e. high efficiency and selectivity, stability and easy recovery/recycling.

The great interest in catalytic systems at the nanoscale can be ascribed to the fact that their properties deeply differs from the ones of the corresponding *bulk*, due to two principal factors:³

- *increased surface area effect*: as the size decreases, a larger amount of atoms will be found at the surface of the material. Both physical and chemical interactions occur at surfaces, thus this result in a much higher reactivity of materials at the nanoscale.
- *quantum effects*: when the size decreases to the nanometres range, quantum effects dominates the properties of matter, affecting its chemical, optical, electrical and magnetic behaviour.

Over the years, the relation between nanocatalysts reactivity and size has been extensively investigated, exploring the possibility to predict and tune the activity of a system on the base of its dimensions in order to achieve optimized performances for a given reaction.⁴

Indeed, reactions could be classified in three groups, represented in Figure 1.2: 1) *positive size-sensitivity reactions*, for which turnover frequency increases with decreasing particles size (e.g. methane activation); 2) *negative size-sensitivity reactions*, for which turnover frequency decreases with decreasing particles size (e.g. dissociation of CO and N₂); and 3) *size-insensitivity reactions*, for which no significant dependence of turnover frequency on the catalyst size is observed (e.g. hydrocarbon hydrogenation on transition metal catalysts).^{3,5,6,7}

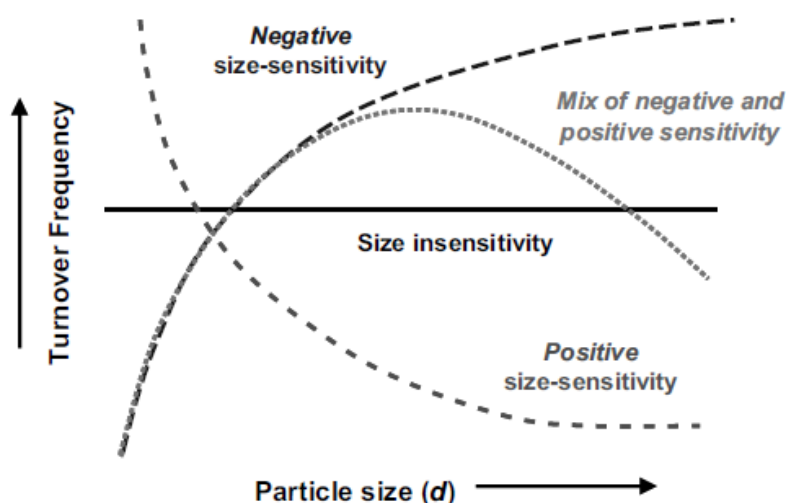


Figure 1.2. Relationship between catalyst size and turnover frequency for a given combination of reaction and catalytic system.³

Nevertheless, it is worth noting that while it is true that much knowledge has been achieved on nanocatalysis as experimental work keeps increasing, it is still difficult to identify a unified theory to explain and predict the behaviour of different catalytic systems, with different particle size and for different types of reaction.⁸

1.2.1 Catalysis by metal nanoparticles

The first catalytic applications of metallic nanoparticles (NPs) were reported by Nord in 1940, regarding the study of nitrobenzene reduction by means of palladium and platinum catalysts in which synthetic high polymers were employed as protective colloids.⁹ In 1970, Parravano published a study on the use of gold nanoparticles (AuNPs) in the hydrogen-atom transfer between benzene and cyclohexane and oxygen-atom transfer between CO and CO₂.¹⁰ However, the real milestone in the field of metal nanoparticles catalysis can be identified in the discovery of the efficient low-temperature CO oxidation over supported AuNPs, reported by Haruta in 1989.¹¹ Thereafter, an exponential growth of the studies regarding the use of metallic NPs as catalysts was observed and nowadays this is a well established area of research.

While in the case of mononuclear metal complexes the electronic structure is strongly related to their coordination environment (i.e. ligands and solvent), when it comes to metal NPs the situation is much more complicated due to overlapping between metal atoms. Moving from a small cluster to a bigger nanoparticle, the coordination number of the surface atoms increases and the contribution of the atoms inside the particle to the composition of the frontier orbitals becomes more important (Figure 1.3).

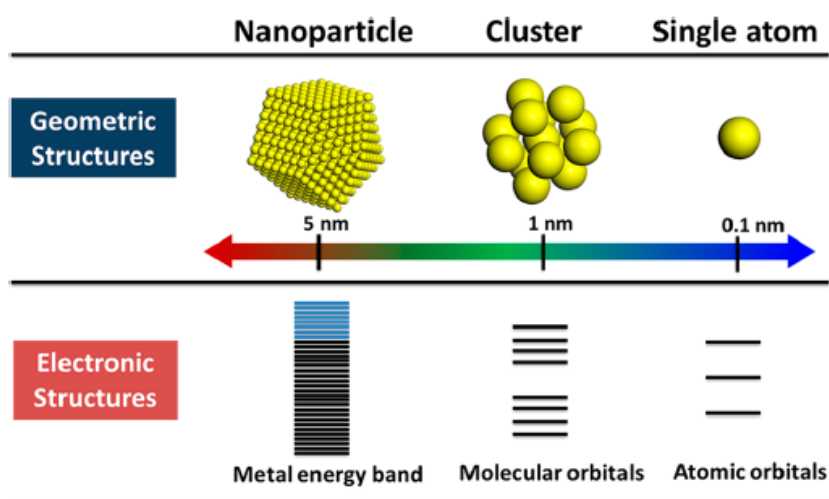


Figure 1.3. Geometric and electronic structures of single atoms, clusters and nanoparticles.⁸

This results in a less efficient overlap of the metal orbitals, that become less accessible, with the ones of the substrate molecules.⁸ For this reason, one of the key points in the development of metal NPs catalysts is the optimal control of particles size during the preparation process, combined to the stability of the system in the reaction environment.

The typical synthetic methods follow a *bottom-up* approach from molecular precursors including a metal salt, a reducing agent and a stabilising agent.

The stabilisation can be provided by electrostatic effect, steric effect or by means of ligands.¹² Polymers are often used for this purpose, since they can contribute to the system stability both by steric hindrance effect and by binding weakly the surface of NPs, thus preventing aggregation phenomena. The most commonly used polymer stabiliser is poly(N-vinyl-2-pyrrolidone) (PVP), which has been successfully used also in the preparation of core-shell bimetallic Au-PdNPs.¹³ Another type of macromolecules employed in this area are dendrimers, which form molecular cages that can encapsulate metal NPs. In additions, by choosing the dendrimers terminal groups it is possible to tune the solubility of the system in the desired solvent media. Finally, the size control and stability of metallic NPs can be provided by various type of ligands, for example polyoxometallates,¹⁴ cyclodextrins¹⁵ and silanes,¹⁶ which allow to finely tailor the properties of the catalytic system.

Furthermore, nanoparticles are often immobilized onto a support, which provides further stabilisation as well as giving the system all the advantages of heterogeneous catalysts. Traditional supports include silica, alumina, titania, ceria, carbon and even magnetic substrates.^{17,18,19,20}

The structure and electronic properties of the support have a significant influence on the spatial location and stability of the immobilized nanoparticles, which on the other hand are likely to influence their catalytic behaviour. Indeed, when metal species are deposited on a solid substrate, their location is expected to depend on the surface structure of the support, but is also related to the type of metal NPs.⁸ For example, when gold is deposited on TiO₂, the formation of AuNPs occurs preferentially on the edge sites, while PtNPs are formed both on terrace and edge sites. The electronic interaction between Au-TiO₂ and Pt-TiO₂ may explain the different stability and mobility of the nanoparticles on the titania surface.²¹

The metal/support interaction can also be reflected on the shape of supported metal species, in particular when doping agents are introduced in the substrates causing charge transfer phenomena. For instance, the common 3D growth of AuNPs on pure CaO can be transformed in the formation of 2D gold monolayers by simply adding the 1-2 % of Mo, which is oxidised by transferring electrons to the Au orbitals thus resulting in a reinforced bonding of gold onto the oxide surface.^{22,23}

As previously discussed, the electronic structure of the metal NPs depends on the particles size, so that every electron transfer process between the support and the immobilized metal will be affected by the nanoparticles dimension. On a ceria support, PtNPs composed of 30 – 70 atoms present the highest positive charge, which indicates a strong electronic metal-support interaction. Following DFT calculations, this was attributed to the particle size of Pt, the density of Pt species and the concentration of Ce(III) on the CeO₂ surface. In many experimental works, the Pt-based catalysts with the highest efficiency were found to be those in the range of 1 – 3 nm, suggesting how the electronic interactions between metal and support influence the catalytic activity.^{8,24}

In general, supported large metal NPs (especially from noble metals such as Au, Ag, Pt) are preferentially found in the metallic state, while smaller metal clusters prefers to be positively charged, which is a medium state between metallic nanoparticles and isolated atoms. Furthermore, when NPs are deposited on electron-donor supports it is likely that the metal species will be in the electron-rich state, but when they are immobilized on electron-acceptor supports, a positive charge could be observed, resulting in a significant difference in the catalytic activity for a given reaction.

1.3 An overview on gold nanoparticles

1.3.1 Optical properties of gold nanoparticles

Gold chemistry had a late start, since the noble metal had been considered to be completely inert for centuries, but after the breakthrough discovery of the catalytic activity of supported gold nanoparticles (AuNPs) in the low-temperature oxidation of CO, it has evolved very rapidly.^{11,25}

The first investigation of the properties of AuNPs was reported by Faraday in 1857, after he accidentally observed the formation of a deep red colloidal gold solution by reduction of $[\text{AuCl}_4]^-$ ions in the presence of phosphorous in carbon sulfide. As a result, Faraday began to study the optical properties of thin films prepared from dried colloidal solutions and observed reversible colour changes upon mechanical compression.^{26,27}

Indeed, one of the most fascinating properties of AuNPs is the relation between their colour and dimension, which is caused by a phenomenon known as *Localised Surface Plasmon Resonance* (LSPR). When the size of metal particles is in the nanometres region, a large portion of electrons is located at the surface. This electron density is subjected to polarization and oscillation in resonance with the frequency of incident light (Figure 1.4).

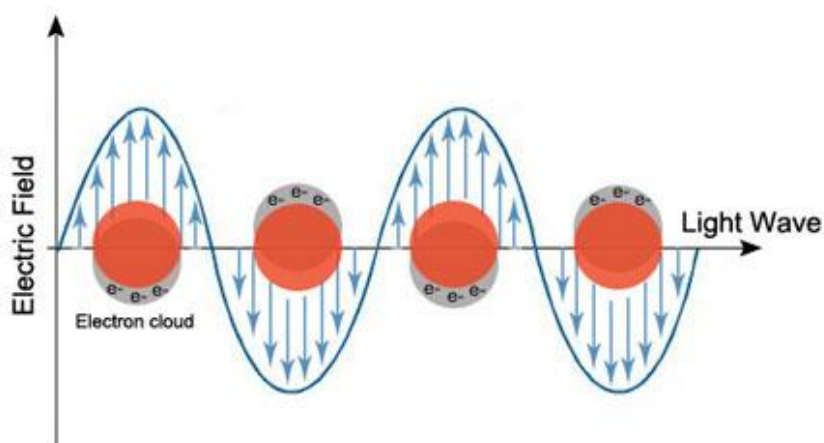


Figure 1.4. Localized surface plasmon resonance.²⁸

In the case of small monodisperse gold nanoparticles (~ 30 nm), the SPR phenomenon causes an absorption of light in the blue-green portion of the spectrum (450 - 550 nm) while red light is reflected, resulting in a rich red colour. However, by varying the AuNPs size and morphology, as well as the dielectric constant of the surrounding medium, the oscillation frequency of the surface electrons can be changed resulting in a variation of the absorption spectra (Figure 1.5).²⁹

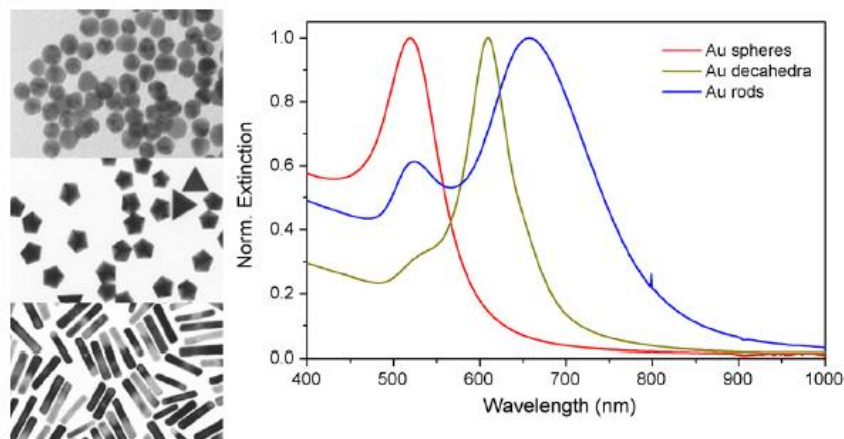


Figure 1.5. Transmission electron micrographs and UV-vis spectra of gold nanoparticle colloids with various geometries.³⁰

1.3.2 Synthesis of gold nanoparticles

There are two general approaches for the preparation of nanomaterials: 1) *top-down*, in which the bulk material is broken down to obtain particles of the desired dimensions (e.g. photolithography and electron beam lithography) and 2) *bottom-up*, in which nanoparticles are formed by assembling atoms and molecules.

Gold nanoparticles are generally prepared by reduction of a metal salt, in the presence of reducing and stabilising agents. The process consists of two stages, namely nucleation and particles growth. In *in situ* synthesis the two stages occur at the same time, resulting in the formation of spherical or quasi-spherical AuNPs, while in *seed-growth* methods the particles start to grow only once nucleation has stopped. The latter has emerged as an efficient strategy for the synthesis of mono-dispersed AuNPs with larger dimensions and well-defined shapes, e.g. rods, cubes, disks, etc.^{31,32,33,34,35}

The two most common approaches for the synthesis of colloidal AuNPs are the Turkevitch and the Brust-Schiffrin methods.

The Turkevich synthesis, first reported in 1951, consists in the reduction of aqueous HAuCl_4 by means of sodium citrate, which leads to the formation of AuNPs with an average size of 15 nm.³⁶ The citrate anion plays the role of both reducing and stabilising agent, by firstly reducing Au(III) ions to Au(0) and secondly providing electrostatic and steric stabilisation to the formed colloidal system (Figure 1.6).

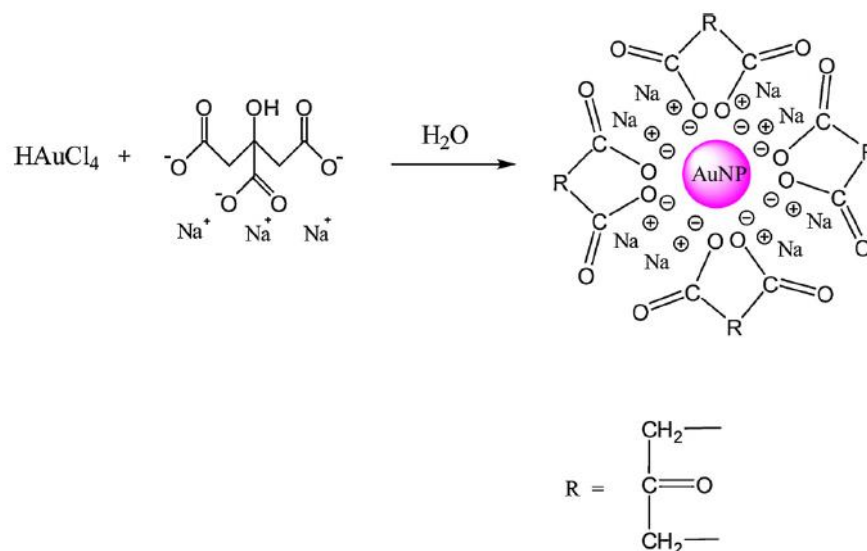


Figure 1.6. AuNPs synthesis by Turkevich method.³⁷

By changing parameters such as gold/citrate ratio, order of the addition, reagent concentrations, pH and temperature it is possible to control the size distribution of the formed gold nanoparticles. For instance, in 1973 Frens published a study on the modulation of AuNPs size (in the range 15 – 150 nm) by controlling the sodium citrate to gold ratio³⁸ while several groups recently reported the synthesis of nearly monodispersed AuNPs with size ranging from 20 to 40 nm upon variation of pH.^{37,39,40}

The stabilisation of gold nanoparticles by means of thiolates was first investigated by Mulvaney and Giersig with the employment of alkylthiols of various chain lengths.⁴¹ In 1994, Brust and Schiffrin reported a new method for the *in situ* synthesis of thiolate stabilised AuNPs in a two-phase system: $[\text{AuCl}_4]^-$ ions were transferred to toluene by the phase-transfer agent tetraoctylammonium bromide (TOAB) and then reduced with sodium borohydride (NaBH_4) in the presence of dodecanethiol (Figure 1.7).⁴²

The high impact of this novel procedure was due to the simplicity of the synthesis carried out under mild ambient conditions, the high thermal and air stability of the obtained system, the possibility to isolate and re-dissolved the AuNPs without aggregation or decomposition and the easy functionalisation and modification by ligand substitution. In addition, since NaBH_4 is a much stronger reductant compared to the sodium citrate used in Turkevich synthesis, the rate of AuNPs formation is faster, resulting in smaller nanoparticles (< 5 nm) with a narrow size distribution.³⁷

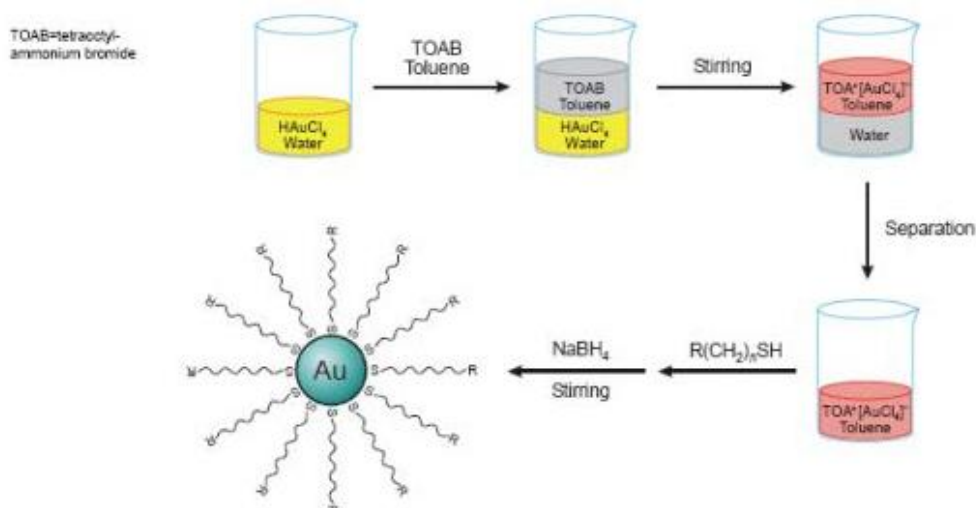


Figure 1.7. AuNPs synthesis by Brust-Schiffrin method.⁴²

Furthermore, an improvement of this method consists in conducting a single-phase synthesis in a solvent which is able to dissolve both $\text{H[AuCl}_4\text{]}$ and the stabilising thiolate agent. For example, *p*-mercaptophenol was used as a stabiliser for AuNPs synthesized in methanol⁴³ and (1-mercaptoundec-11-yl)tetraethylene glycol was employed for the preparation of biocompatible and water soluble AuNPs with size below 10 nm.⁴⁴

Since the stabilisation of gold nanoparticles systems is a key aspect for their application, over the years many research works focused on the study of possible stabilising ligands. Alongside the most commonly used sulphur based stabilisers, oxygen and nitrogen-based ligands containing electronegative groups such as amine, carboxyl, carbonyl and phenol have also been exploited.^{45,46,47} Besides, more recently N-heterocyclic carbenes (NHCs) have emerged as an alternative ligand class to functionalise gold surfaces and NPs, due to their strong gold-carbene bond and diverse design strategies.⁴⁸

1.4 Catalysis by supported gold nanoparticles

1.4.1 Preparation of heterogeneous catalysts based on gold nanoparticles

The method of preparation of supported gold nanoparticles strongly influences the resulting particles size, which in turn is fundamental in defining the catalytic activity. In general, the preparation strategies can be divided in two classes: 1) *coprecipitation*, in

which the support and the gold precursor are formed at the same time and 2) *impregnation*, in which the gold precursor is deposited on the preformed support (i.e. *ion adsorption* and *deposition-precipitation*).

The gold precursors are gold salts or complexes usually containing Au(III) ions, though sometimes precursors with Au(I) could be employed. The most common precursor is chloroauric acid (HAuCl_4), which is an orange solid with strong acidic properties in aqueous solution, but gold chloride (AuCl_3) is also occasionally used. Hence, in the majority of the preparation methods, gold ions are easily reduced by thermal treatments, which are usually performed in air. Nonetheless, it is very important to reduce the metal under controlled conditions, since parameters such as the nature of the gas, the flow rate, the heating rate and the final temperature determine the final particles size.⁴⁹

Gold nanoparticles supported on various oxides, i.e. Fe_2O_3 , NiO and Co_3O_4 , by *coprecipitation* were obtained by adding sodium carbonate to an aqueous solution of HAuCl_4 and the nitrate of the metal that will form the support. The coprecipitates were then washed, dried and calcinated to obtain AuNPs. However, this method was found to work only for certain metal oxides, since the rate of precipitation and the affinity of the metal with gold determine the AuNPs size.^{49,50}

The first supported gold catalysts were prepared by *impregnation*, which can be applied to any oxide support by filling its pores with a solution of the gold precursor and subsequently drying the system.^{51,52} When the deposition of the precursor is carried out in an aqueous media, the pH value plays a fundamental role in controlling the distribution of the gold ions and the net charge of the solid support surface. Indeed, at the pH value corresponding to the isoelectric point (IEP) the surface is neutral, but below or above this value it becomes positively or negatively charged as a result of protonation or deprotonation. On the basis of the isoelectric point, metal oxides were classified as acidic or basic, depending on the ability of the surface to release or acquire protons.^{53,54}

In *ion adsorption* methods, the anionic gold species in solution are spontaneously adsorbed through electrostatic interactions on the hydroxyl groups of the support. For instance, one of the most common supports for heterogeneous gold catalysts is titania (TiO_2), which is positively charged at $\text{pH} < 6$ ($\text{IEP}_{\text{TiO}_2} = 6$) and can absorb gold anions such as $[\text{AuCl}_4]^-$ and $[\text{AuCl}_3(\text{OH})^-]$. In fact, it has been reported that up to the 60 % of a HAuCl_4 solution can be absorbed on titania at pH 3, when $[\text{AuCl}_3(\text{OH})^-]$ is predominant,

since the interaction of gold species with the support surface is supposed to be more favourable for hydrolysis species containing Au-OH groups than Au-Cl.

Deposition-precipitation is an alternative to ion adsorption consisting in the hydrolysis of $[\text{AuCl}_4]^-$ by raising the pH of the solution, to obtain the formation of insoluble $\text{Au}(\text{OH})_3$ which precipitates and adsorbs on the support.^{55,56} This method was first proposed by Haruta⁵⁷ and quickly became the most common one for gold catalysts preparation, but over the years several studies demonstrated the complexity of the precipitation/adsorption mechanism, strongly dependent on the nature of the support. Indeed, this methodology works well for supports with high IEP such as magnesia, titania, alumina, zirconia and ceria, but not for silica (IEP = 2).⁵⁸

By comparison of the experimental results of the ion adsorption and deposition-precipitation methods, it was proved that the main difference between the two is the mobility of the gold species on the support. In particular, the initial metal dispersion obtained in the former is higher than that observed in the latter, nonetheless this results in the formation of larger particles after the thermal treatment following ion adsorption, due to the higher mobility of anionic gold species.⁵⁹

Furthermore, one of the critical point in the preparation of supported gold catalysts from classical methods is the removal of chloride ions. Indeed, it was reported that the presence of Cl^- promotes nanoparticles aggregation during thermal treatment by favouring the mobility of gold atoms and, in addition, has a negative influence on gold catalytic activity.^{60,61} Since in order to efficiently remove chloride, temperatures higher than 600 °C are required, washing and hydrogen stream treatments are the preferred choice.⁵⁴

Finally, an interesting alternative to the previously illustrated methods is the adsorption of preformed AuNPs, particularly useful in the case of silica and carbon supports, which are not suitable for impregnation methods due to the nature of their surfaces.⁶² For this purpose, gold nanoparticle can be obtain as stabilised-colloidal solutions by the classic Turkevich and Brust-Schiffrin synthesis, or can be formed by chemical vapour deposition and sonochemical or photochemical irradiation, prior to their deposition on the support.⁵⁴

1.4.2 Characterisation of gold catalysts

The study of the physical and chemical properties of supported AuNPs catalysts is fundamental in order to understand the nature of the active sites and improve their performances. A large variety of techniques can be applied for this purpose, as summarised in Figure 1.8.^{63,64}

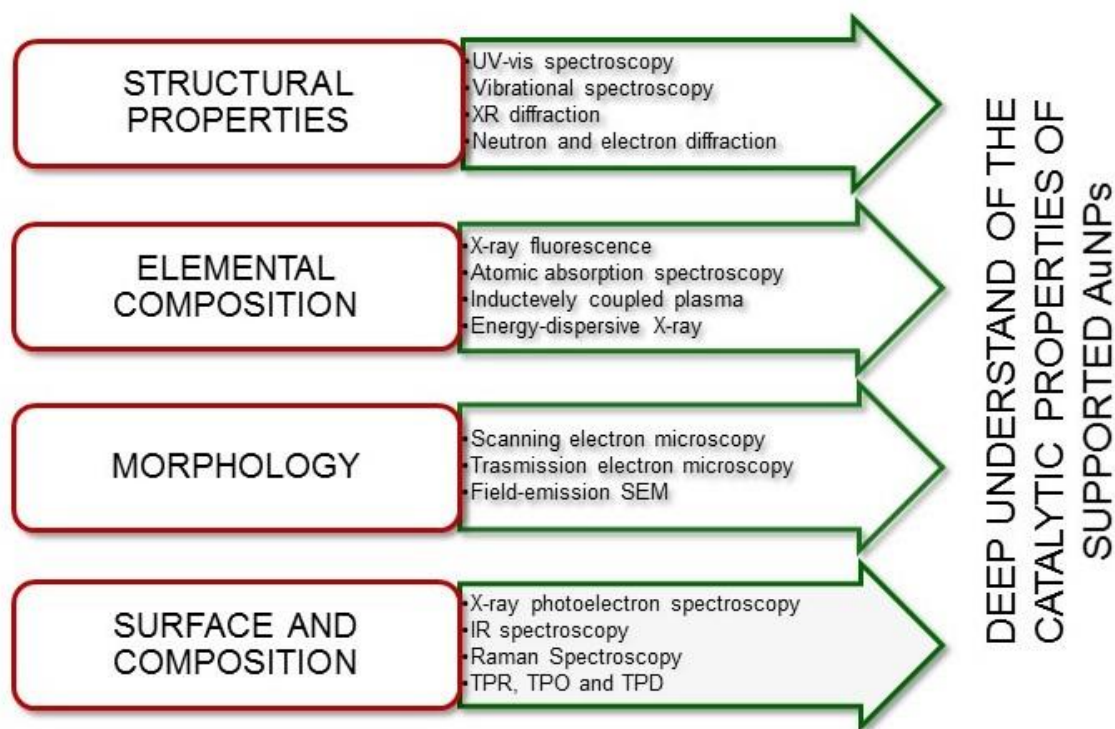


Figure 1.8. Characterisation techniques for AuNPs catalysts, reproduced from reference 63.

Information regarding the structural properties can be obtained by X-ray diffraction (XRD), UV-vis and vibrational spectroscopy and neutron and electron diffraction. X-ray fluorescence (XRF), atomic absorption spectroscopy (AAS), inductively coupled plasma (ICP) and energy-dispersive X-ray (EDX) can help investigating the elemental composition, while microscopic techniques such as transmission electron microscopy (TEM) and scanning electron microscopy (SEM) are commonly used to study the morphology and size of AuNPs. Finally the surface structure and composition is often investigated by means of Raman and X-ray photoelectron spectroscopy (XPS).

1.4.3. The importance of the support

In heterogeneous gold nanoparticles catalysis the primary role of the support is to avoid agglomeration of the immobilised AuNPs, since their catalytic activity decreases significantly with the increasing of particle size, as shown in Figure 1.9.

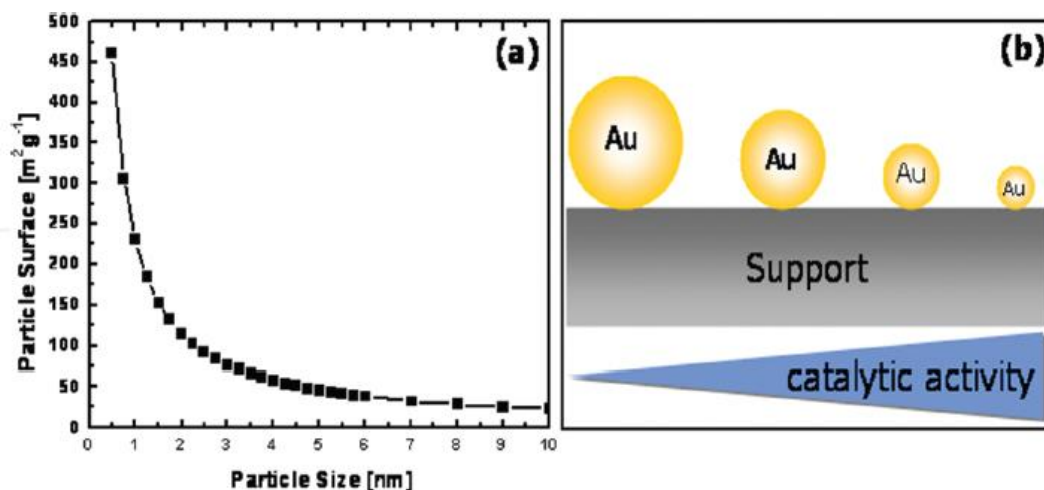


Figure 1.9. Relation between size of AuNPs and a) surface area and b) catalytic activity.⁶³

Furthermore, the support can improve the thermal and mechanical stability of the catalyst, provides enhanced surface area and dispersion of active components and can influence the electronic properties of the supported AuNPs.

In general, the definition of the electronic interactions between the metal nanoparticles and the support is rather complex. Indeed, charge transfer can occur in either directions, depending on the metal, the nature of the support and the presence of defects.⁶⁵ The Au4f core level binding energy (BE) of supported AuNPs, measured by XPS analysis, is generally shifted to higher values when decreasing particle size, due to the occurrence of Au-support transitions.^{66,67} For instance, in the case of Au/SiO₂ and Au/TiO₂ systems, this BE shift was found to be 1.6 and 0.8 eV respectively, because of the little charge transfer occurring with the poorly conductive silica support as opposed to the charge transfer from surface oxygen vacancies of TiO₂ to Au.^{68,69}

The supports can even play a direct or indirect role in the catalytic mechanism.⁷⁰ For example, the oxidation of CO at low temperatures (< 200 °C) does not occur in the presence of AuNPs nor TiO₂, but when the catalytic system consists of gold nanoparticles supported on titania (Au/TiO₂) the reaction can take place at 25 °C. On the contrary, different supports such as alumina and activated carbon do not produce similar results.⁶³

1.4.4 Supported gold nanoparticles catalysts for organic reactions

The extraordinary interest in gold catalysis is clearly evident from the remarkable increasing of the number of publications concerning this topic which occurred over the years (Figure 1.10).

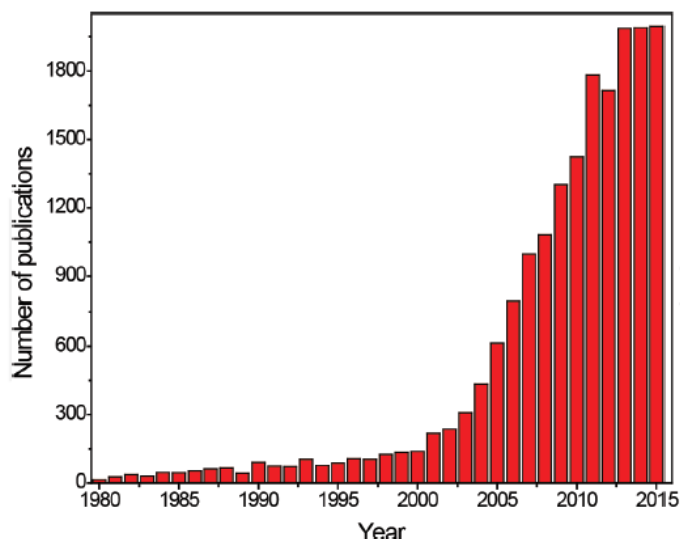


Figure 1.10. Publications on gold catalysis in the academic literature (source: SciFinder Scholar).⁶³

Considering the large number of reaction catalysed by gold, the following section aims to briefly illustrate only a few examples concerning some of the most common transformations in organic chemistry.

Gold-catalysed hydrogenations generally require high temperatures (100 – 250 °C), for instance AuNPs supported on silica were found to be efficient in the hydrogenation of pentene, 1,3-butadiene and 2-butyne at 100°C.⁷¹ Besides, a study involving the use of a Au/ZrO₂ system hypothesized that isolated Au(III) ions on the support were the active catalytic sites for the hydrogenation of 1,3-butadiene and that the presence of surface hydroxyl groups in zirconia was of fundamental importance for an efficient transformation of the substrate.^{72,73,74}

The synergism between AuNPs and other metal nanoparticles in the hydrogenation of unsaturated compounds was also investigated. For instance, the hydrogenation of acetylene and phenylacetylene was successfully carried out on a Au-Ni/Al₂O₃ bimetallic catalyst, possibly due to the formation of new active sites with improved adsorption and catalytic properties as a result of the electron transfer from Au to Ni.⁷⁵ Furthermore, in the

presence of a bimetallic Au-PtNPs catalyst, the selective hydrogenation of the double bond of cinnamaldehyde was observed, while the carbonyl functionality was unaffected.^{76,77}

Another important class of organic reactions catalysed by gold is the formation of C-C bonds. Surprisingly, in the typical reaction conditions for the Suzuki-Miyaura cross-coupling between phenylboronic acid and iodobenzene, Au/CeO₂ promotes the formation of the homo-coupling product.⁷⁸ The same reaction is also catalysed by small AuNPs stabilised on biopolymers such as poly(N-vinyl-2-pyrrolidone), chitosan and other oxide supports, in the presence of gold cationic additives.^{79,80,81}

Furthermore, Au/CeO₂ is able to promote the Sonogashira cross-coupling between iodobenzene and phenylacetylene in moderate yields. In fact, by working in DMF at 150 °C the complete conversion of iodobenzene was achieved after 24 h, though leaching of gold from the support was observed.⁸² In addition, AuNPs supported on silica were found to be active in the Sonogashira coupling of a series of terminal alkynes and aryl iodides in DMF under microwave irradiation.⁸³

The use of AuNPs-based catalysts in other two important transformations in organic synthesis, i.e. oxidation of alcohols and hydroamination of alkynes, will be addressed in more detail in the upcoming chapters.

Moreover, gold heterogeneous catalysis is starting to find interesting applications also at the industrial scale. One of the most representative examples is the recent development of a recyclable gold catalyst for the production of vinyl chloride by acetylene hydrochlorination, as a more sustainable alternative to the classic mercury based catalyst (HgCl₂ supported on carbon).

Initially, the simple adsorption of HAuCl₄ on activated carbon led to a novel system which displayed activity and selectivity almost comparable to the ones of the mercury based catalyst, but deactivated rather quickly. Even if the catalytic activity could be easily restored by HCl treatments, this deactivation problem posed serious limits to real industrial applications. After extensive studies on the deactivation mechanism, a highly active catalyst was finally obtained by supporting Na₃Au(S₂O₃)₂ on carbon extrudates. The presence of the sulfur-containing anions contributed to the stabilisation of the gold species and significantly enhanced the catalyst resistance to deactivation.^{84,85}

1.5 Flow chemistry

1.5.1 An introduction to flow chemistry

The concept of *flow chemistry* refers to the conduction of chemical reactions in continuous-flow conditions, as opposed to the classic discontinuous *batch* synthesis. While the introduction of flow chemistry at the laboratory scale is a relatively new topic, industrial production of both bulk and fine chemicals have been carried out in continuous conditions for a much longer time.

In flow chemistry, the reactants are pumped into tubes and mixers and the stoichiometry of the reaction is determined by the concentration of the reagents streams and the ratio of their flow rate. Moreover, the reaction time is defined by the volume of the reactor and the total flow rate, while in batch systems it simply depends on how long the reactor is held at a given temperature to reach the desired conversion (Figure 1.11).⁸⁶

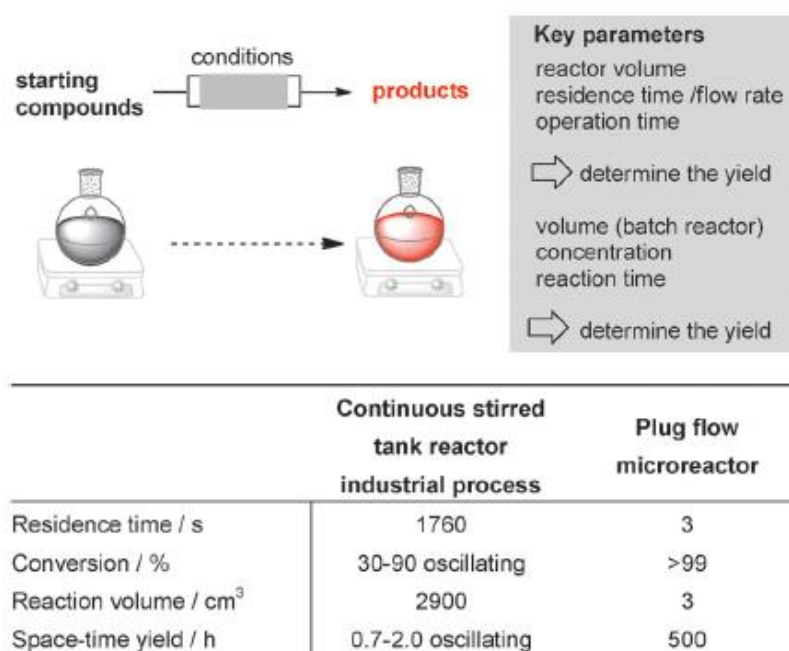


Figure 1.11. Key parameters in flow versus batch reaction and comparative example of a batch and flow process.⁸⁷

In order to maximise the productivity of a flow process, full conversion should be reached by working at the highest possible flow rates, as the correlation between flow rate and residence time (the ratio between reactor volume and volumetric flow rate) determines

how much product is formed in a unit time. Under optimised conditions, a flow reactor can operate in a continuous way as long as starting materials are pumped inside the system.⁸⁷

The size of a flow reactor, in particular its internal diameter, is an important parameter to take into account during the set-up of a continuous-flow system. Indeed, the heat transfer capacity of a tubular reactor is strongly influenced by channel size since it determines the heat transfer area per unit volume, hence higher heat transfer capacities are achieved with smaller diameters. As a drawback, high pressure drops, limited flow capacity and tendency to block set a limit to the miniaturisation of the reactors.⁸⁷ For these reasons, the reactor diameters commonly used for continuous-flow applications range between 10 μm to several millimetres.

The great interest in the field of flow chemistry is due to the many advantages associated to continuous processing.

One of the major benefits is related to process safety, since microfluidic reactors have intrinsic properties that make them ideal environments for the performance of dangerous reactions. The small volumes involved in these systems provide an excellent control over heat transfer during exothermic reactions with the risk of thermal runaways, which are particularly challenging to control in batch conditions. In fact, in classic batch processes, reagents such as organometallics, strong bases and highly active electrophiles need to be added slowly to the reaction mixture and cryogenic conditions are often required. Since this problem becomes even more difficult to manage at larger scale, the use of flow microreactors comes as a good solution. Indeed, the high surface to volume ratio of these systems makes the heat transfer more efficient, with a rapid removal of thermal energy. As a result, many works report the possibility to perform reactions in flow at 0 °C or room temperature, while the same transformation in batch would require cryogenic conditions.^{88,89} This also result in an overall reduced processing time, as reactions will occur faster at elevated temperatures and inefficient cooling and warming steps are avoided.⁹⁰

Furthermore, hazardous reagents and highly unstable intermediates can be treated with reduce risks by avoiding their accumulation in large quantities. In particular, flow chemistry can give access to those transformations which otherwise would be impossible, because of the harsh conditions required (high pressure and temperature) or the necessity to handle problematic chemicals (toxic or hazardous reagents and intermediates).^{91,92}

Even though it would not be correct to state that microfluidic reactors increases the intrinsic reaction rate compared to batch, since the reaction kinetics are generally not related to large-scale diffusion, it is often observed that the space-time yields (product formed per reactor volume and time) reported for flow conditions are higher than those obtained in batch reactors. This is because batch process often incorporate extra time to ensure the achievement of complete conversion, while flow reaction are usually more efficiently optimised.⁹² In addition, flow processes can be run for much longer times compared to the batch ones, without the need to interrupt the production for products recovery or catalyst regeneration.

At the industrial scale, the enhanced heat and mass transfer of flow reactors allow to reduce significantly the energy costs. Besides, the modular nature of this technology gives access to a certain flexibility in the production, since the amount of synthesized products can be easily regulated in order to meet the market demand. In fact, the scale-up of a flow process can be obtained by simply increasing the operating time or the reactor length, while in order to change the total production of a batch system, the reaction needs to be run multiple times in a small reactor or the reactor volume must be increased, which may require changing the experimental conditions.⁹²

Another interesting advantage of flow processing is the possibility to easily run multi-step reactions avoiding work-up and purifications steps, which requires significant input of energy and solvents that end up as wastes.

Finally, the integration of in-line analysis, such as UV-vis, Raman, IR, NMR and mass spectrometry, enables obtaining a large amount of information in real time, making it possible to operate directly on the process to enhance its efficiency and quality.⁹³

1.5.2 Nanocatalysis in continuous-flow systems

The combination of continuous-flow technology and heterogeneous catalysis allows to perform chemical reactions in a more sustainable way, avoiding wasteful isolation and purification procedures.

The immobilization of the catalytic system in microfluidic devices can be carried out following three different approaches: 1) *packed-bed*, where the reactor is filled with the supported catalyst, 2) *monolithic*, which consists of a regular or irregular network of porous channels obtained by copolymerization of different monomer, one containing the catalyst and 3) *wall-coated*, where the catalyst is immobilised on the inner walls of the reactor itself (Figure 1.12).^{94,95,96}

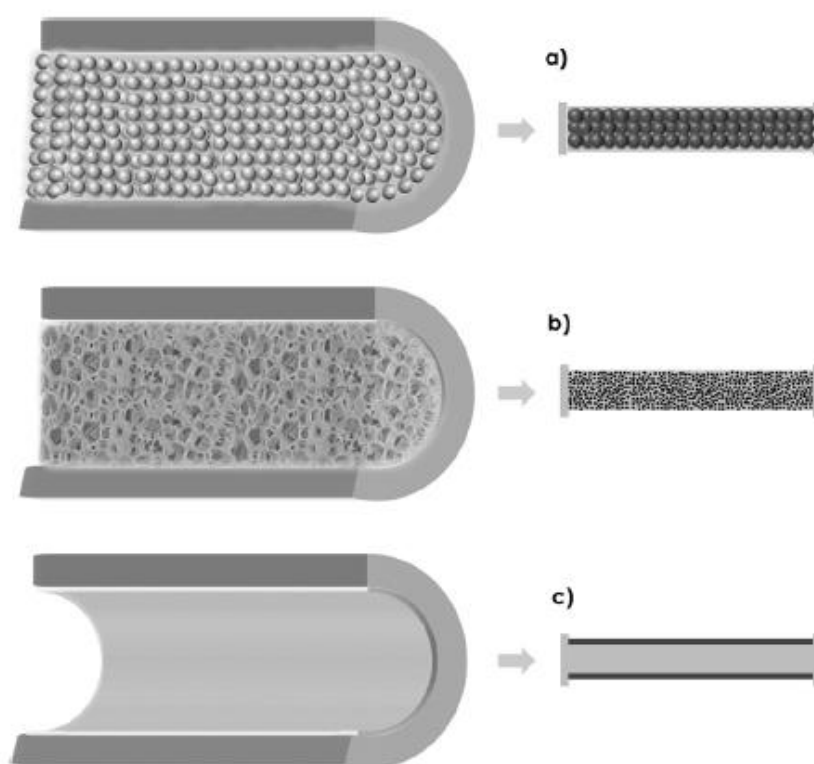


Figure 1.12. Schematic representation of the cross-section of a microchannel in a) packed-bed, b) monolithic, and c) wall-coated microreactors.⁹⁴

Among these, the easiest way to prepare a catalytic flow reactor is to fill it with catalyst-supported beads, resins or polymers.⁹⁵ The main advantages of this system are associated to the high catalyst loading, the easy characterisation and quantification of the catalyst, the possibility to use a wide range of supports and the simple manufacturing. However, limits can arise from uncontrolled fluid dynamics, heat transfer limitation and

significant pressure drops. In particular, the pressure drop increases with $1/D_p$ (where D_p is the particles size), so that there is a limit to the use of small particles for the packing of these systems.⁹⁶

Typically, the catalysts employed in packed-bed reactors are metals or metal oxides nanoparticles immobilized on oxide, carbon or polymers supports. For example, PdNPs supported on alumina catalysed both the full and partial oxidation of methane in a microreactor, using gas compositions in the explosive regime under controlled conditions.⁹⁷ Moreover, a Pd/Fe₂O₃ catalyst was found to catalyse the sequential transfer hydrogenation/hydrogenolysis of furfural and 5-(hydroxymethyl)furfural using 2-propanol as hydrogen donor. When working with low residence time, the selectivity was shifted towards the formation of furfuryl alcohol, but by simply changing this parameter by decreasing the flow rate, significant amounts of 2-methylfuran and ring-hydrogenated products were observed. On the contrary, in batch processes, the two latter products were formed only in trace amounts.⁹⁸

Monoliths are solids with an interconnected continuous porous network that can be formed from organic and inorganic polymers. Due to their peculiar structure, these materials present a large surface area and a high void volume, resulting in low pressure drops and efficient contact between reagents and catalytic sites.⁹⁹ The most used monoliths consist of polymers, hybrid polymers/glass composites and inorganic matrices such as silica and zeolites, which can be easily functionalised with catalytically active species.⁹⁵ As an example, Lev's group developed an organic monolithic reactor with a quaternary ammonium functionalisation and immobilised PdNPs (Figure 1.13). This system was tested in the continuous-flow Heck reaction, achieving quantitative conversions and high selectivity for a wide range of aryl halides and alkenes.¹⁰⁰

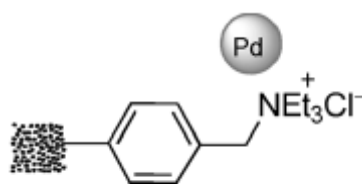


Figure 1.13. Macroporous organic monolith functionalised with PdNPs.⁹⁴

Finally, in wall-coated microreactors the catalyst active phase is deposited directly on the reactor walls, with a substantial minimisation of the problems related to pressure

drops and reactor clogging. Generally, the reactor surface is subjected to a chemical treatment or to the application of thin films which can be catalytically active or serve as a support for a catalytic phase.⁹⁴ In this regard, both nanoparticulate ceria and AuNPs supported on ceria were deposited as a thin film on the inner walls of a flow microreactor used for the selective production of N-phenyl carbamate from aniline and dimethyl carbonate. The two catalysts displayed a high selectivity and the AuNPs/CeO₂ system was found to be more active (Figure 1.14).¹⁰¹

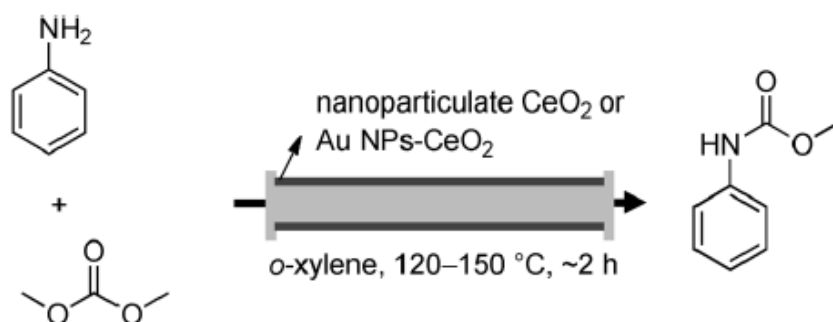


Figure 1.14. Carbamoylation of aniline catalysed by nanoparticulate CeO_2 and AuNPs/ CeO_2 catalysts.⁹⁴

References

- ¹ The Royal Society & The Royal Academy of Engineering, *Nanoscience and nanotechnologies. Opportunities and uncertainties*, Royal Society, London, **2004**.
- ² www.nano.gov
- ³ P. Serp, K. Philippot, *Concepts in Nanocatalysis*, in *Nanomaterials in Catalysis*, Wiley-VCH Verlag GmbH & Co, **2013**.
- ⁴ K. J. Klabunde, *Introduction to nanotechnology*, in *Nanoscale Materials in Chemistry*, John Wiley & Sons, Inc., Hoboken, **2001**.
- ⁵ G. A. Somorjai, J. Carrazza, *Ind. Eng. Chem. Fundam.*, **1986**, *25*, 63.
- ⁶ M. Che, C. O. Bennett, *Adv. Catal.*, **1989**, *36*, 55.
- ⁷ R. A. Van Santen, *Acc. Chem. Res.*, **2009**, *42*, 57.
- ⁸ L. Liu, A. Corma, *Chem. Rev.*, **2018**, *118*, 4981.
- ⁹ L. D. Rampino, F. F. Nord, *J. Am. Chem. Soc.*, **1941**, *63*, 2745.
- ¹⁰ D. Y. Cha, G. Parravano, *J. Catal.*, **1970**, *18*, 320.
- ¹¹ M. Haruta, N. Yamada, T. Kobayashi, S. Iijima, *J. Catal.*, **1989**, *115*, 301.
- ¹² D. Astruc, F. Lu, J. R. Aranzas, *Angew. Chem. Int. Ed.*, **2005**, *44*, 7852.
- ¹³ R. Sablong, U. Schlotterbeck, D. Vogt, S. Mecking, *Adv. Synth. Catal.*, **2003**, *345*, 333.
- ¹⁴ A. M. Fargo, J.F. Odzak, F. S. Lai, B. C. Gates, *Nature*, **2002**, *415*, 623.
- ¹⁵ L. Strimbu, J. Liu, A. E. Kaifer, *Langmuir*, **2003**, *19*, 483.
- ¹⁶ M. K. Chung, G. Orlova, J. D. Goddard, M. Schlaf, R. Harris, T. J. Beveridge, G. White, F. R. Hallett, *J. Am. Chem. Soc.*, **2002**, *124*, 10508.
- ¹⁷ S. Jansat, K. Pelzer, J. García-Anton, R. Raucoles, K. Philippot, A. Maisonnat, B. Chaudret, Y. Guari, A. Mehdi, C. Reye, R. J. P. Corriu, *Adv. Funct. Mater.*, **2007**, *17*, 3339.
- ¹⁸ H. P. Kormann, G. Schmid, K. Pelzer, K. Philippot, B. Chaudret, *Z. Anorg. Allg. Chem.*, **2004**, *630*, 1913.
- ¹⁹ E. Castillejos, P. J. Deboutiere, L. Roiban, A. Solhy, V. Martinez, Y. Kihn, O. Ersen, K. Philippot, B. Chaudret, P. Serp, *Angew. Chem. Int. Ed.*, **2009**, *48*, 2529.
- ²⁰ D. Rosario-Amorin, X. Wang, M. Gaboyard, R. Clerac, S. Nlate, K. Heuze, *Chem. Eur. J.*, **2009**, *15*, 12636.
- ²¹ X. Q. Gong, A. Selloni, O. Dulub, P. Jacobson, U. Diebold, *J. Am. Chem. Soc.*, **2008**, *130*, 370.

-
- ²² S. Schauermaun, N. Nilius, S. Shaikhutdinov, H. J. Freund, *Acc. Chem. Res.*, **2013**, *46*, 1673.
- ²³ X. Shao, S. Prada, L. Giordano, G. Pacchioni, G. Nilius, H. J. Freund, *Angew. Chem. Int. Ed.*, **2011**, *50*, 11525.
- ²⁴ P. Serna, A. Corma, *ACS Catal.*, **2015**, *5*, 7114.
- ²⁵ H. G. Raubenheimer, H. Schmidbaur, *J. Chem. Educ.*, **2014**, *91*, 2024.
- ²⁶ M. Faraday, *Philos. Trans.*, **1857**, *147*, 145.
- ²⁷ M. C. Daniel, D. Astruc, *Chem. Rev.*, **2004**, *104*, 293.
- ²⁸ <http://www.cytodiagnosics.com>
- ²⁹ S. Eustis, M. A. El-Sayed, *Chem. Soc. Rev.*, **2006**, *35*, 209.
- ³⁰ B. Sepùlveda, P. C. Angelomé, L. M. Lechuga, L. M. Liz-Marzàn, *Nano Today*, **2009**, *4*, 244.
- ³¹ B. Nikoobakht, M. A. E. I. Sayed, *Chem. Mater.*, **2003**, *15*, 1957.
- ³² J. Perez-Juste, L. M. Liz-Marzan, S. Carnie, D. Y. C. Chan, P. Mulvaney, *Adv. Funct. Mater.* **2004**, *101*, 571.
- ³³ J. Rodriguez-Fernandez, J. Perez-Juste, F. J. Garcia, L. M. Liz-Marzan, *Langmuir*, **2006**, *22*, 7007.
- ³⁴ S. D. Perrault, W. C. W. Chan, *J. Am. Chem. Soc.*, **2009**, *131*, 17042.
- ³⁵ N. G. Bastus, J. Comenge, V. Puentes, *Langmuir*, **2011**, *27*, 11098.
- ³⁶ J. Turkevich, P. C. Stevenson, J. Hillier, *Discuss. Faraday Soc.*, **1951**, *11*, 55-75.
- ³⁷ P. Zhao, N. Li, D. Astruc, *Coord. Chem. Rev.*, **2013**, *257*, 638.
- ³⁸ G. Frens, *Phys. Sci.*, **1973**, *241*, 20.
- ³⁹ C. Li, D. Li, G. Wan, J. Xu, W. Hou, *Nanoscale Res. Lett.*, **2011**, *6*, 440.
- ⁴⁰ M. R. Rahman, F. S. Saleh, T. Okajima, T. Ohsaka, *Langmuir*, **2011**, *27*, 5126.
- ⁴¹ M. Giersig, P. Mulvaney, *Langmuir*, **1993**, *9*, 3408.
- ⁴² M. Brust, M. Walker, D. Bethell, D. J. Schiffrin, R. J. Whyman, *J. Chem. Soc., Chem. Commun.*, **1994**, *0*, 801.
- ⁴³ M. Brust, J. Fink, D. Bethell, D. J. Schiffrin, C. J. Kiely, *J. Chem. Soc., Chem. Commun.*, **1996**, *0*, 1655.
- ⁴⁴ A. G. Kanaras, F. S. Kamounah, K. Schaumburg, C. J. Kiely, M. Brust, *Chem. Commun.*, **2002**, *20*, 2294.

-
- ⁴⁵ A. Kumar, S. Mandal, P. R. Selvakannan, R. Paricha, A. B. Mandale, M. Sastry, *Langmuir*, **2003**, *19*, 6277.
- ⁴⁶ F. Porta, Z. Krpetic, L. Prati, A. Gaiassi, G. Scari, *Langmuir*, **2008**, *24*, 7061.
- ⁴⁷ R. Shomura, K. J. Chung, H. Iwai, M. Higuchi, *Langmuir*, **2011**, *27*, 7972.
- ⁴⁸ S. Engel, E. C. Fritz, B. J. Ravoo, *Chem. Soc. Rev.*, **2017**, *46*, 2057.
- ⁴⁹ G. C. Bond, C. Louis, D. T. Thompson, *Catalysis by gold*, Imperial College Press, London, **2006**.
- ⁵⁰ S. Tsubota, M. Haruta, T. Kobayashi, A. Ueda, Y. Nakahara, *Stud. Surf. Sci. Catal.*, **1991**, *72*, 695.
- ⁵¹ G. C. Bond, D. T. Thompson, *Catal. Rev. Sci. Eng.* **1999**, *41*, 319.
- ⁵² P. A. Sermon, G. C. Bond, P. B. Wells, *J. Chem. Soc. Faraday Trans.*, **1979**, *75*, 385.
- ⁵³ C. H. Sun, J. C. Berg, *Adv. Colloid Interface Sci.*, **2003**, *105*, 151.
- ⁵⁴ A. Corma, H. Garcia, *Chem. Soc. Rev.*, **2008**, *37*, 2096.
- ⁵⁵ J. W. Geus, J. A. R. van Veen, *Stud. Surf. Sci. Catal.*, **1999**, *123*, 459.
- ⁵⁶ M. Haruta, *Gold Bull.*, **2004**, *37*, 27.
- ⁵⁷ M. Haruta, S. Tsubota, T. Kobayashi, H. Kageyama, M. J. Genet, B. Delmon, *J. Catal.*, **1993**, *144*, 175.
- ⁵⁸ M. Haruta, *CATTECH*, **2002**, *6*, 102.
- ⁵⁹ W. C. Li, M. Comotti, F. Schuth, *J. Catal.*, **2006**, *237*, 190.
- ⁶⁰ S. Ivanova, V. Pitchon, C. Petit, H. Herschbach, A. Van Dorsselaer, E. Leize, *Appl. Catal.*, **2006**, *298*, 203.
- ⁶¹ S. C. Parker, C. T. Campbell, *Top. Catal.*, **2007**, *44*, 3.
- ⁶² L. Prati, G. Martra, *Gold Bull.*, **1999**, *32*, 96.
- ⁶³ A. Alshammari, V. N. Kalevaru, *Supported gold nanoparticles as promising catalysts in Catalytic application of nano-gold catalysts*, IntechOpen, London, **2016**.
- ⁶⁴ A. Villa, N. Dimitratos, C. E. Chan-Thaw, C. Hammond, G. M. Veith, D. Wang, M. Manzoli, L. Prati, G. J. Hutchings, *Chem. Soc. Rev.*, **2016**, *45*, 4953.
- ⁶⁵ G. Kumar, L. Tibbitts, J. Newell, B. Panthi, A. Mukhopadhyay, R. M. Rioux, C. J. Pursell, M. Janik, B. D. Chandler, *Nature Chemistry*, **2018**, *10*, 268.
- ⁶⁶ S. B. DiCenzo, S. D. Berry, E. H. Hartford, *Phys. Rev. B: Condens. Matter Mater. Phys.*, **1988**, *38*, 8465.
- ⁶⁷ O. Cordes, M. Harsdorff, *Appl. Surf. Sci.*, **1988**, *33*, 152.

-
- ⁶⁸ C. Chusuei, X. Lai, K. Luo, D. W. Goodman, *Top. Catal.*, **2001**, *14*, 71.
- ⁶⁹ W. Huang, G. Sun, T. Cao, *Chem. Soc. Rev.*, **2017**, *46*, 1977.
- ⁷⁰ S. J. Tauster, S. C. Fung, R. T. K. Baker, J. A. Horsley, *Science*, **1981**, *211*, 1121.
- ⁷¹ G. C. Bond, P. A. Sermon, G. Webb, D. A. Buckanan, P. B. J. Wells, *Chem. Soc., Chem. Commun.*, **1973**, *0*, 444.
- ⁷² M. Stratakis, H. Garcia, *Chem. Rev.*, **2012**, *112*, 4469.
- ⁷³ X. Zhang, H. Shi, B. Q. Xu, *Angew. Chem. Int. Ed.*, **2005**, *44*, 7132.
- ⁷⁴ X. Zhang, H. Shi, B. Q. Xu, *J. Catal.*, **2011**, *279*, 75.
- ⁷⁵ S. A. Nikolaev, V. V. Smirnov, *Catal. Today*, **2009**, *147*, 336.
- ⁷⁶ Y. C. Hong, K. Q. Sun, G. R. Zhang, R. Y. Zhong, B. Q. Xu, *Chem. Commun.*, **2011**, *47*, 1300.
- ⁷⁷ K. Q. Sun, Y. C. Hong, G. R. Zhang, B. Q. Xu, *ACS Catal.*, **2011**, *1*, 1336.
- ⁷⁸ S. Carrettin, J. Guzman, A. Corma, *Angew. Chem. Int. Ed.*, **2005**, *44*, 2242.
- ⁷⁹ H. Tsunoyama, H. Sakurai, N. Ichikuni, Y. Negishi, T. Tsukuda, *Langmuir*, **2004**, *20*, 11293.
- ⁸⁰ A. Primo, F. Quignard, *Chem. Commun.*, **2010**, *46*, 5593.
- ⁸¹ N. G. Willis, J. Guzman, *J. Appl. Catal. A*, **2008**, *339*, 68.
- ⁸² C. Gonzalez-Arellano, A. Abad, A. Corma, H. Garcia, M. Iglesias, F. Sanchez, *Angew. Chem. Int. Ed.*, **2007**, *46*, 1536.
- ⁸³ R. O. M. A. de Souza, M. S. Bittar, L. V. P. Mendes, C. M. F. da Silva, V. T. da Silva, O. A. C. Antunes, *Synlett.*, **2008**, 1777.
- ⁸⁴ R. Ciriminna, E. Falletta, C. Della Pina, J. Henrique Teles, M. Pagliaro, *Angew. Chem. Int. Ed.*, **2016**, *55*, 14210.
- ⁸⁵ P. Bishop, N. A. Carthey, WO 2013/008004, **2013**.
- ⁸⁶ J. Wegner, S. Ceylan, A. Kirschning, *Adv. Synth. Catal.*, **2012**, *354*, 17.
- ⁸⁷ J. Wegner, S. Ceylan, A. Kirschning, *Chem. Commun.*, **2011**, *47*, 4583.
- ⁸⁸ V. Hessel, C. Hofmann, H. Löwe, A. Meudt, S. Scherer, F. Schönfeld, B. Werner, *Org. Process Res. Dev.*, **2004**, *8*, 511.
- ⁸⁹ T. Gustafsson, H. Sörensen, F. Pontén, *Org. Process Res. Dev.*, **2012**, *16*, 925.
- ⁹⁰ S. G. Newman, K. F. Jensen, *Green Chem.*, **2013**, *15*, 1456.
- ⁹¹ K. S. Elvira, X. Casadevall i Solvas, R. C. R. Wootton, A. J. deMello, *Nature Chemistry*, **2013**, *5*, 905.

-
- ⁹² C. Wiles, P. Watts, *Green Chem.*, **2014**, *16*, 55.
- ⁹³ V. Sans, L. Cronin, *Chem. Soc. Rev.*, **2016**, *45*, 2032.
- ⁹⁴ R. Munirathinam, J. Huskens, W. Verbooma, *Adv. Synth. Catal.*, **2015**, *357*, 1093.
- ⁹⁵ R. Ricciardi, J. Huskens, W. Verboom, *Chem. Sus. Chem.*, **2015**, *8*, 2586.
- ⁹⁶ A. Tanimu, S. Jaenicke, K. Alhooshani, *Chem. Eng. J.*, **2017**, *327*, 792.
- ⁹⁷ O. Younes-Metzler, J. Svagin, S. Jensen, C. H. Christensen, O. Hansen, U. Quaade, *Appl. Catal. A*, **2005**, *284*, 5.
- ⁹⁸ D. Scholz, C. Aellig, I. Hermans, *Chem. Sus. Chem.*, **2014**, *7*, 268.
- ⁹⁹ R. M. Heck, S. Gulati, R. J. Farrauto, *Chem. Eng. J.*, **2001**, *82*, 149.
- ¹⁰⁰ N. Nikbin, M. Ladlow, S. V. Ley, *Org. Process Res. Dev.*, **2007**, *11*, 458.
- ¹⁰¹ R. Ju.rez, H. Pennemann, H. Garc.a, *Catal. Today*, **2011**, *159*, 25.

2. SYNTHESIS AND CHARACTERISATION OF GOLD NANOPARTICLES SUPPORTED ON FUNCTIONALISED OXIDES

2.1 Introduction

2.1.1 Previous work of the research group

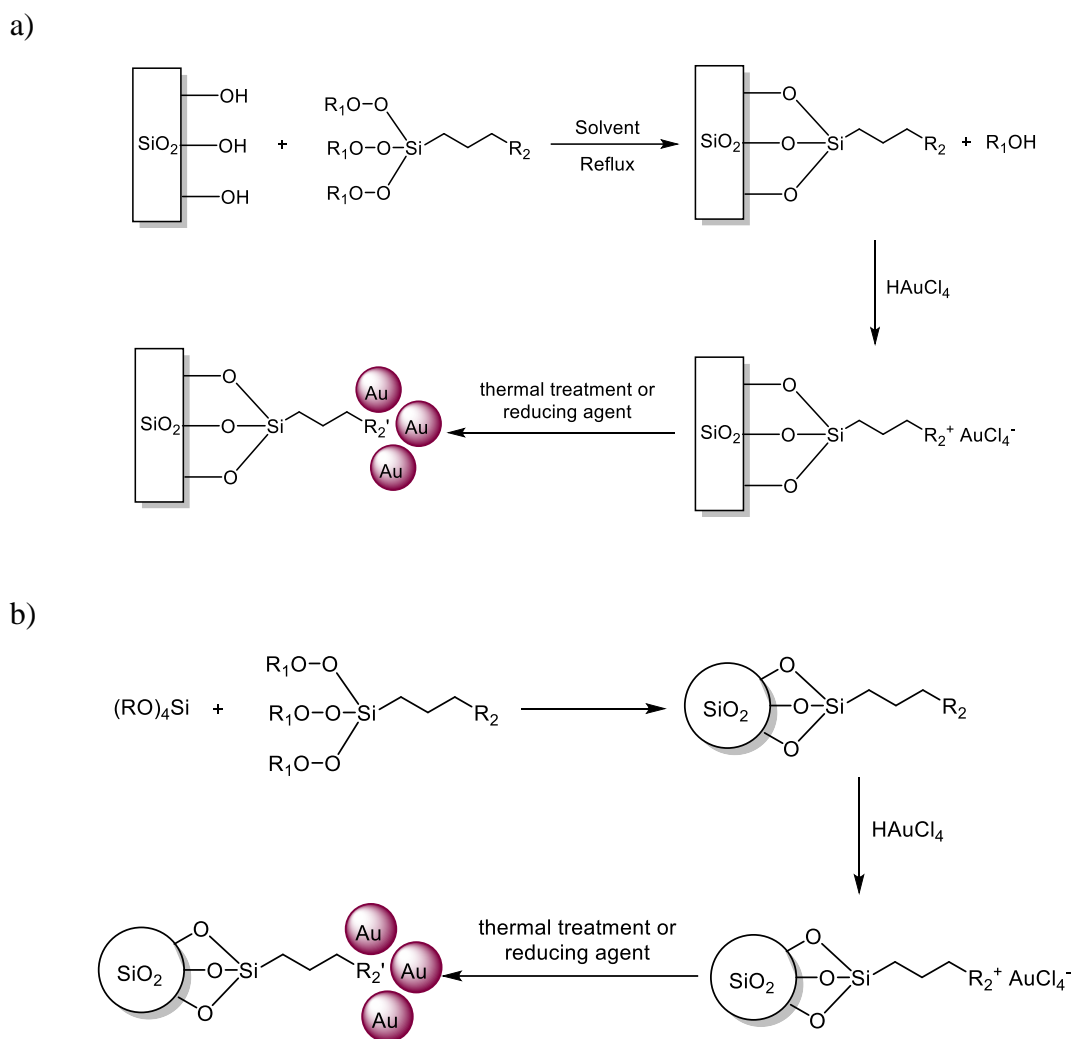
In the last years, the work of the research group in which I carried out my PhD has been oriented towards the preparation of heterogeneous catalysts based on gold nanoparticles supported on different functionalised silica supports.

Indeed, silica is considered an attractive material due to its large abundance, stability, commercial availability, low cost and ease of functionalisation with organic moieties. When the silica surface is functionalised with groups with a high affinity for gold species, such as amine and thiols, the addition of a gold precursor (HAuCl_4) results in the immobilisation of Au(III) ions which can be reduced by thermal treatment or chemical reduction to obtain supported gold nanoparticles.

The two common approaches for the introduction of organic functionalities on the silica surface are *grafting* (or *silanization*) and *co-condensation*.

The modification of the silica surface by *grafting* occurs by adding a functionalised organosilane to a refluxing suspension of silica in toluene or ethanol, so that the methoxyl or ethoxyl groups of the organosilane react with the hydroxyl groups of silica forming a stable covalent bond (Scheme 2.1a).¹

On the contrary, *co-condensation* is carried out by reacting the organosilane with a silica source, such as tetraethylortosilicate (TEOS). The co-hydrolysis and polycondensation of the two silanes lead to the formation of functionalised silica nanoparticles (Scheme 2.1b).¹



Scheme 2.1. Preparation of Au/SiO₂ catalyst by a) *grafting* and b) *co-condensation* (R₁ = -CH₃ or -CH₂CH₃).

In this context, the work of the research group started with the preparation of AuNPs supported on commercial polyethyleneimine-functionalised silica beads (SiO₂-PEI), a material commonly used as a cationic ion-exchange resin.²

The formation of AuNPs was obtained in one step, by simply adding the SiO₂-PEI beads to an aqueous solution of HAuCl₄ at room temperature. As suggested by the rapid variation in the colour of the solution, from yellow to transparent, the adsorption of the gold precursor on the silica surface occurred in the first minutes of the reactions, with a concomitant change in colour of the solid which became brownish-red. This indicates the formation of supported AuNPs, following the reduction of Au(III) by the amino groups of PEI, without the need of any additional reducing or stabilising agent (Figure 2.1).

In fact, the preparation of stabilised AuNPs in the presence of amine have been reported in several studies, even if the detailed mechanism of the nanoparticles formation has not been clarified yet.^{3,4,5,6,7,8}

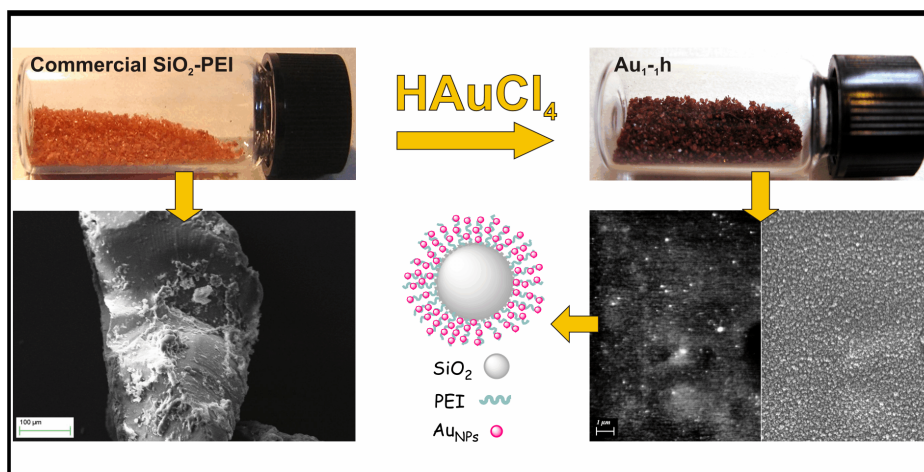


Figure 2.1. Synthesis of AuNPs supported on commercial SiO₂-PEI beads.²

Six different types of Au/SiO₂-PEI were prepared by varying the initial HAuCl₄ concentration (1.5 and 10 mM) and the reaction time (1 h and 24 h), then the total amount of gold immobilised on the support was indirectly estimated by analysing the supernatant solution immediately after reaction completion. The obtained results indicated that the effective gold loading found in each sample corresponded to the theoretical one.

Furthermore, the SEM analysis revealed how the particles size distribution decreased with the increasing HAuCl₄ concentration (70 – 100 nm for HAuCl₄ 1 mM and 40 - 70 nm for HAuCl₄ 5 mM and 10 mM), while at longer reaction times the aggregation phenomena became predominant over nucleation, promoting the formation of bigger aggregates.

The catalytic activity of the prepared materials was then tested in the reduction of 4-nitrophenol (4-NP) to 4-aminophenol (4-AP) with an excess amount of NaBH₄, monitoring the reaction by *in situ* UV-vis measurements (Figure 2.2). As shown in Table 2.1, for a Au/4-NP ratio of 1/0.44, the catalyst prepared with an initial concentration of HAuCl₄ 1 mM gave the best overall performances, with rate constants in the range of previously reported literature data.⁹

Moreover, the obtained results showed only minor differences in the catalytic activity of samples with different Au particle size, due to the fact that the size range of these systems was beyond the range in which the effect of particle size is significant.¹⁰

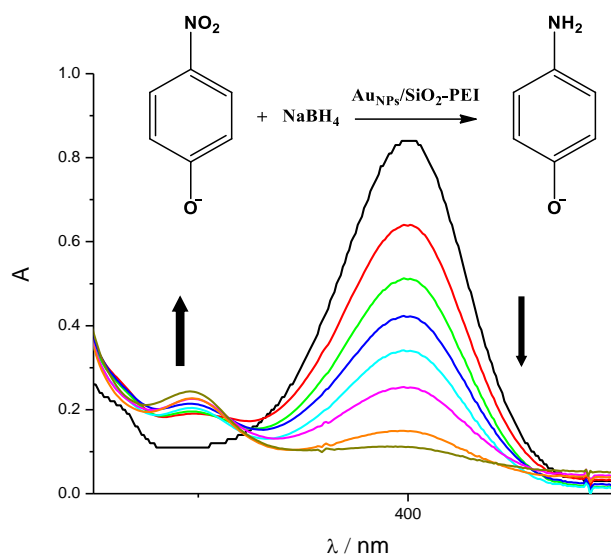


Figure 2.2. UV-vis spectra of 4-NP reduction catalysed by Au/SiO₂-PEI.²

Table 2.1. Kinetic constants of 4-NP reduction catalysed by Au/SiO₂-PEI (Au_{x-y} where x = initial HAuCl₄ concentration and y = reaction time).²

Entry	Sample	wt Au (%)	Au/4-NP/NaBH ₄ (mol/mol/mol)	<i>k</i> (s ⁻¹)	R ²
1	Au _{1-1h}	0.5	1/0.44/711	6.84 x 10 ⁻⁴	0.999
2	Au _{1-24h}	0.5	1/0.44/711	5.98 x 10 ⁻⁴	0.997
3	Au _{5-1h}	2.4	1/0.44/711	1.33 x 10 ⁻⁴	0.998
4	Au _{5-24h}	2.4	1/0.44/711	1.02 x 10 ⁻⁴	0.988
5	Au _{10-1h}	4.9	1/0.44/711	3.39 x 10 ⁻⁴	0.986
6	Au _{10-24h}	4.9	1/0.44/711	1.06 x 10 ⁻⁴	0.987

Afterwards, the possibility to exploit the functionalisation of the support for the straightforward reduction/immobilization of gold was further investigated by preparing silica nanoparticles functionalised with [3-(2-propynylcarbamate)propyl]triethoxysilane (PPTEOS).¹¹

The synthesis of **SiO₂NPs@Yne** (Yne = organic functionality) was carried out by a one-pot hydrolytic *co-condensation* of the alkynyl-carbamate organosilane (23 % molar) and TEOS (77 % molar) in the presence of ammonia at 40 °C. The use of two different

amounts of ammonia, namely 1.0 and 0.5 M, led to the formation of silica nanoparticles with a particle size distribution of 79 ± 23 nm (**SiO₂NPs@Yne-a**) and 45 ± 6 nm (**SiO₂NPs@Yne-b**) respectively (Figure 2.3).

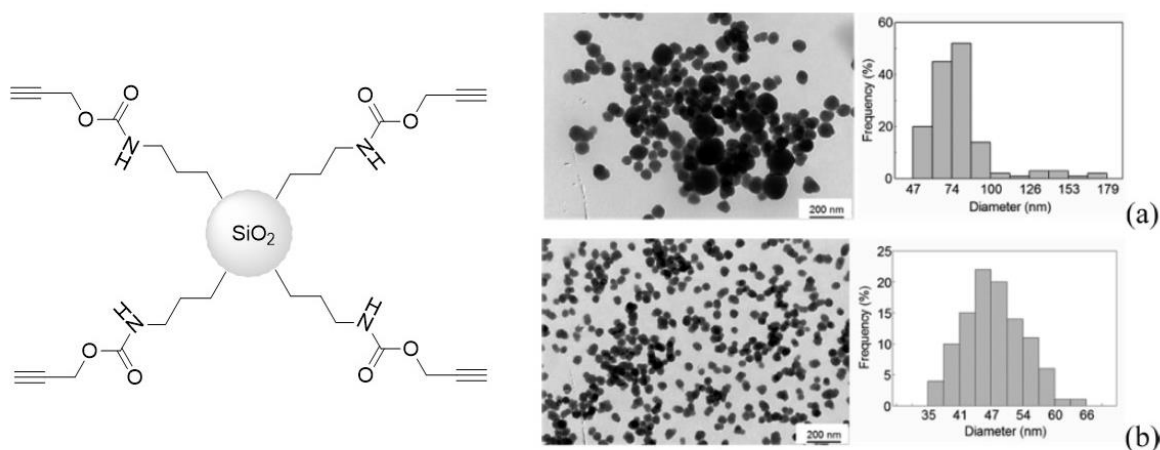


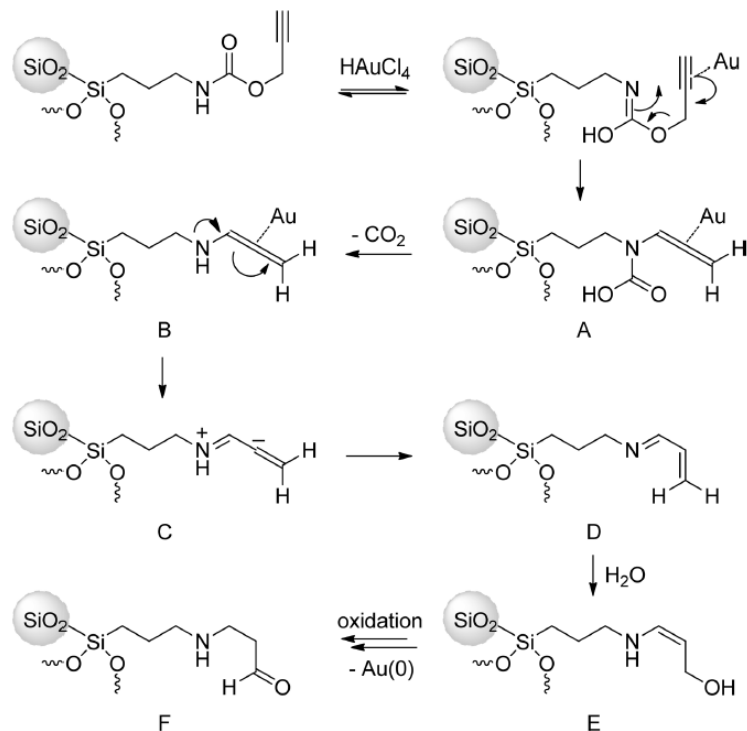
Figure 2.3. Schematic representation of **SiO₂NPs@Yne** and particles size of a) **SiO₂NPs@Yne-a** and b) **SiO₂NPs@Yne-b**.¹¹

The successful incorporation of the organic functionalisation was confirmed by thermogravimetric (TGA) analysis, in which a 9 – 10 % weight loss was observed between 150 °C and 320 °C due to the degradation of the organic material, and by FT-IR, Raman and XPS spectroscopies.

The decoration of the prepared functionalised supports with gold was performed in an ultrasonic bath, by adding an aqueous solution of HAuCl₄ 1 mM to a suspension of **SiO₂NPs@Yne** in water. As previously observed in the presence of polyethyleneimine, the colour of the solid rapidly changed to afford a purple powder, indicating the formation of AuNPs.

The gold content determined by atomic absorption spectroscopy (AAS) was found to be 4.7 wt %, which corresponded to the exact amount of the theoretical gold loading. Furthermore, the size of the supported AuNPs was determined by transmission electron microscopy (TEM), obtaining an average diameter of 15 ± 3 nm for **Au/SiO₂NPs@Yne-a** and 11 ± 3 nm for **Au/SiO₂NPs@Yne-b**, significantly smaller than the ones previously observed in the Au/SiO₂-PEI systems (40 – 100 nm).²

Regarding the mechanism of formation of gold nanoparticles in the presence of the PPTEOS-derived functionality, the hypothesis formulated on the base of XPS and FT-IR results is reported in Scheme 2.2.



Scheme 2.2. Proposed mechanism for the $\text{SiO}_2\text{@Yne}$ mediated reduction of HAuCl_4 .¹¹

After the coordination of Au(III) to the alkyne group, the system would undergo a 1,3-migration involving the carbamic nitrogen, a decarboxylation and eventual rearrangement with formation of the unsaturated imine **D**. The imine, as well as the hydrolysis product (**E**) could be responsible for the reduction of gold, with consequent formation of the oxidised product **F**.

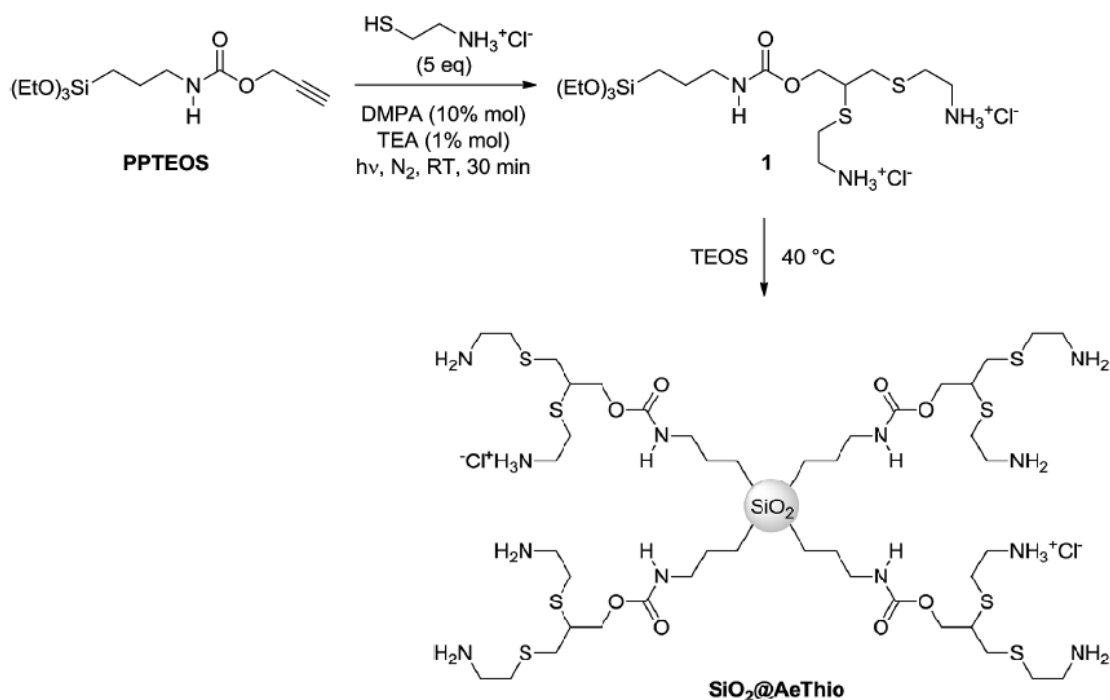
Finally, the catalytic activity of $\text{Au/SiO}_2\text{NPs@Yne-a}$ and $\text{Au/SiO}_2\text{NPs@Yne-b}$ was studied in the reduction of 4-NP with different 4-NP/ NaBH_4 /Au molar ratios, achieving a total conversion after a few minutes with both the catalysts (Table 2.2).

Table 2.2. Kinetic constants of 4-NP reduction catalysed by **Au/SiO₂NPs@Yne-a** and **Au/SiO₂NPs@Yne-b**.¹¹

Entry	Sample	4-NP/NaBH ₄ /Au (mol/mol/mol)	<i>k</i> (10 ⁻² s ⁻¹)
1	Au-SiO₂@Yne-a	1/1560/1	2.7 ± 0.1
2	Au-SiO₂@Yne-a	4/6250/1	2.2 ± 0.1
3	Au-SiO₂@Yne-a	10/15600/1	1.7 ± 0.1
4	Au-SiO₂@Yne-b	1/1560/1	2.5 ± 0.1
5	Au-SiO₂@Yne-b	4/6250/1	1.9 ± 0.1
6	Au-SiO₂@Yne-b	10/15600/1	2.0 ± 0.1

In particular, the rate constant values were found to be higher than the ones previously obtained with the same gold content in the Au/SiO₂-PEI system and comparable to the values typically associated to homogeneous catalysis.^{2,12} This significant difference was attributed to the increased surface area of silica nanoparticles and lower AuNPs average size.

The choice of PPTEOS for the modification of the silica surface was related to the possibility to use it as an intermediate for the further functionalisation of the silica support. Indeed, the research group has demonstrated how it is possible to obtain amino-sulfide functionalised silica (**SiO₂@AeThio**) through a thiol-yne radical coupling performed between cysteamine hydrochloride and PPTEOS followed by co-condensation with TEOS (Scheme 2.3).¹³ The presence of both amino and sulfide moieties allowed the immobilisation of AuNPs with an average size of 13 ± 5 nm, without the need of additional reducing or stabilising agents. Interestingly, the synthesis of these **Au/SiO₂@AeThio** systems was the first example of application of radical click chemistry in the field of silica-supported metal nanoparticles.



Scheme 2.3. Synthesis of **SiO₂@AeThio**.¹³

Furthermore, **Au/SiO₂@AeThio** showed a remarkable catalytic activity in the reduction of 4-NP by NaBH₄, with rate constants of the order of 10⁻² s⁻¹ mg_{cat}⁻¹, and could be successfully recycled without any significant decrease in its catalytic performances.

2.1.2 Principles of Solid State NMR spectroscopy

Solid states NMR spectroscopy (SS NMR) is one of the most powerful tools for the characterisation of systems in the solid phase. Indeed, it is a non-destructive technique and can be applied to any type of solid material, such as powders, films, crystalline and amorphous solids, giving information about their structural and dynamic properties.

At the base of an NMR spectrum there are transitions between nuclear spin states induced by low energy electromagnetic radiations (10 – 1000 MHz), in the presence of an external magnetic field, which generates signals at the frequency of the adsorbed radiation (Larmor frequency). Therefore, the first requirement to perform an NMR experiment is that the sample possess nuclei with a spin different from zero, a condition easily satisfied since almost every chemical element has at least once isotope with non-zero spin. Nonetheless, the intensity of the generated signals will be influenced by the natural abundance of the nuclei.¹⁴

Due to the different behaviour of a solid sample compared to a dissolved one, SS NMR is much more complex than standard solution NMR and requires the use of particular techniques in order to overcome specific problems.

If the NMR spectrum of a solid sample was measured with the routine equipment for solution NMR, the result would consist of extremely broad lines covering the whole range of the spectrum, due to the direct neighbourhood of atoms in the lattice causing strong dipolar-dipolar and chemical shift anisotropy interactions. The influence of both these interactions depends on the orientation θ to the external magnetic field and strongly relates to $3\cos^2\theta-1$. Hence, line broadening effects can be cancelled by setting the term $3\cos^2\theta-1$ equal to 0, resulting in a “magic angle” of 54.7° to the magnetic field. Rotating a sample at this angle (magic angle spinning, MAS) with a rotation speed higher than the frequency range of interactions (3000 – 4000 Hz) will cause a collapse of disturbances and results in narrow NMR line widths (Figure 2.4).¹⁵

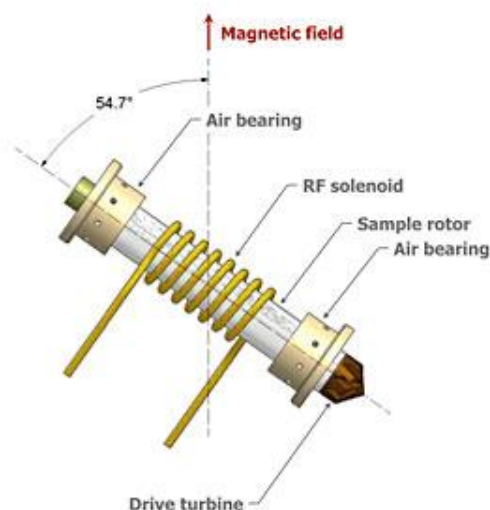


Figure 2.4. Scheme of the magic angle spinning probe.¹⁶

Besides, in order to solve the problem related to strong heteronuclear interactions, a high-power decoupling is necessary when acquiring NMR spectra on a solid phase. Finally, by means of cross polarisation (CP) it is possible to enhance the signal to noise ratio by transferring the polarisation from abundant spins such as ^1H to dilute spins, such as ^{13}C or ^{15}N , for which the relaxation time can be in the range of hours.

SS NMR requires the use of complex and expensive instrumentation. In particular, it is necessary to work with high-power radiations and, in the case of high resolution spectra specific apparatus, such as CP/MAS probe, pneumatic system for MAS, etc. are

required. Moreover, the acquisition times are generally long and standard protocols of analysis are rarely available. Nevertheless, the potential of this technique resides in the possibility to carry out detailed analysis on the composition of a wide variety of materials, obtaining information that in many cases would otherwise be inaccessible.

2.1.3 Aim of the chapter

On the basis of the successful results described in paragraph 2.1.1, the research group decided to further exploit the catalytic system based on AuNPs supported on silica functionalised with alkynyl carbamate moieties, for an application in continuous-flow conditions.

Since the previously reported SiO₂NPs support would not be suitable for the packing of a continuous-flow reactor, due to the high pressure drops that would arise in the presence of such small silica nanoparticles (40 – 80 nm), it was necessary to prepare a similar catalyst supported on *micrometer* sized silica. For this purpose, commercial silica gel for column chromatography (63 ± 210 µm) was modified with the organosilane PPTEOS by a simple *grafting* procedure and the obtained material was then decorated with AuNPs by the straightforward *in situ* reduction of HAuCl₄. Furthermore, the same preparation method was extended to alumina (Al₂O₃) and titania (TiO₂) supports.

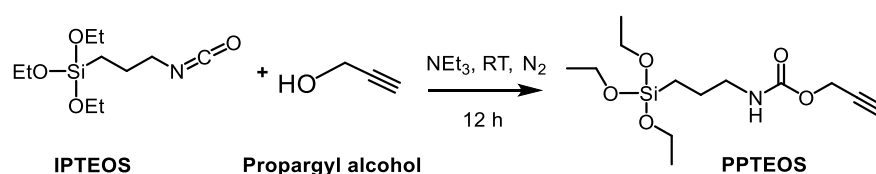
The resulting **Au/OS@Yne** (OS = Oxide Support) materials were characterized by means of several complementary techniques (i.e. TGA, ATR-IR, AAS, TEM, XPS and SSNMR) in order to thoroughly comprehend the physical and chemical properties of these systems.

Part of the work reported in the present chapter was published in *ACS Sustainable Chemistry and Engineering*.¹⁷

2.2 Results and discussion

2.2.1 Preparation of OS@Yne and Au/OS@Yne

The alkyne-terminated organosilane (PPTEOS) was synthesized according to a reported procedure,¹⁸ by the simple addition of 3-(triethoxysilyl)propyl isocyanate (IPTEOS) to a propargyl alcohol solution in dichloromethane, catalysed by NEt₃ (Scheme 2.4).



After 24 h, the solvent was evaporated under reduced pressure, but the ¹H-NMR analysis of the crude reaction mixture revealed that the excess of propargyl alcohol was still present. In order to isolate the product and remove the unreacted alcohol, a further drying at 0.5 atm was then carried out. The final ¹H-NMR spectrum is shown in Figure 2.5.

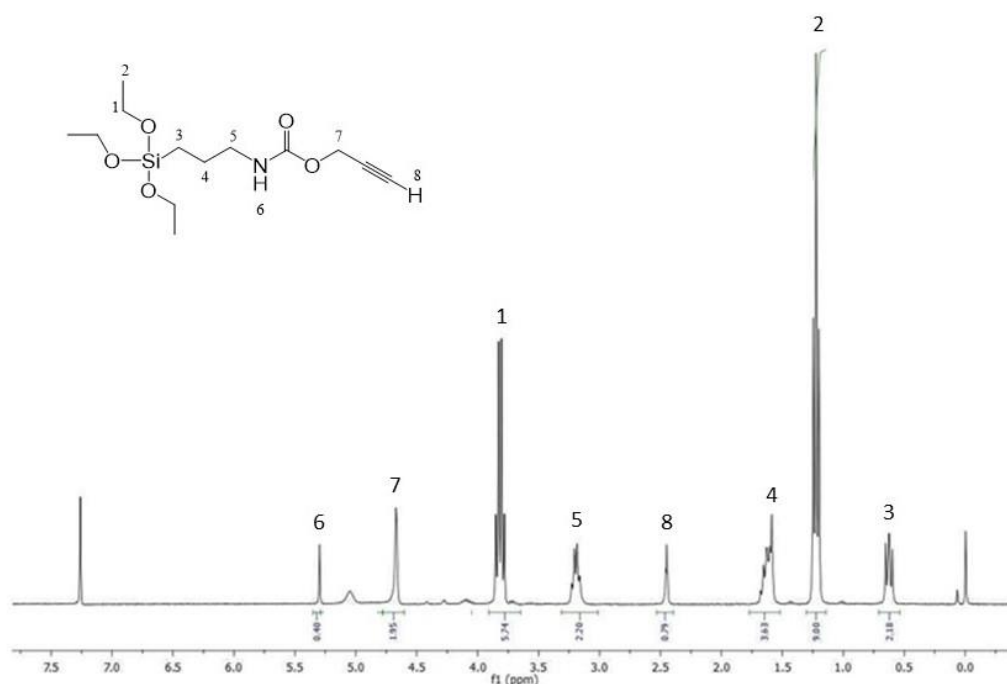
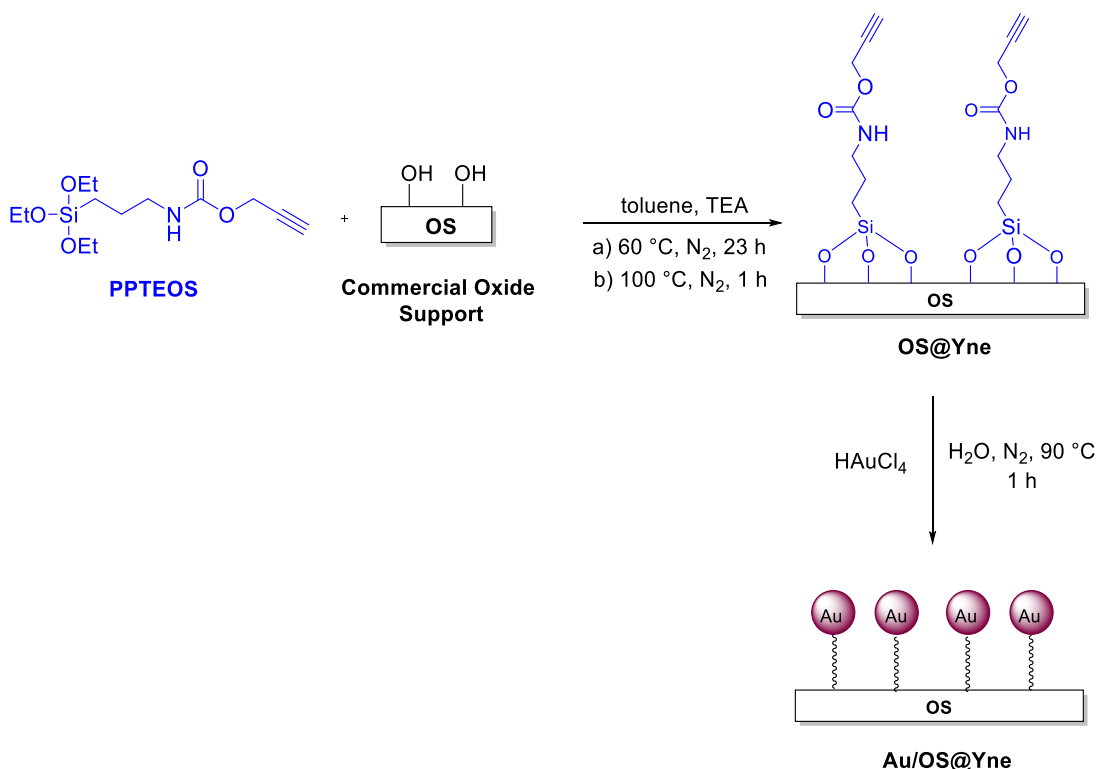


Figure 2.5. ¹H-NMR spectrum of PPTEOS.

The synthesis of the **Au/OS@Yne** catalysts was carried out in two steps: 1) functionalisation of the oxide supports with PPTEOS and 2) decoration with gold nanoparticles. First, the modified supports (**OS@Yne**) were obtained by condensation between the hydroxyl groups present on the oxide surface and the ethoxyl groups of PPTEOS. The reaction was carried out in toluene, under nitrogen atmosphere and in the presence of NEt_3 . Secondly, the functionalised supports were decorated with AuNPs by simple addition of the gold precursor HAuCl_4 (1 mM) to an aqueous suspension of **OS@Yne**, at 90 °C under nitrogen atmosphere (Scheme 2.5).



Scheme 2.5. Preparation of **Au/OS@Yne** (OS = SiO_2 , Al_2O_3 , TiO_2).

Within the first minutes following the addition of HAuCl_4 , the colour of the reaction mixture rapidly changed from pale-yellow to violet indicating the successful formation of gold nanoparticles. Thus, the presence of the alkynyl-carbamate functionalities allows the straightforward reduction of Au(III) to Au(0) and the immobilization of the resulting AuNPs, without the need of any additional reducing or stabilising agent.

On the contrary, when HAuCl_4 was added to a suspension of bare oxide no reduction was observed, indicating that the presence of the organic functionalisation is essential for the formation of gold nanoparticles on the support.

2.2.2 Characterisation of OS@Yne and Au/OS@Yne

The physical and chemical properties of **OS@Yne** and **Au/OS@Yne** were first investigated by means of TGA analysis, TEM microscopy, AAS and ATR-FTIR spectroscopies, and X-ray diffraction (XRD). The most important data are summarised in Table 2.3.

Table 2.3. TGA, AAS and TEM data for **Au/OS@Yne**.

Sample	Yne (wt %) ^a	Au (wt %) ^b	AuNPs d _{TEM} (nm)
Au/SiO₂@Yne	12 ± 1	3.7 ± 0.1	15 ± 4
Au/Al₂O₃@Yne	6 ± 1	2.0 ± 0.1	18 ± 7
Au/TiO₂@Yne	2 ± 1	1.7 ± 0.1	large distribution

a) Weight loss determined by TGA; b) gold loading determined by AAS.

The TGA analysis of **Au/SiO₂@Yne** (Figure 2.6a), used to evaluate the efficiency of the grafting process, showed three regions of mass loss associated to the evaporation of adsorbed water and ethanol (30 – 150 °C), degradation of the organic material (150 – 500 °C) and dehydration of Si-OH groups (500 – 700 °C). Specifically, the weight loss due to the decomposition of the organic functionalisation was 12 ± 1 wt %, in keeping with the expected organic moieties incorporation. Analogue thermograms were obtained for the **Au/Al₂O₃@Yne** (Figure 2.6b) and **Au/TiO₂@Yne** (Figure 2.6c) samples, with a mass loss in the region of the organic material degradation of 6 ± 1 wt % and 2 ± 1 wt % respectively.

This difference in the efficiency of functionalisation could be attributed to the different acidity of the surface of the oxide supports. Indeed, the reported isoelectric point (IEP) for silica is around 2, while in the case of alumina and titania higher values are typically found (between 6 and 9).^{19,20}

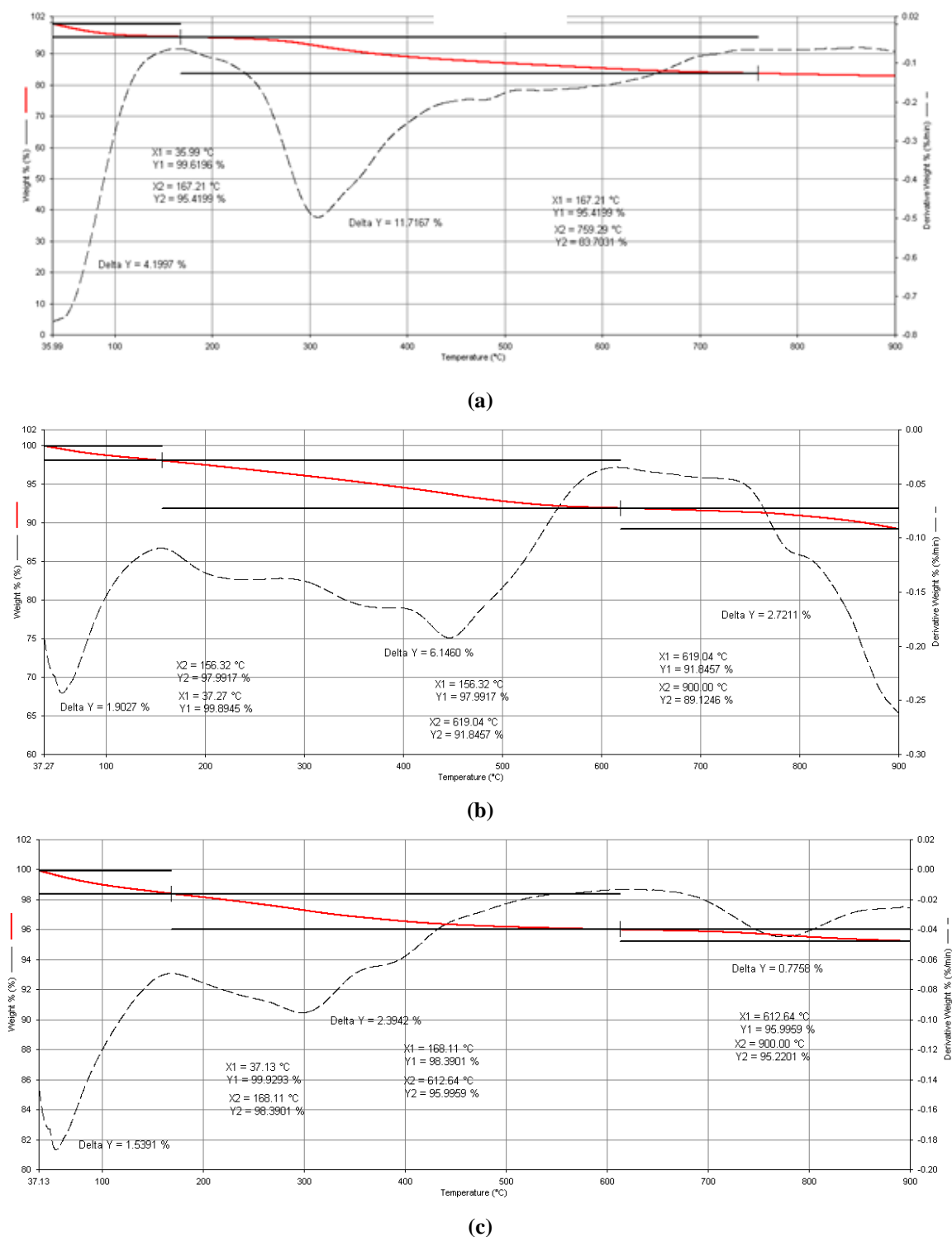
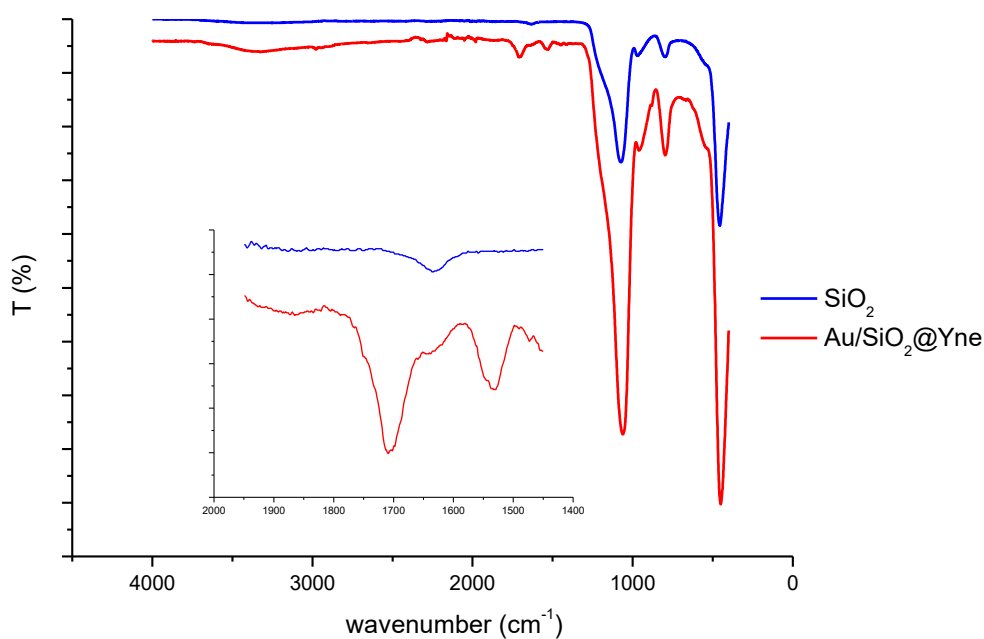


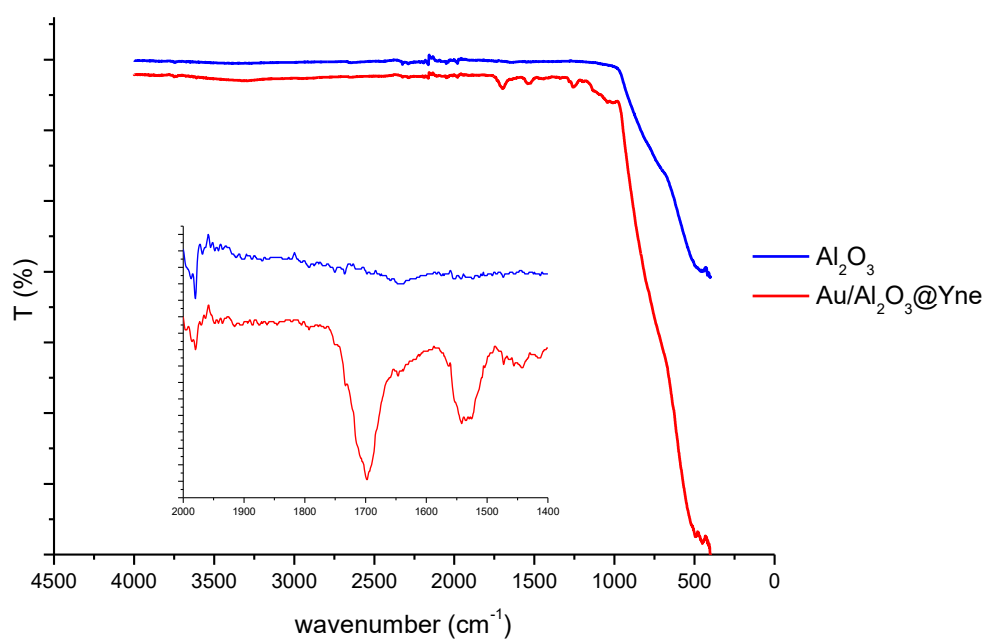
Figure 2.6. TGA analysis of a) Au/SiO₂@Yne, b) Au/Al₂O₃@Yne and c) Au/TiO₂@Yne. The red line represents the weight loss percentage while the dotted line is the derivative of weight loss percentage.

The ATR-FTIR spectra of Au/OS@Yne were also recorded (Figure 2.7a-c) and in all cases the presence of the carbamate moiety of the organic functionalisation was evidenced by the appearance of two bands at ca. 1700 and 1530 cm⁻¹, associated to the C=O stretching and the N-H bending vibrations respectively.²¹

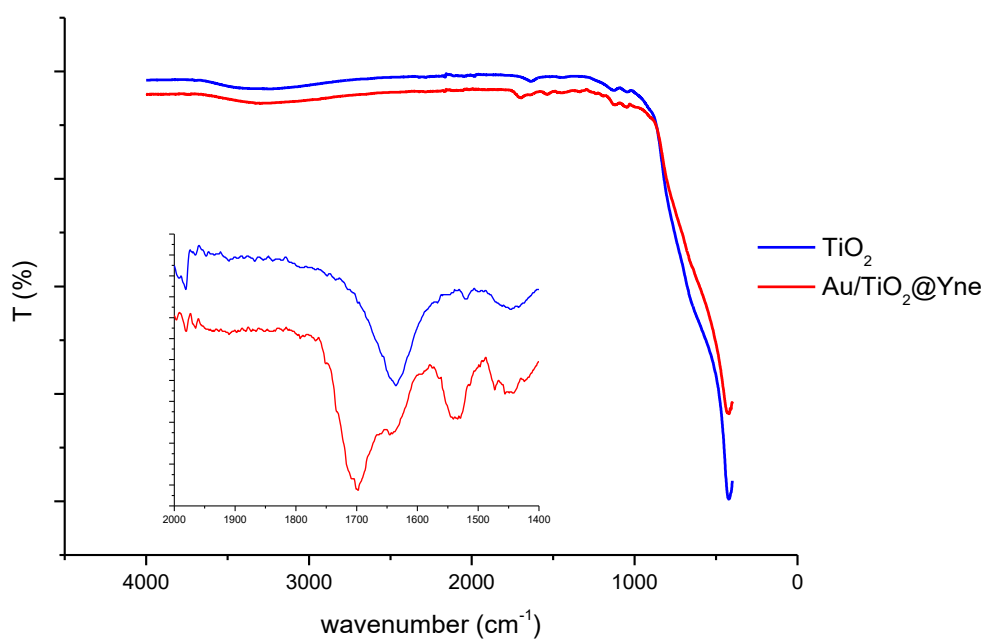
In addition, the **Au/SiO₂@Yne** spectrum (Figure 2.7a) presented a series of bands in the SiO₂ fingerprint region (1250 – 400 cm⁻¹), with the main band at 1064 cm⁻¹ ascribable to the Si-O-Si stretching.²² The spectrum of **Au/Al₂O₃@Yne** (Figure 2.7b) showed a large band between 1000 and 400 cm⁻¹ related to Al-O-Al stretchings,^{23,24} while in the spectrum of **Au/TiO₂@Yne** (Figure 2.7c) an intense band related to the Ti-O vibrations was observed at 400 – 600 cm⁻¹.²⁵ Furthermore, no substantial differences between the **Au/OS@Yne** and **OS@Yne** spectra were observed.



(a)



(b)



(c)

Figure 2.7. ATR-FTIR spectra of a) $\text{Au}/\text{SiO}_2@Yne$, b) $\text{Au}/\text{Al}_2\text{O}_3@Yne$ and c) $\text{Au}/\text{TiO}_2@Yne$.

The exact content of gold in the catalysts was determined by AAS after each synthesis. The preparation of the **Au/SiO₂@Yne** samples was carried out by addition of NaOH 50 wt % (for the dissolution of silica) and aqua regia (for the dissolution of gold), while in the case of **Au/Al₂O₃@Yne** and **Au/TiO₂@Yne** this procedure was not efficient since a precipitate was clearly still present in the solution, even after sonication. Hence, several attempts to dissolve the samples were carried out:

- addition of a mixture of H₂SO₄ 99 % and H₂O₂ 30 % (3:1 v/v);
- addition of NaOH pellets;
- addition of 10 mL of HNO₃ 65 % followed by heating at 200 °C for 30 min in a microwave oven.

Finally, following a procedure reported in literature,²³ the **Au/Al₂O₃@Yne** and **Au/TiO₂@Yne** samples were completely dissolved in a mixture of 10 mL of HNO₃ 65 %, 0.5 mL of H₂SO₄ 98 % and 1 mL of H₂O₂ 30 % heated in a microwave oven at 200 °C for 1 h. The results of the AAS analysis suggested that the extent of gold immobilization is related to the degree of organic functionalisation of the support. Indeed, the silica-supported catalyst showed the highest gold loading (average value 3.7 wt %), while in the case of alumina and titania lower values were found (2.0 wt % and 1.7 wt % respectively).

Moreover, when the synthesis was carried out in the presence of an excess of HAuCl₄ (18 wt %), the final gold content was found to be 13 wt % (**Au-13/SiO₂@Yne**), suggesting that the maximum limit of the AuNPs loading is dictated by the functionalisation of the support (12 wt %). Interestingly, in the thermogram of this sample no significant decomposition at 300 °C was observed, suggesting a difference in the organic pendant anchored on the silica support (Figure 2.8).

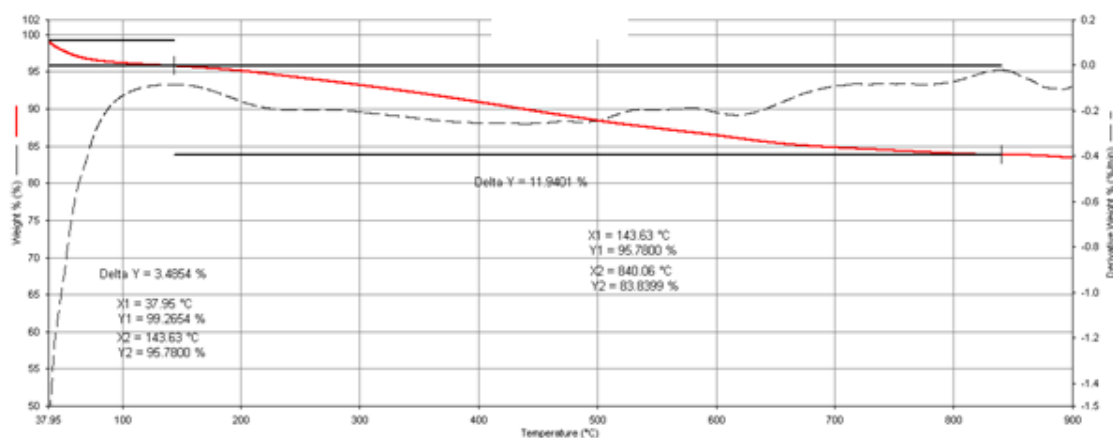
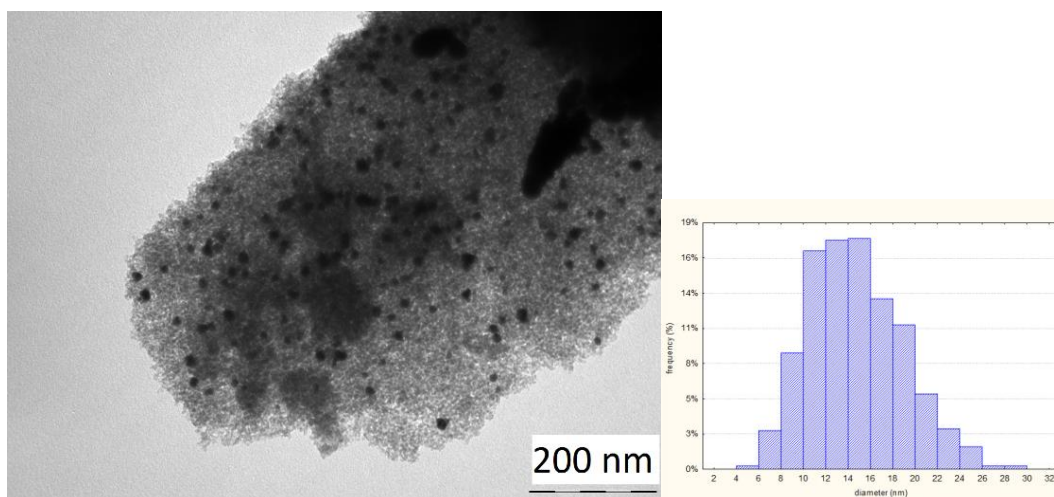
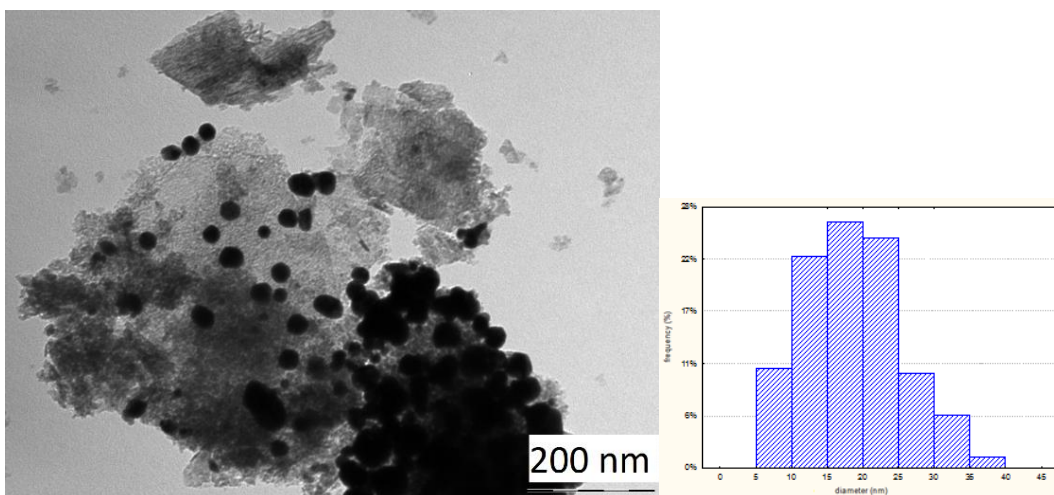


Figure 2.8. TGA analysis of **Au-13/SiO₂@Yne** (13 wt % of gold loading).

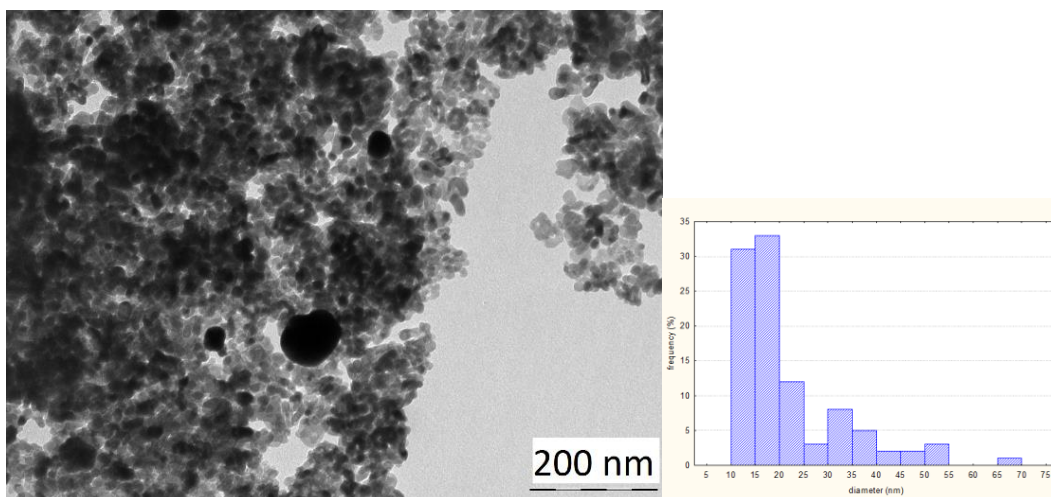
The morphology and AuNPs size of the **Au/OS@Yne** samples was investigated by TEM microscopy. The immobilised gold nanoparticles presented a spherical shape and were found to be attached on the support. In particular, **Au/SiO₂@Yne** showed a quite uniform distribution of AuNPs with an average diameter of 15 ± 4 nm (Figure 2.9a), whereas in the case of **Au/Al₂O₃@Yne** the nanoparticles seemed to form more aggregates and were on average larger (18 ± 7 nm) compared to ones supported on silica (Figure 2.9b). Finally, the TEM images of **Au/TiO₂@Yne** presented a more random size distribution since the majority of the particles had a diameter ranging from 10 to 20 nm, but some very large aggregates (up to 70 nm) were also observed (Figure 2.9c).



(a)



(b)

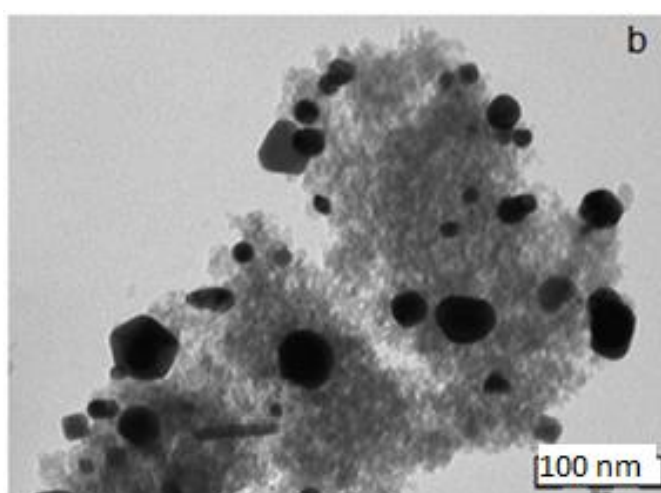


(c)

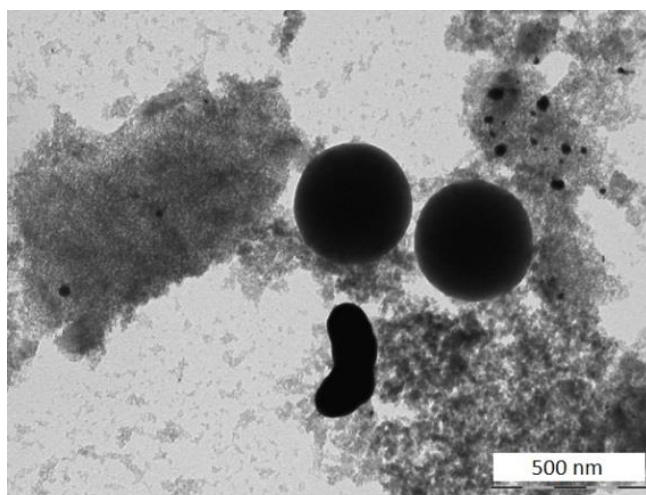
Figure 2.9. TEM images and particle size distribution of a) **Au/SiO₂@Yne** (15 ± 4 nm), b) **Au/Al₂O₃@Yne** (18 ± 7 nm) and c) **Au/TiO₂@Yne** (large distribution).

The TEM analysis of a **Au/SiO₂@Yne** sample prepared using a more concentrated solution of HAuCl₄ (2.3 mM instead of 1 mM) confirmed that the initial concentration of the gold precursor in the reaction mixture plays a fundamental role in the definition of the particle size. In fact, the AuNPs in the examined sample presented a larger average diameter and a broader size distribution (25 ± 10 nm) as shown in Figure 2.10a.

Furthermore, the sample with a 13 wt % of gold loading was found to present even larger aggregates (Figure 2.10b).



(a)



(b)

Figure 2.10. TEM image of a) **Au/SiO₂@Yne** prepared with 2.3 mM H₂AuCl₄ and b) **Au₁₃/SiO₂@Yne**.

Finally, the **Au/SiO₂@Yne** sample was analysed by means of X-ray diffraction. The XRD pattern, reported in Figure 2.11, presented peaks located at 38.2 °, 44.4 °, 64.6 ° and 77.7 °, related to (111), (200), (220) and (311) crystallographic planes of cubic Au respectively.

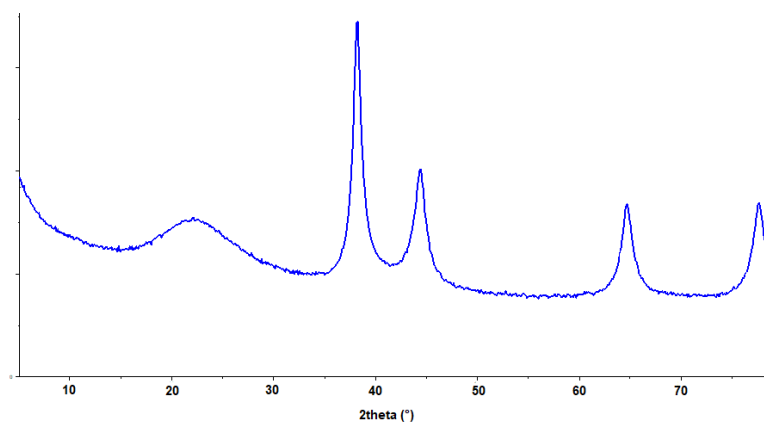


Figure 2.11. XRD pattern of **Au/SiO₂@Yne**.

2.2.3 Investigation of the gold reduction/immobilisation mechanism by Solid State NMR spectroscopy

Using **Au/SiO₂@Yne** as a model system, the surface functionalisation and the corresponding chemical modification along the synthetic pathway were monitored by ¹³C SS NMR spectroscopy, both directly and via Cross Polarization experiments, with the aim of gaining more insight into the mechanism of formation/immobilisation of AuNPs.

Figure 2.12 illustrates the comparison between the ¹³C CP/MAS NMR spectra of the commercial silica support, the functionalised **SiO₂@Yne** microspheres, and the corresponding **Au/SiO₂@Yne**.

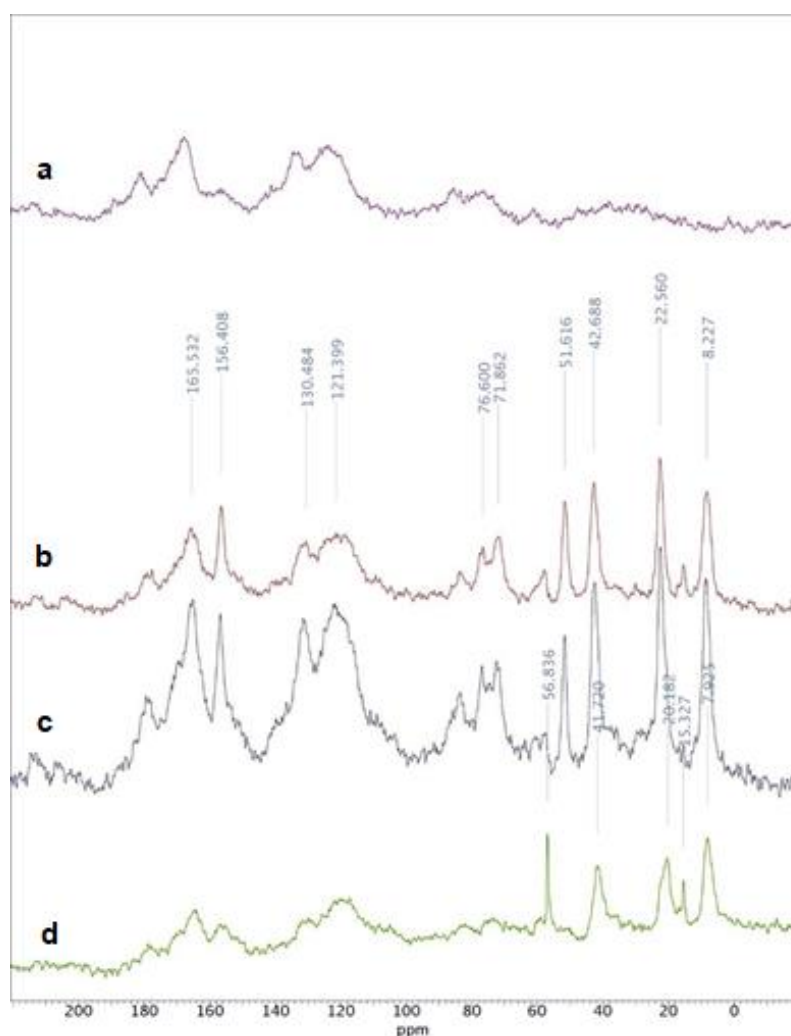
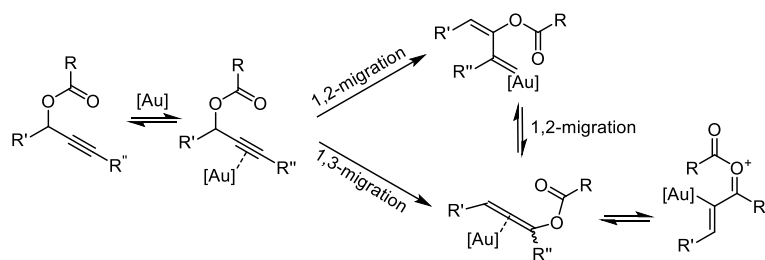


Figure 2.12. ¹³C CP/MAS NMR spectra recorded at 500 MHz of a) commercial SiO₂, b) **SiO₂@Yne**, c) **Au/SiO₂@Yne** (3.7 wt % Au) and d) **Au-¹³C/SiO₂@Yne** (13 wt % Au).

Apart from the very large signals (in the following spectrum regions: 70-90 ppm, 110-140 ppm and 160-180 ppm) belonging to impurities present in the commercial silica sample (Figure 2.12a), the **SiO₂@Yne** sample clearly evidenced all the relevant signals of the PPTEOS derived pendant: the aminopropylsilane linker (8.23, 22.56, and 42.69 ppm), the propargyl methylene (51.62 ppm), both alkyne carbons (76.60 and 83.45 ppm), and the carbamic carbonyl at 156.41 ppm (Figure 2.12b).² At the same time, **Au/SiO₂@Yne** (Figure 2.12c) containing 3.7 wt % of gold showed no relevant modification of the organic functionalisation, in keeping with what previously suggested by the ATR-FTIR spectra. Therefore, in order to investigate the effect of the Au(III) to Au(0) reduction on the carbamate branch, a sample containing a higher loading of gold (**Au-13/SiO₂@Yne**, Au 13 wt %) was appositely prepared. The corresponding CP/MAS NMR spectrum (Figure 2.12d) showed a significant decrease in the signals of the alkynyl and carbonyl carbons of the starting pendant but three quite strong signals (at 7.92, 20.18, and 41.72 ppm) ascribable again to an aminopropylsilane linker. This suggests that gold reduction led to some modification of the starting functionalisation, likely involving the degradation of the propynylcarbamate moiety and resulting in an aminopropyl chain, responsible in turn for the eventual stabilisation of the gold nanoparticles.²⁶

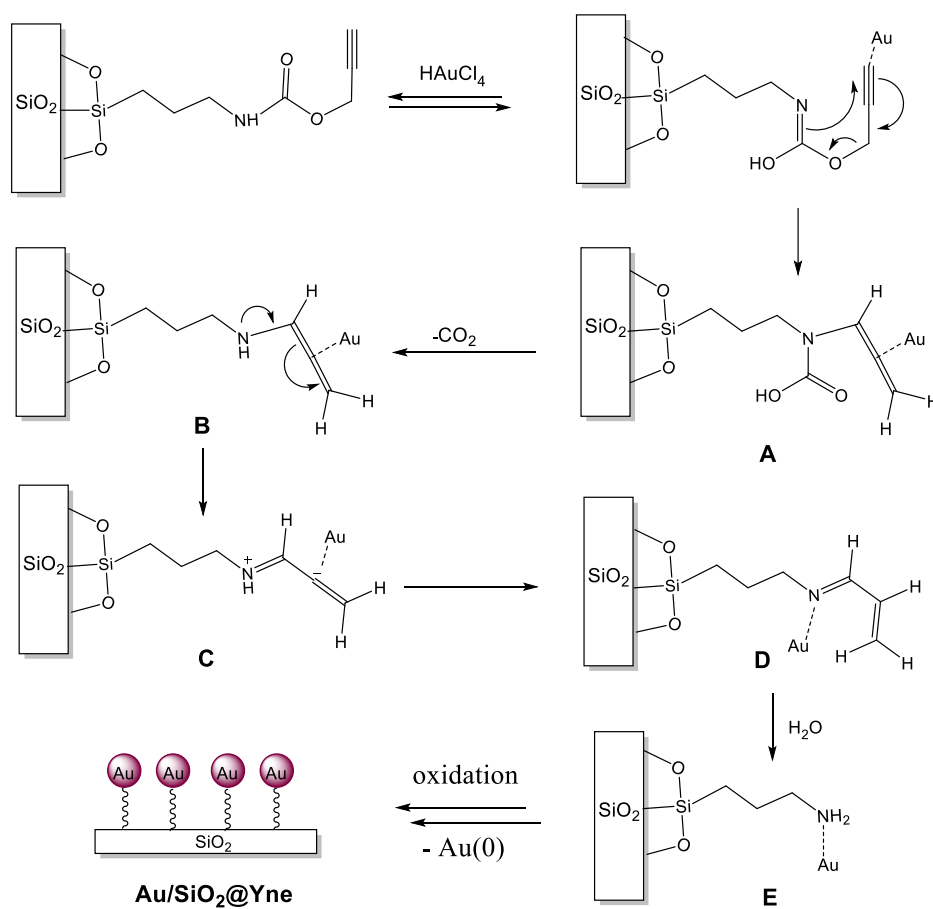
Finally, the other two strong singlets at 15.33 and 56.84 ppm could be tentatively assigned to the methyl and methylene carbon atoms, respectively, of surface-bound ethoxy groups, deriving from condensation of the ethanol produced during the silica modification with the silica silanols, a process much more evident upon using larger amounts of chloroauric acid.²⁷

It is well documented in literature that Au(III) and Au(I) complexes can activate alkyne moieties by coordination to the triple bond, which in turn becomes more reactive towards nucleophiles.^{28,29,30,31} In particular, the work of Zhang^{32,33,34,35} demonstrates how propargyl esters can undergo a great variety of chemical transformations catalysed by Au(III)/Au(I) complexes, through reaction mechanisms that could involve a structural rearrangement by either 1,2- or 1,3-acyl migrations to give an α -vinyl gold oxocarbenium ion (Scheme 2.6).



Scheme 2.6. Au(III)-catalysed propargyl ester rearrangement.

However, no reduction to Au(0) was reported in the case of propargyl esters contrary to what was observed with our propargyl-carbamate functionalisation. This suggests that the presence of the carbamic nitrogen in the **OS@Yne** systems might be crucial for the efficient formation of AuNPs. On the basis of the SS NMR results, the previously proposed mechanism¹¹ for the reduction/immobilization of gold by means of the organic functionalisation was revised as reported in Scheme 2.7.



Scheme 2.7. Proposed mechanism for the reduction of gold on the functionalised support.

In this hypothesis, the addition of the precursor HAuCl_4 to **OS@Yne** results in the coordination of gold to the triple bond, followed by a 1,3-migration involving the carbamic nitrogen with formation of the allene intermediate **A** and subsequent decarboxylation to **B** and rearrangement to the unsaturated imine **D**. The hydration of the amine would then lead to the formation of the amino-propyl moiety **E** observed in the SS NMR spectrum, which can first reduce Au(III) and then stabilise AuNPs, as reported in the literature.^{2,3,4,5,6,7,8}

2.2.4 XPS analysis of Au/OS@Yne

The surface chemical composition of the **Au/OS@Yne** systems was then analysed by XPS.

Wide-scan spectra (Figure 2.13a) displayed the presence of C, O, N and Au lines, in addition to the photopeaks related to the oxide supports (Si, Al, Ti), indicating that the organic functionalisation was successfully obtained. This was further confirmed by the analysis of the main carbon peak. In fact, in all of the analysed samples, the C1s signal (Figure 2.13b) displayed a tailing towards the high BE side and was deconvoluted by means of three different bands, centred at mean BE values of 284.8 (**I**; 52-57 % of the total C signal), 286.4 (**II**; 29-39 % of the total C signal), and 289.2 eV (**III**; 9-14 % of the total C signal). These components could be attributed to C–C, C–H, and/or C–Si (**I**), C–N and/or C–O (**II**), and O–C=O (**III**) bonds, respectively.^{11,13,36}

Besides, additional calculations for the estimation of the number of carbon atoms present on the species anchored on the substrate surface were avoided, due to the fact that band **I** also contains contributions from adventitious carbon, whose occurrence is ubiquitous on the surface of air-exposed samples.

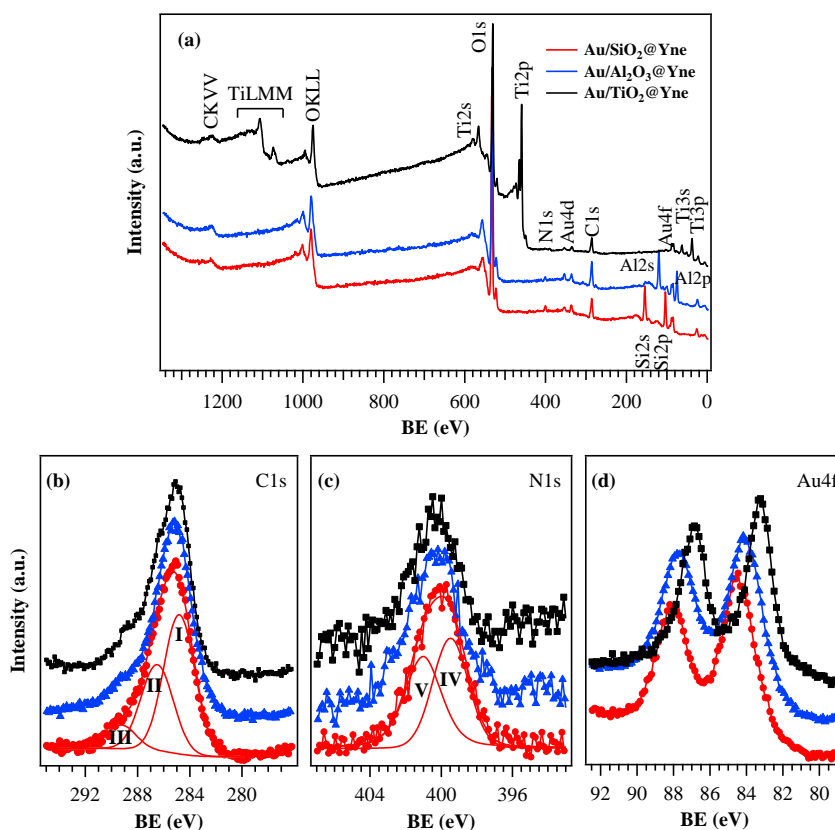


Figure 2.13. a) Surface wide-scan XP spectra and b) representative C1s, c) N1s and d) Au4f photoelectron peaks for the as-prepared specimens.

Although it was not possible to identify the contributions of the oxygen atoms in the ligand chains, due to the overlap with the other more intense oxygen bands,^{11,13} the successful anchoring of the organic functionality on the substrates was confirmed by the analysis of the N1s photopeaks (Figure 2.13c), which resulted from the contributions of a main component (IV, BE = 399.5 eV, 36-50 % of the total nitrogen), due to N in amino-groups³⁶ and an additional band (V, BE = 401.1 eV) related to NH-COO- groups.¹³ This is in line with the presence of an aminopropylsilane chain evidenced by the ¹³C CP/MAS NMR analysis (see paragraph 2.2.3).

Figure 2.13d displays the surface Au4f signals for the different specimens. Irrespective of the used substrate, no signals related to Au(I) and Au(III) species could be clearly identified, thus enabling to highlight the presence of pure Au(0) aggregates, in agreement with previous studies.^{33,34,35} As reported in Table 2.4, the typical surface at.% values for gold were 0.7 at.% for **Au/SiO₂@Yne** and **Au/TiO₂@Yne**, and slightly higher for **Au/Al₂O₃@Yne** (0.8 at.%).

Interestingly, the analysis of the Au4f_{7/2} BE evidenced a progressive downward shift upon going from SiO₂ to TiO₂-supported specimens [BE(Au4f_{7/2}) = 84.3, 84.0 and 83.4 eV for **Au/SiO₂@Yne**, **Au/Al₂O₃@Yne** and **Au/TiO₂@Yne** samples, respectively] (Table 2.4). In general, gold nanoparticles can be either slightly positive or negative, depending on the adopted support, synthesis method and processing conditions.^{37,38} For alumina and titania-supported samples, the peak position was in good agreement with previously reported data for homologous systems.^{39,40,41} In particular, a comparison of the present BE data with the reference position for bulk metallic gold [BE(Au4f_{7/2}) = 84.0 eV]⁴² revealed a downward shift of Au peak position for **Au/TiO₂@Yne**, suggesting the occurrence of electron donation from the titania support to the metal and the consequent formation of an electron-rich (Au^{δ-}) phase.^{41,43} On the contrary, the BE increase with respect to bulk Au observed for **Au/SiO₂@Yne** might suggest the presence of core-level shifts, caused by an incomplete screening of the core-hole typical for nanostructured gold on poorly conducting substrates, such as SiO₂.⁴⁴

Table 2.4. XPS analysis of **Au/OS@Yne**.

Sample	Au surface coverage (at.%)	BE Au4f _{7/2} (eV)
Au/SiO₂@Yne	0.7	84.3
Au/Al₂O₃@Yne	0.8	84.0
Au/TiO₂@Yne	0.7	83.4

Furthermore, the surface O1s photopeaks for the target specimens are reported in Figure 2.14a. For **Au/SiO₂@Yne**, a single band centred at BE = 532.5 eV confirmed the presence of a silica-like network, as also supported by the Si2p position (BE = 103.3 eV; Figure 2.14b)^{42,45} despite overlapped contributions from chemisorbed –OH moieties could not be excluded.⁴⁶ For **Au/Al₂O₃@Yne**, two different signals contributed to the O1s peak, and were attributed to lattice O in Al₂O₃ (**VI**; BE = 531.1 eV, 58 % of the total oxygen signal) and to adsorbed oxygen/chemisorbed -OH groups (**VII**; BE = 532.4 eV) due to atmospheric exposure. The Al2p photoelectron peak position (74.5 eV, Figure 2.14c) also agreed to a good extent with previous values reported for alumina.⁴³ Finally, in the case of **Au/TiO₂@Yne**, the O1s surface peak could be decomposed by means of two different bands, located at BE = 530.0 eV (80 % of the total oxygen) and 531.7 eV. While the former

was ascribed to lattice oxygen in TiO₂ (in line with the energy location of the main spin orbit component of the Ti2p signal, BE(Ti2p_{3/2}) = 458.8 eV, Figure 2.14d), the second oxygen band was attributed both to adsorbed surface -OH groups and adsorbed oxygen.^{42,47,48}

Estimation of the O/M ratios (with M = Si, Al, Ti for **Au/SiO₂@Yne**, **Au/Al₂O₃@Yne** and **Au/TiO₂@Yne**) yielded values of 2.7, 2.3 and 2.8, respectively, higher than the stoichiometric ones expected for the bare supports due to both air exposure and surface functionalisation.

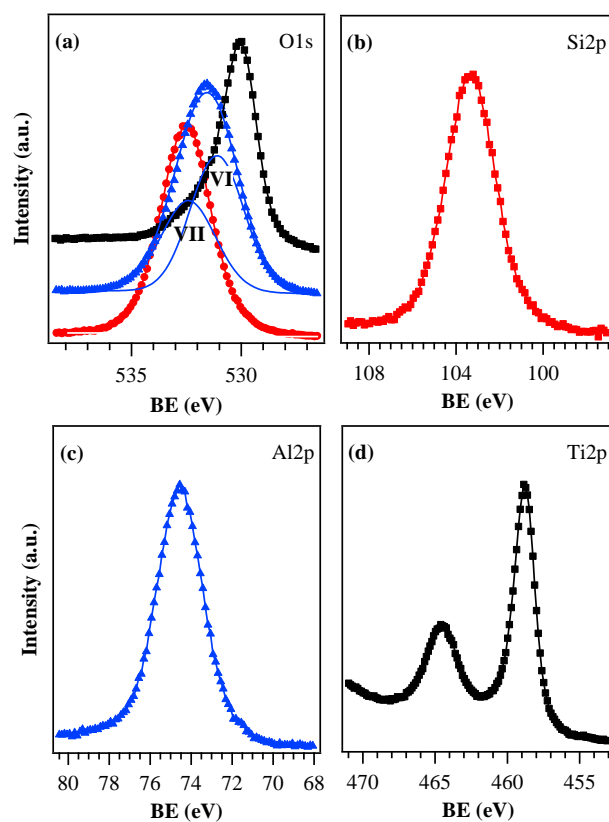


Figure 2.14. Surface XPS signals for a) O1s, b) Si2p, c) Al2p d) and Ti2p. Colour codes: red, sample **Au/SiO₂@Yne**; blue, sample **Au/Al₂O₃@Yne**; black, sample **Au/TiO₂@Yne**.

2.3 Conclusions

Gold nanoparticles were successfully immobilised on the modified surface of commercially available micrometre-sized silica, alumina and titania. The straightforward and highly reproducible synthetic procedure consisted of the grafting of the alkynyl-carbamate organosilane PPTEOS on the surface of the oxide support (**OS@Yne**), followed by reduction of the gold precursor HAuCl_4 and consequent immobilisation of the formed AuNPs (**Au/OS@Yne**).

The support was found to have an influence on the formation and stabilisation of AuNPs. In particular, silica allowed the highest organic functionalisation (12 wt %) as well as the highest gold loading (3.7 wt %). Moreover, TEM microscopy images showed only in the case of **Au/SiO₂@Yne** a homogeneous distribution of spherically shaped AuNPs, with an average diameter of 15 nm.

A more in depth investigation on the immobilisation mechanism was carried out by means of SS NMR spectroscopy for **Au/SiO₂@Yne**, revealing the presence of an amino-propyl linker in the organic functionalisation after the addition of gold.

Furthermore, XPS analysis carried out on the three different **Au/OS@Yne** systems confirmed that the oxide surfaces were decorated with pure Au nanoparticles since no signals related to Au(I) or Au(III) species were identified. Finally, a shift in the Au $4f_{7/2}$ BE was observed in the **Au/SiO₂@Yne** and **Au/TiO₂@Yne** samples (84.3 and 83.4 eV respectively), compared to that of bulk metallic gold (84.0 eV) indicating that the nature of the support can induce a different charge on the immobilized AuNPs.

2.4 Experimental section

2.4.1 Materials

Propargyl alcohol (99%), 3-(triethoxysilyl)propyl isocyanate (IPTEOS, 95%), triethylamine (NEt_3 , 99%), hydrogen peroxide (H_2O_2 , 35% wt. in H_2O), ethanol (EtOH, 99%), dichloromethane (CH_2Cl_2), sodium hydroxide (NaOH, 50% wt. in H_2O), hydrochloric acid (HCl, 37%), nitric acid (HNO_3 , 65%), sulphuric acid (H_2SO_4 , 99%) and deuterated chloroform (CDCl_3) were used as purchased from Sigma-Aldrich. Toluene was dried over Na/K alloy and distilled under nitrogen on 4 Å molecular sieves. Ultrapure water purified with the Milli-Q plus system (Millipore Co, resistivity over 18 M Ω cm) was used in all cases. $\text{HAuCl}_4 \cdot 3\text{H}_2\text{O}$ was prepared according to a literature procedure.⁴⁹ Commercial silica gel for column chromatography (particle size 63 – 210 μm , pore volume ca. 0.8 cm^3/g , surface area 550 m^2/g , Sigma-Aldrich) and aluminum oxide 90 active neutral (particle size 63 – 210 μm , pore volume ca. 0.27 cm^3/g , surface area 120 m^2/g , Merck) were dried prior to use by heating for 6 h at 180 °C in a quartz tube under a slow stream of dry nitrogen and then stored under nitrogen.⁵⁰ Titanium oxide (Cristal ACTIV DT-51, 100% anatase, surface area ca. 90 m^2/g), purchased from Cristal, was first pelletized into a 30 mm diameter disk, then the pellets were gently crumbled and sieved, first on a 60 mesh (250 μm) stainless steel sieve (Filtro Vibraciones S.L.) and successively on a 80 mesh (177 μm) sieve. Only the powder that remained on the 80 mesh sieve was used in the grafting process.

2.4.2 Synthesis of PPTEOS

In a two-necked dry round-bottomed flask under nitrogen atmosphere, a solution of 2.3 mL of propargyl alcohol (0.040 mol) and 5.0 mL of NEt_3 (0.036 mol) in 20 mL of CH_2Cl_2 was prepared and cooled in an ice bath. Then, 8.9 mL of IPTEOS (0.036 mol) previously dissolved in 10 mL of CH_2Cl_2 were added dropwise and the reaction mixture was left under stirring at room temperature for 24 h. The formation of the product was confirmed by TLC analysis (ethyl ether/petroleum ether 7:3). The solvent and the excess of propargyl alcohol were removed by evaporation under vacuum at 40 °C followed by a further drying at 0.5 atm for 5 h, affording PPTEOS as a yellow oil (9.89 g) with a 92% yield.

$^1\text{H-NMR}$ (300.1 MHz, CDCl_3): δ 0.63 (t, 2H, CH_2Si), 1.22 (t, 9H, OCH_2CH_3), 1.63 (m, 2H, SiCH_2CH_2), 2.45 (s, 1H, CH), 3.19 (m, 2H, CH_2NH), 3.81 (q, 6H, OCH_2), 4.67 (s, 2H, COOCH_2), 5.05 (bs, 1H, NH).

$^{13}\text{C-NMR}$ (75.50 MHz, CDCl_3): δ C=O (not visible), 78.55 ($\text{C}\equiv\text{CH}$), 74.37 ($\text{C}\equiv\text{CH}$), 58.47 (OCH_2), 52.27 (COOCH_2), 43.48 (CH_2NH), 23.17 (SiCH_2CH_2), 18.26 (OCH_2CH_3), 7.59 (CH_2Si).

2.4.3 Preparation of OS@Yne

SiO_2 @Yne. The grafting of the PPTEOS on the silica surface was performed under N_2 atmosphere at 60 °C. A 100 mL three-necked dry round-bottomed flask was charged with 4.73 g of SiO_2 , 98 μL of NEt_3 (0.70 mmol) and 17 mL of toluene. An excess of PPTEOS (2.29 g, 7.58 mmol), previously dissolved in 12 mL of toluene, was added to the vigorously stirred mixture. The reaction mixture was stirred for 23 h at 60 °C, then the heating was raised to 100 °C for 1 h and the nitrogen flow was increased in order to remove the ethanol formed as a co-product and to reduce the mixture volume. The obtained **SiO_2 @Yne** was recovered by filtration and thoroughly washed with EtOH in order to remove the excess of PPTEOS. The samples were then dried in oven at 50 °C for 24 h, finally yielding a white powder.

Al_2O_3 @Yne. The grafting of aluminium oxide was performed following the same procedure. A solution of 2.67 g of PPTEOS (8.84 mmol) in 18 mL of toluene was added to a suspension of 6.99 g of Al_2O_3 and 115 μL of NEt_3 (0.83 mmol) in 20 mL of toluene.

TiO_2 @Yne. The functionalisation of titanium oxide (60-80 mesh, prepared as previously described in paragraph 2.4.1) was carried out as follows. A dry round-bottomed flask kept under a nitrogen atmosphere was charged with 2.05 g of TiO_2 , 42 μL of NEt_3 (0.30 mmol) and 10 mL of toluene, then a solution of 0.99 g of PPTEOS (3.29 mmol) in 5 mL of toluene was added. The flask was then connected to a rotary evaporator, heated at 60 °C, and left under stirring at 60 rpm for 9 h.

2.4.4 Preparation of Au/OS@Yne

Au/SiO₂@Yne. The synthesis was carried out in a 500 mL three-necked dry round-bottomed flask under N₂ atmosphere. The flask was first charged with 1.0 g of **SiO₂@Yne** and 100 mL of H₂O and the suspension was heated to 90 °C at stirred at 500 rpm. Once silica was well dispersed in the solvent, 0.0980 g of HAuCl₄·3H₂O (0.25 mmol) previously dissolved in 150 mL of H₂O were added in order to have a 1.0 mM final concentration of HAuCl₄·3H₂O. The reaction mixture was left under stirring for 1 h.

The preparation of the **Au/SiO₂@Yne** sample for SS NMR analysis (containing a 13 wt % of gold) was carried out following the same procedure starting from a suspension of 0.370 g of **SiO₂@Yne** in 90 mL of H₂O and adding 0.106 g of HAuCl₄ (0.27 mmol) previously dissolved in 90 mL of H₂O.

Au/Al₂O₃@Yne. The synthesis was performed following the same procedure of the silica support, starting with a suspension of 1.033 g of **Al₂O₃@Yne** in 100 mL of H₂O, and then adding a solution of 0.0994 g of HAuCl₄ previously dissolved in 150 mL of H₂O.

Au/TiO₂@Yne. The synthesis was carried out in a rotary evaporator, in order to avoid the use of a magnetic stirrer. A two-necked flask was charged with 0.972 g of **TiO₂@Yne** and 100 mL of H₂O and heated to 90 °C. When the desired temperature was reached, a solution of 0.0995 g of HAuCl₄ dissolved in 150 mL of H₂O was rapidly added and the reaction mixture was left under stirring at 60 rpm for 1 h.

In all the three procedures, after the addition of the gold precursor a rapid change in the colour of the solution from pale-yellow to red-purple was observed. At the end of the reaction the obtained solid material was separated from the supernatant solution by filtration and thoroughly washed first with water and then with EtOH, then it was dried in oven at 50 °C for 24 h. Successively, **Au/TiO₂@Yne** was passed again on a 80 mesh stainless steel sieve (Filtru Vibracions S.L.) and only the powder with particle size higher than 80 mesh (ca. 50 %) was used in the catalytic tests.

2.4.5 Instruments and methods

The characterisation of PPTEOS was carried out by ^1H -NMR and ^{13}C -NMR spectroscopy in CDCl_3 using a Varian Gemini XL 300 (^1H 300.1 MHz, ^{13}C 75.5 MHz) instrument; chemical shifts were referenced internally to the residual solvent peak.

Thermogravimetric analyses were carried out using a Perkin Elmer TGA-7. The samples (ca. 10 mg) were heated in a platinum crucible at a rate of $10\text{ }^\circ\text{C min}^{-1}$ from $40\text{ }^\circ\text{C}$ to $900\text{ }^\circ\text{C}$.

ATR-FTIR analysis were performed with a Perkin Elmer Spectrum Two spectrophotometer, equipped with an Universal ATR accessory, in the range $4000\text{--}400\text{ cm}^{-1}$ with a resolution of 0.5 cm^{-1} . Pristine and modified oxides powders were directly analyzed after being ground in a mortar performing 40 scans for each analysis.

The amount of gold present on the different samples was determined by flame atomic absorption spectroscopy (AAS, Thermo Scientific) in air-acetylene flame with a wavelength of 242.8 nm and a spectral band-width of 0.5 nm. Calibration lines were obtained from five standard solutions at a known concentration (2, 4, 6, 8 and 10 ppm) prepared by dilution of a 100 ppm $\text{HAuCl}_4 \cdot 3\text{H}_2\text{O}$ solution in HCl 0.5 M. The samples of **Au/SiO₂@Yne** were prepared by first treating the solid (ca. 10 mg) with a few drops of NaOH 50 wt % and heating in order to completely dissolve the silica support, then aqua regia was added for the dissolution of AuNPs. Finally, the solution was diluted with HCl 0.5 M to a volume of 50 mL. The samples of **Au/Al₂O₃@Yne** and **Au/TiO₂@Yne** were prepared by dissolving the solid (ca. 10 mg) in 10 mL of HNO_3 65%, 0.5 mL of H_2SO_4 68% and 1 mL of H_2O_2 30% and keeping the mixture in a microwave oven (Start Synth Microwave Synthesis Labstation) at $200\text{ }^\circ\text{C}$ for 1 h. Then, the obtained solution was diluted with water to a final volume of 25 mL. The solids used for atomic absorption spectroscopy (AAS) measurements were weighted with a Mettler Toledo AT 21 Comparator balance.

For TEM investigations a Philips CM 100 transmission electron microscope operating at 80 kV was used. To prepare the sample a drop of the suspension was transferred onto holey carbon foils supported on conventional copper micro-grids. The ImageJ[®] picture analyser software⁵¹ was used to estimate the average AuNPs dimensions, averaging the measurements over at least 100 data per sample.

XRD was performed by a Philips X'Pert Pro instrument equipped with a fast X'Celerator detector, working at 40 mA and 40 kV and using $\text{CuK}\alpha$ radiation. For phase

identification, the 2θ angle range was from 10° to 80° (step size 0.1° ; time/step 100 seconds).

Solid State NMR spectra (SS NMR) were recorded using adamantane as reference on an Agilent NMR system, consisting of a 54 mm bore, 11.7 Tesla Premium Shielded superconducting magnet, a DD2 Performa IV NMR console equipped with 100 W highband and 300 W lowband amplifiers, and a NB Agilent 3.2 mm T3 MAS HXY Solid Probe 500 MHz.

X-ray photoelectron spectroscopy (XPS) analyses were conducted on a Perkin-Elmer Φ 5600ci spectrometer using a standard AlK α excitation source ($h\nu = 1486.6$ eV), at a working pressure $< 10^{-8}$ mbar. The reported binding energies (BEs; uncertainty = ± 0.1 eV) were corrected for charging effects by assigning a BE of 284.8 eV to the C1s line of adventitious carbon.^{36,42} After a Shirley-type background subtraction,⁵² atomic percentages (at. %) were calculated by signal integration using sensitivity factors supplied by Perkin-Elmer. Peak fitting was performed adopting Gaussian-Lorentzian peak shapes by means of the XPS Peak software (version 4.1; <http://xpspeak.software.informer.com/4.1/>).

References

- ¹ L. F. Gutiérrez, S. Hamoudi, K. Belkacemi, *Catalysis*, **2011**, *1*, 97.
- ² S. Fazzini, D. Nanni, B. Ballarin, M. C. Cassani, M. Giorgetti, C. Maccato, A. Trapananti, G. Aquilanti, S. I. Ahmed, *J. Phys. Chem. C*, **2012**, *116*, 25434.
- ³ K. Kim, H. B. Lee, J. W. Lee, K. S. Shin, *J. Colloid Interface Sci.* **2010**, *345*, 103.
- ⁴ K. Kim, H. B. Lee, J. W. Lee, H. K. Park, K. S. Shin, *Langmuir*, 2008, *24*, 7178.
- ⁵ X. Sun, S. Dong, E. Wang, *Langmuir*, **2005**, *21*, 4710.
- ⁶ X. Sun, S. Dong, E. Wang, *Polymer*, **2004**, *45*, 2181.
- ⁷ X. Sun, S. Dong, E. Wang, *Macromolecules*, **2004**, *37*, 7105.
- ⁸ M. Aslam, L. Fu, M. Su, K. Vijayamohanan, V.P. David, *J. Mater. Chem.*, **2004**, *14*, 1795.
- ⁹ K. Kuroda, T. Ishida, M. Haruta, *J. Mol. Catal. A*, **2009**, *298*, 7.
- ¹⁰ S. Panigrahi, S. Basu, S. Praharaj, S. Pande, S. Jana, A. Pal, S. K Ghosh, T. Pal, *J. Phys. Chem. C*, **2007**, *111*, 4596.
- ¹¹ S. Fazzini, M. C. Cassani, B. Ballarin, E. Boanini, J. S. Girardon, A. S. Mamede, A. Mignani, D. Nanni, *J. Phys. Chem. C*, **2014**, *118*, 24538.
- ¹² T. Ishida, K. Kuroda, N. Kinoshita, W. Minagawa, M. Haruta, *J. Colloid Interface Sci.*, **2008**, *323*, 105.
- ¹³ B. Ballarin, D. Barreca, E. Boanini, E. Bonansegna, M. C. Cassani, G. Carraro, S. Fazzini, A. Mignani, D. Nanni, D. Pinelli, *RSC Adv.*, **2016**, *6*, 25780.
- ¹⁴ S. Borsacchi, M. Bonaccorsi, M. Mais, L. Calucci, E. Carignani, F. Martini, M. Geppi, *La Chimica e L'Industria*, **2015**, *4*, 20.
- ¹⁵ K. Albert, E. Bayer, *J. Chromatog.*, **1991**, *544*, 345.
- ¹⁶ <https://nationalmaglab.org/about/around-the-lab/meet-the-probes/mas-probe>
- ¹⁷ B. Ballarin, D. Barreca, E. Boanini, M. C. Cassani, P. Dambrosio, A. Massi, A. Mignani, D. Nanni, C. Parise, A. Zaghi, *ACS Sustain. Chem. Eng.*, **2017**, *5*, 4746, <https://pubs.acs.org/doi/abs/10.1021/acssuschemeng.7b00133>.
- ¹⁸ X. Lu, S. Fu, J. Wang, J. Zhìong, D. Qingzhi, *Macromol. Rapid Commun*, **2009**, *30*, 2116.
- ¹⁹ G. A. Parks, *Chem. Rev.*, **1965**, *65*, 2, 177.
- ²⁰ C. Sun, J. C. Berg, *Adv. Colloid Interface Sci.*, **2003**, *105*, 151.
- ²¹ K. L. Furer, *J. Mol. Struct.* **1998**, *449*, 53.

-
- ²² Y. Ding, X. Chu, X. Hong, P. Zou, Y. Liu, *Appl. Phys. Lett.*, **2012**, *100*, 137011.
- ²³ X. Jiao, H. Li, L. Li, F. Xiao, N. Zhao, W. Wei, *RSC Adv.*, **2014**, *4*, 47012.
- ²⁴ A. Suelson, *J. Phys. Chem.* **1970**, *74*, 2574.
- ²⁵ M. Primet, P. Pichat, M. V. Mathieu, *J. Phys. Chem.* **1971**, *75*, 1221.
- ²⁶ P. Dambruoso, M. Ballestri, C. Ferroni, A. Guerrini, G. Sotgiu, G. Varchi, A. Massi, *Green Chem.*, **2015**, *17*, 1907.
- ²⁷ J. Blümel, *J. Am. Chem. Soc.*, **1995**, *117*, 2112.
- ²⁸ A. Arcadi, *Chem. Rev.*, **2008**, *108*, 3266.
- ²⁹ A. S. K. Hashmi, *Chem. Rev.*, **2007**, *107*, 3180.
- ³⁰ C. Obradors, A. M. Echavarren, *Acc. Chem. Res.*, **2014**, *47*, 902.
- ³¹ A. Corma, A. Leyva-Perez, M. J. Sabater, *Chem. Rev.*, **2011**, *111*, 1657.
- ³² L. J. Wang, H. T. Zhu, A. Q. Wang, Y. F. Qiu, X. Y. Liu, Y. M. Liang, *J. Org. Chem.*, **2014**, *79*, 204.
- ³³ L. Zhang, *J. Am. Chem. Soc.*, **2005**, *127*, 16804.
- ³⁴ G. Li, G. Zhang, L. Zhang, *J. Am. Chem. Soc.*, **2008**, *130*, 3740.
- ³⁵ F. Q. Shi, X. Li, Y. Xia, L. Zhang, Z. X. Yu, *J. Am. Chem. Soc.*, **2007**, *129*, 15503.
- ³⁶ J. F. Moulder, W. F. Stickle, P. E. Sobol, K. D. Bomben, *Handbook of X-ray Photoelectron Spectroscopy*; Perkin Elmer Corporation: Eden Prairie, MN, **1992**.
- ³⁷ R. Sui, K. L. Lesage, S. K. Carefoot, T. Fürstenhaupt, C. J. Rose, R. A. Marriott, *Langmuir*, **2016**, *32*, 9197.
- ³⁸ G. A. Filonenko, W. L. Vrijburg, E. J. M. Hensen, E. A. Pidko, *J. Catal.*, **2016**, *343*, 97.
- ³⁹ M. Li, X. Wang, F. Cárdenas-Lizana, M. A. Keane, *Catal. Today*, **2017**, *279*, 19.
- ⁴⁰ B. Panthi, A. Mukhopadhyay, L. Tibbitts, J. Saavedra, C. J. Pursell, R. M. Rioux, B. D. Chandler, *ACS Catal.*, **2015**, *5*, 2232.
- ⁴¹ N. Perret, X. Wang, T. Onfroy, C. Calers, M. A. Keane, *J. Catal.*, **2014**, *309*, 333.
- ⁴² D. Briggs, M. P. Seah, *Practical Surface Analysis by Auger and X-ray Photoelectron Spectroscopy*; Wiley: New York, 2nd edn. **1990**.
- ⁴³ C. Zhao, B. Li, J. Du, J. Chen, Y. Li, *J. Alloy Compd.*, **2017**, *691*, 772.
- ⁴⁴ D. Barreca, A. Bovo, A. Gasparotto, E. Tondello, *Surf. Sci. Spectra*, **2003**, *10*, 21.
- ⁴⁵ D. Barreca, A. Gasparotto, C. Maccato, C. Maragno, E. Tondello, G. Rossetto, *Chem. Vapor. Depos.*, **2007**, *13*, 205.
- ⁴⁶ D. Barreca, A. Gasparotto, C. Maccato, E. Tondello, G. Rossetto, *Thin Solid Films*, **2008**, *516*, 7393.
- ⁴⁷ <http://srdata.nist.gov/xps>.

⁴⁸ M. Fittipaldi, V. Gombac, A. Gasparotto, C. Deiana, G. Adami, D. Barreca, T. Montini, G. Martra, D. Gatteschi, P. Fornasiero, *ChemPhysChem*, **2011**, *12*, 2221.

⁴⁹ G. Braurer, *Handbook of Preparative Inorganic Chemistry*; Academic Press: New York, **1963**, Vol. *II*, 1058.

⁵⁰ D. D. Perrin, W. L. F. Armarego, D. R. Perrin, *Purification of Laboratory Chemicals*; Pergamon Press: New York, 2nd edn, 1980.

⁵¹ <http://imagej.nih.gov/ij/>.

⁵² D. Shirley, *Phys. Rev. B*, **1972**, *5*, 4709.

3. ALCOHOL OXIDATION CATALYSED BY GOLD NANOPARTICLES SUPPORTED ON FUNCTIONALISED OXIDES

3.1 Introduction

3.1.1 Oxidation of alcohols: sustainability and selectivity issues

The oxidation of alcohols is one of the most important transformations in organic chemistry. Indeed, alcohols are common starting materials in the synthesis of a variety of chemicals, intermediates, plastics, detergents, paints, cosmetics, food additives, pharmaceuticals, etc.¹

Nowadays, this reaction represents an open challenge from the point of view of process sustainability, since traditional procedures involve the use of harmful organic solvents, harsh reaction conditions and toxic and expensive stoichiometric oxidants. In fact, some of the most commonly employed oxidising agents are chromic oxides,² Jones reagent,³ PCC (pyridinium chlorocromate),⁴ permanganate,⁵ activated DMSO (Swern oxidation)⁶ and the Dess-Martin periodinane,⁷ which are not only toxic but produce large volumes of wastes at the end of the reaction.¹

In particular, the environmental impact of a chemical process can be evaluated in terms of *atom economy* (AE), defined as the molecular weight of the desired product divided by the sum of the molecular weights of all the substances produced in a stoichiometric equation, expressed as a percentage.⁸ As shown in Figure 3.1, oxidations carried out with the above mentioned reagents result in a low atom economy compared to the process in which molecular oxygen is employed as a green alternative.⁹

However, it must be taken into account that the use of molecular oxygen could present significant safety issues, due to the flammability of mixtures of oxygen and volatile organic solvents in the vapour phase.¹⁰ Even in the case in which these concerns are reduced by using oxygen diluted to 10 % with nitrogen, these methods lie on the edge of acceptability.⁹

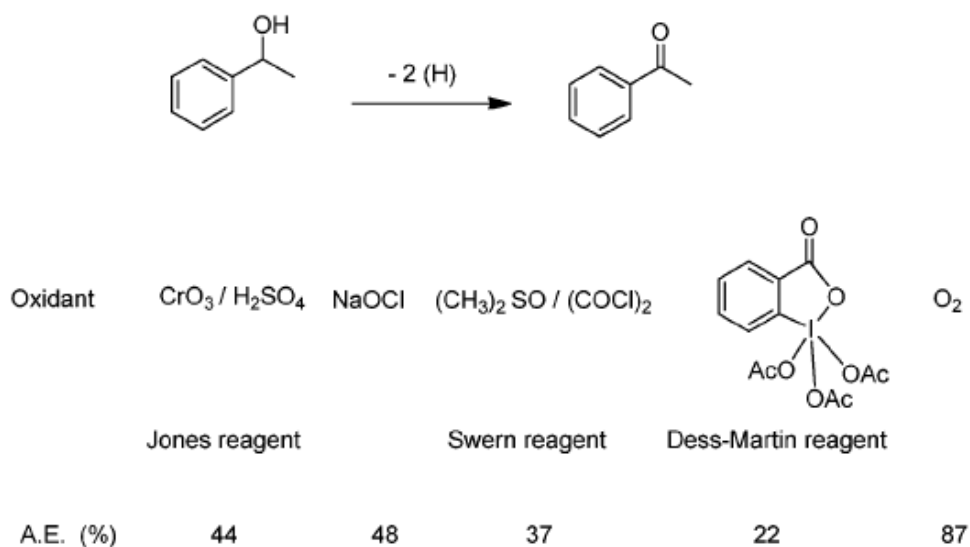
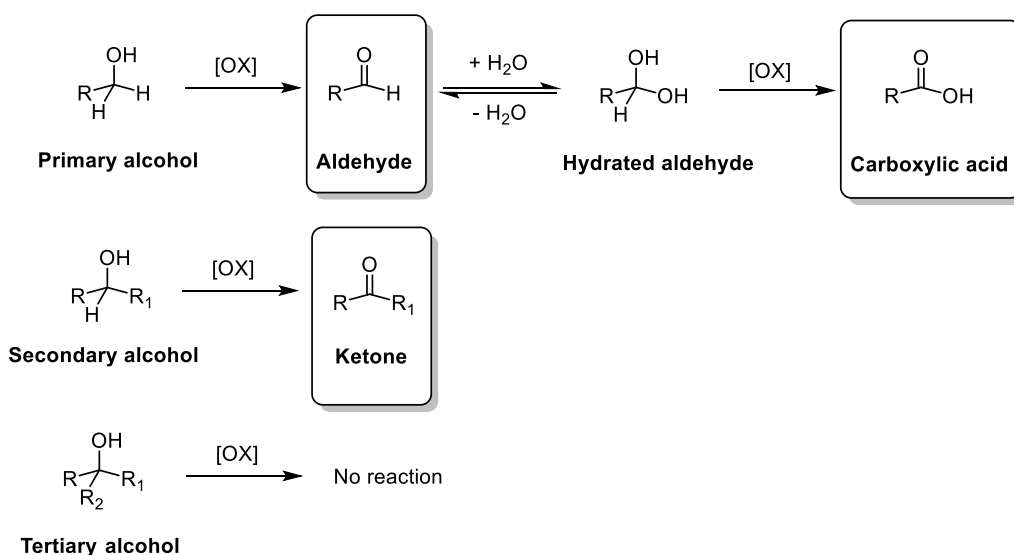


Figure 3.1. Comparison of oxidising agents for alcohol oxidation.⁹

Hence, the development of green, economic, efficient and safe alternatives is a research field in continuous expansion, for both environmental and economic reasons.^{11,12} In particular, the oxidation of alcohols with recyclable heterogeneous catalysts in aqueous media under mild conditions, would be a suitable green solution. In this regard, catalytic systems based on metal nanoparticles, such as Ag, Pd, Ru, Au, Pt and Cu have been reported for the oxidation of both aliphatic and aromatic alcohols.^{13,14,15,16,17}

Another issue related to this organic transformation is that the outcome of the reaction depends on the type of starting alcohol. Indeed, primary alcohols are first oxidised to aldehydes, which may be further oxidised to the corresponding carboxylic acids, through the formation of a hydrated aldehyde intermediate, leading to a selectivity problem. On the contrary, secondary alcohols are oxidised to ketones, while tertiary alcohols are mostly unaffected by oxidation (Scheme 3.1).^{1,18}

In the case of primary alcohols, selectivity can be tuned by changing the reaction conditions, such as the polarity of the solvent media, the oxidising agent and the type of catalyst. Furthermore, the addition of a base, such as KOH and K_2CO_3 , is frequently needed for the oxidation of primary alcohols in water, though this is not a green solution due to problems related to corrosion and waste base treatments.¹¹ Besides, the basic media can induce a shift of selectivity towards the formation of the ester product, deriving from the esterification reaction between the starting alcohol and the carboxylic acid product.



Scheme 3.1. Oxidation of alcohols.

3.1.2 Supported gold nanoparticles as catalysts for alcohol oxidation

Over the years, many studies reported in the literature focused on the oxidation of alcohols catalysed by AuNPs immobilised on different types of supports, such as metal oxides, carbon supports, polymers, etc.¹

Metal oxides are considered ideal supports for many applications, due to the combination of high thermal and chemical stability with high surface areas.

Corma *et al.* reported the efficient and selective solvent-free oxidation of alcohols to aldehyde and ketones using oxygen at atmospheric pressure, in the presence of small crystal-size gold (2–5 nm) and nanocrystalline ceria (5 nm). XPS analysis on the catalytic system revealed the presence of gold in different oxidation states, i.e. Au(0), Au(I) and Au(III), stabilised by the ceria support by creating Ce(III) and oxygen deficient sites.¹⁹ Furthermore, the same group showed that AuNPs supported on nanocrystalline ceria possess high activity and selectivity in the aerobic oxidation of allylic alcohols, suggesting that the lattice oxygen vacancies promoted the interaction and physisorption of molecular oxygen. Primary and secondary aromatic alcohols were converted to the corresponding aldehydes and ketones in quantitative yields and the presence of substituents was found to influence the reaction rate.²⁰

Cao *et al.* studied a base free protocol for alcohol oxidation with hydrogen peroxide (H₂O₂) catalysed by AuNPs supported on different metal oxides, i.e. TiO₂, Al₂O₃, CeO₂,

Fe₂O₃. The best results were obtained with the Au/TiO₂ catalyst, suggesting that the small size of AuNPs and the synergistic interaction with titania favoured the crucial H₂O₂ decomposition (Figure 3.2). Moreover, the catalyst high stability and easy recyclability was reported, alongside the possibility to carry out a hectogram-scale oxidation of 1-hexanol to 1-henoic acid.¹¹

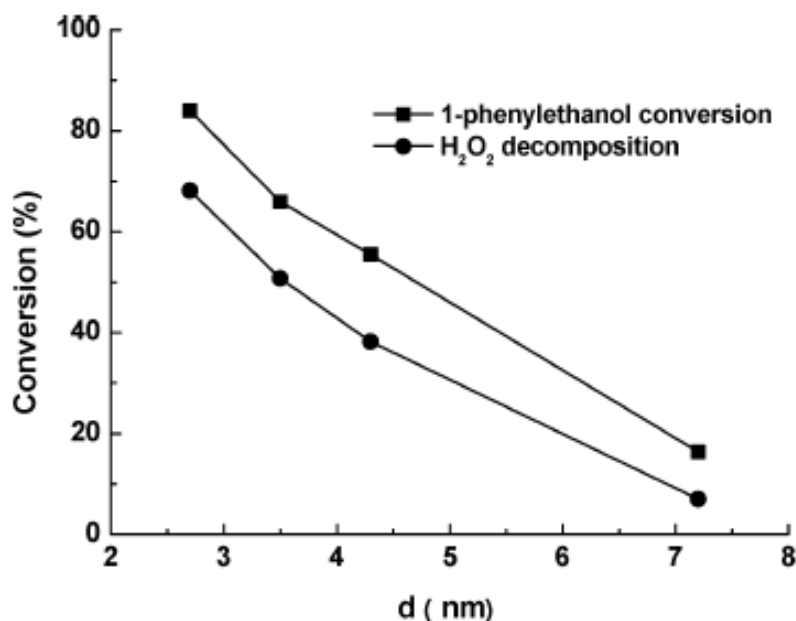


Figure 3.2. 1-phenylethanol conversion and H₂O₂ decomposition *versus* AuNPs size.¹¹

An interesting study on the selective oxidation of benzyl alcohol was carried out by Repo *et al.* by a solvent-controlled catalysis with Au/Al₂O₃. When the reaction was carried out in water, a poor selectivity was observed, due to the over-oxidation of benzaldehyde to benzoic acid and the subsequent reaction to benzyl benzoate. On the contrary, in a non-polar organic solvent, i.e. toluene, over-oxidation was significantly reduced, with the catalyst selectivity shifted towards the formation of the aldehyde. The addition of a base to the water medium was found to have several effects on the oxidation process: the promotion of the selectivity in benzoic acid, the enhancement of the catalytic activity and the stabilisation of the catalytic system. Moreover, when the oxidation was carried out in the presence of methanol as solvent, the oxidative esterification of benzyl alcohol with the solvent occurred (Scheme 3.2).²¹

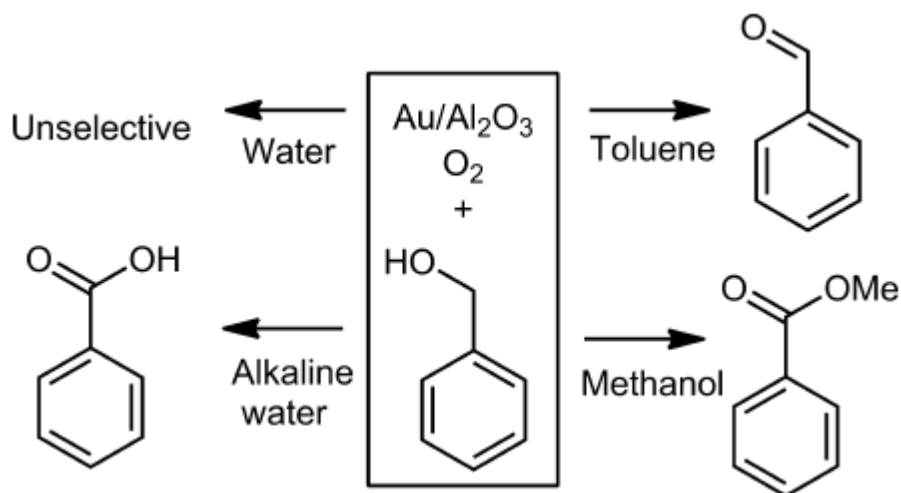


Figure 3.2. Solvent-controlled oxidation of benzyl alcohol with $\text{Au}/\text{Al}_2\text{O}_3$.²¹

Another common type of supports are carbon-based materials, such as mesoporous carbon, carbon nanotubes (CNT), graphene and graphene oxide.

Gold nanoparticles supported on mesoporous carbon, synthesized by Shaabani *et al.* were found to be active in the aerobic oxidation of benzyl alcohol in water, in the presence of K_2CO_3 . In particular, complete conversion in benzaldehyde was observed after 1 h of reaction. Furthermore, similar results were obtained in acetonitrile, toluene, xylene and THF.²²

The same group also prepared a gold catalyst supported on supramolecular ionic liquid grafted graphene, which showed excellent activity and selectivity in the oxidation of benzyl alcohol to benzaldehyde. The catalyst was successfully recycled and employed in the oxidation of several primary and secondary alcohols.²³

With regards to polymer immobilised AuNPs, Tsukuda *et al.* developed highly stable gold nanoclusters using star-like thermosensitive polyvinyl vinyl ether, which effectively catalysed the aerobic oxidation of benzyl alcohol with a complete selectivity in benzoic acid.²⁴

Furthermore, Kobayashi *et al.* reported the synthesis of AuNPs supported on polystyrene for the oxidation of alcohol at room temperature, using molecular oxygen at atmospheric pressure. Among the different solvents studied, the best results were achieved in biphasic media such as toluene/water and benzotrifluoride/water.^{25,26}

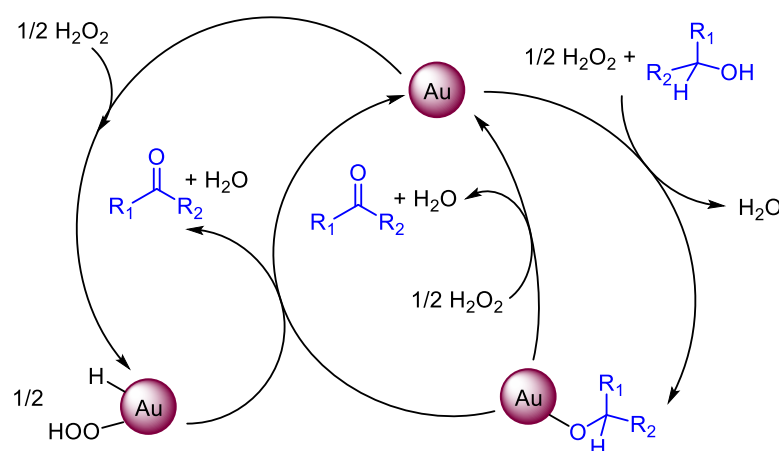
3.1.3 Mechanism of alcohol oxidation over AuNPs catalysts

The mechanism of alcohol oxidation by means of molecular oxygen over supported gold nanoparticles has been studied in several works, with the aim of gaining an insight on the reaction pathway and consequently being able to improve the activity and selectivity of the catalytic systems.

The adsorption and dissociation of molecular oxygen on AuNPs surfaces is energetically unfavourable. In this sense, it is generally believed that the active adsorption of O_2 occurs on the low coordinated gold atoms, thus oxygen dissociation depends on the morphology of AuNPs rather than the size.¹ Furthermore, many experimental results suggest that the support may play a fundamental role in this stage.²⁷

With regards to the oxidation of alcohols, the commonly reported mechanism involves three steps: 1) adsorption of the alcohol molecules on the surface of gold nanoparticles, 2) β -hydride elimination with formation of an active carbonyl species and a metal hydride (Au-H), and 3) oxidation by elemental oxygen to regenerate the gold surface.^{19,28,29}

A similar mechanism was reported for the oxidation in the presence of hydrogen peroxide, as shown in Scheme 3.3. The role of H_2O_2 is to act as a hydrogen scavenger and facilitate the abstraction of the α -hydrogen of the alcohol substrate, leading to the formation of an alcoholate species in the first step of the reaction. Then, the Au-alcoholate complex may be further attacked by H_2O_2 or by the Au-hydroperoxide complex generated from the reaction of Au(0) with H_2O_2 , generating the final carbonyl compound via a β -elimination pathway.¹¹



Scheme 3.3. Proposed mechanism for alcohol oxidation with H_2O_2 on AuNPs, redraw from reference 11.

3.1.4 Gold-catalysed alcohol oxidation in continuous-flow systems

In recent years, the use of the continuous-flow technology for the oxidation of alcohols has become increasingly popular.³⁰

Kobayashi *et al.* described the first quantitative aerobic oxidation process of primary and secondary alcohols in a continuous-flow microreactor system, consisting of a wall coated gold-immobilised capillary column. The reaction was carried out by first mixing a solution of the substrate in an organic solvent and an aqueous solution of K_2CO_3 in a T-mixer and then introducing the oxygen flow immediately prior to the capillary column containing the catalyst (Figure 3.3).^{31,32}

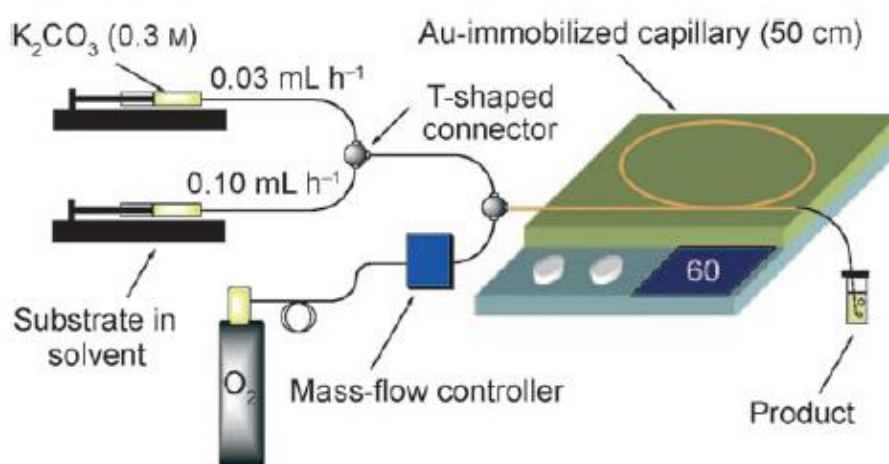


Figure 3.3. Experimental setup for the gold catalysed oxidation of alcohols in a capillary column reactor.³¹

This three-phase system was found to efficiently oxidise a series of benzylic, aliphatic and allylic alcohols, without any leaching of gold after four days of continuous running. However, the system was stabilised only after several hours, as indicated by the lower conversions observed in the beginning of the experiments.

Kirschning *et al.* employed a mixture of gold-doped superparamagnetic nanoparticles and MAGSILICA® for the packing of a continuous-flow reactor. An external inductor was then used to rapidly heat the magnetic particles, as O_2 and reagents flowed in the system. The efficient heating of the magnetic particles obtained by induction allowed the successful oxidation of both allylic and benzyl alcohols. Furthermore, 4-bromobenzyl alcohols was oxidised to the corresponding aldehyde on a gram scale.³³

Finally, Girardon *et al.* reported the preparation of gold-coated capillary reactors by immobilisation of polymer-stabilised AuNPs on the functionalised surface of the reactor

inner walls. These systems were used for the continuous-flow oxidation of benzyl alcohol in the presence of H_2O_2 and K_2CO_3 in water, achieving a high yield in benzoic acid.

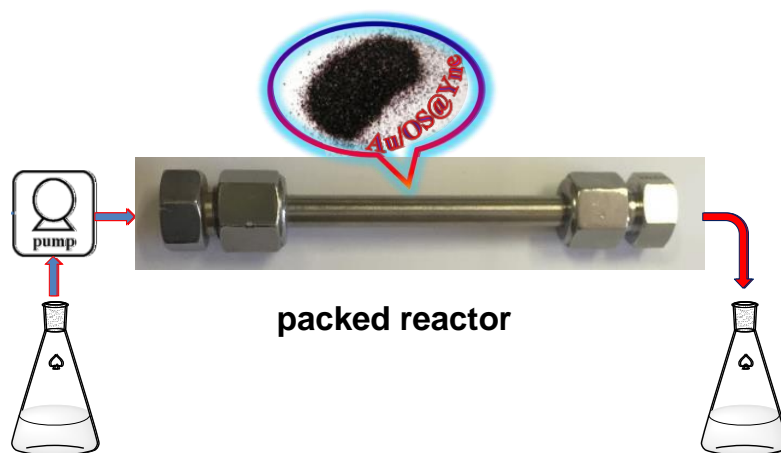
3.1.5 Aim of the chapter

The catalytic activity of **Au/SiO₂@Yne**, **Au/Al₂O₃@Yne** and **Au/TiO₂@Yne** in the oxidation of alcohols was investigated and compared.

First, the activity of the **Au/OS@Yne** catalysts in the oxidation of benzyl alcohol under batch conditions was evaluated employing different oxidising agents (H_2O_2 , $t\text{BuOOH}$) and solvent media (water, toluene), in order to investigate the possibility to tune the selectivity of the reaction. Then, the study with the silica supported catalyst was extended to a series of substituted primary and secondary alcohols both in a batch and in a continuous-flow system (Scheme 3.4).

Finally, the effect of the oxide support on the catalytic properties of the system was studied in the oxidation of 1-phenylethanol.

Part of the work reported in the present chapter was published in *ACS Sustainable Chemistry and Engineering*.³⁴

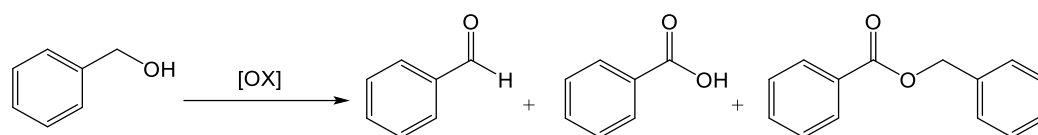


Scheme 3.4. Schematic representation of the continuous-flow setup.

3.2 Results and discussion

3.2.1 Oxidation of benzyl alcohol with Au/OS@Yne in batch conditions

The oxidation of benzyl alcohol was initially studied as a model reaction to evaluate the catalytic activity of the **Au/SiO₂@Yne** system. As previously discussed, the oxidation of this substrate can bring to the formation of different products, i.e. benzaldehyde, benzoic acid and benzyl benzoate (Scheme 3.5), hence the catalyst selectivity is an important aspect to consider when evaluating its efficiency.



Scheme 3.5. Oxidation of benzyl alcohol.

As shown in Table 3.1, a series of experiments were carried out changing some of the reaction parameters such as type of oxidant, catalyst loading and solvent media.

Table 3.1. Oxidation of benzyl alcohol with **Au/SiO₂@Yne** in batch conditions.^a

Entry	Solvent	Oxidant	Au molar equivalents (%)	Conv (%) ^b	Φ_{acid} (%) ^b	Φ_{aldehyde} (%) ^b
1 ^c	H ₂ O	H ₂ O ₂	10	>99	>99	-
2 ^{c,d}	H ₂ O	H ₂ O ₂	10	93	>99	-
3	H ₂ O	H ₂ O ₂	1	52 ^e	63	27
4	Toluene	H ₂ O ₂	1	-	-	-
5	Toluene	^t BuOOH in water	10	61 ^f	38	60
6	Toluene	^t BuOOH in decane	10	66 ^f	46	54

a) Reaction conditions: initial concentration of benzyl alcohol 0.025 M (entries 1 – 3) and 0.020 M (entries 4 – 11), T = 90 °C, 2.5 molar equivalents of oxidant, t = 3 h; b) conversion and selectivity determined by ¹H-NMR; c) t = 6; d) second cycle with the catalyst from entry 1; e) 10 % selectivity in benzyl benzoate; f) trace of benzyl benzoate.

When the reaction was carried out in water, employing H₂O₂ as oxidising agent and with a 10 % molar equivalents amount of gold, complete conversion of the substrate was observed within 6 h with the selectivity completely shifted towards the formation of the carboxylic acid (Table 3.1, entry 1). Furthermore, both conversion and selectivity were found to be almost the same after a second cycle of reaction with the same catalyst (Table 3.1, entry 2). On the other hand, a 52 % conversion was obtained after 3 h with a 1 % molar equivalent of **Au/SiO₂@Yne**, followed by a decrease in selectivity (Table 3.1, entry 3).

Moreover, a series of experiments in toluene were performed in order to obtain the formation of benzaldehyde as the main product.²¹ First, the reaction was carried out in the presence of H₂O₂, but due to the poor solubility of the oxidising agent in the solvent media, no conversion of the starting material was observed (Table 3.1, entry 4). For this reason, tert-butyl hydroperoxide (^tBuOOH) was instead tested as oxidant (Table 3.1, entries 5 - 6) leading to better results in terms of conversion, though only a 50-60 % selectivity in benzaldehyde was achieved.

The catalytic activity of **Au/Al₂O₃@Yne** and **Au/TiO₂@Yne** was then tested in the same reaction (Table 3.2).

Table 3.2. Oxidation of benzyl alcohol with **Au/Al₂O₃@Yne** and **Au/TiO₂@Yne** in batch conditions.^a

Entry	Catalyst	Solvent	Oxidant	Au molar equivalents (%)	Conv (%) ^b	Φ _{acid} (%) ^b	Φ _{aldehyde} (%) ^b
1	Au/Al₂O₃@Yne	H ₂ O	H ₂ O ₂	10	>99	>99	-
2	Au/TiO₂@Yne	H ₂ O	H ₂ O ₂	10	>99 ^c	98	-
3	Au/Al₂O₃@Yne	H ₂ O	H ₂ O ₂	1	17	60	40
4	Au/TiO₂@Yne	H ₂ O	H ₂ O ₂	1	25	91	9
5	Au/Al₂O₃@Yne	Toluene	^t BuOOH in decane	10	15 ^d	-	90
6	Au/TiO₂@Yne	Toluene	^t BuOOH in decane	10	35 ^e	-	83

a) Reaction conditions: initial concentration of benzyl alcohol 0.025 M, T = 90 °C, 2.5 molar equivalents of oxidant, t = 3 h; b) conversion and selectivity determined by ¹H-NMR; c) traces of benzyl benzoate; d) 10 % selectivity in benzyl benzoate; e) 17 % selectivity in benzyl benzoate.

As previously observed with the silica supported catalyst, the use of 10 % molar equivalents of Au, in the presence of H₂O₂ in water, led to the complete conversion of benzylic alcohol to benzoic acid (Table 3.2, entries 1 - 2). On the contrary, when the catalysts amount was decreased to 1 % molar equivalents only a 17 % and 25 % conversion was achieved with **Au/Al₂O₃@Yne** and **Au/TiO₂@Yne** respectively (Table 3.2, entries 3 - 4). Finally, the reaction was carried out in toluene with ^tBuOOH as oxidising agent. In this case, despite the poor conversion of the substrate compared to the analogue silica supported catalyst, a clear shift in selectivity towards the formation of benzaldehyde was observed (Table 3.2, entries 5 - 6).

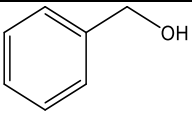
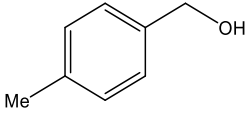
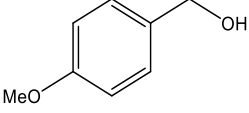
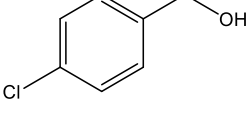
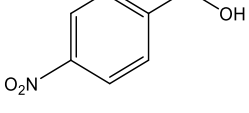
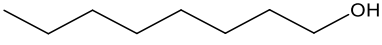
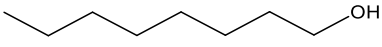
The results obtained in the oxidation of benzyl alcohol catalysed by the different **Au/OS@Yne** systems, could be explained by the difference in the AuNPs size and their distribution on the oxide support. Indeed, it is well known that the catalytic activity of gold nanoparticles is strictly related to their dimension.

Furthermore, the results indicated that also the nature of the support may have an influence on the overall catalytic efficiency, both in terms of conversion and selectivity. As previously described in Chapter 2, XPS analysis suggested the occurrence of different charge levels at the gold particles depending on the support and this could be in principle related to the observed different activities of the three catalysts. Nevertheless, as far as a full rationalization of the experimental results is concerned, this point cannot be conclusive, since a complete understanding of the role of gold in such mechanisms has not been attained yet.^{28,35}

3.2.2 Oxidation of primary and secondary alcohols with Au/SiO₂@Yne in batch conditions

After the results obtained in the benzyl alcohol oxidation with Au/SiO₂@Yne, the study was extended to a series of primary alcohols bearing substituent groups, working with an initial alcohol concentration of 0.05 M, H₂O₂ as oxidising agent and water as the reaction medium (Table 3.3).

Table 3.3. Oxidation of primary alcohols with Au/SiO₂@Yne in batch conditions.^a

Entry	Substrate	t (h)	Conv (%) ^b	Φ _{acid} (%) ^b	Φ _{aldehyde} (%) ^b
1 ^c		3	86 (84)	74 (70)	26 (30)
2		3	>99	>99	-
3		3	>99	61	39
4		5	18	67	33
5		3	-	-	-
6 ^d		5	30	>99	-
7 ^e		1	16	>99	-

^aReaction conditions: starting alcohol solution 0.05 M, solvent: H₂O, 2.5 mol equiv. H₂O₂, T = 90 °C;

^bconversion and selectivity determined by ¹H-NMR; ^cdata in parenthesis referred to GC analysis; ^dstarting alcohol solution 0.1 M; ^ereaction performed with the catalyst AUROLite™, with a 1.0 M alcohol solution and vertical agitation FirstMate™ synthesizer, Argonaut Technology.

In these conditions, oxidation of benzyl alcohol occurred with a 74% selectivity in benzoic acid and a 26% selectivity in benzaldehyde (Table 3.3, entry 1). In the case of this substrate, conversion and selectivity were also determined by GC by directly analysing the aqueous phase isolated at the end of the reaction. Since a comparison between this data

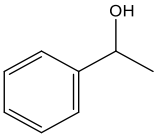
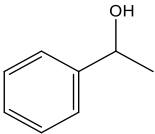
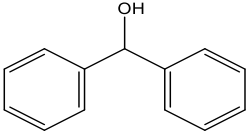
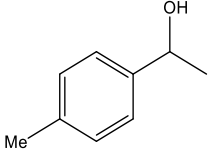
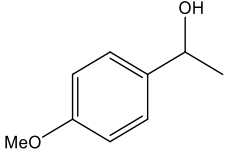
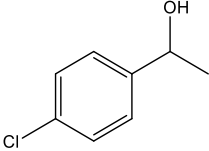
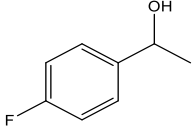
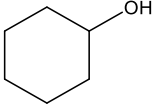
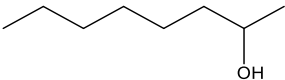
and the ones obtained by $^1\text{H-NMR}$ analysis showed no substantial differences, the latter technique was employed in all the following experiments.

The presence of substituents on the aromatic ring was found to affect the alcohol reactivity (Table 3.3, entries 2 - 5): the alcohols bearing electron-donating groups (-OMe and -Me) were completely oxidised in 3 h, whereas 4-chlorobenzyl alcohol was found to be less reactive and in the case of 4-nitrobenzyl alcohol no conversion was observed.

A low conversion was also observed with aliphatic alcohols such as 1-octanol (Table 3.3, entry 6). In order to have a comparison with literature data, we also performed the oxidation of 1-octanol with the commercial available AUROLiteTM gold catalyst (Au/Mintek) presenting a gold loading of 1 wt %. Before testing, AUROLite was simply ground and sieved to obtain a powder with a granulometry between 60 and 80 mesh, without any further thermal treatment.¹¹ As shown in Table 3.3 (entry 7) with this catalyst we obtained a 16% conversion after 1 h, thus confirming the lower activity of this kind of substrates.

The oxidation of secondary alcohols to the corresponding ketones was then carried out, employing H_2O_2 as oxidising agent and a mixture of $\text{H}_2\text{O}/^t\text{BuOH}$ (6:4 v/v) as solvent media (Table 3.4). The choice of this solvent system was dictated by the low solubility in water of some secondary alcohols, such as diphenylmethanol, as well as the carbonyl products. The use of water-alcohol mixtures is greener than the use of other common organic solvents,³⁶ furthermore $^t\text{BuOH}$ has been classified by the Food and Drug Administration as a class 3 solvent.^{37,38}

Table 3.4. Oxidation of secondary alcohols with **Au/SiO₂@Yne** in batch conditions.^a

Entry	Substrate	t (h)	Conv (%) ^b
1		4.5	74
2	reuse 1 ^c	4.5	69
3	reuse 2 ^c	4.5	73
4 ^d		4.5	47
5		2	>99
6		1	>99
7		1	>99
8 ^e		6	82
9 ^e		6	55
10 ^{f,g}		5	46
11 ^f		5	12

^aReactions conditions: starting alcohol solution 0.1 M, solvent: H₂O/BuOH 6:4 v/v, 2.5 mol equiv. H₂O₂, 1 % mol Au, T = 90 °C; ^bconversion determined by ¹H-NMR; ^cthe catalyst was washed three times with EtOAc before reuse; ^dreaction performed at T = 70 °C; ^eadditional 2.5 mol equiv. of H₂O₂ were added after 5 h; ^freaction performed in water; ^gadditional 2.5 mol equiv. of H₂O₂ were added after 2 h.

The results of these experiments, summarised in Table 3.4, indicated that **Au/SiO₂@Yne** efficiently catalysed the oxidation of 1-phenylethanol and diphenylmethanol (Table 3.4, entries 1 and 5). Additionally, two blank reactions were carried out, one in the absence of the catalyst and one in the absence of the oxidising agent H₂O₂, but no conversion of the alcohol was observed indicating that both the catalyst and hydrogen peroxide are necessary for the reaction to take place.

The oxidation of 1-phenylethanol was also performed at a lower temperature (Table 3.4, entry 4) leading to a lower conversion value. Therefore, all the subsequent reactions were performed at the temperature of 90 °C.

In keeping with what previously observed with primary alcohols, the presence of substituents influenced the alcohol reactivity: indeed 1-(p-tolyl)ethanol and 1-(4-methoxyphenyl)ethanol were completely oxidised in only 1 h of reaction (Table 3.4, entries 6 - 7), while in the case of 1-(4-chlorophenyl)ethanol and 1-(4-fluorophenyl)ethanol a higher amount of oxidising agent and a longer reaction time were needed in order to achieve a good conversion (Table 3.4, entries 8 - 9).

Finally, the catalytic activity of **Au/SiO₂@Yne** was tested in the oxidation of an alicyclic and an aliphatic alcohol, i.e. cyclohexanol and 2-octanol, using only water as the reaction medium, but a lower activity was observed with both substrates (Table 3.4, entries 10 - 11).

Recycling experiments of the **Au/SiO₂@Yne** catalyst in the oxidation of 1-phenylethanol were also performed. After a first reaction run, the catalyst was recovered by centrifugation, thoroughly washed first with water and then with CH₂Cl₂, dried under vacuum and reused. With this procedure a decrease of about 50 % in the conversion was observed already in the second cycle. Conversely, when the catalyst was washed with EtOAc before being reused, the conversion remained essentially the same after three cycles of reaction (Table 4, entries 2 - 3).³⁹

The AAS analysis on the recycled catalyst showed that the gold loading after three cycles was essentially the same of the fresh one. Furthermore, TEM analysis indicated that the nanoparticles size and distribution remained almost unchanged, though a few larger aggregates were found (Figure 3.4).

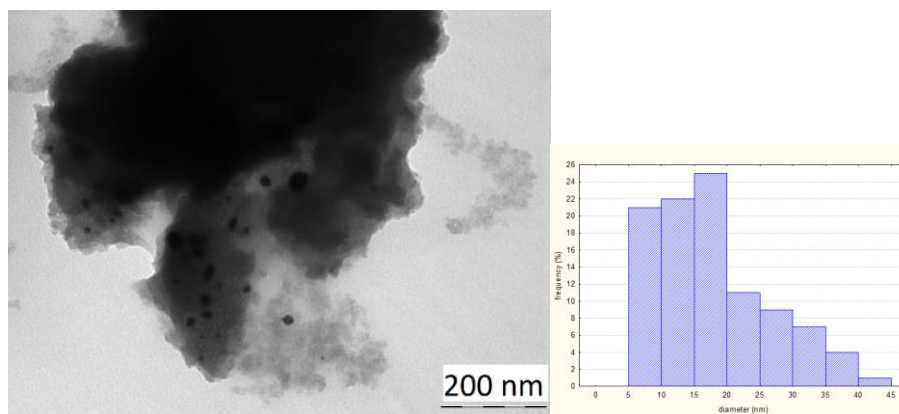


Figure 3.4. TEM image and particle size distribution of reused **Au/SiO₂@Yne**.

The results of the XPS analysis of **Au/SiO₂@Yne** after use (Figure 3.5) were almost identical to the ones obtained with the pristine catalyst, with no significant variations in the relative weight of the different species contributing to C1s and N1s photopeaks. Moreover, the presence of the starting alcohol and the carbonyl product could not be completely ruled out, since the corresponding signals would be overlapped with components **I** and **II** in the C1s signal and would be indistinguishable from the main O1s photopeak.

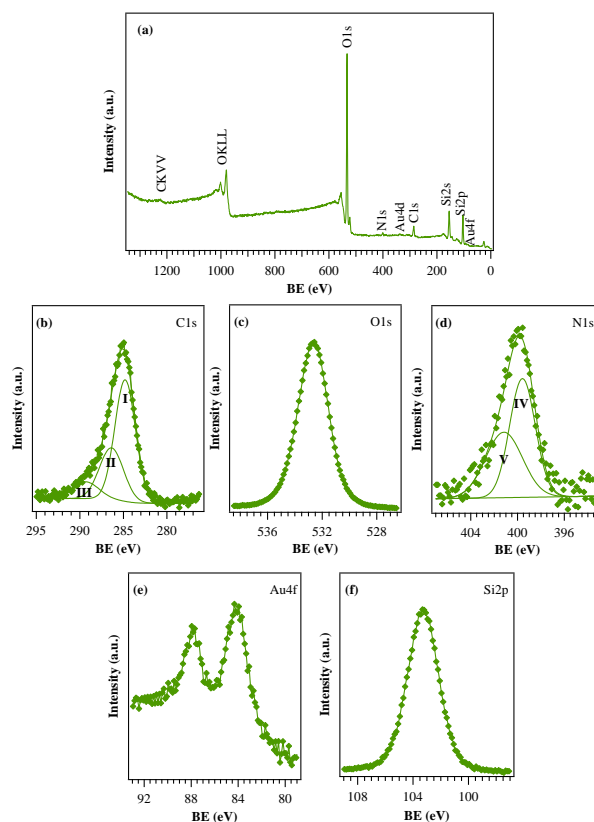


Figure 3.5. a) Surface wide-scan XP spectra and representative b) C1s, c) O1s, d) N1s, e) Au4f and f) Si2p signals for **Au/SiO₂@Yne** after catalytic tests.

3.2.3 Oxidation of primary and secondary alcohols with Au/SiO₂@Yne in continuous-flow conditions

On the basis of on the above results, the oxidation of alcohols catalysed by Au/SiO₂@Yne was also performed in a continuous-flow system (Table 3.5). The flow reactor was packed with the catalyst, heated to 90 °C and fed with the reagent mixture containing the alcohol and H₂O₂ at the constant flow rate of 0.1 mL min⁻¹.

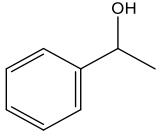
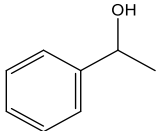
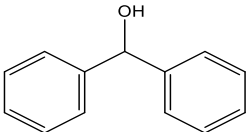
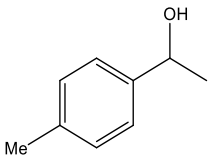
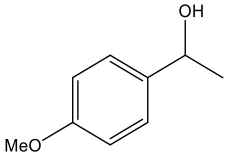
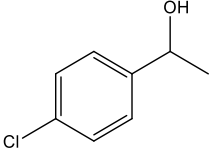
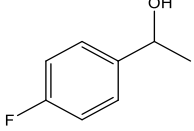
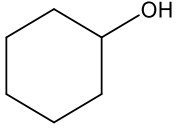
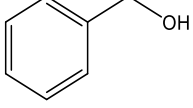
Under these conditions, 1-phenylethanol was converted to acetophenone with an 85 % yield, with the system achieving the steady-state regime after 2 h (Table 3.5, entry 1). In order to enhance the conversion of the substrate, a catalytic test at a lower flow rate was also performed (Table 3.5, entry 2), however no significant differences were observed. Furthermore, the long-term stability of Au/SiO₂@Yne was investigated and it was found that the catalyst could work for over 50 h at 90 °C without observing any decrease in the catalytic activity.

The general improvement in the catalyst performances under continuous-flow conditions was particularly evident in the oxidation of the less reactive substrates. Indeed, in the case of 1-(4-chlorophenyl)ethanol and 1-(4-fluorophenyl)ethanol the conversions achieved after only 1 h (Table 3.5, entries 6 - 7) were comparable to those achieved in the batch system in 6 h (Table 3.4, entries 8 - 9).

Moreover, the oxidation of benzyl alcohol was successfully carried out in the continuous-flow system (Table 3.5, entries 9), giving an almost complete conversion with a 100 % selectivity in the corresponding carboxylic acid.

Finally, it is worth noting that the residence time of the employed flow system was 2.5 min at the working flow rate (0.1 mL min⁻¹), as determined by pycnometric measurements. If compared to the reaction time of the batch experiments, this data further confirms the significant improvement of the catalyst performances moving from batch to flow conditions.

Table 3.5. Oxidation of alcohols with **Au/SiO₂@Yne** in continuous-flow system.^a

Entry	Substrat	t (h) ^b	Conversion (%) ^c
1		2	85
2 ^d		2	90
3		3	96
4		1	>99
5		1	>99
6		1	77
7 ^e		1	68
8 ^f		2	15
9 ^g		2	>99 ^h

^aReactions conditions: starting alcohol solution 0.1 M, solvent: H₂O/^tBuOH 6:4, 2.5 mol equiv. H₂O₂, T_{solution} = 30 °C, T_{reactor} = 90 °C; flow rate: 0.1 mL min⁻¹; ^btime needed to achieve the steady-state regime; ^csteady-state conversion determined by ¹H-NMR; ^dreaction performed at a flow rate of 0.075 mL min⁻¹; ^ethe reaction was performed at 80 °C, ^freaction performed in water, with 5 equivalents of H₂O₂, at a flow rate of 0.05 mL min⁻¹; ^greaction performed in water at a flow rate of 0.3 mL min⁻¹ with a starting alcohol concentration of 0.025 M; ^hcomplete selectivity in the corresponding carboxylic acid.

3.2.4 Oxidation of 1-phenylethanol with Au/OS@Yne in continuous-flow conditions

The catalytic activity of **Au/Al₂O₃@Yne** and **Au/TiO₂@Yne** in the oxidation of 1-phenylethanol, in batch and continuous-flow conditions, was evaluated and compared to the catalytic activity of **Au/SiO₂@Yne** (Table 3.6).

Table 3.6. Oxidation of 1-phenylethanol with **Au/OS@Yne** in batch^a and flow.^b

Entry	Catalyst	BATCH		FLOW
		Conversion (%) ^c	Conversion (%) ^c	Productivity (h ⁻¹) ^d
1	Au/SiO₂@Yne	74	85	12.8
2	Au/Al₂O₃@Yne	28	85	10.2
3	Au/TiO₂@Yne	2 ^e	80 ^f	19.2

^aReactions conditions: starting alcohol solution 0.1 M, solvent: H₂O/^tBuOH 6:4 v/v, 2.5 mol equiv. H₂O₂, 1 % mol Au, T = 90°C, 4.50 h; ^breactions conditions: starting alcohol solution 0.1 M, solvent: H₂O/^tBuOH 6:4 v/v, 2.5 mol equiv. H₂O₂, T_{solution} = 30 °C, T_{reactor} = 90 °C; flow rate: 0.1 mL min⁻¹, steady-state achieved after 2 h; ^cconversion determined by ¹H-NMR; ^dcalculated as mole of product per mole of Au per time. ^evertical agitation was performed with the FirstMateTM synthesizer, Argonaut Technology; ^f steady-state achieved after 4 h.

In the batch experiment **Au/SiO₂@Yne** was found to be the most active among the three catalysts, leading to a 74 % conversion of the substrate after 4.50 h (Table 3.6, entry 1), while with **Au/Al₂O₃@Yne** a final conversion of only 28 % was achieved in the same amount of time (Table 3.6, entry 2).

Besides, the titania supported catalyst showed almost no catalytic activity in the target reaction (Table 3.6, entry 3) and this could be due to the fact that during the batch experiment the starting size (60 – 80 mesh) of the support was completely lost to give a very fine powder, difficult to separate from the supernatant at the end of the reaction. Therefore, it is probable that not all of the AuNPs were exposed on the catalyst surface and so able to take part in the reaction. No improvements were observed when the reaction was carried out with the FirstMateTM synthesizer, which provides a milder vertical agitation compared to magnetic stirring.

On the other hand, when the reaction was carried out in continuous-flow conditions, significantly better performances of the catalysts were observed. Upon using the **Au/Al₂O₃@Yne** catalyst, the conversion increased from 28 % to 85 % (Table 3.6, entry 2), hence becoming comparable to that achieved with **Au/SiO₂@Yne**, while with **Au/TiO₂@Yne** a dramatic increase from 2 % to 80 % occurred (Table 3.6, entry 3).

These results clearly demonstrate that for these systems the flow approach also plays a strategic role in preserving the physical and chemical integrity of the catalytic system during its use.

3.3 Conclusions

At first, the catalytic activity of **Au/SiO₂@Yne**, **Au/Al₂O₃@Yne** and **Au/TiO₂@Yne** in the oxidation of benzyl alcohol was studied in different reaction conditions, in order to shift the selectivity towards the formation of benzoic acid or benzaldehyde. In particular, when the reaction was carried out in water, with H₂O₂ as oxidising agent and with 10 % molar equivalents of Au catalyst, a complete conversion of the substrate to the corresponding carboxylic acid was observed within 3 h. On the contrary, the formation of benzaldehyde was observed when working in toluene and with ^tBuOOH, but in this case lower conversions were obtained.

Then, the oxidation of a variety of primary and secondary alcohols catalysed by **Au/SiO₂@Yne** was carried out, both in batch and flow conditions. The catalyst was found to have a remarkable stability in the continuous-flow system, where it could work for over 50 h at 90 °C without observing any significant decrease in the catalytic activity.

Finally, the comparison of the catalytic activities of **Au/SiO₂@Yne**, **Au/Al₂O₃@Yne** and **Au/TiO₂@Yne** in the oxidation of 1-phenylethanol revealed that the silica-supported catalyst gave the best overall performances. Furthermore, the flow methodology was found to play a strategic role in preserving the physical and chemical integrity of the solid catalyst, with dramatic consequences in the case of **Au/TiO₂@Yne**, as far as the reaction conversion is concerned (from 2 % in batch to 80 % in flow).

3.4 Experimental section

3.4.1 Materials

Hydrogen peroxide (H₂O₂, 35 wt% in H₂O), benzyl alcohol, 4-nitrobenzyl alcohol, 4-methylbenzyl alcohol, 4-methoxybenzyl alcohol, 1-octanol, 2-octanol, 1-phenylethanol, diphenylmethanol, cyclohexanol, 1-(4-chlorophenyl)ethanol, 1-(4-fluorophenyl)ethanol, 1-(p-tolyl)ethanol, 4-methoxy- α -methylbenzyl alcohol, α -methyl-2-naphthalenemethanol, 1,7-heptanediol, tert-butylhydroperoxide (TBHP) 70 % in water, tert-butylhydroperoxide (TBHP) 5.5 M in decane, dichloromethane (CH₂Cl₂, 99%), tert-butanol (^tBuOH, 99%), ethyl acetate (EtOAc), and deuterated chloroform (CDCl₃) were of analytical grade and were used as purchased from Sigma-Aldrich. Ultrapure water purified with the Milli-Q plus system (Millipore Co, resistivity over 18 M Ω cm) was used in all cases. The commercial Au/TiO₂ catalyst AUROLite™ (Gold 1 wt% on titanium dioxide extrudates purchased from Strem) was mildly ground in an agate mortar and then passed on a 80 mesh stainless steel sieve. Only the material with particle size higher than 80 mesh was employed in the catalytic tests. **Au/SiO₂@Yne**, **Au/Al₂O₃@Yne** and **Au/TiO₂@Yne** were prepared as previously described in Chapter 2.

3.4.2 Catalytic tests

Batch experiments. In a typical experiment a solution of the starting alcohol in the appropriate solvent medium and the Au catalyst were charged in a flask and stirred for a few minutes at 90 °C, then 2.5 molar equivalents of H₂O₂ were added. At the end of the reaction the solid catalyst was separated from the mixture by centrifugation and washed once with water and once with CH₂Cl₂. The reactants and the products were recovered from the aqueous phase by extraction with CH₂Cl₂ and analysed by ¹H-NMR to evaluate conversion and selectivity. A comparison between the conversion determined by ¹H-NMR analysis and GC analysis was also carried out in the case of the benzyl alcohol substrate.

For the GC analysis the aqueous phase isolated at the end of the reaction was directly analysed.

For recycling tests, the catalyst was recovered by centrifugation and washed first with H₂O and then three times with ethyl acetate before being reused in the next cycle.

With the titania supported catalyst vertical agitation was performed with the FirstMate™ synthesizer, Argonaut Technology.

Continuous-flow experiments. The microreactors used for the continuous-flow experiments were prepared by gravity packing of a column reactor with **Au/OS@Yne** (300 - 400 mg). In a typical procedure, the continuous-flow system was fed with a 0.1 M solution of the alcohol at 30 °C and operated at a flow rate of 0.1 mL min⁻¹, with the packed microreactor heated to 90 °C. Hydrogen peroxide was added to the reagent mixture just before running. The eluate was collected in several fractions and analysed by ¹H-NMR after extractions with CH₂Cl₂.

3.4.3 Instruments

The system used for continuous-flow reactions was composed of an HPLC pump (Agilent 1100 micro series), an in-line pressure transducer, a stainless-steel column reactor (length: 10 cm, internal diameter: 2.1 mm), a sand bath and a data acquisition system (Agilent ChemStation). The units were connected by peek tubing (internal diameter 0.01 inch from Upchurch Scientific). The system hold-up volume was smaller than 80 μL. The temperature was controlled by inserting a thermometer inside the sand bath (temperature measurement error: ± 0.5 °C).

NMR spectra were recorded in CDCl₃ using a Varian Gemini XL 300 (¹H 300.1 MHz, ¹³C 75.5 MHz) instrument; chemical shifts were referenced internally to residual solvent peaks. An absolute error of ± 5% affects the peaks integration.

In the case of benzyl alcohol the final conversion and selectivity were also determined by GC analysis, using an Agilent Technologies 7890A GC system. Calibration lines for benzyl alcohol, benzoic acid and benzaldehyde were obtained after injection of four aqueous solutions at a known concentration, employing 1,7-heptanediol as internal standard. The samples were introduced into the column using a split mode (30:1). The oven temperature during the analysis was: initial temperature of 50 °C held for 1 minute, a first ramp at 20 °C min⁻¹ to 150 °C and finally a ramp at 35 °C min⁻¹ to 250 °C.

The amount of gold present in the catalyst after recycling tests was determined by atomic absorption spectroscopy (AAS, Thermo Scientific) in air-acetylene flame with a wavelength of 242.8 nm and a spectral band-width of 0.5 nm. Calibration lines were obtained from five standard solutions at a known concentration (2, 4, 6, 8 and 10 ppm)

prepared by dilution of a 100 ppm $\text{HAuCl}_4 \cdot 3\text{H}_2\text{O}$ solution in HCl 0.5 M. The catalyst samples were prepared by first treating the solid (ca. 10 mg) with a few drops of NaOH 50 wt % and heating in order to completely dissolve the silica support, then aqua regia was added for the dissolution of AuNPs. Finally, the solution was diluted with HCl 0.5 M to a volume of 50 mL.

For TEM investigations a Philips CM 100 transmission electron microscope operating at 80 kV was used. To prepare the sample a drop of the suspension was transferred onto holey carbon foils supported on conventional copper micro-grids. The ImageJ[®] picture analyser software⁴⁰ was used to estimate the average AuNPs dimensions, averaging the measurements over at least 100 data per sample.

X-ray photoelectron spectroscopy (XPS) analyses were conducted on a Perkin-Elmer Φ 5600ci spectrometer using a standard $\text{AlK}\alpha$ excitation source ($h\nu = 1486.6$ eV), at a working pressure $< 10^{-8}$ mbar. The reported binding energies (BEs; uncertainty = ± 0.1 eV) were corrected for charging effects by assigning a BE of 284.8 eV to the $\text{C}1\text{s}$ line of adventitious carbon.^{36,41} Peak fitting was performed adopting Gaussian-Lorentzian peak shapes by means of the XPS Peak software (version 4.1; <http://xpspeak.software.informer.com/4.1/>).

References

- ¹ A. S. Sharma, H. Kaur, D. Shah, *RSC Adv.*, **2016**, *6*, 28688.
- ² J. C. Collins, W. W. Hess, F. J. Frank, *Tetrahedron Lett.*, **1968**, *9*, 3363.
- ³ C. Wiles, P. Watts, S. J. Haswell, *Tetrahedron Lett.*, **2006**, *47*, 5261.
- ⁴ E. J. Corey, J. W. Suggs, *Tetrahedron Lett.*, **1975**, *16*, 2647.
- ⁵ W. J. Mijs, C. R. H. de Jonge, *Organic Synthesis by Oxidation with Metal Compounds*, Plenum Press, New York, **1986**.
- ⁶ A. J. Mancuso, S. L. Huang, D. Swern, *J. Org. Chem.*, **1978**, *43*, 2480.
- ⁷ D. B. Des, J. C. Martin, *J. Org. Chem.*, **1983**, *48*, 4155.
- ⁸ B. M. Trost, *Science*, **1991**, *254*, 1471.
- ⁹ R. A. Sheldon, *Chem. Soc. Rev.*, **2012**, *41*, 1437.
- ¹⁰ J. Auge, *Green Chem.*, **2008**, *10*, 225.
- ¹¹ J. Ni, W. J. Yu, L. He, H. Sun, Y. Cao, H. Y. He, K. N. Fan, *Green Chem.*, **2009**, *11*, 756.
- ¹² T. Mallat, A. Baiker, *Chem. Rev.*, **2004**, *104*, 3037.
- ¹³ N. Dimitratos, A. Villa, D. Wang, F. Porta, D. Su, L. Prati, *J. Catal.*, **2006**, *244*, 113.
- ¹⁴ N. Zotova, K. Hellgardt, G. H. Kelsall, A. S. Jessiman, K. K. Hii, *Green Chem.*, **2010**, *12*, 2157.
- ¹⁵ X. Yang, X. Wang, J. Qui, *Appl. Catal. A*, **2010**, *382*, 131.
- ¹⁶ Y. Shiraishi, D. Tsukamoto, Y. Sugano, A. Shiro, S. Ichikawa, S. Tanaka, T. Hirai, *ACS Catal.*, **2012**, *2*, 1984.
- ¹⁷ B. Karimi, M. Khorasani, H. Vali, C. Vargas, R. Luque, *ACS Catal.*, **2015**, *5*, 4189.
- ¹⁸ J. March, *Advanced Organic Chemistry: Reactions; Mechanism, and Structure*, Wiley, New York, 3rd edn, **1985**.
- ¹⁹ A. Abad, P. Concepcion, A. Corma, H. Garcia, *Angew. Chem.*, **2005**, *44*, 4066.
- ²⁰ A. Abad, C. Almela, A. Corma, H. Garcia, *Chem. Commun.*, **2006**, 3178.
- ²¹ S. Rautiainen, O. Simakova, H. Guoa, A. R. Leinoc, K. Kordás, D. Murzin, M. Leskelä, T. Repo, *Appl. Catal. A*, **2014**, *485*, 202.
- ²² M. Mahyari, A. Shaabani, M. Behbahani, A. Bagheri, *Appl. Organomet. Chem.*, **2014**, *28*, 576.
- ²³ M. Mahyari, A. Shaabani, Y. Bide, *RSC Adv.*, **2013**, *3*, 22509.
- ²⁴ S. Kanaoka, N. Yagi, Y. Fukuyama, S. Aoshima, H. Tsunoyama, T. Tsukuda, H. Sakurai, *J. Am. Chem. Soc.*, **2007**, *129*, 12060.

-
- ²⁵ H. Miyamura, R. Matsubara, Y. Miyazaki, Kobayashi, *Angew. Chem., Int. Ed.*, **2007**, *46*, 4151.
- ²⁶ C. Lucchesi, T. Inasaki, H. Miyamura, R. Matsubara, S. Kobayashi, *Adv. Synth. Catal.*, **2008**, *350*, 1996.
- ²⁷ M. Boronat, A. Corma, *Dalton Trans.*, **2010**, *39*, 8538.
- ²⁸ M. Conte, H. Miyamura, S. Kobayashi, V. Chechik, *J. Am. Chem. Soc.*, **2009**, *131*, 7189.
- ²⁹ S. Nishimura, Y. Yakita, M. Katayama, K. Higashimine, K. Ebitani, *Catal. Sci. Technol.*, **2013**, *3*, 351.
- ³⁰ H. P. L. Gemoets, Y. Su, M. Shang, V. Hessel, R. Luqueb, T. Noel, *Chem. Soc. Rev.*, **2016**, *45*, 83.
- ³¹ N. Wang, T. Matsumoto, M. Ueno, H. Miyamura, S. Kobayashi, *Angew. Chem., Int. Ed.*, **2009**, *48*, 4744.
- ³² K. Kaizuka, K.-Y. Lee, H. Miyamura, S. Kobayashi, *J. Flow Chem.*, **2012**, *2*, 1–4.
- ³³ S. R. Chaudhuri, J. Hartwig, L. Kupracz, T. Kodanek, J. Wegner, A. Kirschning, *Adv. Synth. Catal.*, **2014**, *356*, 3530.
- ³⁴ B. Ballarin, D. Barreca, E. Boanini, M. C. Cassani, P. Dambruoso, A. Massi, A. Mignani, D. Nanni, C. Parise, A. Zaghi, *ACS Sustain. Chem. Eng.*, **2017**, *5*, 4746.
- ³⁵ A. Abad, A. Corma, *Chem. Eur. J.*, **2008**, *14*, 212.
- ³⁶ C. Capello, U. Fischer, K. Hungerbühler, *Green Chem.*, **2007**, *9*, 927.
- ³⁷ U.S. Food and Drug Administration, <http://www.fda.gov/default.htm>.
- ³⁸ T. Osako, K. Toriia, Y. Uozumi, *RSC Adv.*, **2015**, *5*, 2647.
- ³⁹ M. Giorgetti, G. Aquilanti, B. Ballarin, M. Berrettoni, M. C. Cassani, S. Fazzini, D. Nanni, D. Tonelli, *Anal. Chem.*, **2016**, *88*, 6873.
- ⁴⁰ <http://imagej.nih.gov/ij/>
- ⁴¹ D. Briggs, M. P. Seah, *Practical Surface Analysis by Auger and X-ray Photoelectron Spectroscopy*; Wiley: New York, 2nd edn. 1990.

4. GOLD NANOPARTICLES SUPPORTED ON FUNCTIONALISED SILICA AS CATALYSTS FOR ALKYNES HYDROAMINATION

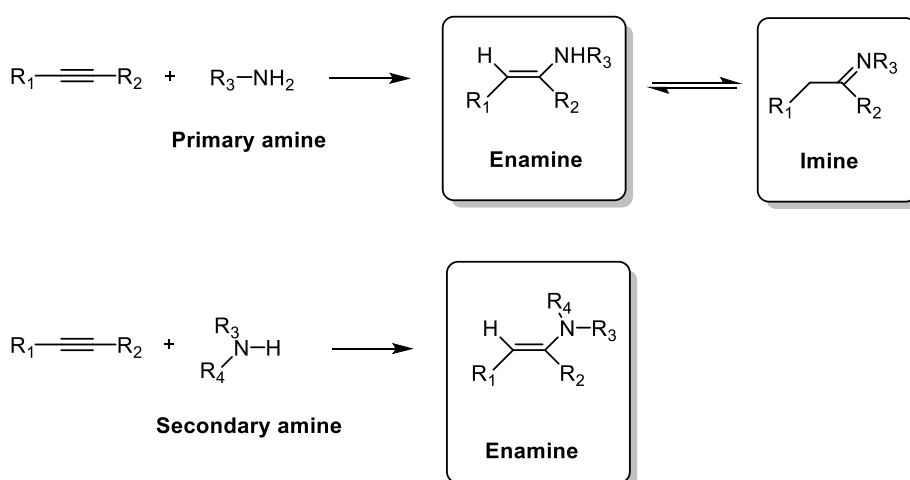
4.1 Introduction

4.1.1 Hydroamination of alkynes

Hydroamination reactions consist in the addition of an amine N-H bond across an unsaturated C-C bond, leading to the formation of valuable nitrogen-containing compounds.

This transformation is of great significance in synthetic organic chemistry, since it represents an atom-economical route for the preparation of a series of N-containing organic molecules which are important constituents of various basic and fine chemicals.^{1,2,3} On the one hand, *intermolecular* hydroamination affords structurally complex amines, on the other hand, *intramolecular* hydroamination provides access to a wide range of N-heterocyclic compounds.⁴

In the case of alkenes, the hydroamination products are stable secondary or tertiary amine, while alkynes are transformed into reactive species, i.e. enamines and imine, which can be useful intermediates for multistep synthesis (Scheme 4.1).^{5,6}



Scheme 4.1. Hydroamination of alkynes.

For instance, enamines and imines are widely encountered in the scaffolds of natural products or synthetic drugs, as well as in reactions of polymerization,⁷ asymmetric hydrogenation,⁸ cycloaddition,⁹ cross coupling,¹⁰ etc.¹¹

The addition of an amine to a C-C unsaturated bond is a slightly exothermic or approximately thermoneutral process.^{2,12} However, it is kinetically difficult due to the electron repulsion between the π system of the multiple bond and the high electron density located on the nitrogen atom, which results in a high activation barrier. Furthermore, the high temperature required to cross this energetic barrier causes a shift of the equilibrium towards the reagents, since the variation of entropy associated to this transformation is negative.¹³

Therefore, many research works have been recently focused on the development of efficient metal-based catalysts for this type of reactions.¹¹

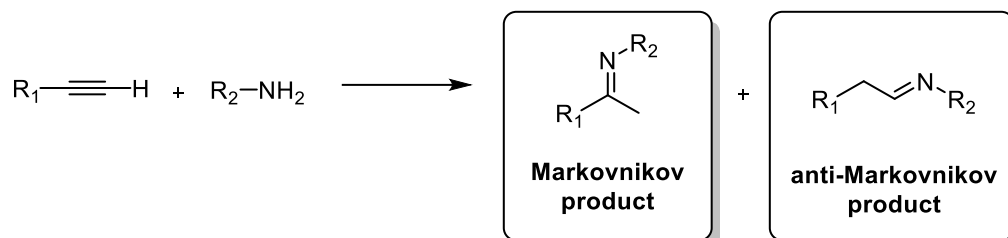
Non-catalytic hydroaminations involve the use of either strong acids to protonate the C-C multiple bond, thus facilitating the attack of amine,^{14,15,16} or strong bases to generate strongly nucleophilic amines, which react more easily with the C-C unsaturated bond.^{17,18} Metal catalysts can play a similar role by coordinating to the C-C multiple bond, therefore reducing its electron density or by replacing the nitrogen-bound proton allowing the insertion of C-C multiple bonds.

In particular, hydroamination of alkynes occurs more easily than hydroamination of alkenes, due to sterical reasons and to the weakness of the π bond, which is approximately 70 kJ mol⁻¹ weaker than the π system of alkenes.⁶ Furthermore, in the case of a metal catalyst, the strength of the metal coordination to the unsaturated substrate determines the reagent reactivity. Hence, the formation of a strong interaction between the metal and the π bond of alkenes can result in the inhibition of the subsequent nucleophile attack, while in the case of alkynes the weaker coordination allows the reaction to proceed more smoothly.

Another issue related to hydroaminations concerns the selectivity of the reaction. Indeed, in order to obtain the efficient and selective formation of a single product, the addition of the N-nucleophile to the C-C multiple bond needs to be performed under regio-, chemo- and stereo- controlled conditions.

When an amine adds to the C \equiv C bond of unsymmetrically substituted alkynes, two isomeric products can be formed, identified as the Markovnikov and the anti-Markovnikov

addition products (Scheme 4.2). A strategy to control the regioselectivity in the case of internal C-C multiple bonds is the introduction of strongly electron-withdrawing or extremely bulky substituents on one side of the triple bond, but the most efficient solution consists in the use of a selective catalyst.



Scheme 4.2. Regioselectivity in hydroamination reactions.

The chemoselectivity of hydroamination reactions depends on the tolerance of the alkyne functional groups to the amine nucleophilic attack. In the absence of catalysts, the N-nucleophile tends to react more easily with electrophilic centres, such as carbonyl groups, than C≡C bonds. Hence, in order to ensure a selective transformation, the catalyst must coordinate preferentially to the N-H and/or C≡C systems, without reacting with other functionalities.

Finally, depending on whether the attack of the nucleophile occurs from the top or the bottom of the C-C triple bond, the formation of different enantiomers or diastereoisomers can be observed. The stereochemical outcome of a hydroamination reaction is influenced by factors related both to the substrates (acidity of the N-H bond, electronic properties of the C-C triple bond and steric hindrance effects) and to the catalyst.¹¹

The understanding of the reaction mechanism of catalysed alkynes hydroamination still remains an open challenge, since the addition of amines across C-C triple bonds can potentially follow various pathways depending on the substrate combination, the catalytic system and the reaction conditions.

In general, the possible mechanisms can be divided in four categories on the base of the initial step: 1) activation of the C≡C bond by π coordination of a Lewis-acidic metal complex, followed by nucleophilic addition of the N-nucleophile, 2) initial interaction of the catalyst with the amine, followed by insertion of the alkyne, 3) initial formation of a metal-hydride by catalyst abstraction of the nitrogen-bound proton and migratory insertion of the alkyne into the M-H bond, and 4) rearrangement of initially formed η^2 alkyne-metal species into vinylidene complexes, which are then attacked by the N-nucleophile.¹¹

4.1.2 Supported gold nanoparticles as catalysts for hydroamination of alkynes

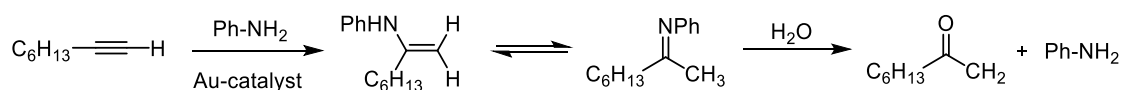
Significant research efforts have led to the development of efficient catalytic systems for inter- and intramolecular hydroamination reactions, based on transition metals and main group metals. However, the majority of these catalysts are confined to a limited set of substrates, for example, requiring activated C-C multiple bonds.^{19,20,21,22}

Among all transition metals, the affinity of gold towards C≡C bonds has no comparison. In fact, Au is sometimes referred to as “*alkynophile*” for its remarkable ability to coordinate preferentially to C-C triple bonds even in the presence of other functional groups, making the substrate more reactive towards nucleophilic attack.

In particular, the gold-catalysed activation of alkynes has been generally performed using homogenous Au(I) complexes,^{23,24} but more recently research on the use of supported AuNPs catalysts has flourished.

Corma *et al.* reported the regioselective hydroamination of alkynes catalysed by AuNPs immobilised on a polysaccharide biopolymer (chitosan), without the need for acidic promoters and inert atmosphere.²⁵ In this work, the catalyst performances in the hydroamination of 1-octyne with aniline were compared with the results obtained by using commercially available Au/Fe₂O₃, Au/TiO₂, Au/SiO₂ and Au/CeO₂. In all cases, the selective formation of the Markovnikov imine was observed and the highest yields were obtained with the synthesized Au/chitosan catalyst, even though rather harsh conditions were required (100 °C for 22 h). These findings were attributed to the differences in Au particle size of the starting materials, as well as to the enhanced stability of the biopolymer-supported system, which prevented nanoparticles agglomeration and leaching.

Moreover, the authors addressed the presence of 2-octanone among the reaction products, whose formation was ascribed to the hydrolysis of the imine in the presence of traces of water (Scheme 4.3).

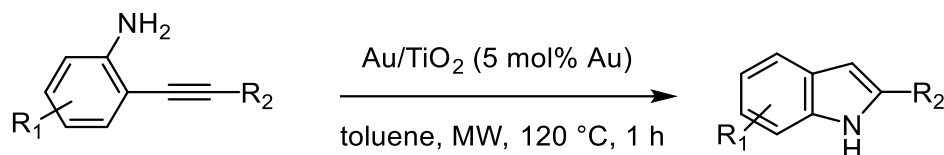


Scheme 4.3. Hydroamination of 1-octyne with aniline, redraw from reference 25.

Zhao's groups employed gold nanoclusters encapsulated within interfacially cross-linked micelles for the hydroamination of alkynes at room temperature.²⁶ In this case, the reaction was carried out under solvent-free conditions, but the final imine product was intentionally hydrolysed to the corresponding ketone in order to facilitate the determination of the yield by ¹H-NMR spectroscopy.

Hammond *et al.* described the regioselective hydroamination of a series of substituted terminal alkynes, in the presence of commercially available gold nanoparticles supported on titania.⁴ In order to improve the catalyst performances, different reaction conditions were tested for the hydroamination of phenylacetylene with aniline. The increase of the reaction temperature from 80 °C to 100 °C did not lead to significantly higher yields, while the addition of acidic promoters, such as phosphotungstic acid resulted in better conversions.

Furthermore, the same Au/TiO₂ catalysts was successfully employed in the synthesis of a series of indoles by microwave assisted intramolecular hydroamination (Scheme 4.4).



Scheme 4.4. Au/TiO₂-catalysed indole synthesis through intramolecular hydroamination, redraw from reference 4.

Finally, Zhu *et al.* reported the highly efficient and selective photocatalytic hydroamination of alkynes by titania-supported gold nanoparticles using visible light at ambient temperature.⁴ During the photocatalytic process, both AuNPs and the support contributed to the activation of the reactants. On the basis of experimental results, it was suggested that upon activation by visible light absorption, gold conducting electrons migrate to the conduction band of the support, resulting in the formation of positively charged AuNPs. The nucleophilic aniline could interact with these positively charged centres forming N-centred radical cations, which would lead to the amine activation for an electrophilic attack to the electron rich sites of alkynes.

4.1.3 Aim of the chapter

On the basis of the results obtained with the **Au/SiO₂@Yne** catalyst in the oxidation of alcohols, the potential of this catalytic system was further exploited in the hydroamination of alkynes.

For this purpose, a new series of catalysts based on AuNPs supported on functionalised silica were prepared by further modifying the support surface in order to decrease the presence of acidic sites, which could be detrimental for the catalyst performances in the examined reaction. In particular, two approaches were studied: 1) silanization with ethoxytrimethylsilane (TMS) and 2) treatment with triethylamine (NEt₃). The preparation of **Au/SiO₂@Yne-TMS** and **Au/SiO₂@Yne-NEt₃** was carried out in several steps and both the final products and the intermediates were thoroughly characterised by means of TGA, TEM, AAS and SS NMR.

Finally, the catalytic activity of the new systems was studied in the hydroamination of phenylacetylene with aniline, comparing the observed performances with the results obtained with the **Au/SiO₂@Yne** system.

4.2 Results and discussion

4.2.1 Preparation of Au/SiO₂@Yne-TMS and Au/SiO₂@Yne-NEt₃

As discussed in the previous chapters, the preparation of the **Au/SiO₂@Yne** catalyst is extremely straightforward and reproducible, starting from a commercially available support. Furthermore, this system showed a remarkable catalytic activity in the oxidation of alcohols both in batch and continuous-flow conditions. For these reasons, the work reported in the present chapter focused on the use of **Au/SiO₂@Yne** based catalysts in another important organic transformation, i.e. hydroamination of alkynes.

However, it is well known that silica displays acidic properties and consequently basic moieties, such as amines, can remain stuck on its surface. Indeed, the SS NMR spectrum of a sample prepared by stirring a suspension of silica in a 1 M solution of aniline in toluene, showed the presence of the peaks corresponding to aniline at 117.60, 120.34, 129.04 and 165.88 ppm (Figure 4.1).

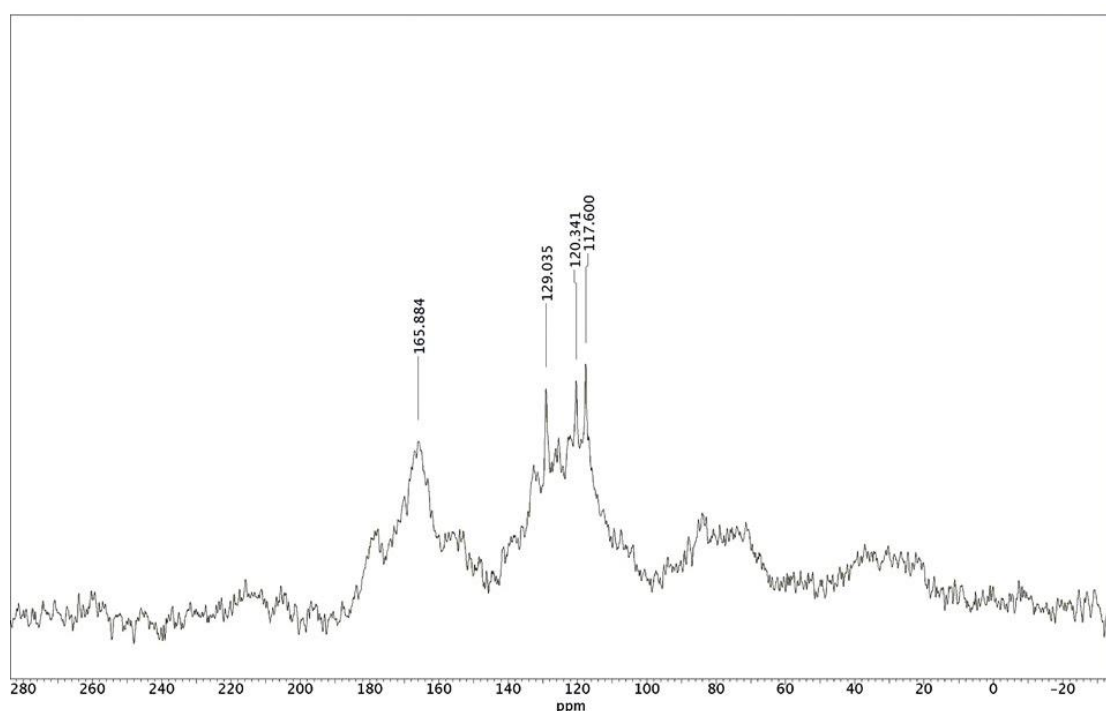


Figure 4.1. ¹³C CP/MAS NMR spectra recorded at 500 MHz of aniline on SiO₂.

In addition, the TGA analysis of the same sample presented a weight loss of 7.9 % between 100 – 200 °C, ascribable to the adsorbed aniline (Figure 4.2).

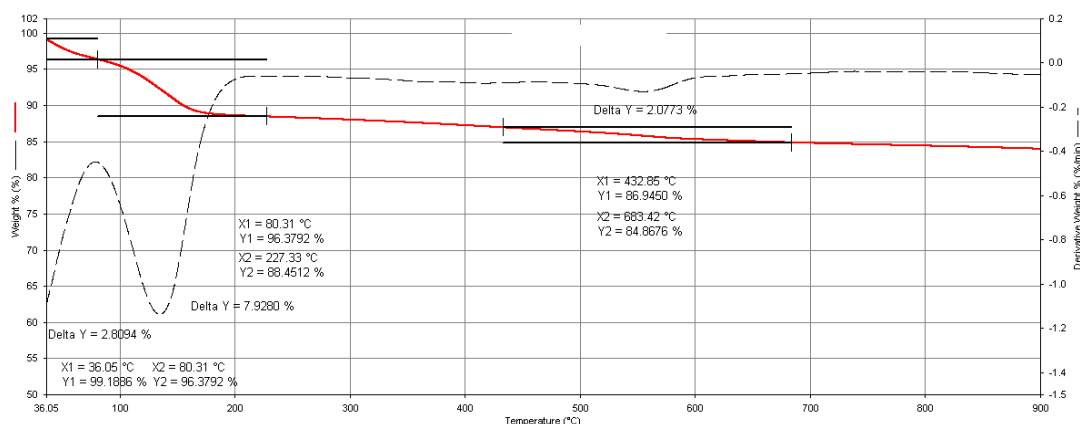
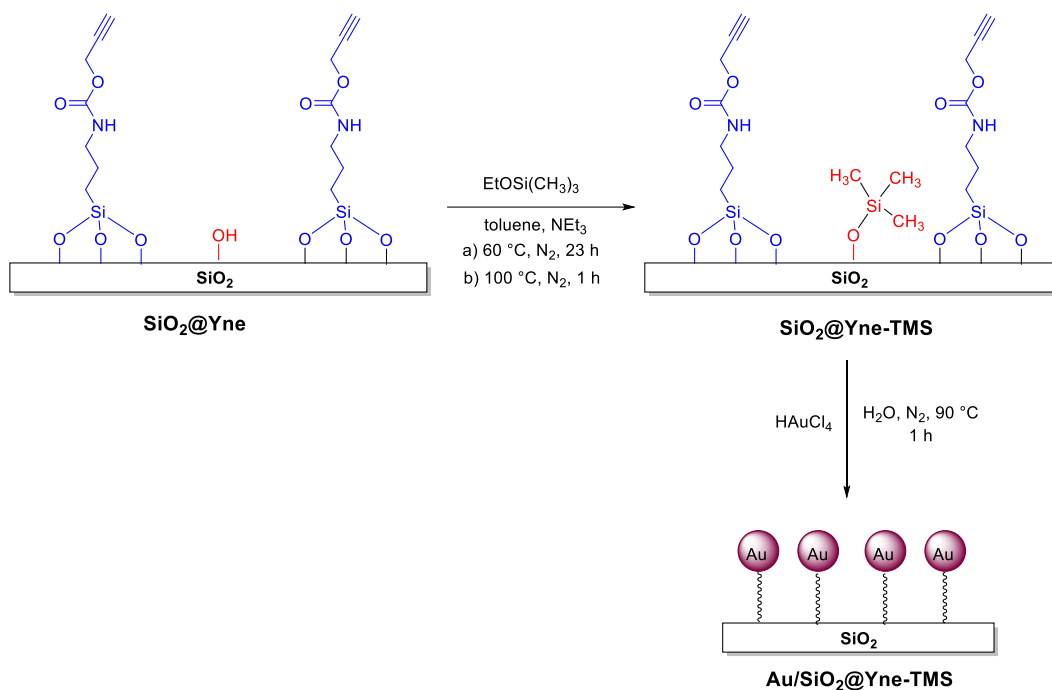


Figure 4.2. TGA of aniline adsorbed on SiO₂.

Since hydroamination reactions consist in the attack of an aminic group to a C-C unsaturated bond, we decided to modify the silica-based catalyst **Au/SiO₂@Yne**, with the aim of reducing the presence of acidic sites, thus decreasing its affinity towards the amine reagent that could result in the poisoning of the catalytic system.

The new **Au/SiO₂@Yne-TMS** catalyst was prepared by further modifying the functionalised silica support, prior to the final gold decoration step. For this purpose, a silanization treatment of **SiO₂@Yne** was carried out employing ethoxytrimethylsilane (TMS). Indeed, the condensation between the hydroxyl groups on the silica surface and the ethoxyl groups of TMS resulted in the capping of free -OH groups.

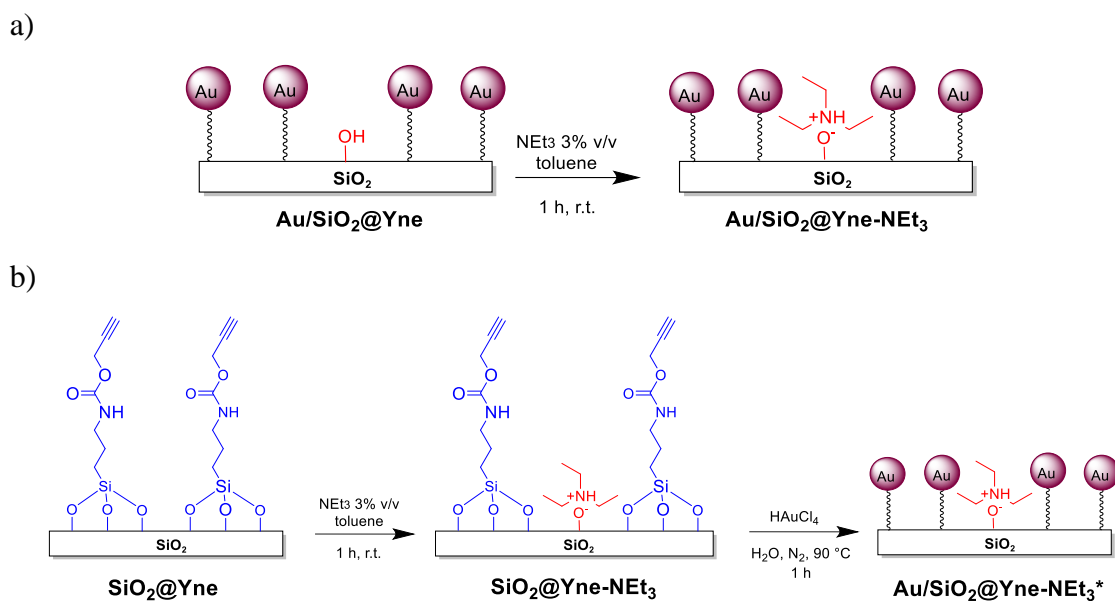
Thereafter, the formation of AuNPs was obtained by addition of a 1 mM solution of HAuCl₄ as previously described in Chapter 2 (Scheme 4.5).



Scheme 4.5. Preparation of **Au/SiO₂@Yne-TMS**.

On the contrary, the synthesis of the catalyst modified with triethylamine was carried out following two slightly different approaches.²⁷

In the first strategy, **Au/SiO₂@Yne** was treated with a 3% v/v solution of **NEt₃** in toluene (**Au/SiO₂@Yne-NEt₃**, Scheme 4.6a), whereas in the second the impregnation of **SiO₂@Yne** with **NEt₃** was conducted *before* the addition of gold to the system (**Au/SiO₂@Yne-NEt₃***, Scheme 4.6b). Since the subsequent decoration of the support with AuNPs was carried out at 90°C, which corresponds to the boiling point of **NEt₃**, during the characterisation particular attention was given to the detection of triethylamine in the material prepared following the second method.



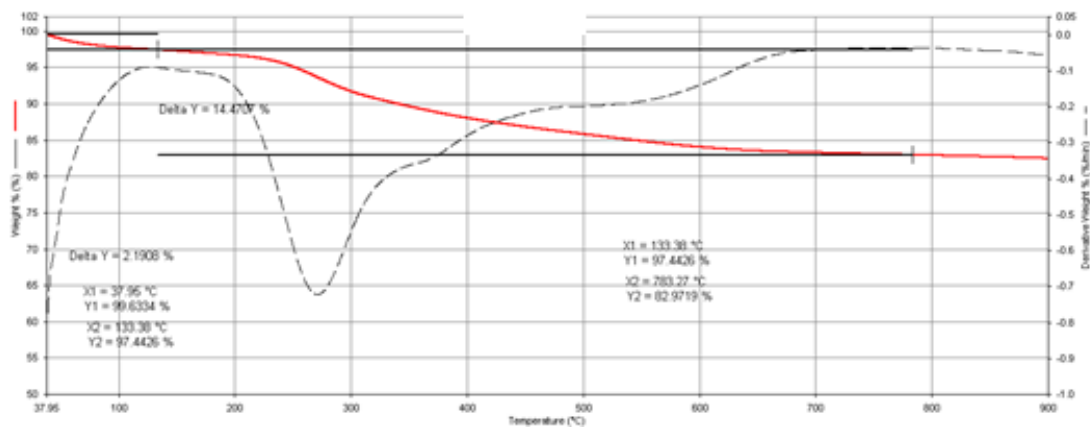
Scheme 4.6. Preparation of a) $\text{Au/SiO}_2\text{@Yne-NEt}_3$ and b) $\text{Au/SiO}_2\text{@Yne-NEt}_3^*$.

4.2.2 Characterisation of $\text{Au/SiO}_2\text{@Yne-TMS}$ and $\text{Au/SiO}_2\text{@Yne-NEt}_3$

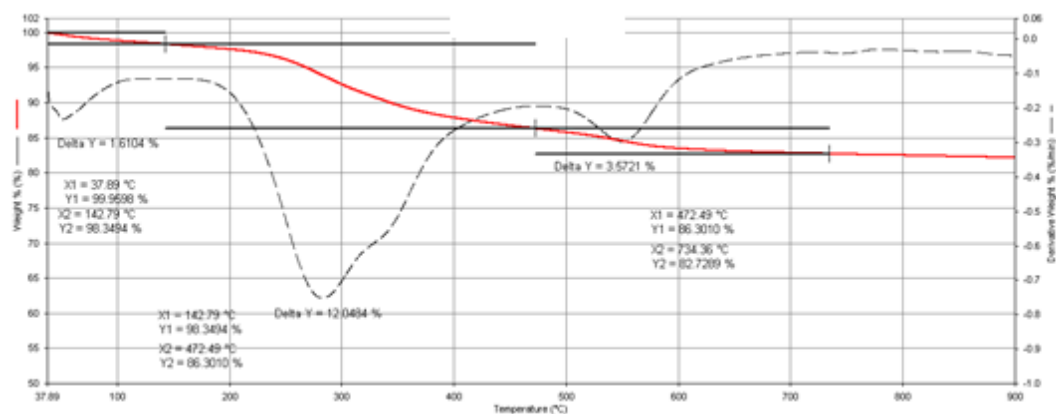
Both $\text{Au/SiO}_2\text{@Yne-TMS}$ and $\text{Au/SiO}_2\text{@Yne-NEt}_3$ were characterised, analysing also the intermediate products obtained during the preparation of the final materials, and results were compared with those previously reported for $\text{Au/SiO}_2\text{@Yne}$.

In the first place, $\text{SiO}_2\text{@Yne}$, $\text{SiO}_2\text{@Yne-TMS}$ and $\text{Au/SiO}_2\text{@Yne-TMS}$ were analysed by thermogravimetric analysis, as reported in Figure 4.3.

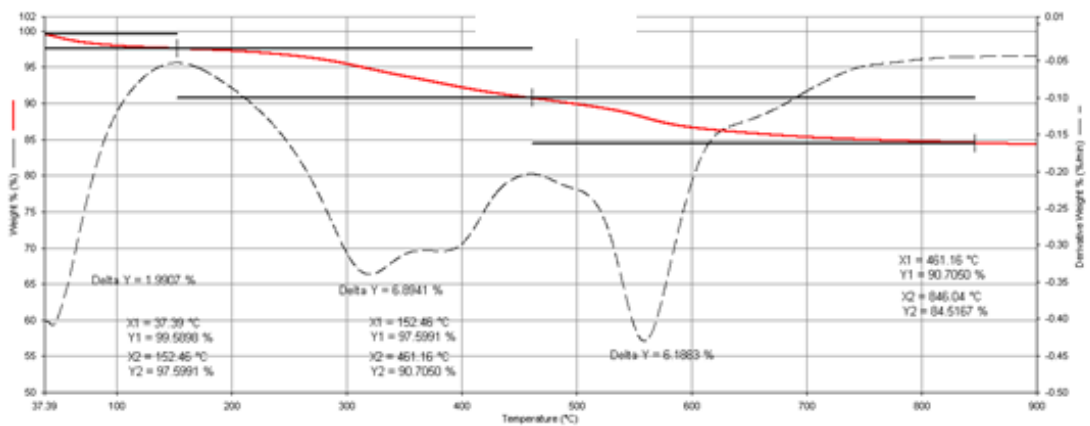
The decomposition of the organic material grafted on the silica surface in $\text{SiO}_2\text{@Yne}$ resulted in a total weight loss of 14 wt % (200 – 750 °C) (Figure 4.3a). The weight loss observed in the same region for $\text{SiO}_2\text{@Yne-TMS}$ was found to be higher (16 wt %), as expected following the introduction of a further functionalisation (Figure 4.3b), while in the case of $\text{Au/SiO}_2\text{@Yne-TMS}$ the organic degradation led to a slightly lower weight loss (13 wt %), possibly due to the fact that part of the carbamic moieties undergo a significant transformation during the reduction of Au(III) to Au(0) (Figure 4.3c).



(a)



(b)



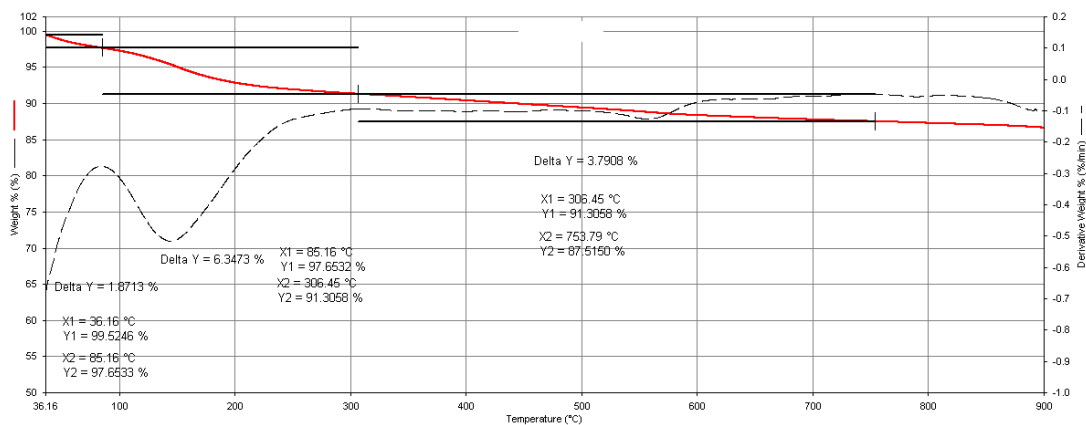
(c)

Figure 4.3. TGA analysis of a) $\text{SiO}_2@\text{Yne}$, b) $\text{SiO}_2@\text{Yne-TMS}$, c) $\text{Au/SiO}_2@\text{Yne-TMS}$.

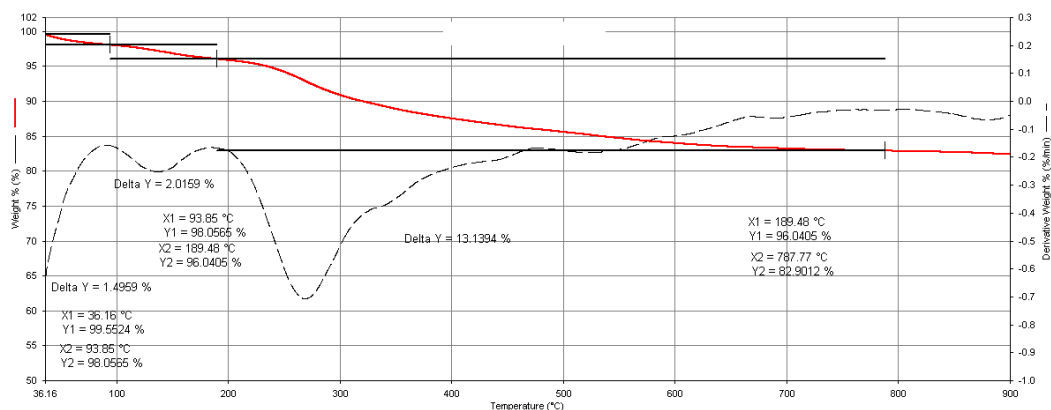
In the case of the triethylamine functionalisation, the thermogram of a sample prepared by impregnation of bare silica with NEt_3 ($\text{SiO}_2\text{-NEt}_3$) showed a weight loss of 6.3 % around 150 °C (Figure 4.4a). In the same region, a 2.0 % weight loss was observed for the $\text{SiO}_2@\text{Yne-NEt}_3$ sample, confirming the successful introduction of triethylamine on the already functionalised silica support (Figure 4.4b). However, after the gold

decoration step ($\text{Au/SiO}_2\text{@Yne-NEt}_3^*$) no decomposition was observed at 150 °C, suggesting that during the treatment with chloroauric acid the loss of NEt_3 from the support occurred, possibly due to the working temperature and the acidity of the reaction mixture arising from the presence of HAuCl_4 (Figure 4.4c).

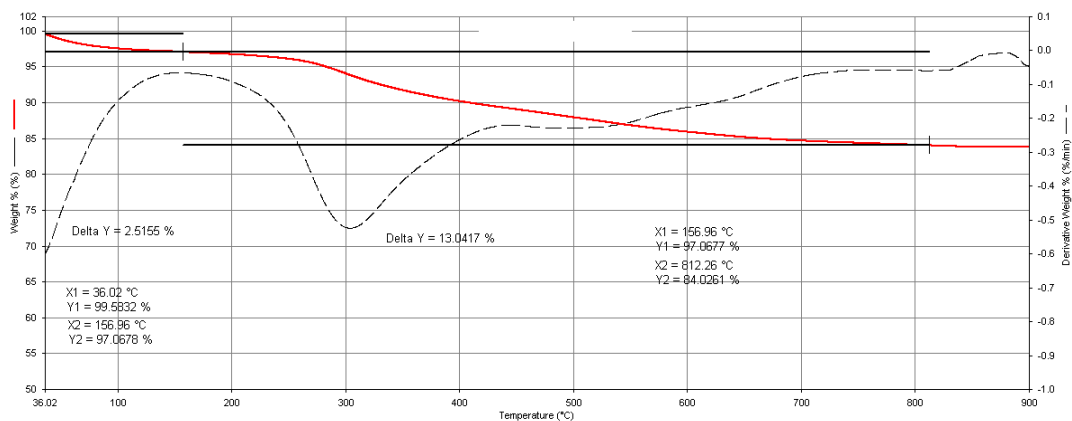
On the contrary, in the thermogram of $\text{Au/SiO}_2\text{@Yne-NEt}_3$ the presence of triethylamine adsorbed on the silica surface was confirmed by a 1.6 % weight loss (Figure 4.4d). These results indicated that the preparation of AuNPs supported on silica functionalised with both PPTEOS and NEt_3 must be carried out by *first* immobilising AuNPs on the $\text{SiO}_2\text{@Yne}$ support and *then* treating the obtained product with triethylamine.



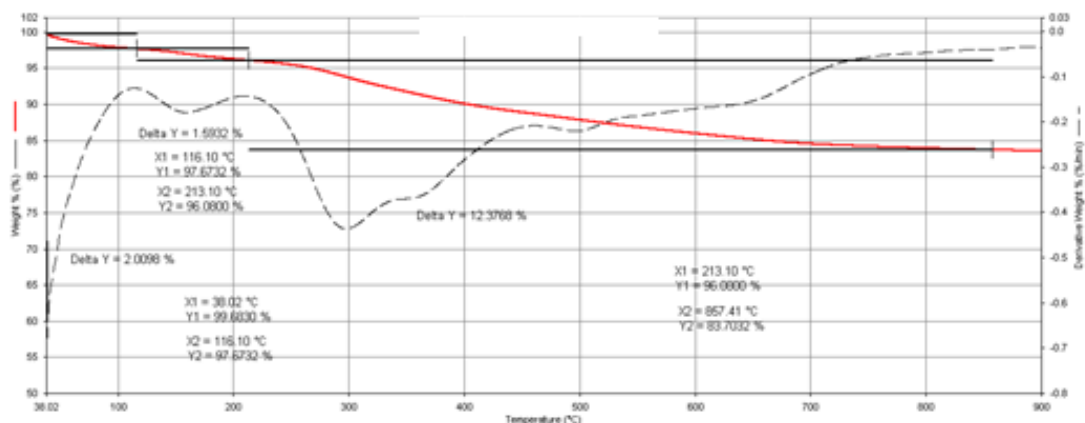
(a)



(b)



(c)



(d)

Figure 4.4. TGA analysis of a) $\text{SiO}_2\text{-NEt}_3$, b) $\text{SiO}_2\text{@Yne-NEt}_3$, c) $\text{Au/SiO}_2\text{@Yne-NEt}_3^*$ and d) $\text{Au/SiO}_2\text{@Yne-NEt}_3$.

The determination of the gold content in $\text{Au/SiO}_2\text{@Yne-TMS}$ and $\text{Au/SiO}_2\text{@Yne-NEt}_3$ by AAS analysis indicated that the weight percentage of gold anchored on the support in the new catalysts is 4.4 ± 0.1 wt %, completely comparable to the one previously found for $\text{Au/SiO}_2\text{@Yne}$. These results suggested that further modifications of the silica surface do not influence the amount of gold that can be immobilised by means of the alkynyl-carbamate functionalities of PPTEOS.

Furthermore, the morphology and size of the gold nanoparticles anchored on the new supports were investigated by TEM. The analysis of the $\text{Au/SiO}_2\text{@Yne-TMS}$ sample indicated the presence of spherically shaped AuNPs with an average size of 33 ± 10 nm (Figure 4.5a), significantly bigger than the ones present in the $\text{Au/SiO}_2\text{@Yne}$ catalyst (15 ± 4 nm).

On the contrary, the analysis of the TEM images of **Au/SiO₂@Yne-NEt₃** resulted in the finding that smaller particles were formed on this support (14 ± 5 nm), suggesting that the treatment with triethylamine did not affect the dimension of the already immobilised AuNPs (Figure 4.5b).

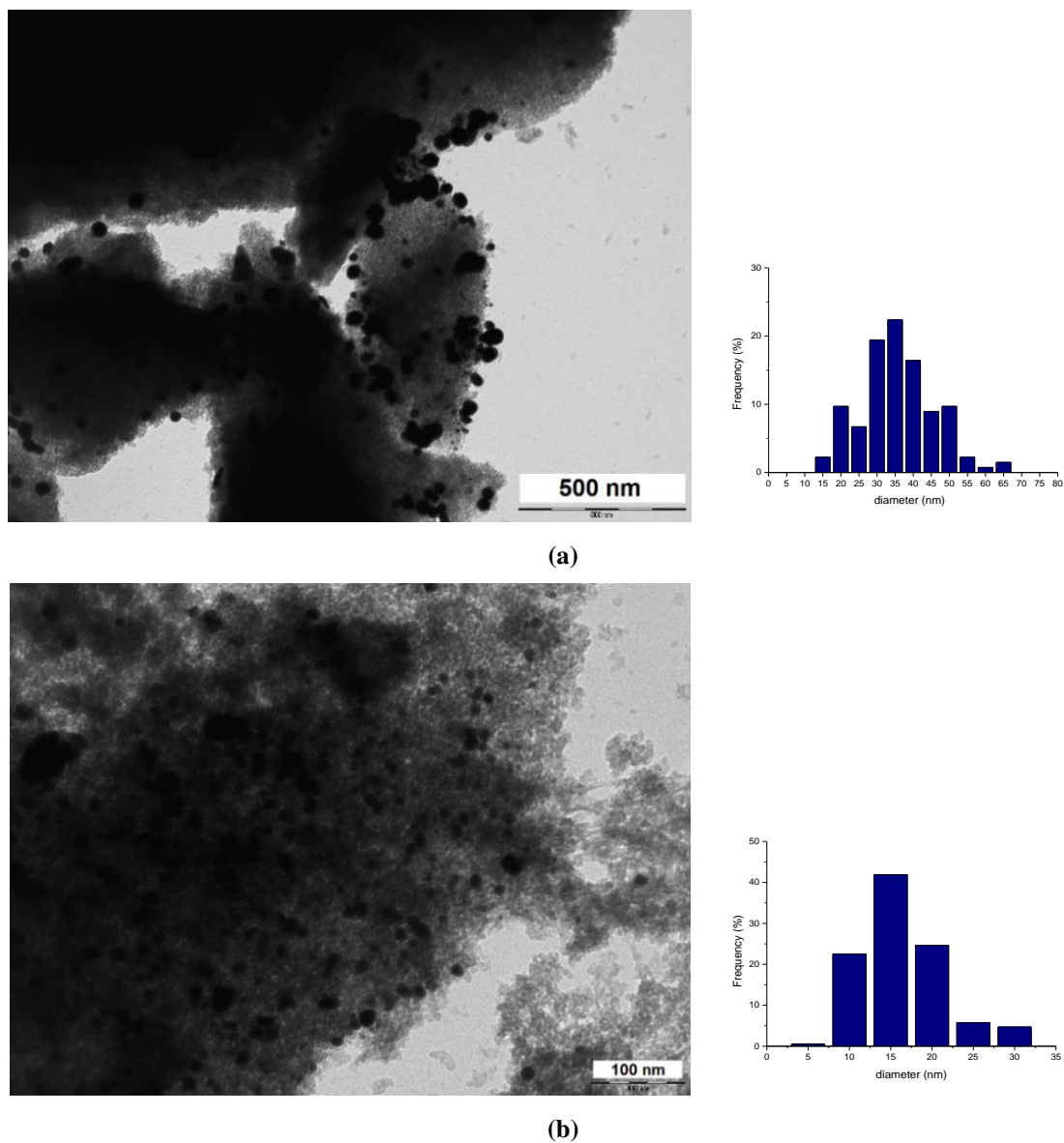


Figure 4.5. TEM images and particle size distribution of a) **Au/SiO₂@Yne-TMS** (33 ± 10 nm) and b) **Au/SiO₂@Yne-NEt₃** (14 ± 5 nm).

4.2.3 Solid State NMR characterisation

In addition, the functionalisation of the silica support was monitored by SS NMR spectroscopy, in each step of the preparation of the new catalysts.

In Figure 4.6 are reported the ^{13}C CP/MAS NMR spectra of bare silica, **SiO₂@Yne**, **SiO₂@Yne-TMS**, **Au/SiO₂@Yne-TMS** (with a gold content of 4.4 wt %) and **Au-₁₃/SiO₂@Yne-TMS** (with a gold content of 13 wt %).

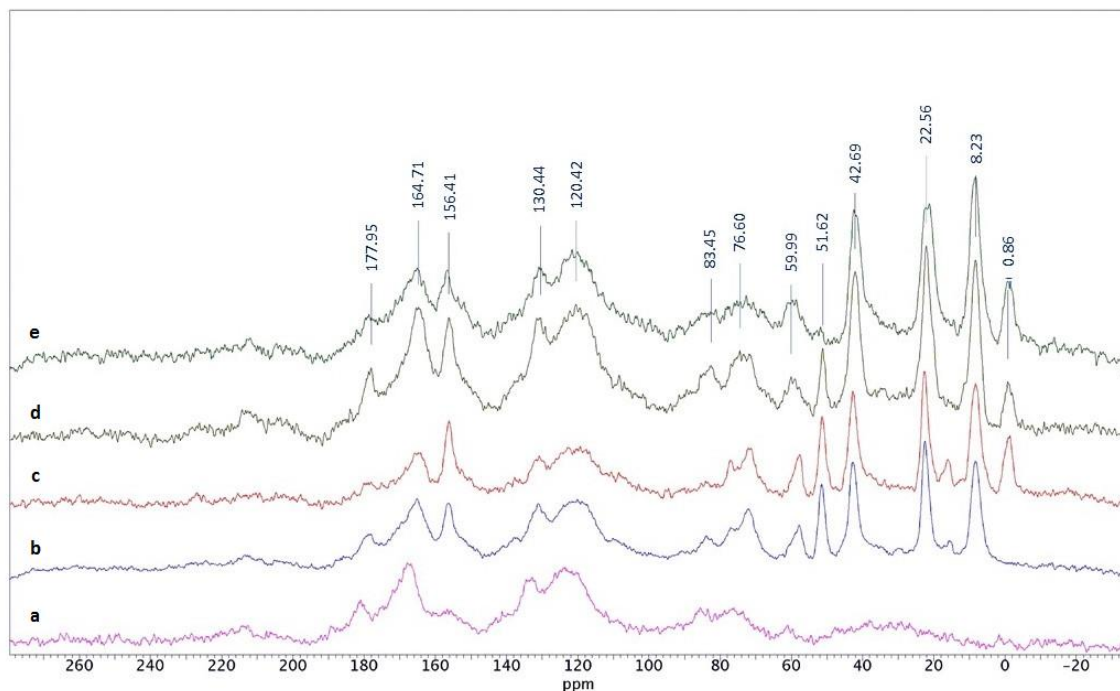


Figure 4.6. ^{13}C CP/MAS NMR spectra recorded at 500 MHz of a) bare silica, b) **SiO₂@Yne**, c) **SiO₂@Yne-TMS**, d) **Au/SiO₂@Yne-TMS** (with a gold content of 4.4 wt %) and e) **Au-₁₃/SiO₂@Yne-TMS** (with a gold content of 13 wt %).

As previously reported in Chapter 2, the large signals in the regions 70 – 90 ppm, 110 -140 ppm and 160 – 180 ppm belonged to impurities contained in the commercial silica substrate (Figure 4.6a), while the successful functionalisation with PPTEOS was confirmed by the presence of the following characteristic signals (Figure 4.6b): 8.23, 22.56 and 42.69 ppm (propylic chain), 51.62 ppm (propargyl methylene), 76.60 and 83.45 ppm (alkyne carbons) and 156.41 ppm (carbamic carbonyl).

The spectrum of **SiO₂@Yne-TMS** presented an additional peak at 0.86 ppm, ascribable to the $-\text{Si}(\text{CH}_3)_3$ groups introduced in the further functionalisation step (Figure 4.6c).²⁸ The presence of the 4.4 wt % of gold anchored on the support only resulted in a slight decrease in the intensity of the peaks associated to the alkynyl-carbamate moieties

(Figure 4.6d), that almost completely disappeared in the spectrum of **Au-13/SiO₂@Yne-TMS** due to the complete transformation of the 3-(2-propynylcarbamate)silane to an aminopropylsilane (Figure 4.6e).

Before analysing the samples bearing the additional triethylamine modification, the SS NMR spectrum of NEt₃ immobilised on bare silica was recorded (Figure 4.7a). The comparison of the chemical shifts of the supported NEt₃ signals [6.82 ppm (-CH₃), 44.41 ppm (-CH₂)] with the ones reported for NEt₃ in solution [¹H-NMR in CDCl₃: 11.78 ppm (-CH₃), 46.46 ppm (-CH₂)] evidenced the effect of the interaction between the silica surface and the amine, which was found to be more pronounced on the first signal.

The spectrum of **SiO₂-NEt₃** was then compared to the one recorded for **SiO₂@Yne-NEt₃**. As shown in Figure 4.7b, the presence of triethylamine in this sample is clearly confirmed by the presence of the two characteristic peaks, partially overlapped with the signals of the alkynyl-carbamate functionalisation.

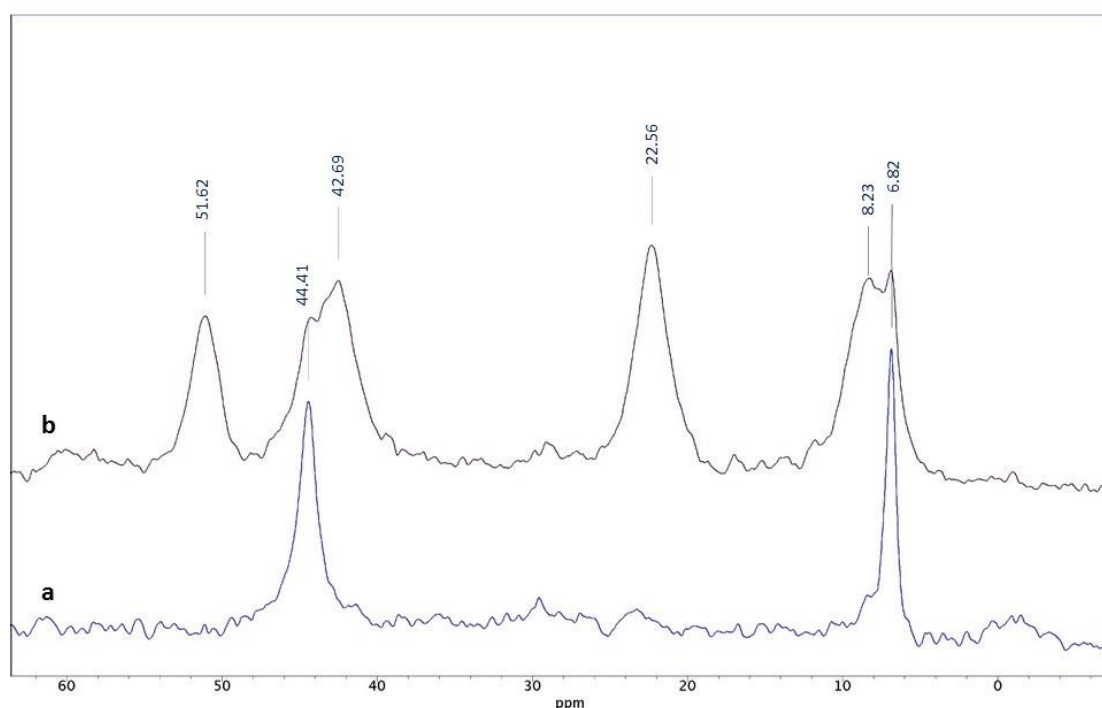


Figure 4.7. Magnification of the ¹³C CP/MAS NMR spectra recorded at 500 MHz of a) **SiO₂-NEt₃** and b) **SiO₂@Yne-NEt₃**.

On the contrary, the SS NMR analysis of **Au/SiO₂@Yne-NEt₃** and **Au/SiO₂@Yne-NEt₃*** could not give significant and definitive information regarding the presence of triethylamine (Figure 4.8).

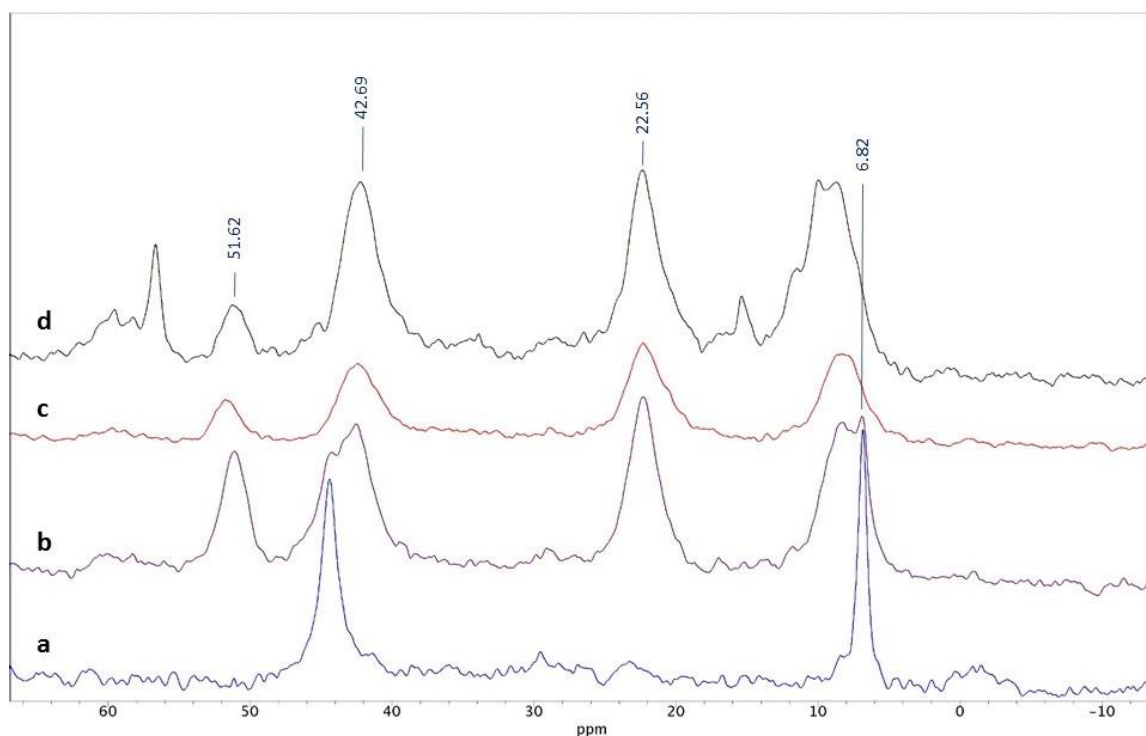
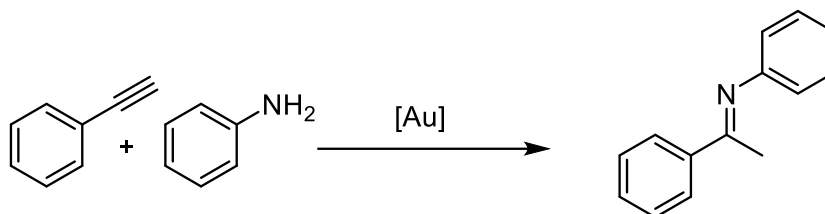


Figure 4.8. Magnification of the ¹³C CP/MAS NMR spectra recorded at 500 MHz of a) **SiO₂-NEt₃** b) **SiO₂@Yne-NEt₃**, c) **Au/SiO₂@Yne-NEt₃** and d) **Au/SiO₂@Yne-NEt₃***.

While in the case of **Au/SiO₂@Yne-NEt₃** (Figure 4.8c) this could be simply due to the overlap of the NEt₃ signals with the ones of the organic functionalisation, in the case of the sample prepared by impregnation of silica with NEt₃ prior to gold decoration (**Au/SiO₂@Yne-NEt₃***, Figure 4.8d), the absence of triethylamine was already suggested by the TGA investigation. As previously discussed, this could be related to the poor stability of the immobilised NEt₃ in the strong acid environment generated by HAuCl₄ in the reaction mixture, during the AuNPs formation.

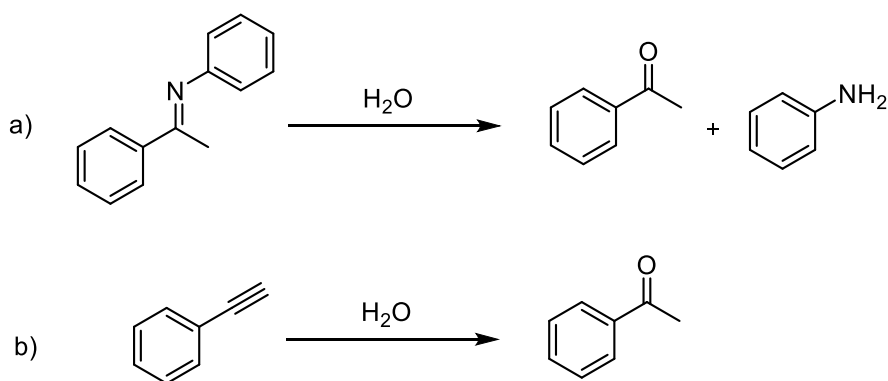
4.2.4 Hydroamination of alkynes

The catalytic activity of **Au/SiO₂@Yne**, **Au/SiO₂@Yne-TMS** and **Au/SiO₂@Yne-NEt₃** in the hydroamination of alkynes was investigated and compared. The model reaction chosen for this study was the hydroamination of phenylacetylene with aniline, which in all the below reported experiments led to the regio-selective formation of the Markovnikov product phenyl-(1-phenylethylidene)amine (Scheme 4.7).



Scheme 4.7. Hydroamination of phenylacetylene with aniline.

Nevertheless, the formation of acetophenone as a by-product was observed in some cases, due to a secondary reaction involving the hydrolysis of the obtained imine to the corresponding ketone and amine, which can occur in the presence of traces of water (Scheme 4.8a).^{6,25,29} Furthermore, the detection of the ketone in the reaction mixture could also be ascribable to the hydration of the alkyne, which is another reaction known to be catalysed by gold nanoparticles (Scheme 4.8b).³⁰ However, when the reaction was carried out in the absence of aniline, only a negligible amount of ketone was observed, suggesting that in the chosen experimental conditions the hydration of phenylacetylene is not the main source of formation of the secondary product.



Scheme 4.8. Side reactions of a) hydrolysis of phenyl-(1-phenylethylidene)amine and b) hydration of phenylacetylene.

The conversion and selectivity results reported below were obtained from GC-MS analysis of an aliquote of the reaction mixture diluted in chloroform (CHCl₃). Notably, in some cases a low reproducibility of the experimental data obtained by repeating the same analysis several times was observed, possibly due to the poor stability of the imine product. Indeed, these anomalous results were accompanied by a drastic increase in the amount of detected acetophenone, suggesting the occurrence of the imine hydrolysis which could be promoted by the intrinsic acidity of chloroform. Hence, the problem was solved by preparing the GC-MS samples in CHCl₃ stored on basic alumina and under nitrogen.

At first, some preliminary tests for the evaluation of the catalytic activity of **Au/SiO₂@Yne** were conducted in solvent free-conditions, varying some of the experimental parameters such as reaction temperature, reagents ratio and catalyst loading (Table 4.1). Furthermore, these experiments were carried out in the presence of an acid additive, i.e. phosphotungstic acid (H₃PO₄·12WO₃). Indeed, several works in the literature reported that gold based catalysts for the hydroamination of alkynes can be activated by the presence of acid promoters through the *in situ* formation of cationic Au(I) species.^{4,31,32,33,34}

Table 4.1. Hydroamination of phenylacetylene with aniline catalysed by **Au/SiO₂@Yne** in solvent-free conditions.^a

Entry	Alkyne/amine ^b	T (°C)	t (h)	Conv (%) ^c	Φ _{imm} (%) ^c	Φ _{ket} (%) ^c
1	1/1.2	80	24	71	82	18
2 ^d	1/1.2	80	24	42	73	27
3	1/1.2	110	24	91	88	12
4	1/1	110	24	91	90	10

a) Reaction conditions: N₂ atm, 0.4 % molar equivalents of Au catalyst, 0.2 % molar equivalents of H₃PO₄·12WO₃; b) phenylacetylene/aniline molar ratio; c) conversion and selectivity determined by GC-MS (absolute error: ± 5%); d) 0.2 % molar equivalents of Au catalyst, 0.1 % molar equivalents of H₃PO₄·12WO₃.

When the reaction was carried out at 80 °C, with 0.4 % molar equivalents of Au and with an excess of aniline, a 71 % conversion was observed after 24 h (Table 4.1, entry

1). On the other hand, a significantly lower value was found by decreasing the catalyst loading by half (Table 4.1, entry 2), whereas the increase in the reaction temperature to 110 °C resulted in the achievement of a 91 % conversion (Table 4.1 entry 3). Finally, the use of an excess of amine was found to be unnecessary since the same conversion could be obtained when working with an equimolar amount of the two reagents (Table 4.1, entry 4).

On the basis of these preliminary results, the further optimisation of the reaction conditions was studied by conducting the experiments summarised in Table 4.2.

Table 4.2. Optimisation of the hydroamination of phenylacetylene with aniline catalysed by **Au/SiO₂@Yne**.^a

Entry	Solvent	T (°C)	t (h)	Additive ^b	Conv (%) ^c	Φ_{imm} (%) ^c	Φ_{ket} (%) ^c
1	Toluene	110	5	H ₃ PO ₄ ·12WO ₃	70	86	14
2	Toluene	110	5	SiO ₂ -SO ₃ H	70	68	32
3	Toluene	110	5	-	50	93	7
4	Toluene	110	24	-	78	82	18
5	CH ₃ CN	80	5	-	42	74	26
6	1,2-dimethoxyethane	85	5	-	7	-	>99
7	THF	66	5	-	27	27	73
8	2-methoxyethanol	124	5	-	>99	17	83

a) Reaction conditions: N₂ atm, 1 % molar equivalents of Au catalyst, phenylacetylene/aniline 1:1, initial reagents concentration 1 M; b) 0.5 % molar equivalents of acid additive; c) conversion and selectivity determined by GC-MS (absolute error: ± 5%).

When the hydroamination of phenylacetylene with aniline catalysed by **Au/SiO₂@Yne** was carried out in toluene at 110 °C, the conversion obtained after 5 h in the presence of the H₃PO₄·12WO₃ acid promoter was found to be 70 % (Table 4.2, entry 1). The same result was observed when using H₂SO₄ immobilised on commercial silica (SiO₂-SO₃H) as acid additive (Table 4.2, entry 2). However, the presence of acid species in the reaction environment resulted in a general decrease of the selectivity in imine, due to the occurrence of the hydrolysis reaction, while a 93 % selectivity could be obtained when no additives were employed (Table 4.2, entry 3). Furthermore, in the absence of additives, the conversion achieved after 24 h was found to be around 80 % (Table 4.2, entry 4).

Finally, the possibility to perform the reaction in different solvent media was investigated. In particular, all of the experiments were conducted under reflux conditions, so the reaction temperature was determined by the solvent boiling point. The use of CH₃CN as solvent resulted in a lower conversion, possibly due to the lower working temperature (Table 4.2, entry 5), whereas the selectivity of the reactions carried out in 1,2-dimethoxyethane, THF and 2-methoxyethanol was found to be completely shifted towards the formation of the ketone (Table 4.2, entries 6-8).

After having identified the optimal reaction conditions (toluene, 110°C, 1 % molar equivalents of Au, 1:1 stoichiometric ratio of phenylacetylene/aniline and 1 M reagent concentration), the catalytic activity of **Au/SiO₂@Yne-TMS** and **Au/SiO₂@Yne-NEt₃** was also evaluated (Table 4.3).

Table 4.3. Hydroamination of phenylacetylene with aniline catalysed by **Au/SiO₂@Yne**, **Au/SiO₂@Yne-TMS** and **Au/SiO₂@Yne-NEt₃**.^a

Entry	Catalyst	t (h)	Conv (%) ^b	Φ_{imm} (%) ^b	Φ_{ket} (%) ^b
1	Au/SiO₂@Yne	5	50	93	7
2	Au/SiO₂@Yne-TMS	5	51	95	5
3	Au/SiO₂@Yne-NEt₃	5	43	>99	-
4	Au/SiO₂@Yne	24	78	82	18
5	Au/SiO₂@Yne-TMS	24	83	86	14
6	Au/SiO₂@Yne-NEt₃	24	98	96	4
7 ^c	Au/SiO₂@Yne	24	65	85	15
8 ^c	Au/SiO₂@Yne-NEt₃	24	85	92	8
9 ^c	Au/SiO₂@Yne + NEt₃ in situ^d	24	52	81	19
10 ^c	Au/SiO₂@Yne + NEt₃ in situ^e	24	65	88	12

a) Reaction conditions: initial concentration of phenylacetylene and aniline 1 M in toluene, T = 110 °C, N₂ atm, 1 % molar equivalents of Au catalyst; b) conversion and selectivity determined by GC-MS (absolute error: ± 5%); c) reaction performed on a larger scale (10x, 300 mg of catalyst); d) 1 % v/v NEt₃; e) 3 % v/v NEt₃.

After 5 h of reaction, the results obtained with the different catalysts were found to be comparable, in terms of both conversion and selectivity (Table 4.3, entries 1-3). In particular, while the conversion achieved was c.a. 50 %, the occurrence of the side reactions that leads to the formation of acetophenone was found to be negligible, resulting in a very high selectivity in the desired imine product.

Moreover, after 24 h a general increase in conversion was observed (Table 4.3, entries 4-6), but in this case the **Au/SiO₂@Yne-NEt₃** catalyst remarkably differed from the other two and exhibited the best performance with a 98 % conversion and 96 % selectivity in imine.

Interestingly, when the reaction was carried out on scale ten times larger, i.e. working with 300 mg of catalyst instead of 30 mg, a slight decrease in the conversion values for **Au/SiO₂@Yne** and **Au/SiO₂@Yne-NEt₃** was observed, though the triethylamine modified catalyst still displayed a higher activity (Table 4.3, entries 7-8). For this reason, two additional tests were performed with the **Au/SiO₂@Yne** catalyst by adding NEt₃ directly in the reaction mixture. Unfortunately, no significant enhancements were observed with the *in situ* addition of triethylamine (Table 4.3, entries 9-10).

Among the three prepared systems, **Au/SiO₂@Yne-NEt₃** was found to be the most active in the studied reaction, so recycling tests were initially conducted with this catalyst. After the first cycle of reaction, the catalyst was recovered by centrifugation, washed with toluene and dried before being reused. Following this procedure, a sharp decrease in conversion (~ 40-50 %) was observed already after the second cycle. In order to investigate the causes of this finding, a thermogravimetric analysis of the reused catalyst was carried out, which suggested the loss of NEt₃ from the silica surface, possibly due to the high temperature in the reaction environment (Figure 4.9).

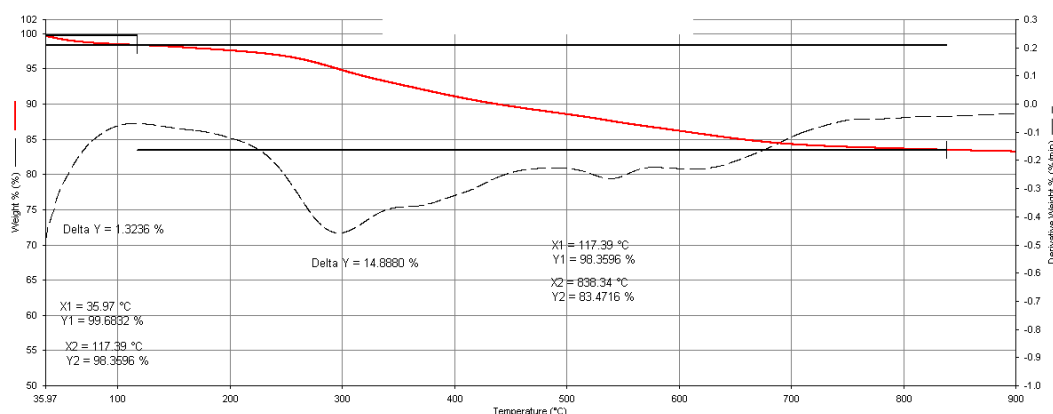


Figure 4.9. TGA analysis of **Au/SiO₂@Yne-NEt₃** post-catalysis.

For this reason, the exhausted catalyst was treated again with NEt₃ before being reused, but even in this case no recovery of the initial activity was obtained.

On the contrary, when the catalyst was washed with acetone by ultrasonic cleaning, no significant drop of conversion occurred in the second cycle. Furthermore, the same results were observed when using the **Au/SiO₂@Yne** catalyst and even in this case acetone and ultrasound washings were required in order to restore the initial catalytic activity.

In particular, the ¹H-NMR analysis of the acetone washings suggested the presence of polyphenylacetylene oligomers (PPA), as revealed by the characteristic peak at 6.09 ppm associated to the vinyl proton of the PPA chain, alongside the multiplets at 6.60 ppm and 7.05 ppm corresponding to the aromatic protons (Figure 4.10).^{35,36,37}

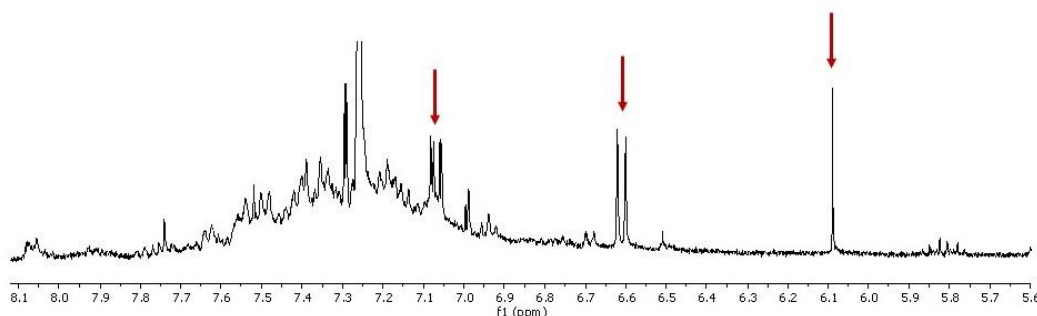


Figure 4.10. Magnification of the ¹H-NMR spectrum of the acetone washings.

Furthermore, the IR spectra of the washings presented peaks at 696 cm⁻¹, 754 cm⁻¹, 849, cm⁻¹ and 1443 cm⁻¹, which can be associated to PPA.³⁸

The formation of PPA oligomers in the reaction environment and their consequent adsorption on the catalyst surface could result in the poisoning of the active sites and the drastic reduction of the catalytic performances after the first cycle of reaction. On the contrary, no signals related to polyphenylacetylene could be identified in the toluene washings, which indicates that this treatment was not efficient in removing the adsorbed PPA.

4.3 Conclusions

The preparation of two novel catalytic systems was carried out by 1) immobilisation of AuNPs on a silica support functionalised with PPTEOS and TMS (**Au/SiO₂@Yne-TMS**) and 2) impregnation of **Au/SiO₂@Yne** with triethylamine to obtain **Au/SiO₂@Yne-NEt₃**. In particular, the study of the synthetic procedure for **Au/SiO₂@Yne-NEt₃** by TGA and SS NMR analysis indicated that, in order to successfully immobilise both triethylamine and AuNPs, it is necessary to carry out the treatment with NEt₃ *after* the gold decoration step.

The TEM characterisation of **Au/SiO₂@Yne-TMS** revealed the presence of AuNPs with an average size of 33 ± 10 nm, significantly bigger than the ones present in the **Au/SiO₂@Yne** catalyst (15 ± 4 nm). On the other hand, completely comparable dimensions were found in the case of **Au/SiO₂@Yne-NEt₃** (14 ± 5 nm), suggesting that the treatment with triethylamine did not affect the AuNPs size.

Finally the catalytic activity of **Au/SiO₂@Yne**, **Au/SiO₂@Yne-TMS** and **Au/SiO₂@Yne-NEt₃** in the hydroamination of phenylacetylene with aniline was evaluated. At first, preliminary tests conducted with the **Au/SiO₂@Yne** catalyst allowed to identify the optimal reaction conditions: toluene, 110°C, 1 % molar equivalents of Au, 1:1 stoichiometric ratio of phenylacetylene/aniline and 1 M reagent concentration. Then, the comparison of the catalytic efficiency of the three systems highlighted that the best results were obtained with the **Au/SiO₂@Yne-NEt₃** catalyst, achieving a 98 % conversion after 24 h. At last, the recyclability of both the **Au/SiO₂@Yne** and **Au/SiO₂@Yne-NEt₃** systems was evaluated, resulting in the finding that a thorough washing procedure is necessary in order to remove oligomeric species from the catalyst surface thus restoring the initial activity.

4.4 Experimental section

4.4.1 Materials

Triethylamine (NEt₃, 99%), ethoxytrimethylsilane (TMS, 98%), phenylacetylene, aniline, 1,3,5-trimethoxybenzene (1,3,5-TMB, 99 %), phosphotungstic acid (H₃PO₄·12WO₃, 99 %), acetophenone, phenyl-(1-phenylethylidene)amine, ethanol (EtOH), chloroform (CHCl₃, stored under nitrogen and on basic alumina), hydrochloric acid (HCl, 37%), nitric acid (HNO₃, 65%), sodium hydroxide (NaOH, 50% wt. in H₂O), sulfuric acid (H₂SO₄, 99 %), toluene, acetonitrile (CH₃CN), 1,2-dimethoxyethane, THF, 2-methoxyethanol, acetone were of analytical grade and were used as purchased from Sigma-Aldrich. Commercial silica gel for column chromatography (particle size 63 – 210 μm, pore volume ca. 0.8 cm³/g, surface area 550 m²/g, Sigma-Aldrich) was dried prior to use by heating for 6 h at 180 °C in a quartz tube under a slow stream of dry nitrogen and then stored under nitrogen. Toluene was dried over Na/K alloy and distilled under nitrogen on 4 Å molecular sieves. Ultrapure water purified with the Milli-Q plus system (Millipore Co, resistivity over 18 MΩ cm) was used in all cases. HAuCl₄·3H₂O was prepared according to a literature procedure.³⁹ SiO₂-SO₃H (H₂SO₄ 3 wt % supported on silica) was prepared following a slightly modified known procedure:⁴⁰ 87 μL of H₂SO₄ were added to 5.0 g of anhydrous SiO₂ previously suspended in 20 mL of Et₂O. The mixture was stirred at room temperature for 10 minutes, then the solvent was evaporated under vacuum and the obtained solid was dried in oven at 50 °C for 24 h and stored under nitrogen.

The preparation of **SiO₂@Yne** and **Au/SiO₂@Yne** was carried out as previously reported in Chapter 2.

4.4.2 Preparation of Au/SiO₂@Yne-TMS

SiO₂@Yne-TMS. A dry round-bottomed flask kept under nitrogen atmosphere was charged with 3.0 g of **SiO₂@Yne**, 2 mL of TMS (1.28 mmol), 178 μL of NEt₃ (1.28 mmol) and 40 mL of toluene. The mixture was stirred for 23 h at 60 °C, then the heating was raised to 100 °C for 1 h and the nitrogen flow was increased. The obtained **SiO₂@Yne-TMS** was isolated by centrifugation (5600 rpm, 15 min) and re-dispersed in EtOH. The re-dispersion/centrifugation procedure was repeated three times. The product was first

dried in oven at 65 °C for 24 h, then under vacuum for 12 h, yielding a white powder (2.8 g) finally stored under nitrogen atmosphere.

Au/SiO₂@Yne-TMS. In a round-bottomed flask, kept under nitrogen atmosphere, 2.5 g of **SiO₂@Yne-TMS** were suspended in 335 mL of H₂O. The mixture was heated to 90 °C and vigorously stirred until a well dispersed suspension was obtained, then 0.250 g of H₂AuCl₄·3H₂O (0.63 mmol) previously dissolved in 300 mL of H₂O were added in order to have a 1.0 mM final concentration of H₂AuCl₄·3H₂O. The reaction mixture was stirred for 1 h at 90 °C. The obtained solid was recovered by centrifugation (5600 rpm, 15 min), washed twice with H₂O and twice with EtOH, dried first in oven at 65 °C for 24 and then under vacuum for 12 h. The product **Au/SiO₂@Yne-TMS** appeared as a purple powder (2.63 g) and was stored under nitrogen.

Au-13/SiO₂@Yne-TMS. The synthesis was carried out following the same procedure starting from a suspension of 0.36 g of **SiO₂@Yne-TMS** in 100 mL of H₂O and adding 0.097 g of H₂AuCl₄ (0.25 mmol) previously dissolved in 140 mL of H₂O.

4.4.3 Preparation of SiO₂-NEt₃

A dry round-bottomed flask was charged with 0.30 g of anhydrous SiO₂ and 10 mL of a 3 % v/v solution of NEt₃ in toluene. The reaction mixture was stirred for 1 h at room temperature, then the suspension was dried in a rotary evaporator at 70 °C for 1h and the solid was dried in oven at 65 °C for 24 h.

4.4.4 Preparation of Au/SiO₂@Yne-NEt₃ and Au/SiO₂@Yne-NEt₃*

Au/SiO₂@Yne-NEt₃. A dry round-bottomed flask was charged with 2.00 g of **Au/SiO₂@Yne** and 67 mL of a 3 % v/v solution of NEt₃ in toluene. The reaction mixture was stirred for 1 h at room temperature, then the solid was separated from the supernatant by decantation and washed three times with toluene. The product was first dried in a rotary evaporator at 70 °C, then in oven at 65 °C for 24 h and finally stored under nitrogen.

SiO₂@Yne-NEt₃. A dry round-bottomed flask was charged with 2.12 g of **SiO₂@Yne** and 100 mL of a 3 % v/v solution of NEt₃ in toluene. The reaction mixture was stirred for 1 h at room temperature, then the solvent was evaporated at the rotary evaporator at 70 °C for 1 h. The obtained solid was dried in oven at 65 °C for 24 h.

Au/SiO₂@Yne-NEt₃*. A dry round-bottomed flask under nitrogen atmosphere was charged with 1.79 g of **SiO₂@Yne-NEt₃** and 300 mL of H₂O. The suspension was heated to 90 °C and stirred until the solid was well dispersed, then an aqueous solution of 0.184 g of HAuCl₄·3H₂O (0.467 mmol) dissolved in 150 mL of H₂O was added. The reaction mixture was stirred for 1 h at 90 °C. The obtained solid was recovered by filtration on a Buchner filter, thoroughly washed twice with H₂O and dried in oven at 65 °C for 48 h.

4.4.6 Catalytic tests

In a typical experiment, a double-neck flask kept under nitrogen atmosphere was charged with the reagent mixture, the eventual acid additive and the Au catalyst. The reaction mixture was stirred under reflux conditions for the set time, then 1,3,5-TMB was added and the catalyst was removed by centrifugation and washed with toluene (3x10 mL). The conversion and selectivity were determined by GC-MS analysis of samples prepared by dilution of the reaction mixture in chloroform (stored on basic alumina under nitrogen atmosphere). In order to obtain reproducible results, the samples should be prepared *immediately* prior to GC-MS analysis.

In the case of the NEt₃ *in situ* addition experiments, the desired amount of triethylamine was added to the solvent and the solution was stirred at room temperature for 20 minutes before adding phenylacetylene and aniline.

For recycling tests, the catalyst was recovered by centrifugation and washed with acetone (3x10 mL) in an ultrasonic bath (30 min) before being dried at 65 °C overnight and reused in the next cycle.

4.4.7 Instruments and methods

Thermogravimetric analyses were carried out using a Perkin Elmer TGA-7. The samples (ca. 10 mg) were heated in a platinum crucible at a rate of 10 °C min⁻¹ from 40 °C to 900 °C.

The amount of gold present on the different samples was determined by flame atomic absorption spectroscopy (AAS, Thermo Scientific) in air-acetylene flame with a wavelength of 242.8 nm and a spectral band-width of 0.5 nm. Calibration lines were obtained from five standard solutions at a known concentration (2, 4, 6, 8 and 10 ppm) prepared by dilution of a 100 ppm HAuCl₄·3H₂O solution in HCl 0.5 M. The samples were

prepared by first treating the solid (ca. 10 mg) with a few drops of NaOH 50 wt % and heating in order to completely dissolve the silica support, then aqua regia was added for the dissolution of AuNPs. Finally, the solution was diluted with HCl 0.5 M to a final volume of 50 mL. The solids used for atomic absorption spectroscopy (AAS) measurements were weighted with a Mettler Toledo AT 21 Comparator balance.

For TEM investigations a Philips CM 100 transmission electron microscope operating at 80 kV was used. To prepare the sample a drop of the suspension was transferred onto holey carbon foils supported on conventional copper micro-grids. The ImageJ[®] picture analyser software⁴¹ was used to estimate the average AuNPs dimensions, averaging the measurements over at least 100 data per sample.

¹H-NMR spectra were recorded in CDCl₃ using a Varian Gemini XL 300 (¹H 300.1 MHz, ¹³C 75.5 MHz) instrument; chemical shifts were referenced internally to the residual solvent peak.

Solid State NMR spectra (SS NMR) were recorded using adamantane as reference on an Agilent NMR system, consisting of a 54 mm bore, 11.7 Tesla Premium Shielded superconducting magnet, a DD2 Performa IV NMR console equipped with 100 W highband and 300 W lowband amplifiers, and a NB Agilent 3.2 mm T3 MAS HXY Solid Probe 500 MHz.

GC-MS analysis were carried out in a Thermo Electron Corporation gas chromatograph equipped with a capillary column SLB[®]-5ms made of fused silica (internal diameter: 0.25 μm) connected to a mass spectrometer detector. Calibration lines for the reagents and the products were obtained after injection of standard solutions at a known concentration (in the range 0.0001-0.0015 M), employing 1,3,5-TMB as internal standard and chloroform as solvent. The temperature of injection port (270 °C), MSD transfer line (270 °C) and MS source (180 °C) was set, and the energy of EI source was 69.9 eV. The samples were introduced into the column in a splitless mode and helium gas was used as a mobile phase at a flow rate of 1.0 mL min⁻¹. The oven temperature during the analysis was varied as follows: initial temperature of 35 °C held for 5 minutes, a first heating ramp at 10 °C min⁻¹ to 60 °C and a final ramp at 20 °C min⁻¹ to 250 °C then held for 5 min. An absolute error of ± 5% affects the peaks integration.

References

- ¹ J. Zhao, Z. Zheng, S. Bottle, A. Chou, S. Sarina, H. Zhu, *Chem. Commun.*, **2013**, 49, 2676.
- ² T. E. Muller, K. C. Hultsch, M. Yus, F. Foubelo, M. Tada, *Chem. Rev.*, **2008**, 108, 3795.
- ³ G. Guillena, D. J. Ramlín, M. Yus, *Chem. Rev.*, **2010**, 110, 1611.
- ⁴ S. Liang, L. Hammond, B. Xu, G. B. Hammond, *Adv. Synth. Catal.*, **2016**, 358, 3313.
- ⁵ J. J. Brunet, D. Neibecker, *Catalytic Heterofunctionalization*, Wiley-VCH, Weinheim, **2001**.
- ⁶ R. Severin, S. Doye, *Chem. Soc. Rev.*, **2007**, 36, 1407.
- ⁷ W. Reppe, *Justus Liebigs Ann. Chem.*, **1956**, 601, 81.
- ⁸ W. Tang, X. Zhang, *Chem. Rev.*, **2003**, 103, 3029.
- ⁹ G. Desimoni, G. Tacconi, *Chem. Rev.*, **1975**, 75, 651.
- ¹⁰ G. Evano, A. C. Gaumont, C. Alayrac, I. E. Wrona, J. Giguere, O. Delacroix, A. Bayle, K. Jouvin, C. Theunissen, J. Gatignol, A. C. Silvanus, *Tetrahedron*, **2014**, 70, 1529.
- ¹¹ L. Huang, M. Arndt, K. Gooßen, H. Heydt, L. J. Gooßen, *Chem. Rev.*, **2015**, 115, 2596.
- ¹² F. Pohlki, S. Doye, *Chem. Soc. Rev.*, **2003**, 32, 104.
- ¹³ J. Haggins, *Chem. Eng. News*, **1993**, 71, 23.
- ¹⁴ B. Schlummer, J. F. Hartwig, *Org. Lett.*, **2002**, 4, 1471.
- ¹⁵ I. Dion, A. M. Beauchemin, *Angew. Chem. Int. Ed.*, **2011**, 50, 8233.
- ¹⁶ X. Cheng, Y. Xia, H. Wei, B. Xu, C. Zhang, Y. Li, G. Qian, X. Zhang, K. Li, W. Li, *Eur. J. Org. Chem.*, **2008**, 1929.
- ¹⁷ M. T. Herrero, J. D. de Sarralde, R. San Martín, L. Bravo, E. Domínguez, *Adv. Synth. Catal.*, **2012**, 354, 3054.
- ¹⁸ M. Joshi, R. Tiwari, A. K. Verma, *Org. Lett.*, **2012**, 14, 1106.
- ¹⁹ P. W. Roesky, T. E. Muller, *Angew. Chem.*, **2003**, 42, 2708.
- ²⁰ K. C. Hultsch, *Adv. Synth. Catal.*, **2005**, 347, 367.
- ²¹ K. C. Hultsch, *Org. Biomol. Chem.*, **2005**, 3, 1819.
- ²² I. Aillaud, J. Collin, J. Hannedouche, E. Schulz, *Dalton Trans.*, **2007**, 5105.
- ²³ A. S. K. Hashmi, G. J. Hutchings, *Angew. Chem., Int. Ed.*, **2006**, 45, 7896.
- ²⁴ S. A. K. Hashmi, *Chem. Rev.*, **2007**, 107, 3180.
- ²⁵ A. Corma, P. Concepción, I. Domínguez, V. Fornés, M. J. Sabater, *J. Catal.*, **2007**, 251, 39.
- ²⁶ L. C. Lee, Y. Zhao, *ACS Catal.*, **2014**, 4, 688.

-
- ²⁷ M. C. Pirrung, *The Synthetic Organic Chemist's Companion*, Wiley, **2007**.
- ²⁸ K. Hara, S. Akahane, J. W. Wiench, B. R. Burgin, N. Ishito, V. S.Y. Lin, A. Fukuoka, M. Pruski, *J. Phys. Chem. C*, **2012**, *116*, 7083.
- ²⁹ V. A. Solovyeva, K. B. Vu, Z. Merican, R. Sougrat, V. O. Rodionov, *ACS Comb. Sci.*, **2014**, *16*, 513.
- ³⁰ F. X. Zhu, W. Wang, H. X. Li, *J. Am. Chem. Soc.*, **2011**, *133*, 11632.
- ³¹ K. Fujita, A. Fujii, J. Sato, H. Yasuda, *Synlett*, **2016**, *27*, 1941.
- ³² J. E. Perea-Buceta, T. Wirtanen, O. V. Laukkanen, M. K. Makela, M. Nieger, M. Melchionna, N. Huittinen, J. A. Lopez-Sanchez, J. Helaja, *Angew. Chem. Int. Ed.*, **2013**, *52*, 11835.
- ³³ Y. P. He, H. Wu, D. F. Chen, J. Yu, L. Z. Gong, *Chem. Eur. J.*, **2013**, *19*, 5232.
- ³⁴ E. Mizushima, T. Hayashi, M. Tanaka, *Org. Lett.*, **2003**, *5*.
- ³⁵ H. Katayama, K. Yamamura, Y. Miyaki, F. Ozawa, *Organometallics*, **1997**, *16*, 4497.
- ³⁶ J. Sedlacek, M. Pacovska, D. Redrova, H. Balcar, A. Biffis, B. Corain, J. Vohlidal, *Chem. Eur. J.*, **2002**, *8*, 366.
- ³⁷ K. Freitag, J. Gracia, A. Martín, M. Mena, J. M. Poblet, J. P. Sarasa, C. Yelamos, *Chem. Eur. J.*, **2001**, *7*, 3645.
- ³⁸ V. Durà-Vilà, D. Michael, P. Mingos, R. Vilar, A. J. P. White, D. J. Williams, *J. Organomet. Chem.*, **2000**, *600*, 198.
- ³⁹ G. Braurer, *Handbook of Preparative Inorganic Chemistry*; Academic Press: New York, **1963**, Vol. II, 1058.
- ⁴⁰ J. Manna, B. Roy, P. Sharma, *J. Power Sources*, **2015**, *275*, 727.
- ⁴¹ <http://imagej.nih.gov/ij/>.

5. SYNTHESIS AND CHARACTERISATION OF Au/Fe₃O₄ NANOCOMPOSITES

5.1 Introduction

5.1.1 Magnetism in materials

The macroscopic magnetic properties of materials arise from the interaction between an external magnetic field and the magnetic dipole moment of the constituent atoms. The magnetic moment of each atom is generated by the orbital movement of the electrons around the nucleus and the spin movement of the electrons around their own axis. In addition, due to a quantum exchange force that aligns in a parallel or antiparallel way the electron spins in neighbouring atoms, the resulting magnetic moment is given only by the unpaired electrons in the material.^{1,2}

When a material is inserted in a magnetic field H , the magnetic response B (intrinsic magnetic field) can be expressed as:

$$B = \mu_0 (H + M)$$

where μ_0 is the magnetic permeability under vacuum, and M is the magnetisation of the material. Magnetisation can be described as the vectorial measure of the magnetic dipole moment by volume unit in all the considered volume, and is represented by:

$$M = m/V = n\mu_B/V$$

where m is the total magnetic moment, which corresponds to the number of atoms (n) that have unpaired electrons multiplied by the elemental magnetic moment μ_B and divided by the volume V occupied by the material. The proportionality between magnetisation M and exciting field H is described by the magnetic susceptibility χ and is characteristic of each substance, at a given temperature.¹

On the basis of the magnetic behaviour, it is possible to make a distinction between materials that do not have permanent magnetisation and exhibit a linear response to a

moderate applied field, and materials that have an intrinsic magnetisation and exhibit a non-linear response to the applied field (Figure 5.1).³

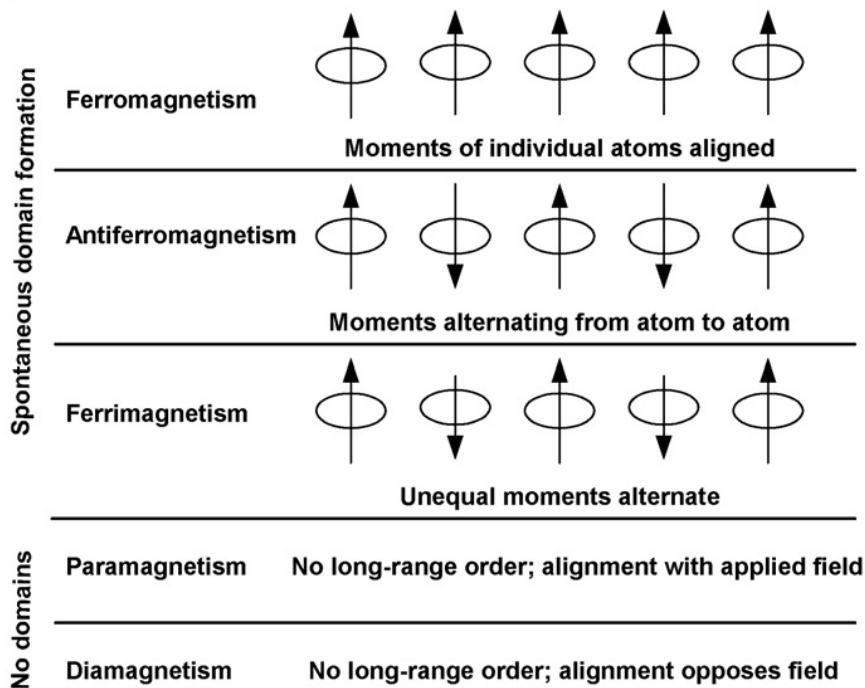


Figure 5.1. Different type of magnetic behaviour.⁴

In general, all materials display a weak repulsion to an applied magnetic field, known as *diamagnetism*, due to the motion of electrons which generates atomic current loops to oppose the external field ($\chi < 0$). Typically, diamagnetic materials, such as quartz SiO_2 and calcite CaCO_3 , are characterised by filled electronic subshells where the magnetic moments are paired and overall cancel each other. Since diamagnetism is very weak, any other form of magnetic behaviour that a material may possess usually overpowers the effects of these current loops.

Paramagnetism is associated to materials whose atomic magnetic moments are uncoupled, resulting in a small positive susceptibility in the presence of applied external fields ($\chi \sim 0$). In *ferromagnetic* materials (Fe, Ni, Co) the parallel alignment of atomic magnetic moments of equal magnitude causes a spontaneous permanent magnetisation, while in the case of *antiferromagnetism* the antiparallel coupling of these moments results in a zero net magnetisation. Finally, *ferrimagnetism* is a property exhibited by materials, such as Fe_3O_4 , in which two types of atoms or ions with moments of different strengths are arranged in an antiparallel way, generating a net magnetisation.⁴

Furthermore, the magnetic behaviour also depends on the size of the material, as indicated by the shape of the magnetic susceptibility curve. In the case of ferromagnetic and ferrimagnetic bulk materials, a hysteresis loop can be observed, due to the multi-domain structure in which regions of uniform magnetisation are separated by domain walls. The application of a sufficiently large magnetic field causes the spins within the material to align with the field. The maximum value of the magnetisation achieved in this state is called the saturation magnetisation (M_s). As the magnitude of the magnetic field decreases, spins cease to be aligned with the field and the total magnetisation decreases, however a residual magnetic moment at zero field remains (remanent magnetisation, M_r). The coercive field H_c is the magnitude of the field that must be applied in the negative direction to bring the magnetization of the sample back to zero (Figure 5.2).

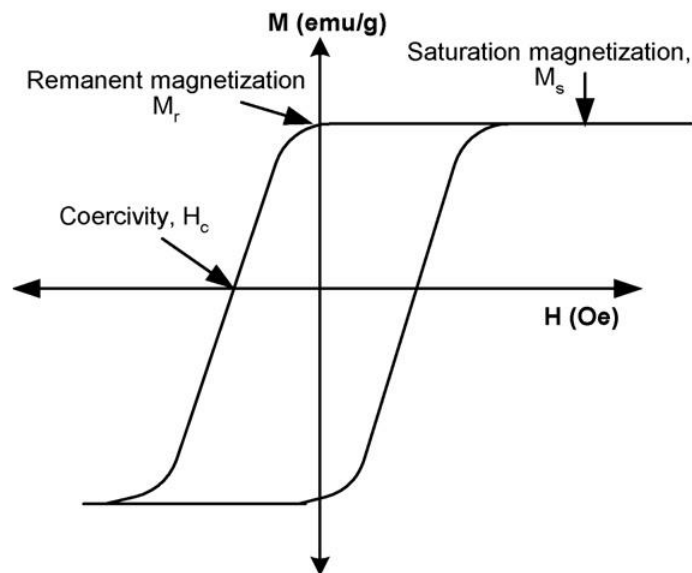


Figure 5.2. Magnetisation M as a function of the applied magnetic field H .⁴

On the contrary, when the sample size is reduced under a critical value at the nanometre scale, the formation of multi-domains is not favourable and the particles remain as a single domain so that their magnetic moments could be visualized as one large magnetic moment. In this case, the application of a magnetic field gives rise to the phenomenon of *superparamagnetism*, in which no hysteresis is observed since no energy is dispersed in the motion of domain walls ($M_r \sim 0$, $H_c \sim 0$). Superparamagnetic nanoparticles are strongly attracted to an applied magnetic field, due to the contribution of large magnetic moments within the individual particles, however they behave as non-

magnetic materials in the absence of external fields. Indeed, repeated cycles of separation and dispersion are possible because of the absence of “magnetic memory”.¹

In the past two decades, the growing interest in the synthesis and application of magnetic nanoparticles has resulted in an advanced understanding of their properties and the demonstration of their great potential in a wide range of applications.^{5,6} Nowadays, magnetic nanosystems find application in catalysis,^{7,8,9} biotechnology and biomedicine,¹⁰ magnetic resonance imaging,¹¹ data storage¹² and environmental remediation.¹³

5.1.2 Magnetite nanoparticles

Magnetite (Fe_3O_4) is a mixed iron oxide with an inverse spinel structure, in which Fe(III) ions occupy 1/4 of the octahedral coordination sites, while Fe(II) ions are equally distributed in 1/8 of the tetrahedral and 1/4 of the octahedral holes (Figure 5.3).

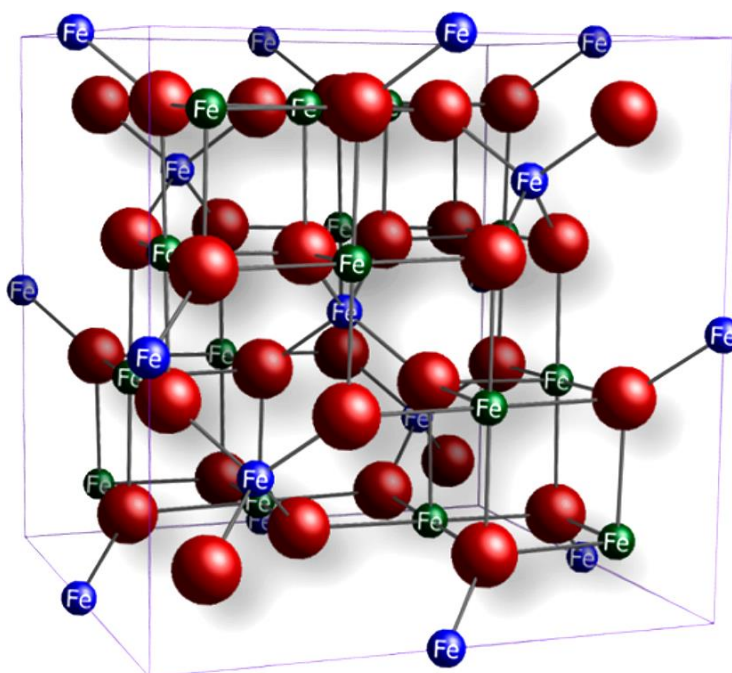


Figure 5.3. Unit cell of magnetite [$\text{Fe(III)}_{\text{oct}}$ and $\text{Fe(II)}_{\text{oct}}$: green, $\text{Fe(III)}_{\text{tet}}$: blue and O^{2-} : red].⁵

The electron spins of Fe(III) ions in the tetrahedral sites are aligned antiparallel to those in the octahedral sites, so that no net magnetisation is observed from these ions. However, the parallel alignment of Fe(II) and Fe(III) spins in the octahedral holes generates a net magnetisation due to electron exchange, making bulk magnetite a ferromagnetic material.¹⁴ On the contrary, Fe_3O_4 nanoparticles display a superparamagnetic behaviour when their size is approximately below 25 nm.¹⁵

Since the properties of magnetic nanoparticles are strongly related to their dimension and shape, extensive efforts have been made to develop synthetic methods which allow to finely control these two parameters.

The *co-precipitation* method is an easy and convenient way to prepare iron oxides from Fe(II) and Fe(III) salt solutions, by addition of a base under inert atmosphere. The type of salts used (e.g. sulphates, nitrates, chlorides), the Fe(II)/Fe(III) ratio, the reaction temperature, the pH value and the ionic strength of the media are all factors which influence the size, shape and composition of the obtained magnetic nanoparticles.¹⁶ In order to obtain monodispersed NPs, the synthesis is often carry out in the presence of organic additives, such as poly vinyl alcohol (PVA), as stabilising agents.¹⁷ With this procedure, once the synthetic conditions are optimised, the quality of the magnetite nanoparticles is fully reproducible.

Another way to synthesized monodispersed magnetic NPs is by thermal decomposition of organometallic compounds, such as iron acetyl acetonates, in high-boiling organic solvents containing stabilising surfactants (e.g. fatty acids, oleic acid, hexadecylamine).^{18,19} In this case the ratios of the starting reagents, i.e. organometallic precursor/surfactant/solvent, the reaction temperature, the reaction time and the aging period are the crucial parameters for the precise control of size and morphology.

In the *sol-gel* method, also known as chemical solution deposition, a sol of nanoparticles is obtained by hydroxylation and condensation of metal precursor solutions, with formation of a three dimensional metal oxide network. The crystalline state is then obtained upon heat treatment. The pH, the temperature, the nature and the concentration of the precursors and the nature of the solvent have been described to influence the synthetic process.^{20,21}

Finally, other known strategies for the preparation of Fe₃O₄ nanoparticles are gas-phase deposition,²² hydrothermal method,²³ electrochemical method²⁴ and sonochemical decomposition.²⁵

5.1.3 Functionalisation of magnetic nanoparticles

The functionalisation of the surface of magnetic nanoparticles is an important step in the design of supported magnetic catalysts, since it allows the immobilisation of a wide range of molecular catalysts, biocatalysts, organocatalysts and metal NPs.^{1,26}

The surface modification can be performed following three main approaches: 1) non-covalent absorption of bifunctional molecules, surfactant or polymers, 2) formation of core-shell structures by coating with other oxides, carbon, polymers or metallic layers, and 3) grafting with organic or inorganic functional molecules, such as carboxylic acids, phosphonic acids or alkoxy silanes (Figure 5.4).

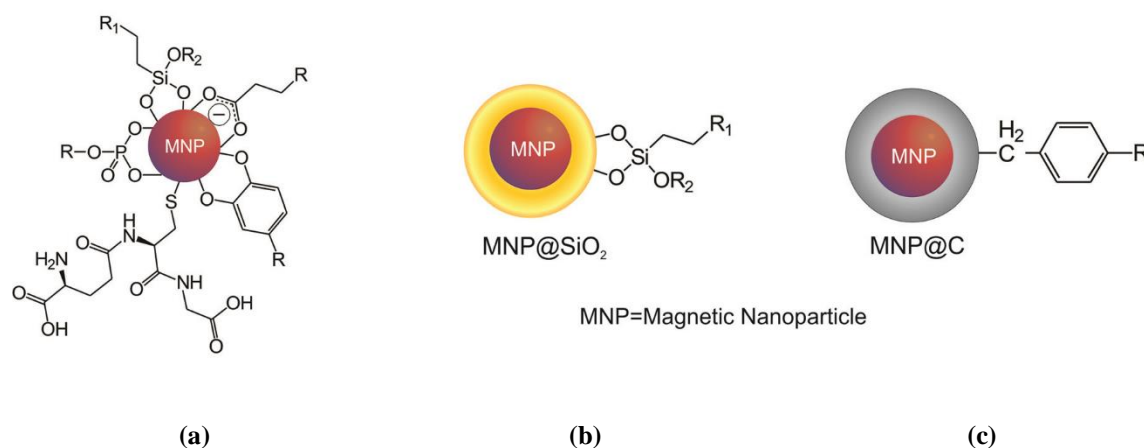


Figure 5.4. Different approaches for the functionalisation of magnetic nanoparticles (MNPs): a) grafting with inorganic/organic functional molecules, b) silica coating and c) carbon coating.¹

The binding of bifunctional carboxylate molecules to the metal oxide surface, by strong bidentate metal-carboxylate bonds, can easily afford surface functionalised Fe_3O_4 nanoparticles. In this regard, oleic acid is often attached to the iron oxide surface so that the hydrophobic tails can provide steric hindrance to stabilise NPs in solution.²⁷ Furthermore, it is possible to introduce $-\text{SH}$ terminal groups by immobilisation of 3-mercaptopropionic acid,²⁸ as well as functional acids containing multiple bonds, such as linolenic and linoleic acids, or pyridine moieties, such as 6-methylpyridine-2-carboxylic acid.²⁹

However, the most studied strategy for the functionalisation of magnetic nanomaterials consist in the condensation of the $-\text{OH}$ groups of the oxide surface with the $-\text{OR}$ terminal groups of alkoxyorganosilanes, which can be exploited both for bare

magnetite nanoparticles and for silica-coated Fe₃O₄NPs. For instance, Wang *et al.* reported the synthesis of magnetite NPs functionalised with 3-aminopropyl(triethoxysilane) for the further immobilisation of a Pd-based catalyst,³⁰ while Yi *et al.* employed the same organosilane for the preparation of highly dispersed PdNPs on silica-coated Fe₃O₄.³¹ Furthermore, Rossi *et al.* described the synthesis of very small supported PdNPs by an impregnation-reduction process using an amine and an ethylenediamine functionalised silica-coated magnetic support.³²

5.1.4 Aim of the chapter

Magnetic Fe₃O₄ (magnetite) nanoparticles were synthesized *via* a chemical precipitation route in different alkaline environments (NH₃ or NaOH) and subsequently functionalised with PPTEOS, with the aim of promoting the nucleation and subsequent stabilisation of gold nanoparticles to obtain **Au/Fe₃O₄@Yne** composites.

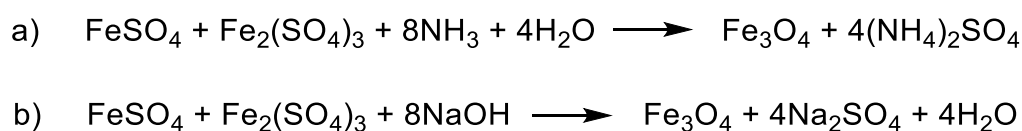
The morphology, structure, composition and AuNPs binding capacity of the modified Fe₃O₄ nanoparticles were investigated by means of complementary characterization techniques. Moreover, their magnetic properties were studied as a function of the adopted processing conditions.

Part of the work reported in the present chapter was published in *Ceramics International*.³³

5.2 Results and discussion

5.2.1 Synthesis of Au/Fe₃O₄@Yne and Au/Fe₃O₄ nanocomposites

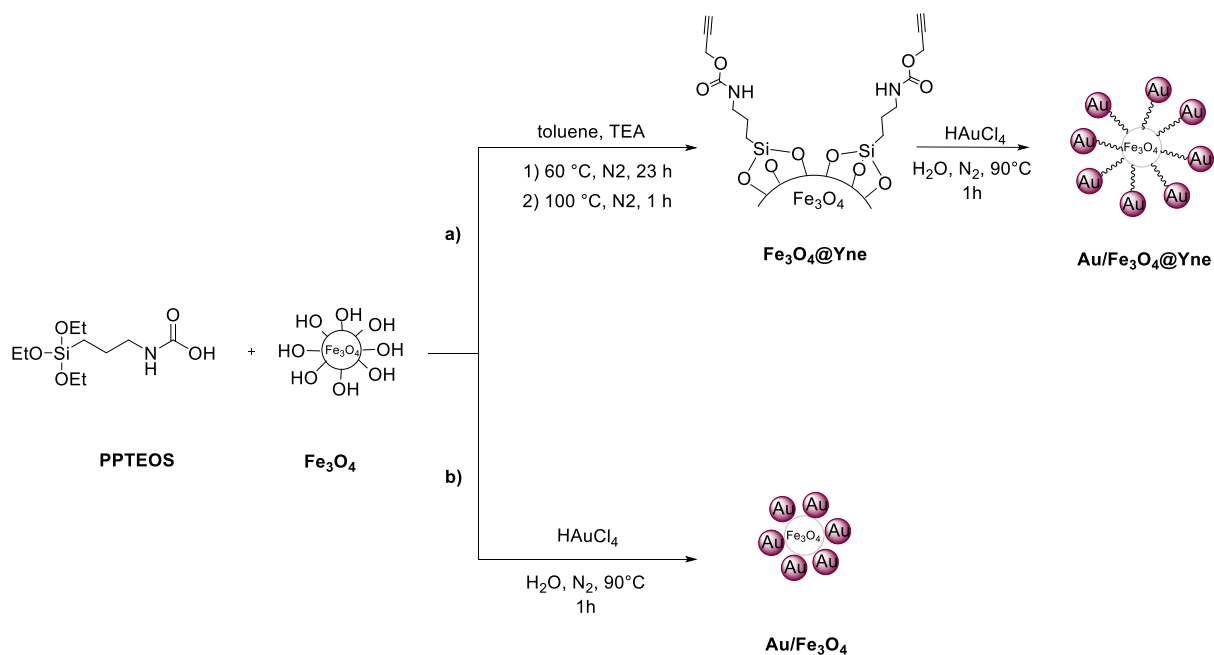
The synthesis of magnetite nanoparticles was carried out *via* a co-precipitation method using two different basic media, i.e. NH₃ and NaOH (**Fe₃O₄-NH₃** and **Fe₃O₄-NaOH**). In particular, the amount of ammonia used was twice the equimolar amount given by the stoichiometry of the reaction (Scheme 5.1a), in order to achieve a basic pH. On the contrary, when the synthesis was performed in the presence of NaOH, the addition of the stoichiometric 8 equivalents of base led to a final pH value of 13.4 (Scheme 5.1b).



Scheme 5.1. Synthesis of magnetite in the presence of a) ammonia and b) sodium hydroxide.

Afterwards, the obtained Fe₃O₄ nanoparticles were functionalised with PPTEOS and decorated with AuNPs, accordingly to the procedure previously employed for micrometre oxide supports (SiO₂, Al₂O₃ and TiO₂).³⁴ Indeed, the first step consisted in the coupling of the silane PPTEOS to the magnetite surface hydroxyl groups to yield **Fe₃O₄@Yne**. Successively in the second step, the addition of aqueous HAuCl₄ led to the *in-situ* formation of **Au/Fe₃O₄@Yne** (Scheme 5.2a). In keeping with previous works the amount of Au(III) precursor was chosen in order to have a nominal total gold amount in the range 4.5 - 5.0 wt %.

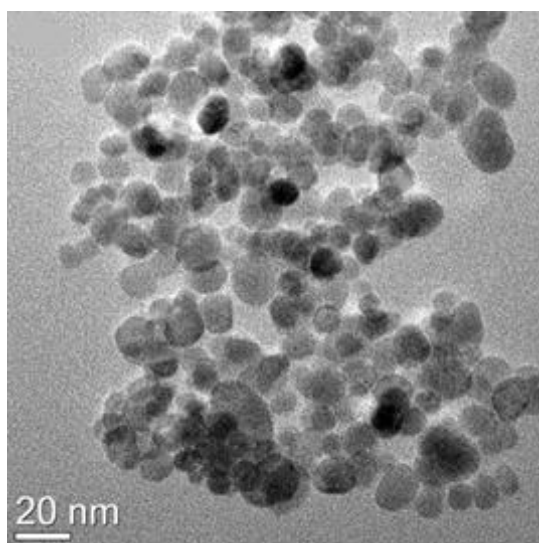
At variance with the previous studies, in which the propynylcarbamate functionalisation was found to be essential for the nucleation and growth of Au(0) nanoparticles on SiO₂, Al₂O₃ and TiO₂ supports, in the present case the formation of metallic gold nanoparticles was obtained even on bare Fe₃O₄ (**Au/Fe₃O₄** composites, Scheme 5.2b). This finding is in line with the results reported by Alorro *et al.*, according to which Au(III) chloride complexes are spontaneously reduced to metallic gold on Fe₃O₄ surfaces.^{35,36}



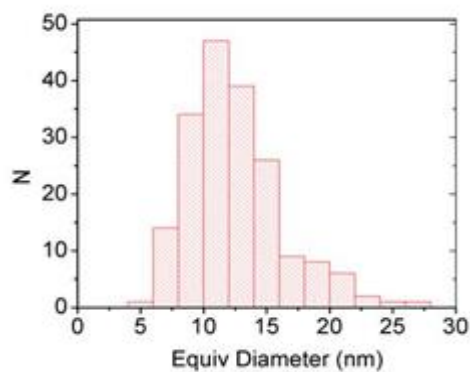
Scheme 5.2. Synthesis of a) Au/Fe₃O₄@Yne and b) Au/Fe₃O₄.

5.2.2 Characterisation of Fe₃O₄ and Fe₃O₄@Yne

Firstly, the morphology and nano-organisation of the synthesized magnetite nanoparticles was investigated by TEM analyses. In line with reported literature data, the material obtained in the presence of ammonia (Fe₃O₄-NH₃) presented spherically shaped nanoparticles with an average size of 12 nm (Figure 5.5a), whereas a different particle shape was observed for Fe₃O₄-NaOH, alongside a larger mean particle diameter of 23 nm (Figure 5.5b).^{37,38,39,40}



(a)



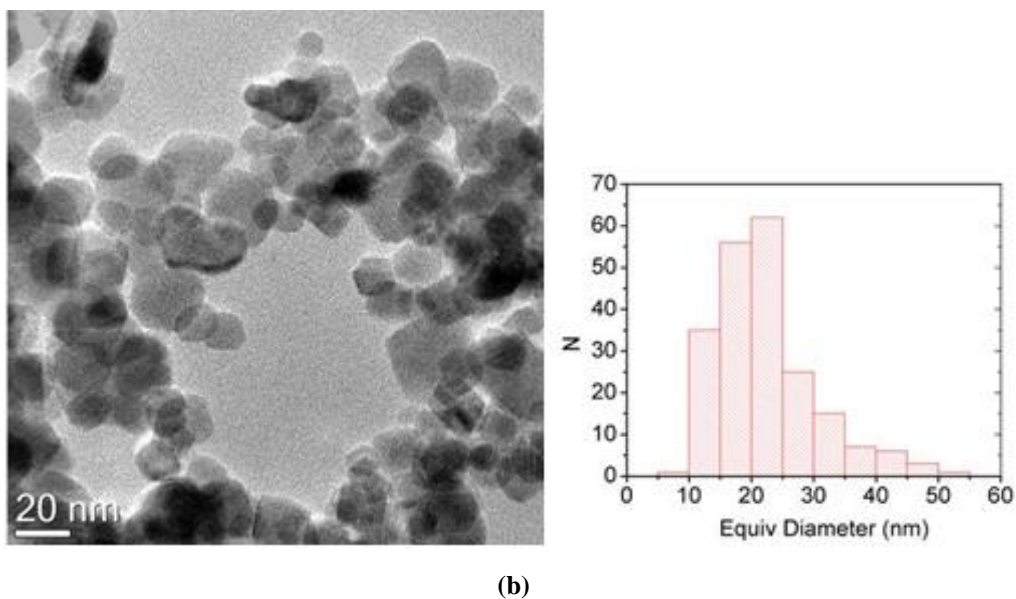


Figure 5.5. Bright field (BF) image and particle size distribution of a) $\text{Fe}_3\text{O}_4\text{-NH}_3$ and b) $\text{Fe}_3\text{O}_4\text{-NaOH}$.

The Select Area Electron Diffraction (SAED) patterns of $\text{Fe}_3\text{O}_4\text{-NH}_3$ and $\text{Fe}_3\text{O}_4\text{-NaOH}$ samples, recorded on a 200 nm^2 area, showed distinct diffraction rings indexed as magnetite (Fe_3O_4 , cubic, space group $Fd-3m$) (Figure 5.6, Table 5.1).

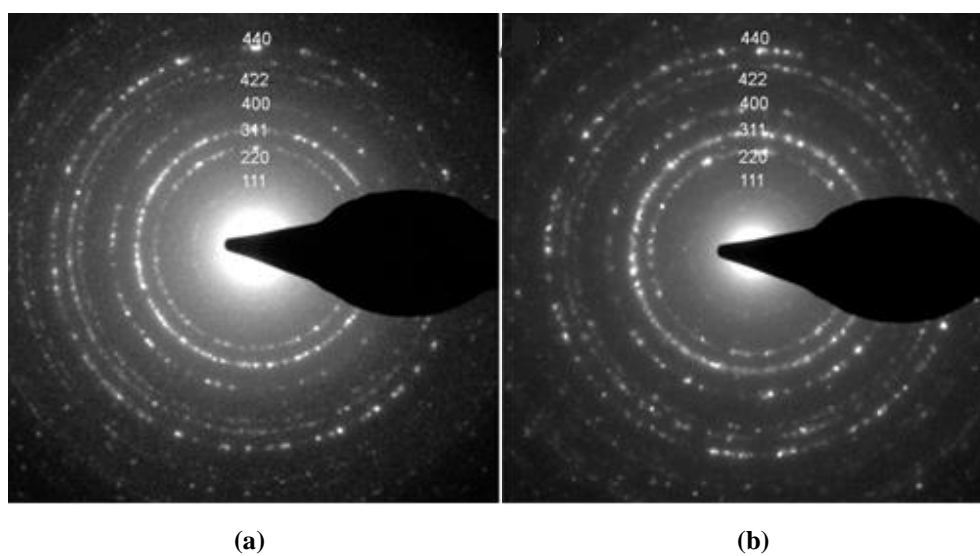


Figure 5.6. Selected Area Electron Diffraction (SAED) recorded on 200 nm^2 area of a) $\text{Fe}_3\text{O}_4\text{-NH}_3$ and b) $\text{Fe}_3\text{O}_4\text{-NaOH}$.

Table 5.1. SAED reflection indexes for **Fe₃O₄-NH₃**.

Reflection N°	hkl	d ⁻¹ (nm ⁻¹) measured	d ⁻¹ (nm ⁻¹) ^a
1	111	2.1	2.066
2	220	3.4	3.374
3	311	4.0	3.956
4	222	4.1	4.131
5	400	4.8	4.770
6	331	-	5.199
7	422	5.9	5.843
8	511 - 333	6.2	6.198
9	440	6.8	6.745

a) JCPDS N°01-075-0033.

The functionalisation of the magnetite support with the organic moieties was confirmed by the presence in the ATR-FTIR spectra of the two characteristic bands at 1700 and 1523 cm⁻¹ associated to the C-O stretching and the N-H bending of the propynylcarbamate group.

Furthermore, the organic functionalisation had no significant influence on the size of the magnetite nanoparticles, nor on the crystalline structure of the materials, as evidence in the XRD spectra reported in Figure 5.7. All samples patterns showed the presence of magnetite as the sole crystalline phase.

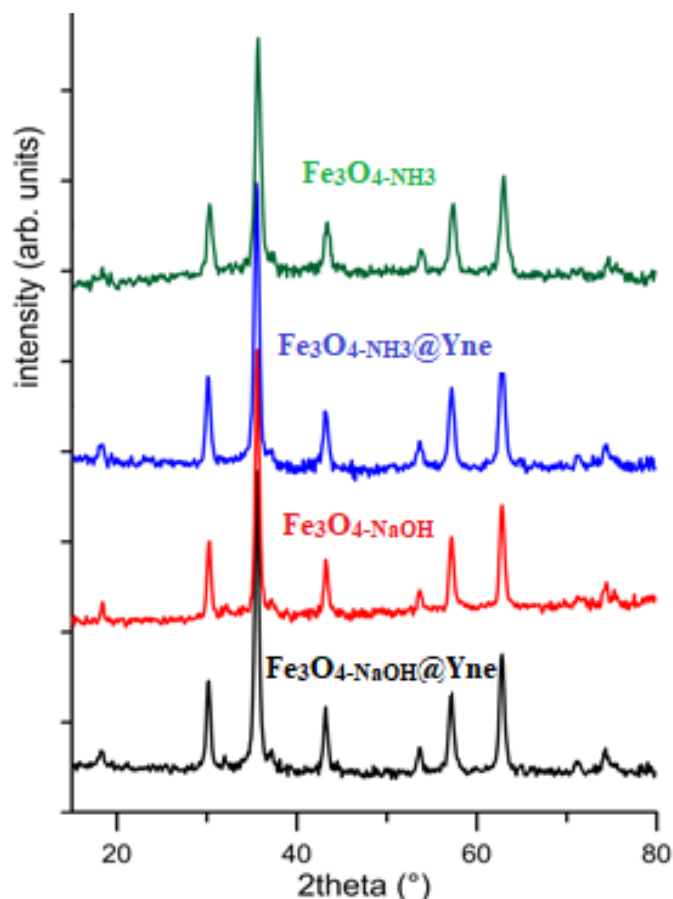


Figure 5.7. XRD patterns of $\text{Fe}_3\text{O}_4\text{-NH}_3$ and $\text{Fe}_3\text{O}_4\text{-NaOH}$ samples as-prepared, and after surface functionalisation.

On the contrary, the introduction of the organic capping resulted in a shift of the zeta potential of magnetite (Table 5.2).⁴¹ Indeed, the zeta potential (measured for a suspension in a 10.0 mM NaCl solution) of $\text{Fe}_3\text{O}_4\text{-NH}_3$ was initially 28.0 mV (at spontaneous pH 5.6) and decreased down to 8.0 mV for $\text{Fe}_3\text{O}_4\text{-NH}_3\text{@Yne}$, whereas the zeta potential of $\text{Fe}_3\text{O}_4\text{-NaOH}$ was decreased from 6.5 mV down to -0.4 mV ($\text{Fe}_3\text{O}_4\text{-NaOH@Yne}$).

Table 5.2. Zeta potentials of bare and functionalised magnetite.

Sample	Zeta potential (mV)	Spontaneous pH
$\text{Fe}_3\text{O}_4\text{-NH}_3$	28.0 ± 1.0	5.14
$\text{Fe}_3\text{O}_4\text{-NH}_3\text{@Yne}$	8.0 ± 0.6	5.24
$\text{Fe}_3\text{O}_4\text{-NaOH}$	6.5 ± 0.9	6.03
$\text{Fe}_3\text{O}_4\text{-NaOH@Yne}$	-0.4 ± 0.2	5.63

Moreover, the TGA analysis of **Fe₃O₄@Yne** showed three regions of mass loss, attributed respectively to the evaporation of adsorbed water and ethanol (30 -170 °C), organic material degradation (170 – 570 °C) and transformation of Fe₃O₄ into FeO (500 – 710 °C) (Figure 5.8). Specifically, the weight loss associated to the organic functionalisation was found to be 5.0 wt % for both **Fe₃O₄-NH₃@Yne** and **Fe₃O₄-NaOH@Yne**.⁴²

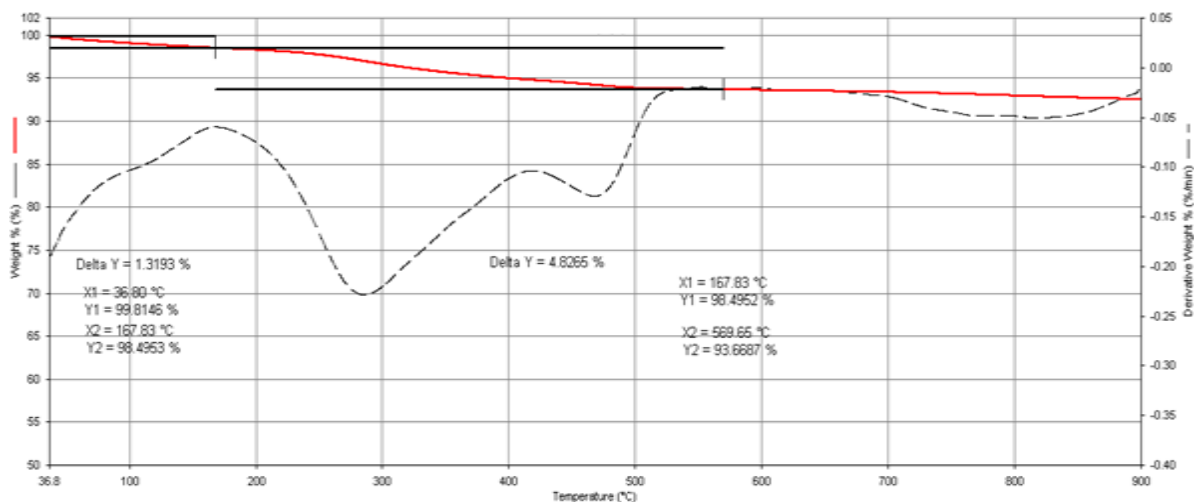


Figure 5.8. TGA analysis of **Fe₃O₄-NH₃@Yne**. The red line represents the weight loss percentage while the dotted line is the derivative of weight loss percentage.

5.2.3. Characterisation of Au/Fe₃O₄@Yne and Au/Fe₃O₄

The gold content determined by AAS spectroscopy was found to be around the 5.0 wt % for all the prepared samples, independently from the presence of the organic functionalisation (Table 5.3).

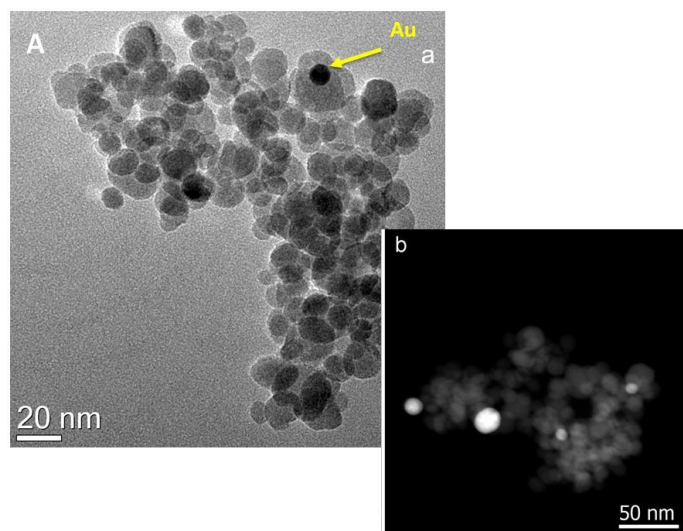
Furthermore, the deposition of gold nanoparticles on magnetite did not influence the particle size and crystallinity of the support, as shown from comparison of the data reported in Table 5.3.

Table 5.3. TEM, XRD and AAS data for Fe₃O₄, Fe₃O₄@Yne, Au/Fe₃O₄@Yne and Au/Fe₃O₄.

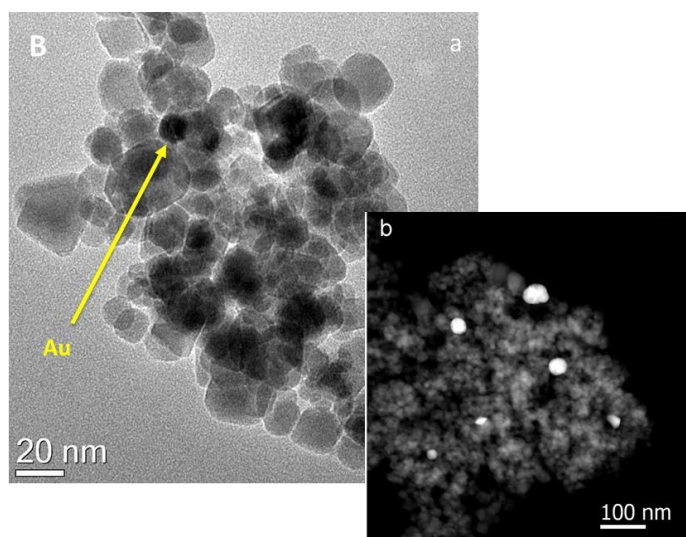
Sample	Fe ₃ O ₄ d _{TEM} ^a (nm)	Au d _{TEM} ^a (nm)	Fe ₃ O ₄ crystal size ^b (nm)	Au crystal size ^b (nm)	Au ^c (wt %)
Fe₃O₄-NH₃	12 ± 1	-	16 ± 2	-	-
Fe₃O₄-NH₃@Yne	12 ± 2	-	18 ± 2	-	-
Au/Fe₃O₄-NH₃@Yne	12 ± 3	15 ± 3	18 ± 1	24 ± 3	4.4 ± 0.1
Au/Fe₃O₄-NH₃	13 ± 3	74 ± 20	19 ± 2	38 ± 5	4.6 ± 0.1
Fe₃O₄-NaOH	23 ± 3	-	23 ± 1	-	-
Fe₃O₄-NaOH@Yne	22 ± 2	-	21 ± 1	-	-
Au/Fe₃O₄-NaOH@Yne	19 ± 5	30 ± 4	21 ± 1	32 ± 2	4.8 ± 0.1
Au/Fe₃O₄-NaOH	23 ± 2	42 ± 8	23 ± 1	36 ± 2	4.8 ± 0.1

a) Estimated on STEM images measurement using a confidence interval of 99%; b) calculated by Scherrer equation; c) determined by AAS spectroscopy.

In particular, Bright Field (BF) and HAADF TEM images showed the presence of spherical shaped gold nanoparticles, whose mean diameter underwent a two-fold increase from **Au/Fe₃O₄-NH₃@Yne** (15 ± 3 nm) to **Au/Fe₃O₄-NaOH@Yne** (30 ± 4 nm) (Figure 5.9).



(a)

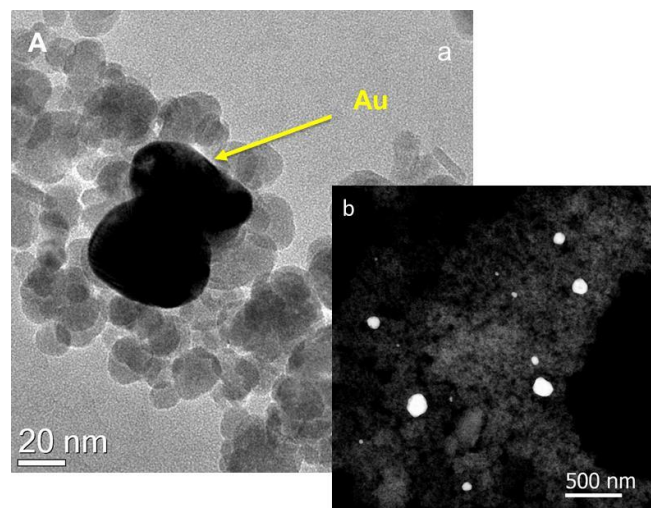


(b)

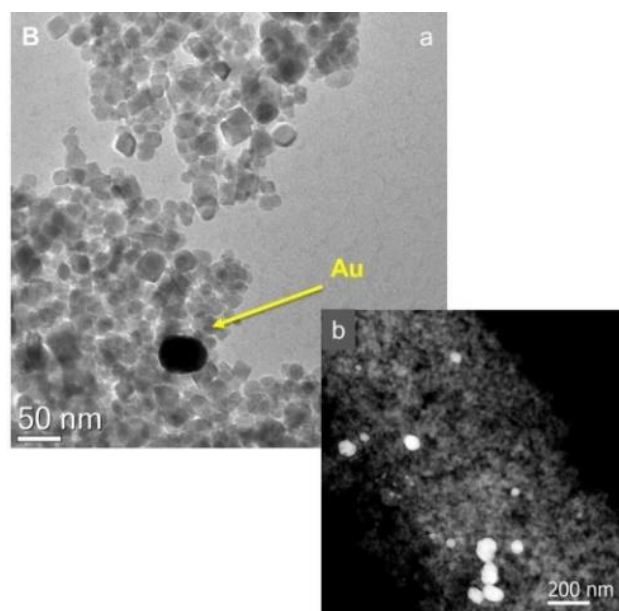
Figure 5.9. Representative BF-TEM and HAADF-STEM micrographs of a) **Au/Fe₃O₄-NH₃@Yne** and b) **Au/Fe₃O₄-NaOH@Yne**.

This difference in the AuNPs size could be tentatively explained by the presence of a higher concentration of adsorbed OH⁻ groups on the **Fe₃O₄-NaOH@Yne** magnetite surface, responsible for the further aggregation of gold nanoparticles.⁴³

Furthermore, in the absence of the propylcarbamate functionalisation, the average diameter of the anchored AuNPs turned out to be higher (74 ± 20 nm for **Au/Fe₃O₄-NH₃** and 42 ± 8 for **Au/Fe₃O₄-NaOH**, Figure 5.10).



(a)



(b)

Figure 5.10. Representative BF-TEM and HAADF-STEM micrographs of a) $\text{Au/Fe}_3\text{O}_4\text{-NH}_3$ and b) $\text{Au/Fe}_3\text{O}_4\text{-NaOH}$.

These findings confirm the influence and importance of the pendant organic group in the reduction and successive stabilisation of the attached gold nanoparticles. Finally, the AuNPs particle diameter obtained from the TEM images of $\text{Au/Fe}_3\text{O}_4\text{-NH}_3$ and $\text{Au/Fe}_3\text{O}_4\text{-NaOH}$ was significantly larger than the crystalline domain size measure by XRD. This discrepancy can be explained with the agglomeration of crystalline domains to form larger nanoparticles but also with the presence of partially crystallized particles and defects.

The XRD patterns of **Au/Fe₃O₄** composites showed, beside Fe₃O₄ peaks, additional reflections located at 38.2 °, 44.4 °, 64.6 ° and 77.7 °, related to (111), (200), (220) and (311) crystallographic planes of cubic Au (Figure 5.11).

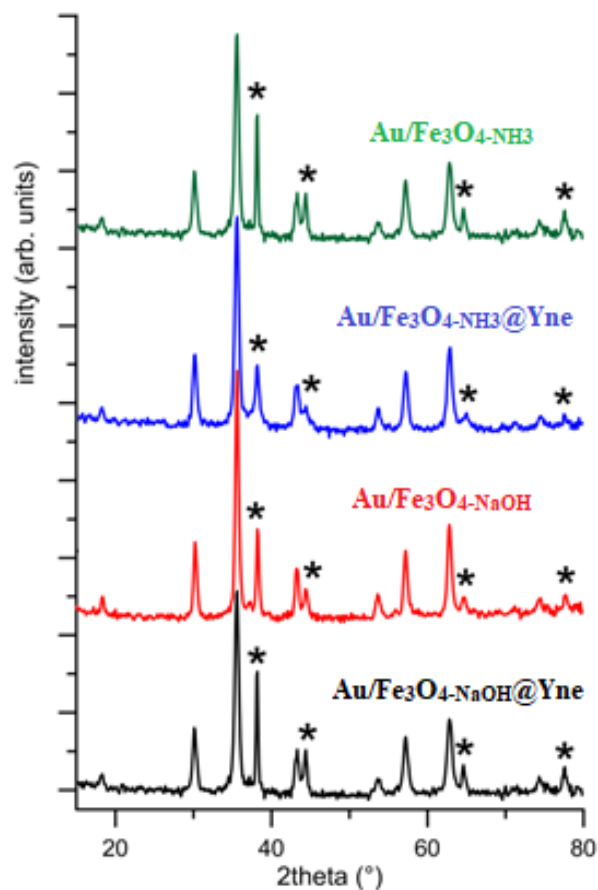


Figure 5.11. XRD patterns of **Au/Fe₃O₄-NH₃**, **Au/Fe₃O₄-NH₃@Yne**, **Au/Fe₃O₄-NaOH** and **Au/Fe₃O₄-NaOH@Yne**. Peaks indicated by (*) are referred to metallic gold. All the other peaks are due to Fe₃O₄.

Moreover, the surface chemical composition of the target systems was analysed by XPS. The wide-scan spectra of the NaOH-based samples are reported as a representative example in Figure 5.12. The spectra displayed the presence of C, O and Fe photopeaks, along with N and Au, depending on the adopted processing conditions.

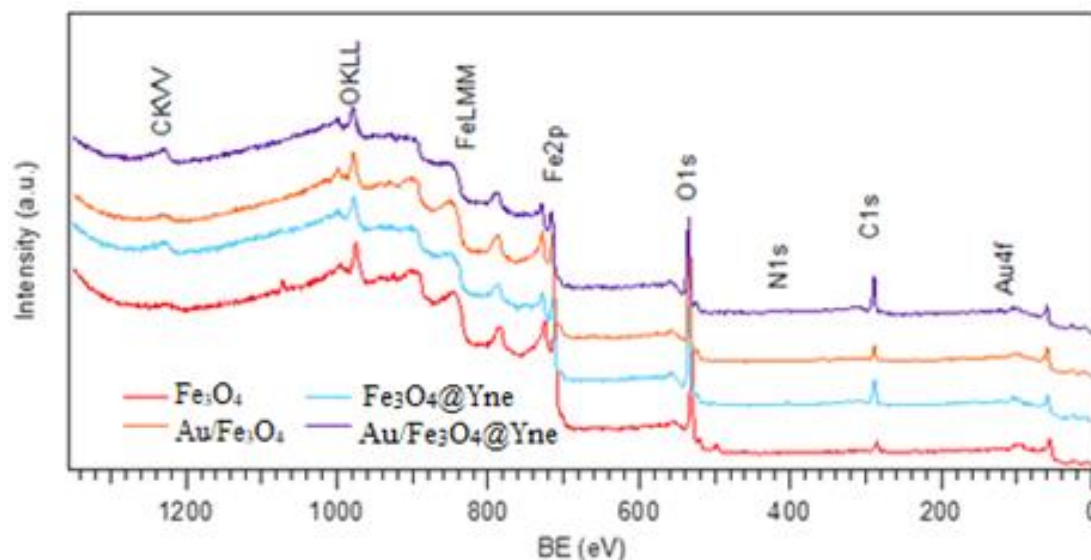


Figure 5.12. Wide-scan X-ray photoelectron spectroscopy analyses of $\text{Fe}_3\text{O}_4\text{-NaOH}$, $\text{Fe}_3\text{O}_4\text{-NaOH@Yne}$, $\text{Au/Fe}_3\text{O}_4\text{-NaOH}$ and $\text{Au/Fe}_3\text{O}_4\text{-NaOH@Yne}$.

XPS analyses confirmed the formation of Fe_3O_4 , as evidenced by the slight shift of the $\text{Fe}2p$ component [$\text{BE}(\text{Fe}2p_{3/2}) = 710.9 \text{ eV}$] to lower BE values with respect to the ones reported for Fe_2O_3 (Figure 5.13a).^{44,45} The $\text{O}1s$ signal (Figure 5.13b) was located at $\text{BE} = 530.3 \text{ eV}$, in line with the occurrence of lattice oxygen in Fe_3O_4 . In addition, the tailing at higher BEs indicated also the presence of surface hydroxyl groups on the oxide surfaces.^{45,46} Due to the presence of the latter, the calculated ratio between O and Fe atomic percentages ($\text{O/Fe} \approx 1.45$) was slightly higher than the value expected for stoichiometric Fe_3O_4 ($\text{O/Fe} = 1.33$). The $\text{N}1s$ signal could be decomposed by means of two different contributing bands, a main component due to N in amino-groups ($\text{BE} \approx 399.5 \text{ eV}$) and an additional higher BE one ($\text{BE} \approx 401 \text{ eV}$) related to NH-CO(O)- moieties (Figure 5.13c).

Regarding gold photopeaks, both Au containing samples showed similar spectral features [$\text{BE}(\text{Au}4f_{7/2}) = 84.0 \text{ eV}$] and no signals related to Au(I) and Au(III) species could be clearly identified, indicating the formation of pure metallic Au aggregates (Figure 5.13d).^{45,46}

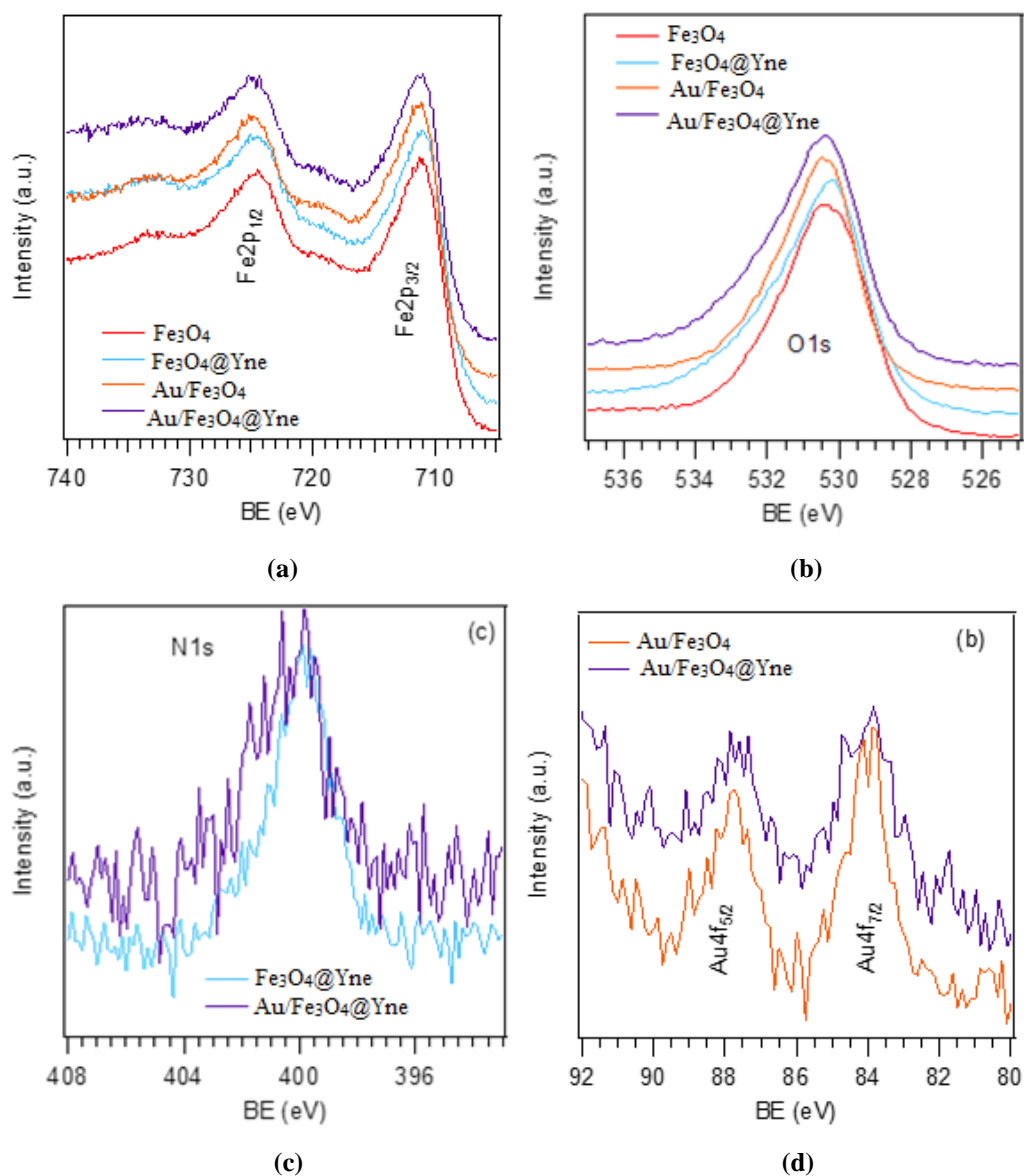
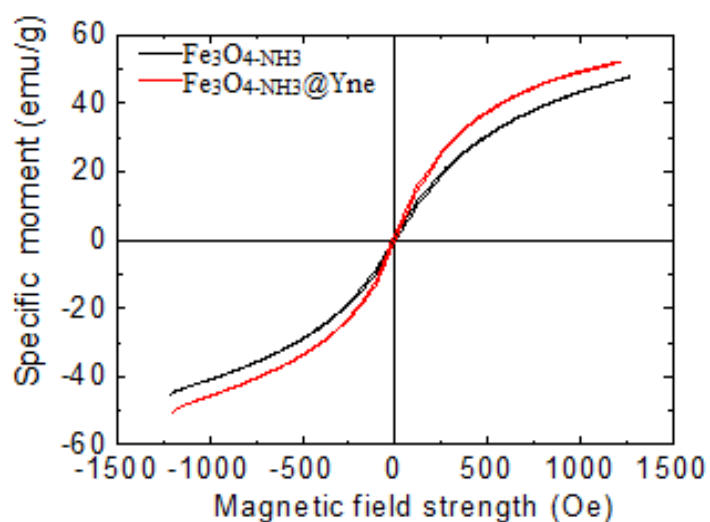


Figure 5.13. Surface a) Fe2p b) O1s, c) N1s and d) Au4f XPS spectra of **Fe₃O₄-NaOH**, **Fe₃O₄-NaOH@Yne**, **Au/Fe₃O₄-NaOH** and **Au/Fe₃O₄-NaOH@Yne**.

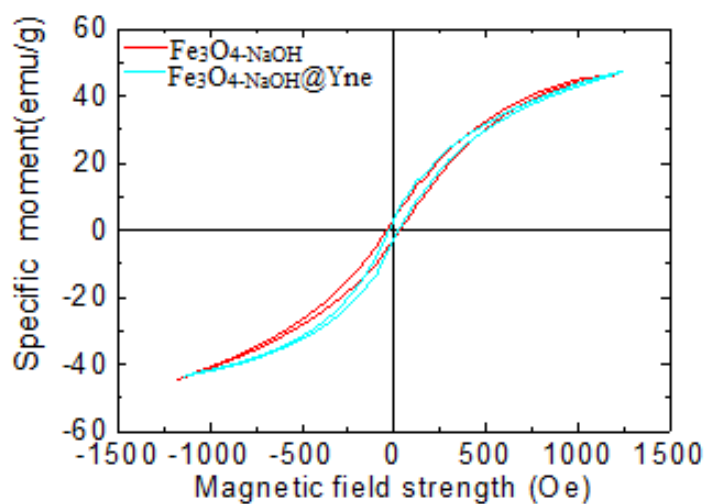
Independently from the preparative conditions, the gold surface concentration was close to 0.2 at.%. The samples functionalised with the propynylcarbamate pendant revealed also the presence of nitrogen with a mean content of 2.0 at.%.

5.2.4 Magnetic properties

The magnetic properties of the synthesized materials were also investigated. The specific moment σ as function of the applied magnetic field (Figure 5.14) was used to calculate some characteristic quantities: the remanent specific moment M_r , which is the specific moment at 0 applied field, the coercive field H_c and the specific moment at an applied magnetic field of 1000 Oe ($\sigma_{1000 \text{ Oe}}$).



(a)



(b)

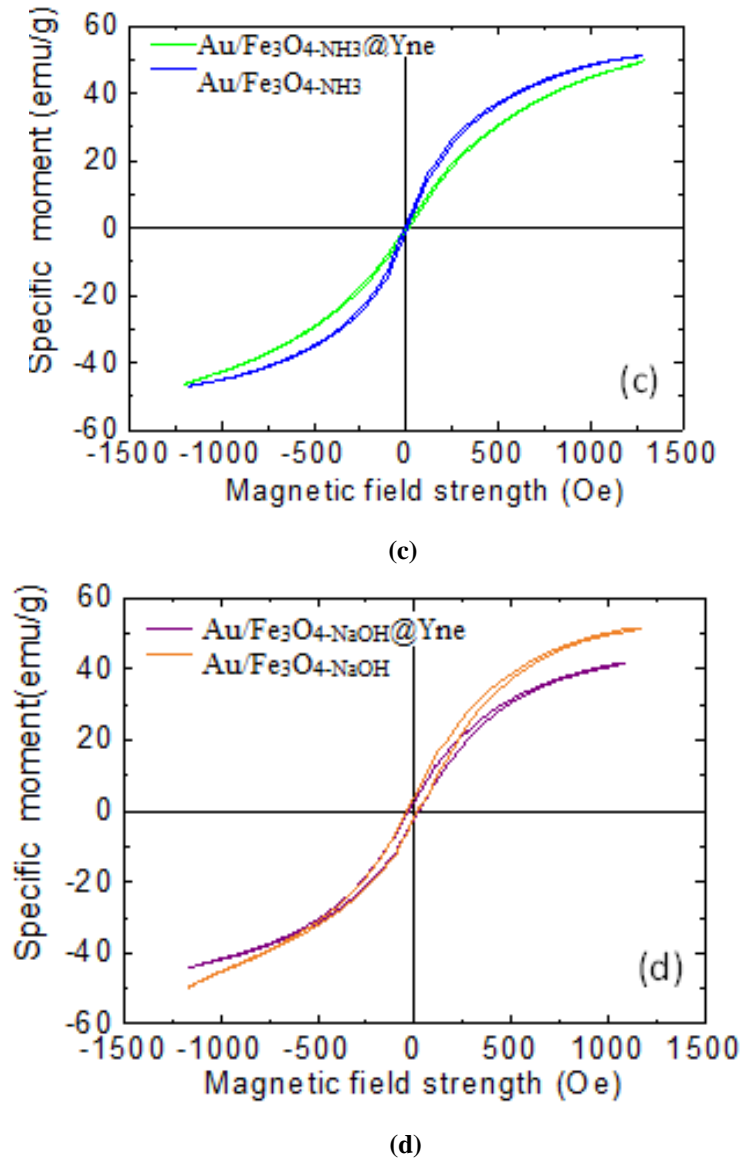


Figure 5.14. Specific moment σ as a function of the applied magnetic field, measured at 300 K. In a) and b) curves refer to Fe_3O_4 and $\text{Fe}_3\text{O}_4\text{@Yne}$ samples, respectively. In c) and d) curves refer to $\text{Au/Fe}_3\text{O}_4$ and $\text{Au/Fe}_3\text{O}_4\text{@Yne}$ samples, respectively.

The magnetic properties of nanoparticles are influenced by the concurrence of various factors, which include the particle size and contributions from their shape and surface functionalisation.^{47,48} In particular, Fe_3O_4 nanoparticles with an average size lower than 25 nm display a superparamagnetic behavior, with no magnetic hysteresis, at variance with bulk Fe_3O_4 . To evaluate the superparamagnetism of the target materials, we considered $M_r/\sigma_{1000 \text{ Oe}}$ and H_c , whose values should be close to 0 for superparamagnetic nanoparticles.^{49,50}

The data reported in Table 5.4 indicate that the organic/inorganic modification did not affect magnetic properties although **Fe₃O₄-NH₃**-based samples showed consistently smaller H_c and M_r values (av. values of 7.4 Oe and 0.8 emu/g) than those observed for **Fe₃O₄-NaOH**-based ones (av. values of 28 Oe and 2.8 emu/g). The specific moment at 1000 Oe ($\sigma_{1000 \text{ Oe}}$) was ca. 45 emu/g in both cases, in agreement with previous literature data.^{51,52}

Table 5.4. Magnetic properties of **Fe₃O₄**, **Fe₃O₄@Yne**, **Au/Fe₃O₄** and **Au/Fe₃O₄@Yne**.

Sample	$\sigma_{1000 \text{ Oe}}$ (emu/g)	H_c (Oe)	M_r (emu/g)	$M_r/\sigma_{1000 \text{ Oe}}$ ($\times 10^{-3}$)
Fe₃O₄-NH₃	44 ± 2	6.0 ± 0.7	0.60 ± 0.07	14 ± 2
Fe₃O₄-NH₃@Yne	49 ± 2	7.5 ± 0.9	0.9 ± 0.1	18 ± 2
Au/Fe₃O₄-NH₃@Yne	45 ± 2	8 ± 1	0.60 ± 0.07	13 ± 2
Au/Fe₃O₄-NH₃	48 ± 2	8 ± 1	1.0 ± 1.2	21 ± 3
Fe₃O₄-NaOH	45 ± 2	35 ± 4	3.0 ± 0.4	67 ± 9
Fe₃O₄-NaOH@Yne	44 ± 2	24 ± 3	2.8 ± 0.3	64 ± 8
Au/Fe₃O₄-NaOH@Yne	40 ± 2	27 ± 3	2.8 ± 0.3	70 ± 9
Au/Fe₃O₄-NaOH	50 ± 2	26 ± 3	2.8 ± 0.3	56 ± 7

The obtained values $M_r/\sigma_{1000 \text{ Oe}}$ ($<70 \times 10^{-3}$) and H_c (< 35 Oe) are compatible with a behavior dominated by superparamagnetism.⁵³ Furthermore, the difference in magnetic behavior between **Fe₃O₄-NH₃**-based and **Fe₃O₄-NaOH**-based samples could be explained by the fact that the **Fe₃O₄-NH₃** nanoparticles are on average smaller than those in **Fe₃O₄-NaOH** samples. The broader size distribution and higher shape anisotropy observed for **Fe₃O₄-NaOH** samples implies a greater number of nanoparticles that exceed the superparamagnetic limit of 25 nm and that have a non-zero coercive field. In addition, their shape anisotropy produces a magnetic anisotropy which, in turn, contributes to the obtainment of a higher coercive field.⁵⁰

5.3 Conclusions

Gold nanoparticles were successfully immobilised on alkynyl-carbamate functionalised Fe_3O_4 nanosystems by a straightforward procedure, without additional reducing and stabilising agents. Indeed, the organic functionalisation was found to promote the *in situ* formation of AuNPs without affecting neither the dimensions nor the magnetic properties of the initial superparamagnetic supports.

Furthermore, when Fe_3O_4 was prepared with ammonia ($\text{Fe}_3\text{O}_4\text{-NH}_3$) instead of sodium hydroxide ($\text{Fe}_3\text{O}_4\text{-NaOH}$), the average size of the supported gold nanoparticles was found to be significantly different (15 ± 3 nm for $\text{Au/Fe}_3\text{O}_4\text{-NH}_3\text{@Yne}$ and 30 ± 4 nm for $\text{Au/Fe}_3\text{O}_4\text{-NaOH@Yne}$). In the latter case, the larger dimensions of AuNPs could be tentatively explained by the presence, even after the organic functionalisation, of a higher concentration of adsorbed OH^- groups on the magnetite surface, responsible for the further aggregation of gold nanoparticles.

Contrary to what previously observed for other oxide supports, i.e. SiO_2 , Al_2O_3 and TiO_2 , the addition of HAuCl_4 to bare magnetite resulted in the immobilisation of AuNPs, though much larger aggregates were observed in this case (av. AuNPs diameters: 74 ± 20 nm for $\text{Au/Fe}_3\text{O}_4\text{-NH}_3$ and 42 ± 8 nm for $\text{Au/Fe}_3\text{O}_4\text{-NaOH}$).

On the base of the obtained results, the most appealing perspectives for future development of the present research activities will concern the use of these nanocomposites in heterogeneous catalysis, exploiting their magnetic nature for an easy and efficient separation of the catalyst from the reaction mixture.

5.4 Experimental section

5.4.1 Materials

Iron(II) heptahydrate sulphate ($\text{Fe}_2\text{SO}_4 \cdot 5\text{H}_2\text{O}$, 95%), sodium hydroxide (NaOH) and triethylamine (TEA, 99%) were purchased from Carlo Erba. Hydrochloric acid (HCl, 37 %), nitric acid (HNO_3 , 65 %), iron(III) pentahydrate sulphate ($\text{Fe}_2(\text{SO}_4)_3 \cdot 5\text{H}_2\text{O}$, 97%), ammonia (NH_3 , 28-30 %, $d = 0.9 \text{ g/cm}^3$) were purchased from Sigma-Aldrich. Toluene was dehydrated by distillation under nitrogen on Na/K amalgam and stored under nitrogen on 4 Å molecular sieves. PPTEOS was synthesized as previously described in Chapter 2 and chloroauric acid ($\text{HAuCl}_4 \cdot 3\text{H}_2\text{O}$) was prepared following a literature procedure.⁵⁴ Ultrapure water purified with the Milli-Q plus system (Millipore Co, resistivity over 18 MΩ cm) was used in all cases.

5.4.2 Synthesis of $\text{Fe}_3\text{O}_4\text{-NH}_3$ and $\text{Fe}_3\text{O}_4\text{-NaOH}$

The synthesis of $\text{Fe}_3\text{O}_4\text{-NH}_3$ was carried out following a previous protocol.⁵⁵

$\text{FeSO}_4 \cdot 7\text{H}_2\text{O}$ (2.788 g, 0.010 mol) and $\text{Fe}_2(\text{SO}_4)_3 \cdot 5\text{H}_2\text{O}$ (5.131 g, 0.010 mol) were dissolved in 100 mL of water and the yellow-orange solution was degassed with three vacuum/nitrogen purging cycles. Subsequently, an excess of ammonia (13.0 mL, 0.200 mol) was added dropwise, up to a final pH value of 10.4.⁵⁶ The black suspension was then continuously stirred for 2 h at 60 °C and finally cooled down to room temperature. Magnetic nanoparticles were first separated from the supernatant solution using an external magnet and then thoroughly washed with water and ethanol, dried at 60 °C and then under vacuum for 12 h. The final material (2.220 g, yield = 96%) was stored under nitrogen.

The synthesis of $\text{Fe}_3\text{O}_4\text{-NaOH}$ was carried out following the same procedure, by dropwise addition of a stoichiometric 1.0 M solution of NaOH (80 mL, 0.08 mol) to the water mixture of Fe(II) and Fe(III) sulphates, reaching a final pH of 13.4. The obtained material (2.199 g, yield = 95%) was stored under nitrogen.

5.4.3 Synthesis of $\text{Fe}_3\text{O}_4\text{-NH}_3\text{@Yne}$ and $\text{Fe}_3\text{O}_4\text{-NaOH@Yne}$

In a typical procedure, Fe_3O_4 (1.011 g), toluene (10 mL) and TEA (20 μL, 0.14 mmol) were mixed with PPTEOS (0.499 g, 1.65 mmol) dissolved in toluene (20 mL) under

vigorous stirring. The reaction mixture was stirred for 23 h at 60 °C, and subsequently maintained at 100 °C for 1 h. The obtained **Fe₃O₄@Yne** was magnetically separated by the supernatant and then washed three times (3x20 mL) with toluene. The samples were first dried at 60 °C for 12 h and then kept under vacuum to remove the residual solvent, finally yielding 0.888 g of black powder.

5.4.4 Synthesis of **Au/Fe₃O₄-NH₃@Yne** and **Au/Fe₃O₄-NaOH@Yne**

In a 500 mL three-necked round bottom flask under nitrogen atmosphere, a suspension of 0.897 g of **Fe₃O₄@Yne** in 50 mL H₂O was heated to 90 °C. Subsequently, a solution of HAuCl₄·3H₂O (0.088 g, 0.22 mmol) in 170 mL of water was rapidly added, in order to have a 1.00 mM final concentration of chloroauric acid. After stirring for 1 h, the obtained **Au/Fe₃O₄@Yne** was magnetically separated from the colorless supernatant solution, thoroughly washed three times with water, and dried at 60 °C for 12 h and finally under vacuum. The brownish-black powder (0.80 g) was stored under nitrogen. The synthesis of **Au/Fe₃O₄** was performed following the same procedure but using bare magnetite.

5.4.5 Instruments and methods

TEM analyses were performed by a TECNAI F20 FEG apparatus operated both in transmission (TEM) and in scanning mode (STEM) at 200 keV. For the target analysis, samples were dispersed in isopropyl alcohol and sonicated for 15 min. A few drops of the solution were then deposited on a holey carbon film supported by a copper grid and dried at 80 °C. High Angle Annular Dark Field (HAADF, Z contrast) images were formed by collecting only Rutherford scattered electrons with an annular dark-field detector. The image intensity is proportional to the mean atomic number Z^2 and the thickness t .⁵⁷

$$I(x, y) \propto Z^2$$

ATR-FTIR analysis were performed with a Perkin Elmer Spectrum Two spectrophotometer, equipped with an Universal ATR accessory, in the range 4000-400 cm⁻¹, with a resolution of 0.5 cm⁻¹. Pristine and modified Fe₃O₄ powders were directly analyzed after being ground in a mortar performing 40 scans for each analysis.

XRD was performed by a Philips X'Pert Pro instrument equipped with a fast X'Celerator detector, working at 40 mA and 40 kV and using CuK α radiation. For phase identification, the 2 θ angle range was from 10° to 80° (step size 0.1°; time/step 100 seconds). The peak broadening was used to evaluate the crystal size (τ_{hkl}), which was calculated from the widths at half maximum intensity ($\beta_{1/2}$) using the Scherrer equation:⁵⁸

$$\tau_{hkl} = \frac{k \lambda}{\beta_{1/2} \cos\theta}$$

where λ is the wavelength, θ the diffraction angle and K a constant depending on crystal habit (chosen as 1). For crystal size calculation, the most intense reflections for each crystalline phase were taken into consideration. i.e. peak (310) for magnetite and (111) for Au.

Zeta potential was measured using Electrophoretic Light Scattering (ZetasizerNano; Malvern Instruments). In each analysis, 5 mg of powder sample were suspended in 50 mL of a 10 mM NaCl solution and sonicated for 4 minutes before measurement. Each analysis was performed in triplicate.⁴¹

TGA characterization was carried out using a Perkin Elmer TGA-7 instrument. In each analysis, 5–10 mg of the target sample was heated in a platinum crucible from room temperature to 900 °C, at a rate of 10 °C/min.

The overall amount of gold present on the different samples was determined by means of flame atomic absorption spectroscopy (AAS, Thermo Scientific) in air-acetylene flame with a wavelength of 242.8 nm and a spectral band width of 0.5 nm. The analyses were conducted by comparison with six calibration standards (2.0, 4.0, 6.0, 8.0, 10.0 ppm) prepared by dilution to 50 mL of different amounts of a concentrated HAuCl₄·3H₂O aqueous solution (100 ppm). The samples of **Au/Fe₃O₄@Yne** and **Au/Fe₃O₄** were prepared by dissolving the solid (ca. 10 mg) in 2 mL of aqua regia under sonication. Subsequently, the solution was diluted with HCl 0.5 M up to a final volume of 50 mL.

X-ray photoelectron spectroscopy (XPS) analyses were conducted on a Perkin-Elmer Φ 5600ci spectrometer using a standard AlK α excitation source ($h\nu = 1486.6$ eV), at a working pressure lower than 10⁻⁸ mbar. The reported binding energies (BEs; uncertainty ± 0.1 eV) were corrected for charging effects by assigning a BE of 284.8 eV to the C1s line of adventitious carbon.⁵⁹ After a Shirley-type background subtraction,⁶⁰ atomic percentages (at. %) were calculated by signal integration using Perkin-Elmer

sensitivity factors (Φ V5.4A). Whenever necessary, peak fitting was performed adopting Gaussian–Lorentzian peak shapes by means of the XPS Peak software (version 4.1).⁶¹

A custom-built Faraday magnetometer was used to measure the sample specific moment σ (i.e. the magnetic moment per unit mass) as a function of the applied field at 300 K.⁶² The magnetometer is based on a Sartorius ME235S analytical balance and a NdFeB permanent magnet, with a maximum applied magnetic field of approximately 0.12 T. The experimental uncertainties were calculated based on the performance of the Faraday magnetometer. For the value of $\sigma_{1000 \text{ Oe}}$, an uncertainty of 5 % of the measured value was considered, while for the M_r and H_c an uncertainty of 12 % of the measured values was used. For the uncertainty on the $M_r/\sigma_{1000 \text{ Oe}}$ ratio, the rule of the composition of uncertainties was applied:

$$\Delta\left(\frac{M_r}{\sigma_{1000 \text{ Oe}}}\right) = \sqrt{\left(\frac{1}{\sigma_{1000 \text{ Oe}}} \Delta M_r\right)^2 + \left(\frac{M_r}{\sigma_{1000 \text{ Oe}}^2} \Delta \sigma_{1000 \text{ Oe}}\right)^2}$$

where $\Delta\left(\frac{M_r}{\sigma_{1000 \text{ Oe}}}\right)$ is the uncertainty on the $M_r/\sigma_{1000 \text{ Oe}}$, ΔM_r is the uncertainty on M_r and $\Delta \sigma_{1000 \text{ Oe}}$ is the uncertainty on the specific moment at 1000 O.

References

- ¹ L. M. Rossi, N. J. S. Costa, F. P. Silva, R. Wojcieszak, *Green Chem.*, **2014**, *16*, 2906.
- ² S. Blundell, *Magnetism in Condensed Matter*, Oxford University Press, Oxford, **2001**.
- ³ D. Jiles, *Introduction to Magnetism and Magnetic Materials*, CRC Press, London, **1998**.
- ⁴ D. S. Mathew, R. S. Juang, *Chem. Eng. J.*, **2007**, *129*, 51.
- ⁵ M. Usman, J. M. Byrne, A. Chaudhary, S. Orsetti, K. Hanna, C. Ruby, A. Kappler, S. B. Haderlein, *Chem. Rev.*, **2018**, *118*, 3251.
- ⁶ L. Wu, A. Mendoza-Garcia, Q. Li, S. Sun, *Chem. Rev.*, **2016**, *116*, 10473.
- ⁷ S. Shylesh, V. Schunemann, W. R. Thiel, *Angew. Chem. Int. Ed.*, **2010**, *49*, 3428.
- ⁸ J. Govan, Y. K. Gun'ko, *Nanomaterials*, **2014**, *4*, 222.
- ⁹ D. Wang, C. Deraedt, J. Ruiz, D. Astruc, *Acc. Chem. Res.*, **2015**, *48*, 1871.
- ¹⁰ L. H. Reddy, J. L. Arias, J. Nicolas, P. Couvreur, *Chem. Rev.*, **2012**, *112*, 5818.
- ¹¹ N. A. Frey, S. Peng, K. Cheng, S. H. Sun, *Chem. Soc. Rev.*, **2009**, *38*, 2532.
- ¹² D. Weller, O. Mosendz, G. Parker, S. Pisana, T. S. Santos, *Phys. Status Solidi A*, **2013**, *210*, 1245.
- ¹³ C. Su, *J. Hazard. Mater.*, **2017**, *322*, 48.
- ¹⁴ P. Berger, N. B. Adelman, K. J. Beckman, D. J. Campbell, A. B. Ellis, *J. Chem. Educ.*, **1999**, *76*, 943.
- ¹⁵ K. M. Krishnan, A. B. Pakhomov, Y. Bao, P. Blomqvist, Y. Chun, M. Gonzales, K. Griffin, X. Ji, B. K. Roberts, *J. Mater. Sci.*, **2006**, *41*, 793.
- ¹⁶ A. Lu, E. L. Salabas, F. Schuth, *Angew. Chem. Int. Ed.*, **2007**, *46*, 1222.
- ¹⁷ J. Lee, T. Isobe, M. Senna, *Colloids Surf. A*, **1996**, *109*, 121.
- ¹⁸ S. Sun, H. Zeng, D. B. Robinson, S. Raoux, P. M. Rice, S. X. Wang, G. Li, *J. Am. Chem. Soc.*, **2004**, *126*, 273.
- ¹⁹ F. X. Redl, C. T. Black, G. C. Papaefthymiou, R. L. Sandstrom, M. Yin, H. Zeng, C. B. Murray, S. P. O'Brien, *J. Am. Chem. Soc.*, **2004**, *126*, 14583.
- ²⁰ L. Harivardhan Reddy, J. L. Arias, J. Nicolas, P. Couvreur, *Chem. Rev.*, **2012**, *112*, 5818.
- ²¹ H. Itoh, T. Sugimoto, *J. Colloid Interface Sci.*, **2003**, *265*, 283.
- ²² S. Mathur, S. Barth, U. Werner, F. Hernandez-Ramirez, A. Romano-Rodriguez, *Adv. Mater.*, **2008**, *20*, 1550.
- ²³ F. Chen, Q. Gao, G. Hong, J. Ni, *J. Magn. Magn. Mater.*, **2008**, *320*, 1775.

-
- ²⁴ L. Cabrera, S. Gutierrez, N. Menendes, M. P. Morales, P. Herrasti, *Electrochem. Acta*, **2008**, *53*, 3436.
- ²⁵ F. Dang, N. Enomoto, J. Hojo, K. Enpuku, *Ultrason. Sonochem.*, **2009**, *16*, 649.
- ²⁶ J. Wang, S. Han, D. Ke, R. Wang, *J. Nanomater.*, **2012**, *1*, 1.
- ²⁷ L. Zhang, R. He, H. C. Gu, *Appl. Surf. Sci.*, **2006**, *253*, 2611.
- ²⁸ L. M. Rossi, L. L. R. Vono, F. P. Silva, P. K. Kiyohara, E. L. Duarte, J. R. Matos, *Appl. Catal. A*, **2007**, *330*, 139.
- ²⁹ S. H. Gage, B. D. Stein, L. Z. Nikoshvili, V. G. Matveeva, M. G. Sulman, E. M. Sulman, D. G. Morgan, E. Y. Yuzik-Klimova, W. E. Mahmoud, L. M. Bronstein, *Langmuir*, **2012**, *29*, 466.
- ³⁰ Z. F. Wang, B. Shen, A. H. Zou, N. Y. He, *Chem. Eng. J.*, **2005**, *113*, 27.
- ³¹ D. K. Yi, S. S. Lee, J. Y. Ying, *Chem. Mater.*, **2006**, *18*, 2459.
- ³² L. M. Rossi, I. M. Nangoi, N. J. S. Costa, *Inorg. Chem.*, **2009**, *48*, 4640.
- ³³ B. Ballarin, M. C. Cassani, D. Nanni, C. Parise, D. Barreca, G. Carraro, A. Riminucci, I. Bergenti, V. Morandi, A. Migliori, E. Boanini, *Ceram. Int.*, **2019**, *45*, 449, <https://doi.org/10.1016/j.ceramint.2018.09.188>.
- ³⁴ B. Ballarin, D. Barreca, E. Boanini, M.C. Cassani, P. Dambrosio, A. Massi, A. Mignani, D. Nanni, C. Parise, A. Zaghi, *ACS Sust. Chem. Eng.*, **2017**, *5*, 4746.
- ³⁵ E. Aghaei, R.D. Alorro, A.N. Encila, K. Yoo, *Metals*, **2017**, *7*, 1.
- ³⁶ R.D. Alorro, N. Hiroyoshi, H. Kijitani, M. Ito, M. Tsunekawa, *Miner. Process. Extr. Metall. Rev.*, **2010**, *31*, 201.
- ³⁷ R.B.N. Baig, R.S. Varma, *Chem. Commun.*, **2012**, *48*, 6220.
- ³⁸ R.Y. Hong, J.H. Li, H.Z. Li, J. Ding, Y. Zheng, D.G. Wei, *J. Magn. Magn. Mater.*, **2008**, *320*, 1605.
- ³⁹ X.C. Yang, Y.L. Shang, Y.H. Li, J. Zhai, N.R. Foster, Y.X. Li, D. Zou, Y. Pu, *J. Nanomater.*, **2014**, *2014*, 1.
- ⁴⁰ H. Iida, K. Takayanagi, T. Nakanishi, T. Osaka, *J. Colloid Interface Sci.*, **2007**, *314*, 274.
- ⁴¹ R. A. Bini, R. F. C. Marques, F. J. Santos, J. A. Chaker, M. Jafelicci, *J. Magn. Mater.*, **2012**, *324*, 534.
- ⁴² M. Khoobi, T. M. Delshad, M. Vosooghi, M. Alipour, H. Hamadi, E. Alipour, M. P. Hamedani, Seyed E. Sadatebrahimi, Z. Safaei, A. Foroumadi, A. Shafie, *J. Magn. Magn. Mater.*, **2015**, *375*, 217.

-
- ⁴³ X. Jiang, J. Hua, H. Deng, Z. Wu, *J. Mol. Catal. A Chem.*, **2014**, 383, 188.
- ⁴⁴ M.E.A. Warwick, D. Barreca, E. Bontempi, G. Carraro, A. Gasparotto, C. Maccato, K. Kaunisto, T.-P. Ruoko, H. Lemmetyinen, C. Sada, Y. Gönüllü, S. Mathur, *Phys. Chem. Chem. Phys.*, **2015**, 17, 12899.
- ⁴⁵ <https://srdata.nist.gov/xps>
- ⁴⁶ J. F. Moulder, W. F. Stickle, P. E. Sobol, K. D. Bomben, *Handbook of X-ray Photoelectron Spectroscopy*, Perkin Elmer Corporation, Eden Prairie, MN., **1992**.
- ⁴⁷ R. Y. Hong, J. H. Li, H. Z. Li, J. Ding, Y. Zheng, D. G. Wei, *J. Magn. Magn. Mater.*, **2008**, 320, 1605.
- ⁴⁸ K. M. Krishnan, A. B. Pakhomov, Y. Bao, P. Blomqvist, Y. Chun, M. Gonzales, K. Griffin, X. Ji, B. K. Roberts, *J. Mater. Sci.*, **2006**, 41, 793.
- ⁴⁹ F. Heider, D. J. Dunlop, N. Sugiura, *Science*, **1987**, 236, 1287.
- ⁵⁰ J. S. Lee, J. M. Cha, H. Y. Yoon, J. K. Lee, Y. K. Kim, *Sci. Rep.*, **2015**, 5, 1.
- ⁵¹ S. Sun, H. Zeng, D. B. Robinson, S. Raoux, P. M. Rice, S. X. Wang, G. Li, *J. Am. Chem. Soc.*, **2004**, 126, 273.
- ⁵² S. H. Gee, Y. K. Hong, D. W. Erickson, M. H. Park, J. C. Sur, *J. Appl. Phys.* **2003**, 93, 7560.
- ⁵³ G. F. Goya, T. S. Berquó, F. C. Fonseca, M. P. Morales, *J. Appl. Phys.*, **2003**, 94, 3520.
- ⁵⁴ G. Braurer, *Handbook of Preparative Inorganic Chemistry*; Academic Press: New York, **1963**, Vol. II, 1058.
- ⁵⁵ R. B. N. Baig, R. S. Varma, *Chem. Commun.*, **2012**, 48, 6220.
- ⁵⁶ P. Berger, N. B. Adelman, K. J. Beckman, D. J. Campbell, A. B. Ellis, G. C. Lisensky, *J. Chem. Educ.*, **1999**, 76, 943.
- ⁵⁷ S.J. Pennycook, P.D. Nellist, eds., *Scanning Transmission Electron Microscopy*, Springer Science+Business Media, **2011**. doi:10.1007/978-1-4419-7200-2_2.
- ⁵⁸ H. P. Klug, L. E. Alexander, *X-ray diffraction procedures for polycrystalline and amorphous materials*; Wiley-Interscience, New York, 2nd edn. 1974.
- ⁵⁹ D. Briggs, M. P. Seah, *Practical Surface Analysis: Vol. 1, Auger and X-ray Photoelectron Spectroscopy*, Wiley, New York, 1990.
- ⁶⁰ L. Armelao, D. Barreca, G. Bottaro, A. Bovo, A. Gasparotto, E. Tondello, *Surf. Sci. Spectra.*, **2003**, 10, 1.
- ⁶¹ <http://xpspeak.software.informer.com/4.1/>
- ⁶² A. Riminucci, M. Uhlarz, R. De Santis, T. Herrmannsdörfer, *J. Appl. Phys.*, **2017**, 121, 94701.

6. SYNTHESIS AND CHARACTERISATION OF ZEOLITIC IMIDAZOLATE FRAMEWORK-8 BICOMPOSITES

6.1 Introduction

6.1.1 An overview on metal organic frameworks

Metal organic frameworks (MOFs) are a class of porous crystalline materials constituted of ordered networks formed by metal cations and organic electron donor linkers. The self-assembly of these components leads to the formation of a rigid porous structure that is stable upon removal of solvent or other “guest” molecules occupying the pores after the synthesis. The presence of both inorganic and organic components allows to modulate the pore size and the chemical environment, in order to achieve specific properties.¹ Indeed, the easy modulation of pore size and functionality, in addition to the high surface areas and the possibility to encapsulate a large variety of molecules inside the pores, have made this type of materials excellent candidates for a series of applications in gas storage and separation,^{2,3} catalysis,^{4,5,6} sensing,^{7,8,9} non-linear optics,¹⁰ drug delivery,^{11,12,13} etc.¹⁴

To date, one of the most widely studied MOF is zeolitic imidazolate framework-8 (ZIF-8), which is a three-dimensional network composed of tetrahedral Zn(II) nodes linked together *via* 2-methylimidazole (2-MIM) ligands (Figure 6.1).

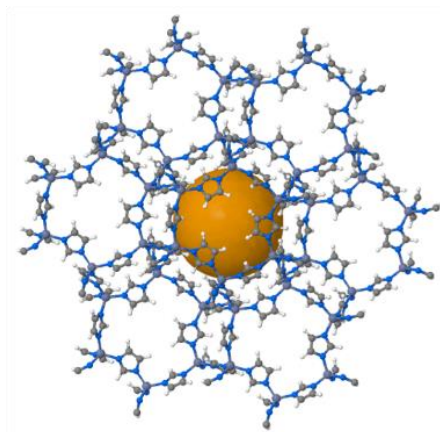


Figure 6.1. ZIF-8 structure, in which the sphere represents the pore size within the framework.¹⁵

Yaghi *et al.* were the firsts to report the preparation of a series of zeolitic imidazolate frameworks by copolymerization of metal ions, such as Zn(II) and Co(II), with imidazolate-type linkers.¹⁶ In particular, the synthesis was carried out by a solvothermal method in which a solution of the hydrated metal salt and the imidazole ligand in N,N-diethylformamide was heated (85 – 150 °C) for 48 – 96 h. The obtained ZIF-8 crystals displayed a sodalite (*sod*) like structure¹⁷ with pore size of 11.6 Å, surface area of 1.947 m²/g and pore volume of 0.663 cm³/g (Figure 6.2).

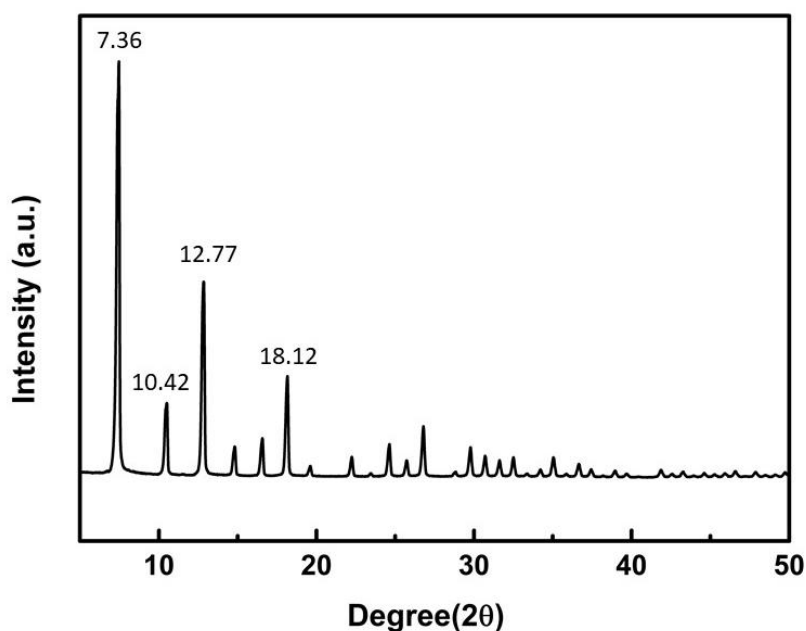


Figure 6.2. X-ray diffraction patter of *sod*-ZIF-8.

Furthermore, the exceptional thermal stability (up to 550 °C) and chemical resistance of these materials was also proved, paving the way for their potential application in many technological fields.

However, the long reaction times and the use of large amounts of expensive organic solvents involved in traditional synthetic procedures, pose a serious limit to the production of ZIF-8, and in general of MOFs, at the industrial scale. For this reason, many efforts have been directed towards the development of alternative methods that require shorter reaction times and lower volumes of solvent.

In this regard, the microwave synthesis of MOFs enables to effectively reduce reaction times, thanks to the enhanced heating efficiency, and to achieve a high control on the properties of the final product.^{18,19,20} For example, the variation of temperature and reaction times allowed to control the crystal phase formation of Cu-1,3,5-

benzotriacarboxylate (BTC) MOFs and to synthesize a CuBTC with higher surface area compared to that produced by classic solvothermal synthesis.²¹

Another method for the production of small MOF crystals with decreased reaction times is sonochemical synthesis, based on the formation and collapse of bubbles in solution that generates very high local temperatures and pressures.¹ For instance, MOF-5 was synthesized with sonochemical irradiation in 1-methyl-2-pyrrolidinone to produce 5 – 25 μm crystals in only 30 min.²²

Even though the microwave and sonochemical methods allow to efficiently reduce reaction times, the use of solvents is still required. On the contrary, mechanochemical synthesis is a solvent-free strategy in which a neat mixture of metal and ligand precursors are grounded together to obtain the desired MOF.²³ In a variation of this methodology Friscic et al. reported a liquid-assisted grinding (LAG) in which a very small amount of solvent was added to the reaction mixture to promote reactivity. In addition, by varying the solvent added to a mixture of fumaric acid and ZnO they were able to obtain several different structures.²⁴

6.1.2 Biomimetic mineralisation of zeolitic imidazolate framework-8

One of the most interesting applications of ZIF-8 is in the field of biomedicine and drug delivery, since they are characterised by a remarkable loading capacity, a high stability in physiological environment and tunable drug release properties. On this purpose, the high surface area and porosity of ZIF-8 can be exploited to efficiently immobilise biomacromolecules, such as proteins, sugars and DNA, cells, antibodies and drugs.^{25,26} Furthermore, recent studies on the suitability of these materials for *in vivo* applications indicated that low ZIF-8 concentrations (< 30 g/mL) assure biocompatibility characteristics.²⁷

The formation of MOFs biocomposites can be carried out following three main approaches: 1) *bioconjugation*, defined as the adsorption or covalent attachment of a biomacromolecule on the outer surface of MOF crystals (Figure 6.3a), 2) *infiltration*, which consists in the insertion of biomolecules into the pores networks through non-covalent interactions (Figure 6.3b) and 3) *encapsulation*, obtained by assembling the MOF under biologically compatible reaction conditions in a medium containing the biomacromolecule (Figure 6.3c).²⁸

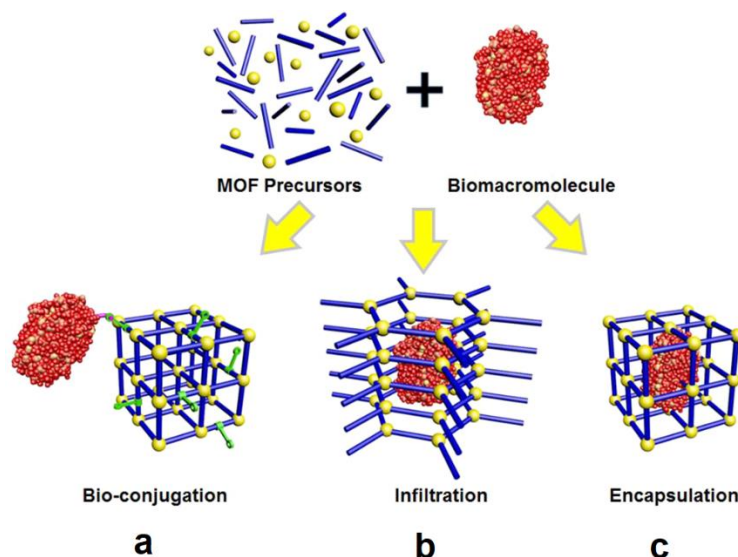


Figure 6.3. Formation of MOFs biocomposites.²⁸

In particular, the third methodology allows to encapsulate molecules within MOFs with pores significantly smaller than the guest.²⁹ In this regard, Falcaro *et al.* recently reported the efficient encapsulation of a series of biomacromolecules, including bovine serum albumin (BSA), human serum albumin (HSA), lipase, insulin and oligonucleotides, within ZIF-8 by a one-pot *biomimetic mineralisation* process.³⁰ This study showed how some biomacromolecules can induce the formation and control the morphology of zeolitic imidazolate frameworks under physiological conditions, similarly to the biomineralisation process which spontaneously occurs in nature in many living organisms (Figure 6.4).

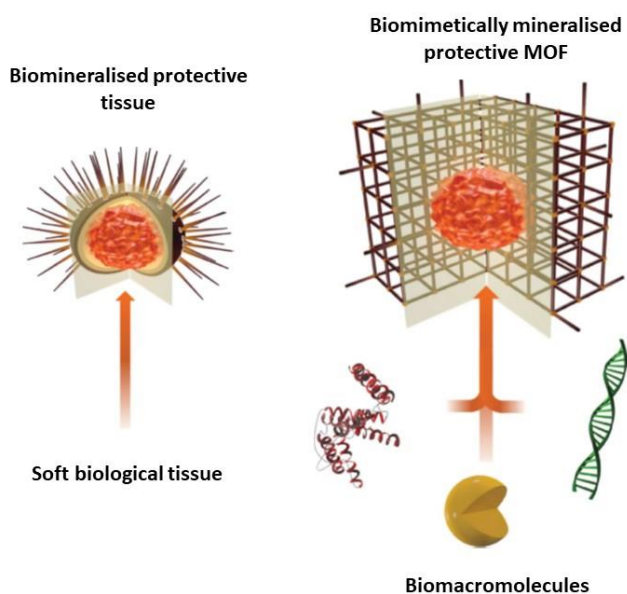


Figure 6.4. Biomimetic mineralisation.³⁰

The synthesis was carried out in aqueous media at room temperature and the formation of the biocomposites occurred almost instantaneously as suggested by the colour change of the reaction mixture, which rapidly turned from transparent to opaque. The resulting ZIF-8 biocomposites were found to be stable under conditions that would normally decompose many biological macromolecules, indicating how the MOF structure provides enhanced stability. Furthermore, the controlled release of the bioactive molecules was achieved by simple pH modification.

In a subsequent work published by the same group, the possibility to control the crystal phase of ZIF-8 biocomposites was examined by changing some parameters such as 2-MIM/Zn ratio and reagents concentration.³¹ Indeed, a number of experimental and theoretical studies have shown that the sodalite structure is only one of the many energetically accessible polymorphs for networks constituted of Zn(II) and 2-methylimidazole building units.^{32,33,34,35} Since different topologies possess different properties, it would be of great importance to develop synthetic procedures for the preparation of structures with an identified crystal phase. The results obtained by Falcaro *et al.* with a **BSA@ZIF-8** composite (bovine serum albumin encapsulated in a ZIF-8 matrix) indicated that the concentration of the metal and ligand precursors played a dominant role in the resulting ZIF-8 structure topology, with dilute or ligand-deficient ratios yielding less desirable dense phases such as diamondoid (*dia*) and amorphous (*amorph*) (Figure 6.5).

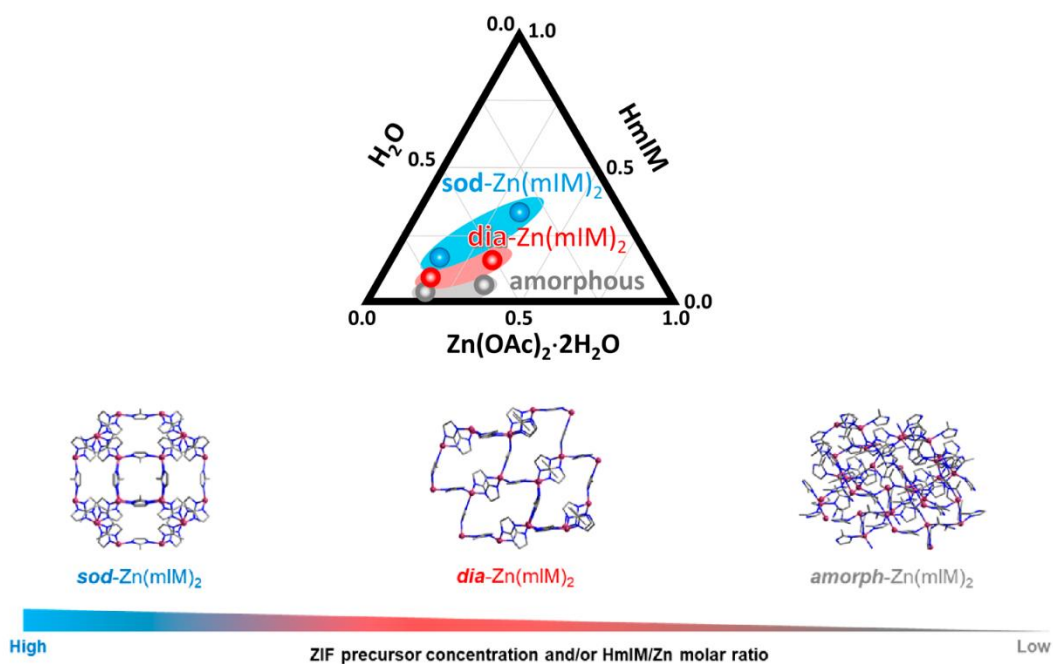


Figure 6.5. Control of structural topology of BSA@ZIF-8 composites.³¹

6.1.3 The importance of size control

In the field of biomedicine and drug delivery, monodispersity of size and shape is a fundamental factor that defines the toxicity, biodistribution and drug release properties of ZIF-8 biocomposites. Indeed, the literature provides extensive evidence that a specific formulation is required for a given administration route. For instance, the intravenous administration requires highly stable suspensions of small (≤ 200 nm) and homogeneous nanoparticles, while the ideal particle size for cancer treatments is between 70 and 200 nm.^{36,37}

The formation of crystals in solution involves a nucleation stage and a growth stage (Figure 6.6). According to La Mer *et al.* the production of monodispersed particles is obtained when a temporally discrete nucleation occurs, followed by a slow controlled growth of the formed nuclei.³⁸

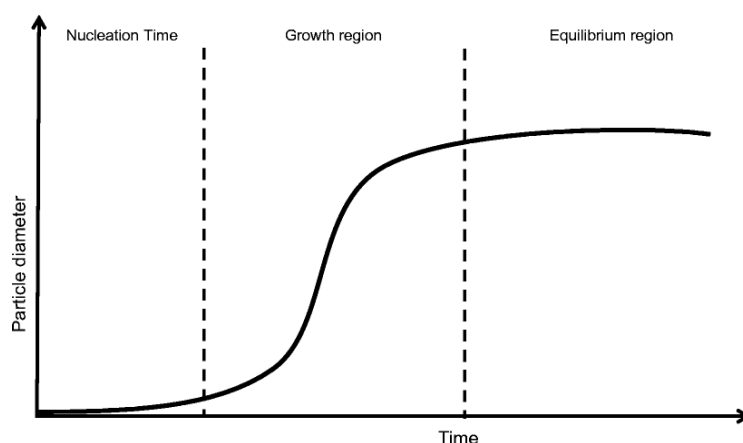


Figure 6.6. Kinetic of particle formation.

The common strategy for the size control of the crystals consists in the addition of crystal size modulators, which are capping ligands that can coordinate to the metal ions. When the addition of these capping agents occurs during the nucleation stage, their coordination to free metal ions results in a decrease in the concentration of metal ions that can be used for the formation of the nuclei, thus decreasing the rate of nucleation and resulting in bigger particles. On the contrary, if the modulating ligand coordinates metal ions on the surface of a growing particle, the growth is inhibited and smaller particles are obtained. As a consequence, the time of addition and the concentration of the crystal size modulator play a fundamental role in the definition of the resulting particle size.³⁹

In the synthesis of ZIF-8, the addition of 1-methylimidazole (1-MIM) has been reported to influence the nucleation and crystal growth to a large extent, since 1-MIM does not work as a linker in the ZIF-8 structure and yet works as a competitive ligand.^{40,41}

Besides, the use of surfactants, such as cetyl trimethylammonium bromide (CTAB) and poly(diallyldimethylammonium) chloride (polyDADMACl), as size modulators was also described. In this case, the effect of the modulator on the particle growth is associated to the steric hindrance provided by the surfactant structure.^{42,43}

Finally, in the case of ZIF-8, the control of particles size is often achieved by simply varying the ration between 2-MIM and Zn(II) ions, without the need of an additional size modulator. Tan *et al.* recently described the successful tailoring of ZIF-8 particle size by manipulating the 2-methylimidazole concentration in the reaction mixture. In particular in the first stages of the reaction (< 2 min), a high molar ratio of 1/70 yielded smaller size crystals than the lower molar ratio 1/8, due to the fast deprotonation of 2-MIM and consequent formation of more nuclei. However, the particle size of ZIF-8 synthesised at higher 2-MIM concentration was eventually bigger than that of lower concentration at prolonged reaction time (≥ 2 min) as more deprotonated imidazolate was available for the particle growth.⁴⁴

6.1.4 Synthesis of BSA@ZIF-8 biocomposites in continuous-flow conditions

As briefly discussed previously, the development of synthetic procedures for the preparation of MOFs at a large scale is currently a key issue for their commercial application. In order for any production process to be industrially viable a number of key aspects have to be considered: 1) the versatility of the method, in order to produce the maximum number of MOF structures with the same piece of equipment, 2) the possibility to avoid harsh processing conditions, such as high temperature and pressure, thus reducing capital and operating costs and alleviating safety concerns, and 4) a high space-time yield, which measures the amount of MOF produced per volume of reaction mixture per day.

In this sense, flow chemistry is one of the most recent and promising technologies exploited in the synthesis of MOFs. Indeed, a switch from batch to continuous processing would be beneficial offering higher output per unit time and a continuous steady-state operation leading to significantly reduced downtimes, labour costs, reactor volumes, as well as constant and consistent production.⁴⁵

Recently, Kaskel *et al.* reported the continuous-flow synthesis of ZIF-8 employing a T-type micromixer connected to an additional residence time unit to ensure sufficient reaction time (Figure 6.7).⁴⁶ The experiments were carried out in methanol varying the concentration of the starting reagent solutions and the final aging time. In particular, the concentration was found to have an impact on the obtained crystal morphology, while different aging times mainly affected the crystal size.

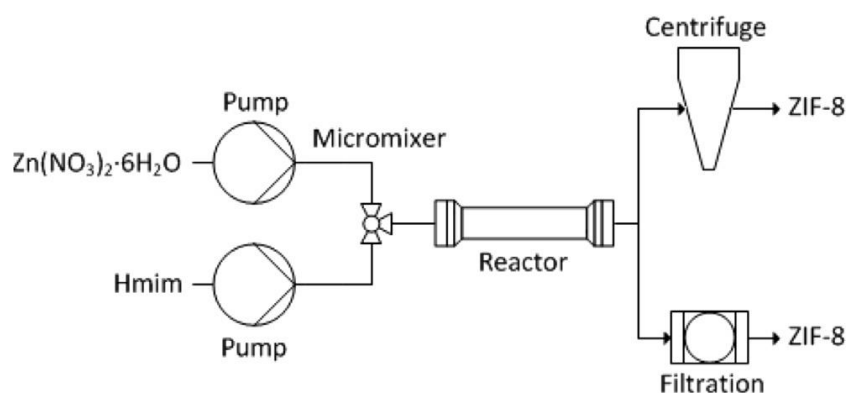


Figure 6.7. Schematic illustration of the experimental setup used by Kaskel *et al.*⁴⁶

Schneider *et al.* described the production of ZIF-8 crystals via continuous processes using either a single water phase or a biphasic water/alkane flow in a three dimensional microchannel (Figure 6.8).⁴⁷ In this way, the fast synthesis (10 min) of ZIF-8 crystals over a wide size range (from ca. 300 to 900 nm) was obtained simply by varying the experimental parameters (flow rates, temperature, residence time) while maintaining the high specific surface of this material (ca. $1700 \text{ m}^2 \text{ g}^{-1}$) and the sodalite crystalline structure.

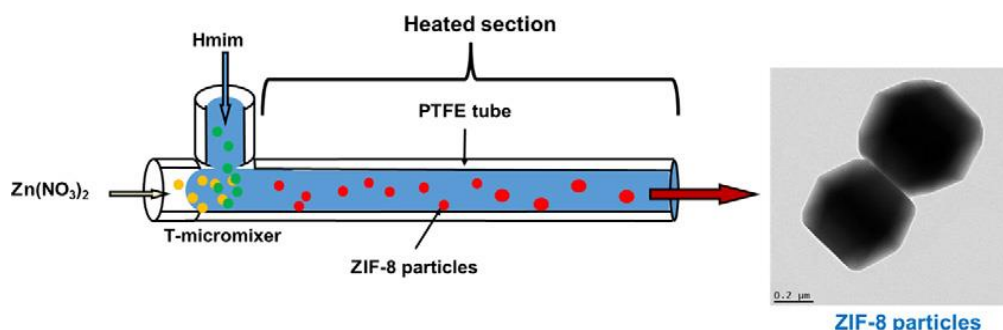


Figure 6.8. Schematic illustration of the experimental setup used by Schneider *et al.*⁴⁷

Finally, Watanabe *et al.* studied the synthesis of ZIF-8 particles of controlled size and shape using a central collision-type microreactor (Figure 6.9).⁴⁸ The size of the

particles produced in this system decreased from 1.8 μm to 51 nm with the increase of the Zn(II) concentration and the ratio of 2-MIM to Zn, or with decrease in the reaction temperature. Furthermore, by taking advantage of the flow microreactor process with high thermal conductivity, the particle size and shape were individually controlled by setting different temperatures in the microreactor and in the collecting vial. Hence, the key factor for the determination of particle size was found to be the mixing process in the microreactor, while for the particle shape the temperature during the aging process in the vial played the dominant role.

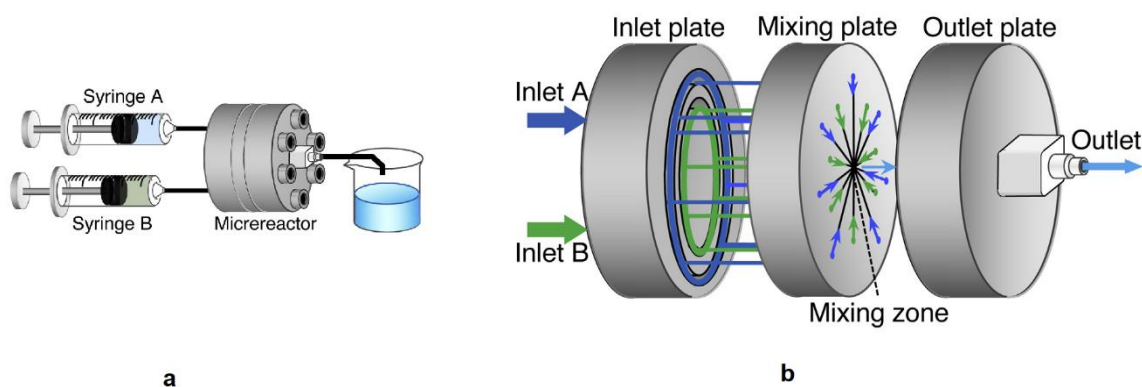


Figure 6.9. Schematic illustration of the a) experimental setup and b) central collision-type microreactor used by Watanabe *et al.*⁴⁸

6.1.5 Aim of the chapter

The work described in the present chapter is part of a project carried out during a six months stay at the Karl-Franzens University of Graz under the supervision of Prof. Oliver Kappe, in close collaboration with the group of Prof. Paolo Falcaro of the Graz University of Technology.

At first, the possibility of tuning the topology of **BSA@ZIF-8** biocomposites was investigated by varying some experimental conditions, such as reagents concentration, 2-MIM/Zn ratio, amount of BSA, stirring and washing procedure.

Then, the synthesis of **BSA@ZIF-8** was carried out in continuous-flow conditions with the aim of tuning the particle size of the obtained material. For this purpose, a series of size modulators, i.e. 1-methylimidazole (1-MIM), cetyl trimethylammonium bromide (CTAB), poly(diallyldimethylammonium) chloride (polyDADMACl) and sodium dodecyl sulphate (SDS) were tested. In addition, *in situ* quenching experiments with ethanol were also carried out.

6.2 Results and discussion

6.2.1 Influence of reaction conditions on the BSA@ZIF-8 topology

Initially, the preparation of **BSA@ZIF-8** composites *via* biomimetic mineralisation was carried out following two previously reported synthetic procedures, hereafter named Recipe A³⁰ and Recipe B,³¹ whose main parameters are summarised and compared in Table 6.1.

Table 6.1. Synthetic protocols for the preparation of **BSA@ZIF-8**.

Recipe	Zn(OAc) ₂ conc (mM) ^a	2-MIM/Zn ^b	BSA conc (mg/mL) ^a
Recipe A	40	4	0.66
Recipe B	80	16	0.66

a) concentration of the premix solution, b) molar ratio.

In both cases, an aqueous solution of zinc acetate Zn(OAc)₂ was rapidly added to an aqueous solution of 2-methylimidazole (2-MIM) and BSA at room temperature. The formation of the **BSA@ZIF-8** composite was confirmed by a rapid change in colour of the reaction mixture, from transparent to white, which occurred after a few seconds from the mixing. Afterwards, the reaction mixture was aged for 24 h in static conditions (without stirring) before proceeding with the isolation and characterisation of the product.

The diffraction patterns of the produced samples were obtained at the Austrian SAXS beamline of the Elettra synchrotron facilities in Trieste (Italy), by measuring simultaneously the small angle x-ray scattering (SAXS) and wide angle x-ray scattering (WAXS). Hereafter, only the latter will be shown, since the majority of the diffraction peaks can be found in the WAXS region.

In accordance with previous results³¹ the variation of the reagents concentration and 2-MIM/Zn ratio resulted in the formation of different crystal phases. In particular, Recipe B (higher concentration and 2-MIM/Zn ratio) afforded a pure sodalite structure, as indicated by the characteristic peaks observed in the WAXS patterns. On the contrary, when Recipe A was used an unknown phase was obtained, whose identification is still under study (Figure 6.10).

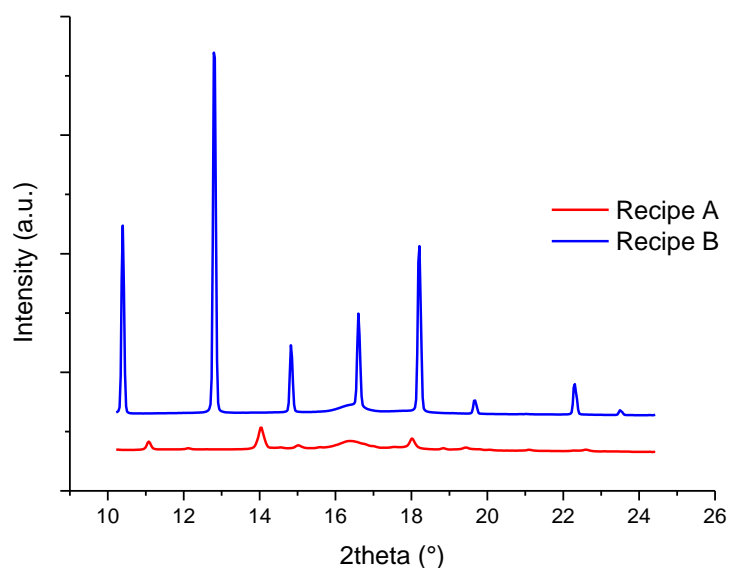
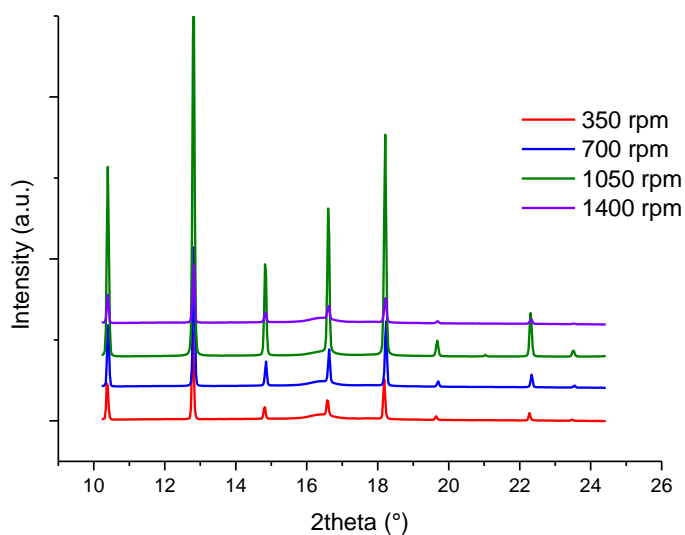


Figure 6.10. WAXS patterns of **BSA@ZIF-8** prepared in static conditions.

Afterwards, the effect of the stirring conditions during the aging step on the crystal phase of the final product were investigated using Recipe B. For this purpose, the stirring was provided both by means of a thermal mixer and by means of a magnetic stir bar, at different stirring speeds. As indicated by the diffraction patterns in Figure 6.11, neither the stirring method nor its intensity influenced the outcome of the reaction in terms of ZIF-8 topology, thus confirming that Recipe B is a completely reliable and highly reproducible procedure for the preparation of a pure sodalite crystal phase.



(a)

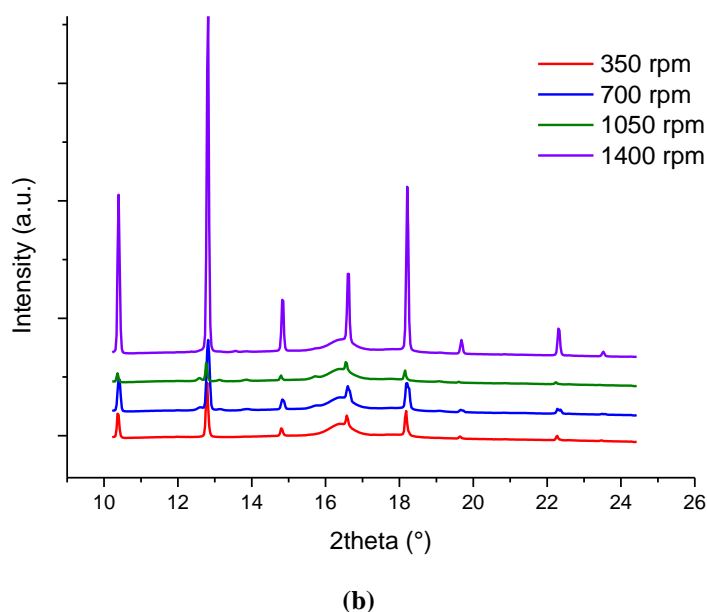
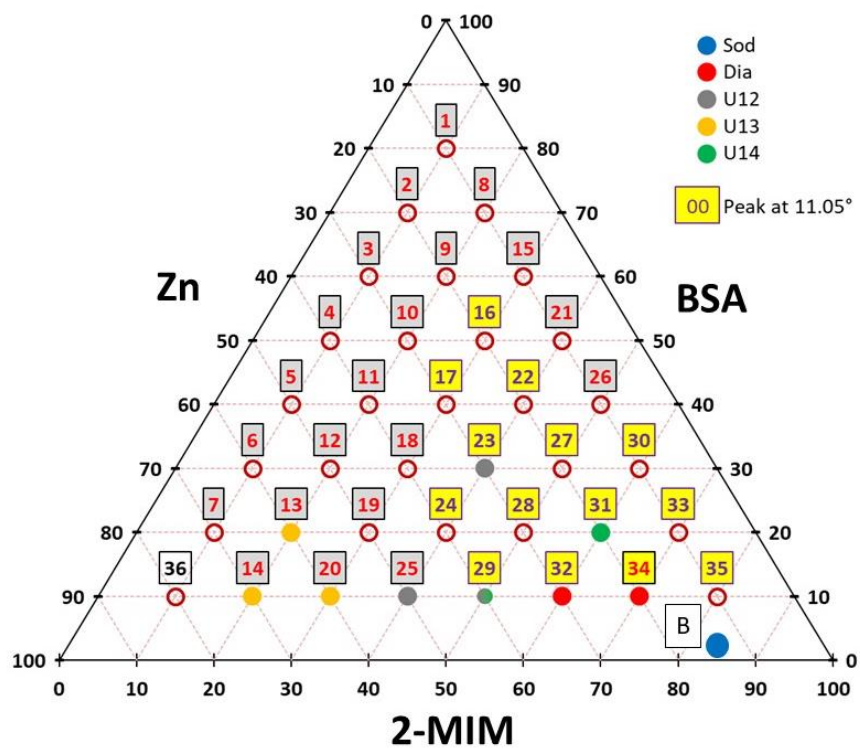


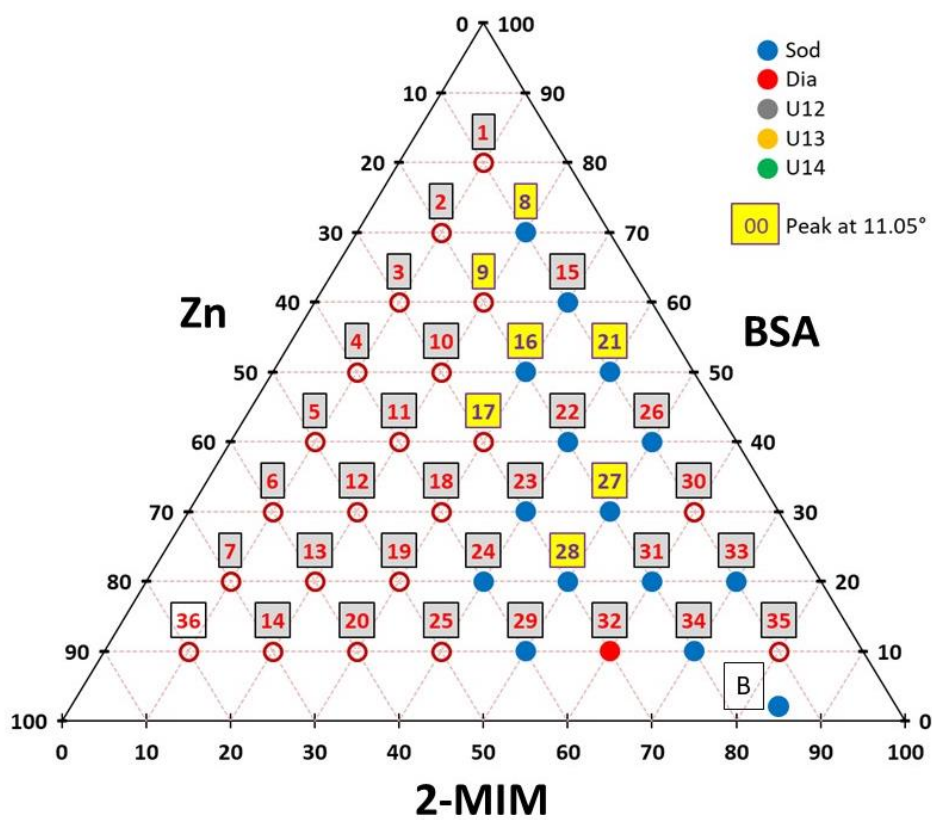
Figure 6.11. WAXS patterns of **BSA@ZIF-8** prepared by stirring with a) thermal mixer and b) magnetic stir bar, at different stirring speeds.

Furthermore, a series of **BSA@ZIF-8** samples with different amounts of BSA were prepared and characterised. The obtained results were collected in a ternary plot, reporting on the x , y and z axis the mass fractions of each component of the reaction mixture, i.e. Zn, 2-MIM and BSA, to obtain a map of the formation of the different crystal phases and amorphous material (Figure 6.12). In particular, five different phases were observed: sodalite (*sod*), diamonoid (*dia*) and three unknown phases labelled as U12, U13 and U14 in reference to literature.³¹ Moreover, the additional peak at 11.05° found in many diffraction patterns could be tentatively attributed to the partial formation of a 2D structure of layered zinc hydroxide.⁴⁹

Interestingly, when the samples were washed only with water, the formation of sodalite was observed only for very low amounts of BSA (Figure 6.12a). On the contrary, when the products obtained in water were washed with ethanol, a phase transition to give sodalite was observed in many of the samples (Figure 6.12b). Although a clear understanding of this experimental finding has not been attained yet, the phase transition could be related to the enhanced stabilisation of the sodalite conformation in the ethanol medium. In this regard, *in situ* synchrotron experiments are currently under study.



(a)

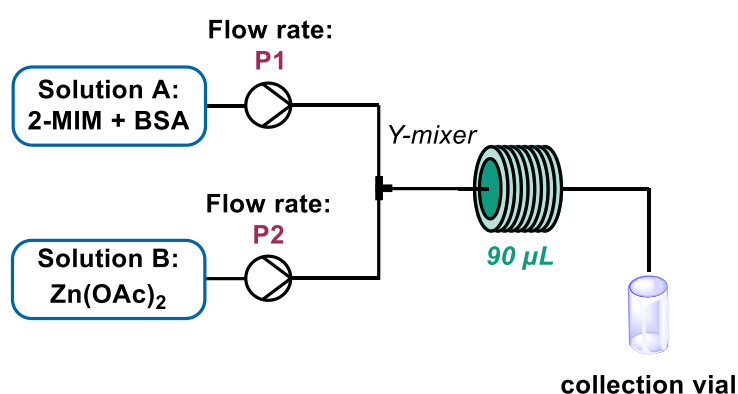


(b)

Figure 6.12. Ternary plot BSA/Zn/2-MIM after washing with a) water and b) ethanol. The empty red circle refers to amorphous material.

6.2.2 Size-controlled synthesis of BSA@ZIF-8 in continuous-flow conditions

The synthesis of **BSA@ZIF-8** biocomposites in continuous-flow conditions was carried out, following Recipe B, by simultaneously feeding the two precursor solutions into a Y-mixer, by means of syringe pumps (Scheme 6.1). The residence time in the flow system was determined by the length of the output tubing (20 cm, $V = 90 \mu\text{L}$) and the total flow rate. In all the experiments, the two syringe pumps were set at an equal flow rate, so that the stoichiometry of the reaction depended only on the concentration of the initial stock solutions ($2\text{-MIM}/\text{Zn} = 16$).



Scheme 6.1. Experimental setup for the continuous-flow synthesis of **BSA@ZIF-8**.

At first the reaction was carried out, both with and without BSA to obtain ZIF-8 and **BSA@ZIF-8**, working with different combined flow rates (Table 6.2)

Table 6.2. Synthesis of ZIF-8 and **BSA@ZIF-8** in continuous-flow conditions.

Entry	Flow rate (mL min^{-1}) ^a	t_{R} (s) ^b	Collecting time (min) ^c
1	2.0	2.7	1
2	1.5	3.6	1.3
3	1	5.4	2
4	0.5	10.8	4
5	0.25	21.6	8
6	0.1	54	20

a) combined flow rate ($P1 + P2$); b) residence time for $V = 90 \mu\text{L}$ at the set flow rate; c) collecting time corresponding to a 2 mL samples.

In all of the experiments, the formation of the product was confirmed by the turbidity and white colour of the suspension coming out of the output tubing, which was more intense in the presence of BSA, since the protein induces the rapid formation of the ZIF-8 structure. The diffraction patterns of the obtained ZIF-8 and **BSA@ZIF-8** samples, after 24 h of aging, presented the peaks associated to a pure sodalite phase, thus suggesting that in the case of Recipe B the flow rate did not affect the final crystal phase of the product.

Furthermore, the SEM analysis of the ZIF-8 sample obtained at 1.5 mL min^{-1} revealed the presence of rhombic dodecahedron particles with an average dimension of $0.62 \pm 0.24 \text{ }\mu\text{m}$ (Figure 6.13). The comparison of this value with the one previously reported for the batch synthesis ($0.85 \pm 0.1 \text{ }\mu\text{m}$)³¹ indicated that on average smaller particles were obtained in flow conditions, though with a higher dispersity.

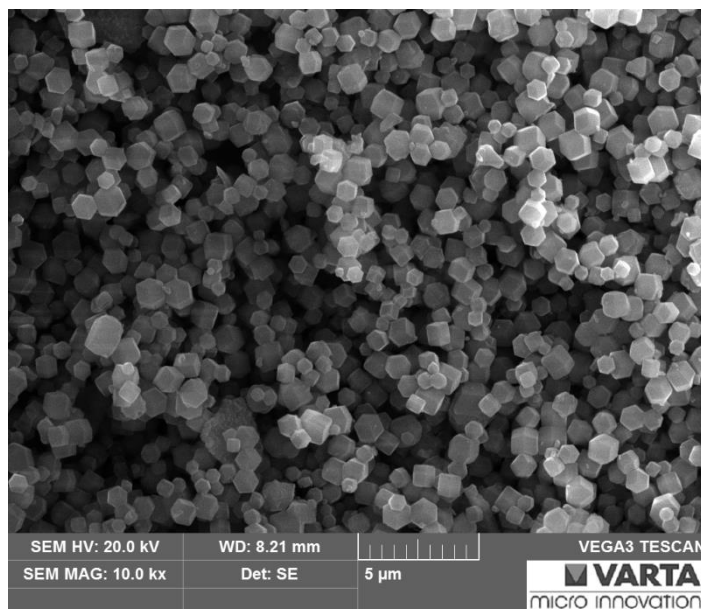


Figure 6.13. SEM image of ZIF-8 synthesized in continuous-flow conditions.

Although many works reported in the literature described the size-controlled synthesis of ZIF-8 crystals by varying the 2-MIM/Zn ratio,⁴⁴ the previously reported results indicated that, in the case the studied **BSA@ZIF-8** systems, the variation of this parameter can drastically influence the crystal phases of the products.

For this reason, the investigation on the control of particle size was carried out by using different size modulators, i.e. 1-methylimidazole (1-MIM), cetyl trimethylammonium bromide (CTAB), poly(diallyldimethylammonium) chloride (polyDADMACl) and sodium dodecyl sulphate (SDS), at the fixed 2-MIM/Zn ratio of 16. The experimental setup used for these experiments was essentially the same previously

adopted, however, in this case the output was collected into a vial containing the modulator solution (quench solution). The experimental conditions employed for these tests are summarised in Table 6.3, as well as the crystal phase of the obtained products.

Table 6.3. Summary of the size modulation tests.

Entry	Modulator	Modulator concentration	Flow rate (mL min⁻¹)^a	t_R (s)^b	Crystal phase^c
1	1-MIM	2.56 M	2	2.7	sod
			0.5	10.8	-
			0.25	21.6	n.a.
		1.28 M	2	2.7	sod
			0.5	10.8	sod
			0.25	21.6	n.a.
2	CTAB	25 mg/mL	2	2.7	n.a.
			0.5	10.8	sod
			0.25	21.6	sod
		2.5 mg/mL	2	2.7	sod
			0.5	10.8	sod
			0.25	21.6	sod
3	SDS	10 wt %	2	2.7	sod
			0.5	10.8	-
			0.25	21.6	sod
		1 wt %	2	2.7	-
			0.5	10.8	-
			0.25	21.6	sod
4	polyDADMACl	25 % v/v	2	2.7	-
			0.5	10.8	-
			0.25	21.6	-
		2.5 % v/v	2	2.7	sod
			0.5	10.8	sod
			0.25	21.6	sod

a) combined flow rate (P1 + P2); b) residence time for V = 90 μL and the set flow rate; c) determined by SAXS analysis. When the crystal phase is not reported its identification was not possible on the base of the recorder diffraction pattern. When n.a. is reported the sample was not analysed.

When 1-methylimidazole was used as modulator (Table 6.3, entry 1), the samples collected at the lower flow rate (0.25 mL min^{-1}) did not afford any precipitate, even after 24 h. This could suggest the presence of very small particles in the turbid solution, not recoverable by centrifugation. In this regard, the direct analysis of the collected solution by dynamic light scattering (DLS) is currently under examination.

Besides, the SEM images of the sample obtained at 0.5 mL min^{-1} and quenched by a 1.28 M solution of 1-MIM revealed the presence of two population of particles. In particular, the average size of the bigger population is centred around $1.0 - 1.3 \text{ }\mu\text{m}$, while for the smaller particles an average size of $0.20 - 0.25 \text{ }\mu\text{m}$ was observed (Figure 6.14).

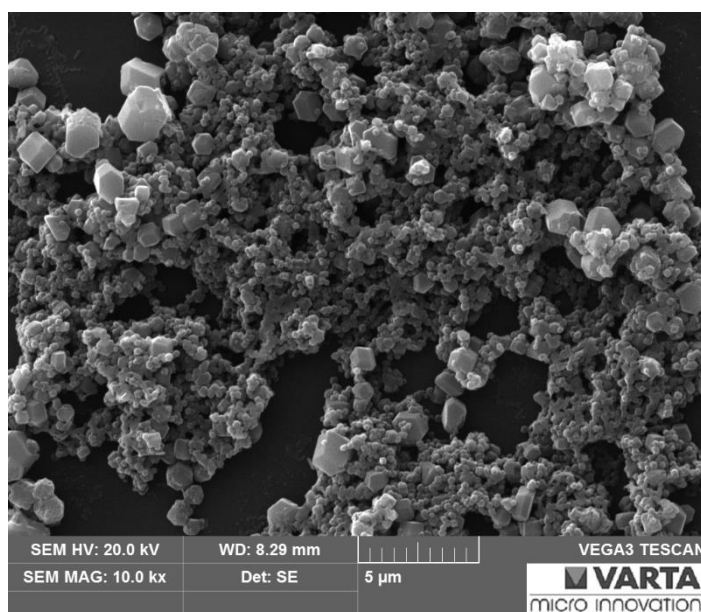
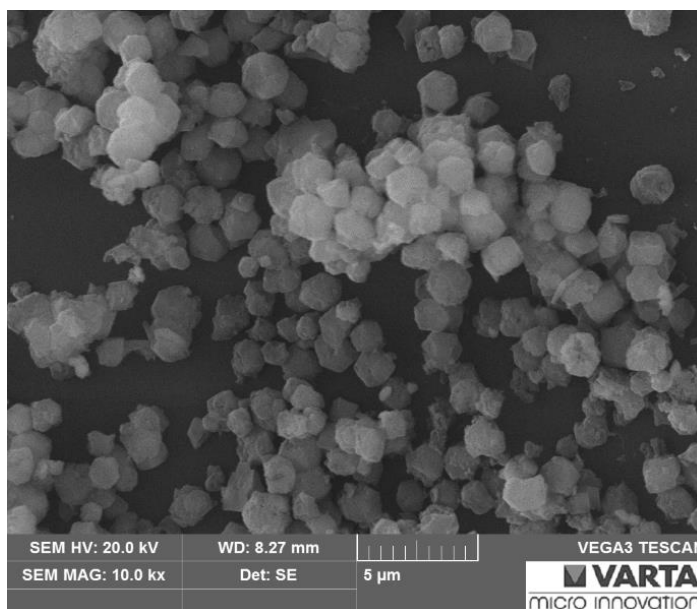


Figure 6.14. SEM image of **BSA@ZIF-8** synthesized at 0.5 mL min^{-1} quenched by a 1.28 M 1-MIM solution.

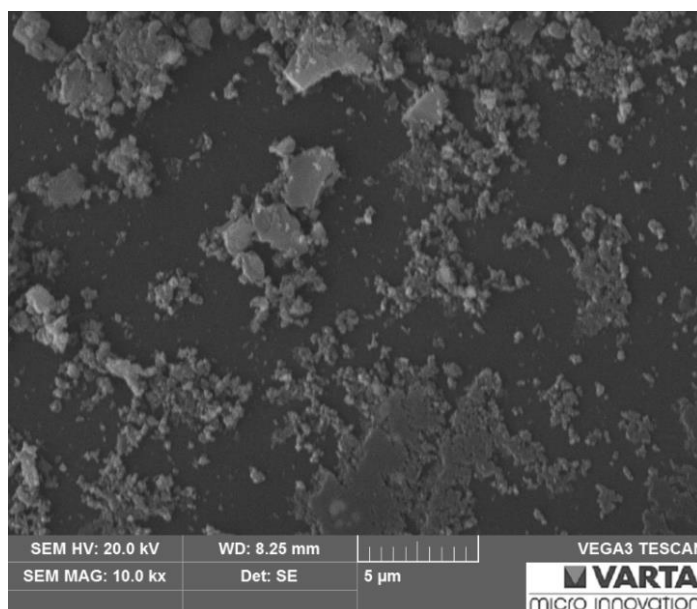
When the **BSA@ZIF-8** output was quenched with the surfactant CTAB (Table 6.3, entry 2), the supernatant solution was found to remain white, even during the washing cycles. This could be attributed to the continuous formation of a suspension due to the interaction between the ZIF-8 biocomposite and the surfactant, resulting in the continuous removal of part of the solid from the precipitate. In the case of SDS, the clear identification of the crystal phase was not possible for half of the samples (Table 6.3, entry 3).

Given the ambiguous results obtained with CTAB and SDS, these samples were not analysed by SEM.

Finally, when the polyDADMCl surfactant was used (Table 6.3, entry 4) with a 2.5 % v/v concentration, no effect on the **BSA@ZIF-8** particle size was observed (Figure 6.15a). In addition, some regions of the sample analysed by SEM displayed a different morphology, which was attributed to the excess of polymer.



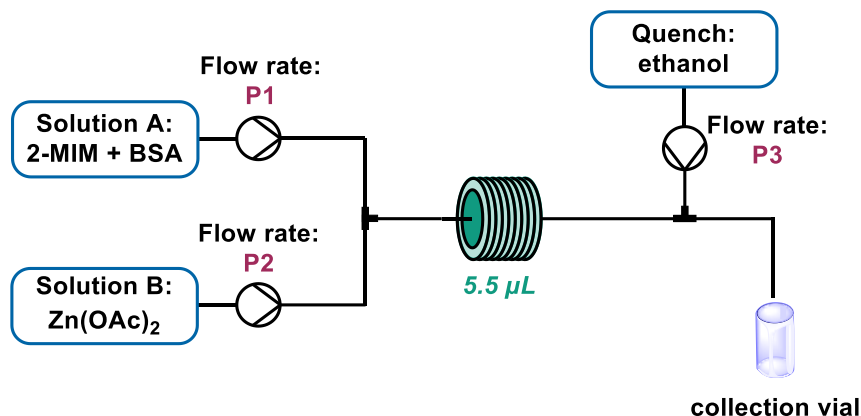
(a)



(b)

Figure 6.15. SEM images of **BSA@ZIF-8** synthesized at 0.5 mL min^{-1} quenched by a 2.5 % v/v solution of polyDADMCl solution.

Finally, the most interesting and promising results in terms of particle size control were obtained in some preliminary tests concerning the *in situ* ethanol quenching of the **BSA@ZIF-8** suspension coming out of the Y-mixer unit (Scheme 6.2 and Table 6.4).



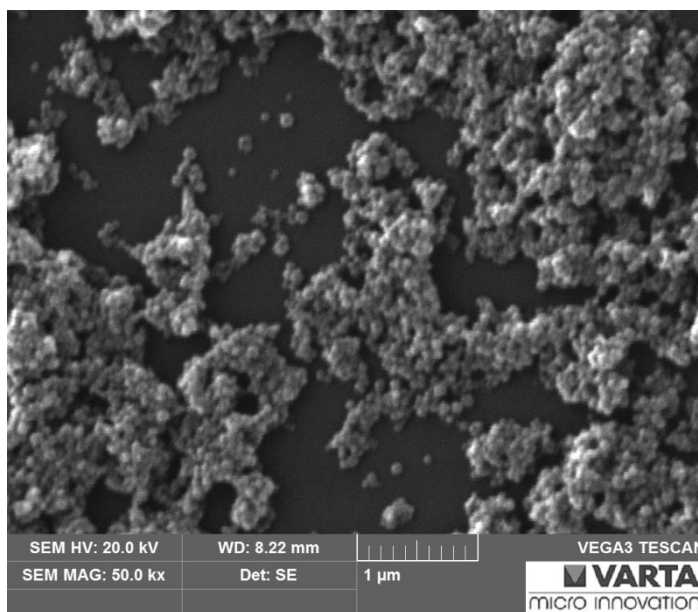
Scheme 6.2. Experimental setup for the ethanol *in situ* quenching experiments of **BSA@ZIF-8**.

Table 6.4. In situ ethanol quenching experiments.

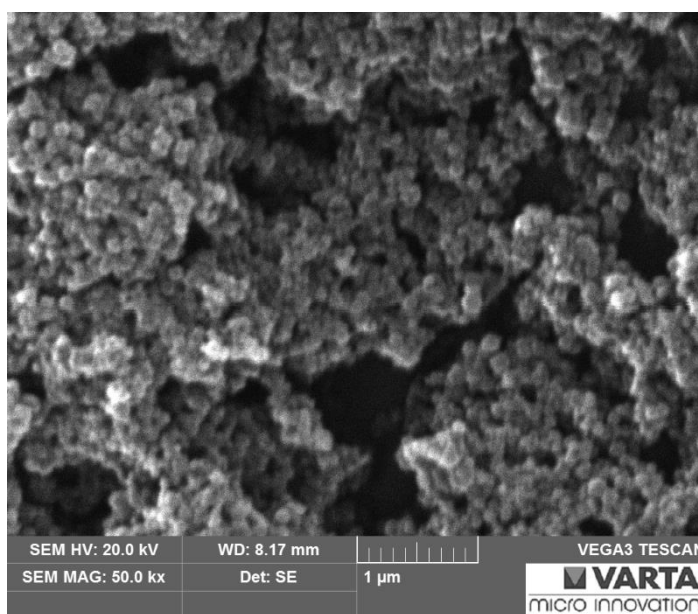
Entry	Flow rate P1 (mL min ⁻¹)	Flow rate P2 (mL min ⁻¹)	Flow rate P3 (mL min ⁻¹)	t _R before quench (s)
1	2.5	2.5	5	0.3
2	1.25	1.25	2.5	0.6

The choice of ethanol was dictated by the proven compatibility of this solvent with the studied biocomposite and by the possibility to extend the procedure to those samples whose undergo a phase transition upon washing with EtOH. In this way, the one-pot formation of sodalite pure phases with a controlled particles size could be potentially carry out.

The SEM images of the samples obtained with a quenching time of 0.3 s and 0.6 s are shown in Figure 6.16a and Figure 6.16b respectively. Unfortunately, the poor quality of the images due to the low resolution of the instrument, did not allow a precise determination of the particle size. However, an average size of approximately 100 nm could be tentatively measured, significantly smaller than that previously observed in both batch and flow experiments. Furthermore, the turbidity of the supernatant solution suggested the possible presence of even smaller particles, not recoverable by centrifugation.



(a)



(b)

Figure 6.16. SEM images of **BSA@ZIF-8** quenched with ethanol after a) 0.3 s and b) 0.6 s.

6.3 Conclusions

The synthesis of **BSA@ZIF-8** biocomposites was carried out by simply mixing two aqueous precursor solutions containing 2-methylimidazole and BSA, and zinc acetate, respectively.

The variation of the mass fraction of these components in the reaction mixture was found to strongly influence the topology of the final product. In particular, the porous sodalite phase was only obtained when a low amount of BSA was used, or after washing with ethanol the solid crystals formed in water.

Furthermore, the synthesis of the studied biocomposite in continuous-flow conditions was also carried out, with a particular focus on the modulation of particle size. In this regard, two main strategies were investigated: 1) quenching of the **BSA@ZIF-8** suspension with a solution containing a size modulator and 2) *in situ* ethanol quenching. The best result obtained with the first approach was observed when the quenching occurred in a 2.56 M solution of 1-methylimidazole. The SEM images of this sample revealed the presence of particles with an average diameter of 0.20 – 0.25 μm , although a second population of much bigger particles ($\sim 1 \mu\text{m}$) was also present.

The most promising results were obtained with the *in situ* ethanol quenching experiments, which afforded particles with an average size of $\sim 100 \text{ nm}$. Given this interesting preliminary results, it is clear that future efforts should be directed towards the optimisation of the product recovery in order to collect even the very small particles that could remain in suspension after centrifugation. Moreover, the identification of high-resolution techniques for the analysis of these small particles is fundamental. In this regard, SAXS *in situ* analysis could afford complete and precise results, both in terms of crystal phase and particle size.

6.4 Experimental section

6.4.1 Materials

Zinc acetate [Zn(OAc)₂], 2-methylimidazole (2-MIM), bovine serum albumin lyophilised powder (BSA, ≥ 96 %), sodium dodecyl sulphate (SDS), cetyl trimethylammonium bromide (CTAB), 1-methylimidazole (1-MIM), poly(diallyldimethylammonium) chloride (polyDADMACl) and ethanol (EtOH) were of analytical grade and used as purchased from Sigma Aldrich.

6.4.2 Synthesis of BSA@ZIF-8

Recipe A. In a typical experiment, a 1 mL aqueous solution of Zn(OAc)₂ (0.04 mM) was rapidly poured into a 1 mL aqueous solution of 2-MIM (0.16 mM) and BSA (0.66 mg/mL) at room temperature. The reaction mixture was vigorously stirred on a vortex for a few seconds, then it was left aging for 24 h. After the aging period, the precipitate was collected by centrifugation and thoroughly washed twice with H₂O and twice with ethanol, then the solid was dried in air to afford a white powder.³⁰

Recipe B. In a typical experiment, a 1 mL aqueous solution of Zn(OAc)₂ (0.08 mM) was rapidly poured into a 1 mL aqueous solution of 2-MIM (1.28 M) and BSA (0.66 mg/mL) at room temperature. The reaction mixture was vigorously stirred on a vortex for a few seconds, then it was left aging for 24 h. After the aging period, the precipitate was collected by centrifugation and thoroughly washed twice with H₂O and twice with ethanol.³¹

6.4.3 Synthesis of BSA@ZIF-8 biocomposites for BSA/Zn/2-MIM ternary plot

Three stock solutions were initially prepared: 2-MIM 0.44 M, BSA 36 mg/mL and Zn(OAc)₂ 0.08 M. Then, two premix solutions named Solution A (2-MIM+BSA) and Solution B (Zn) were prepared according to Table 6.5. Solution B was rapidly added to Solution A and the reaction mixture was left aging for 24 h. After the aging period, the precipitate was collected by centrifugation and thoroughly washed twice with H₂O and twice with ethanol, then the solid product was dried in air.

Table 6.5. Preparation of samples for the BSA/Zn/2-MIM ternary plot.

N°	Solution A			Solution B	
	V 2-MIM (μL)	V H ₂ O (μL)	V BSA (μL)	V Zn(OAc) ₂ (μL)	V H ₂ O (μL)
1	60	450	490	130	870
2	60	510	430	250	750
3	60	570	370	380	620
4	60	640	300	500	500
5	60	700	240	630	370
6	60	760	180	750	250
7	60	820	120	880	120
8	120	450	430	130	870
9	120	510	370	250	750
10	120	580	300	380	620
11	120	640	240	500	500
12	120	700	180	630	370
13	120	760	120	750	250
14	120	820	60	880	120
15	180	450	370	130	870
16	180	520	300	250	750
17	180	580	240	380	620
18	180	640	180	500	500
19	180	700	120	630	370
20	180	760	60	750	250
21	240	460	300	130	870
22	240	520	240	250	750
23	240	580	180	380	620
24	240	640	120	500	500
25	240	700	60	630	370
26	300	460	240	130	870
27	300	520	180	250	750
28	300	580	120	380	620

29	300	640	60	500	500
30	360	460	180	130	870
31	360	520	120	250	750
32	360	580	60	380	620
33	430	450	120	130	870
34	430	510	60	250	750
35	480	460	60	130	870
36	60	880	60	1000	0

6.4.4 Synthesis of BSA@ZIF-8 in continuous-flow conditions

A stock solution of 2-MIM (1.28 M) and BSA (0.66 mg/mL) was prepared by dissolving 5.2544 g of 2-MIM and 0.033 g of BSA in 50 mL of H₂O. Furthermore, a second stock solution of Zn(OAc)₂ 0.08 M was also prepared by dissolving 0.878 g of Zn(OAc)₂ in 50 mL of H₂O.

In a typical experiment, the two precursor solutions were continuously fed with the help of two syringe pumps (Asia Flow Chemistry Syringe Pump) into a Y-type micromixer, connected to an output tubing (length: 20 cm, internal diameter: 0.762 mm, volume: 90 μ L). The output suspension containing the solid product was collected in vials of 2 mL and aged for 24 h. After the aging period, the solid was recovered by centrifugation and washed with water (2 x 2 mL), ethanol (2 x 2 mL), SDS 10 wt % (1 x 2 mL), water (4 x 2 mL) and ethanol (2 x 2 mL) before drying in air.³¹

In a typical size modulation experiment 5 mL of the output suspension were collected into a flask containing 2 mL of the modulator solution. After 24 h of aging the solid was recovered by centrifugation and washed with water (2 x 2 mL), ethanol (2 x 2 mL), SDS 10 wt % (1 x 2 mL), water (4 x 2 mL) and ethanol (2 x 2 mL) before drying in air.³¹

In the ethanol *in situ* quenching experiments, the suspension in the output tubing was fed to another mixing unit (T-mixer) to dilute it with ethanol. The flow rate of the ethanol stream was set at the same value of the combined flow rate of the reagent solutions. The obtained samples were immediately washed twice with water and twice with ethanol.

All experiments were conducted at room temperature and the two solutions were always pumped at an equal flow rate. The collection of the samples started after $3t_R$ (where

t_R is the residence time defined as the volume of reaction divided by the combined flow rate) in order to achieve a steady state regime.

6.4.5 Instruments and methods

Small angle x-ray scattering (SAXS) and wide angle x-ray scattering (WAXS) measurements were performed at the Austrian SAXS beamline of the Elettra synchrotron facilities in Trieste (Italy), using 8 KeV branch corresponding to a wavelength of 1.54 Å. An exposure time of 1 s was set to collect the diffraction images. Data were analysed using the Igor Pro software Package (WaveMetrics Inc.).

Scanning electron microscopy (SEM) images were collected with a Tescan Vega3 field emission scanning electron microscope, with an acceleration voltage of 20.0 kV. The sample powders were dispersed on a carbon sample holder and coated with a gold thin film prior to analysis.

The system used for continuous-flow synthesis was composed of a syringe pump with two independent flow channels (Asia Flow Chemistry Syringe Pump by Syrris) equipped with integrated pressure sensors and two sets of syringes, a Y-mixing unit and peek tubing and connectors. The employed syringes were an Asia Blue Syringe 500 $\mu\text{L}/1$ mL (flow rate: 10 $\mu\text{L min}^{-1}$ – 2.5 mL min^{-1}) and an Asia Red Syringe 2.5 mL/5 mL (flow rate: 50 $\mu\text{L min}^{-1}$ – 10 mL min^{-1}).

References

- ¹ S. T. Meek, J. A. Greathouse, M. D. Allendorf, *Adv. Mater.*, **2011**, *23*, 249.
- ² Y. Lin, C. Kong, Q. Zhang, L. Chen, *Adv. Energy Mater.*, **2017**, *7*, 1601296.
- ³ E. Adatoz, A.K. Avci, S. Keskin, *Sep. Purif. Technol.*, **2015**, *152*, 207.
- ⁴ J. Gascon, A. Corma, F. Kapteijn, F. X. Llabrés i Xamena, *ACS Catal.*, **2014**, *4*, 361.
- ⁵ Y. B. Huang, J. Liang, X. S. Wang, R. Cao, *Chem. Soc. Rev.*, **2017**, *46*, 126.
- ⁶ A. H. Chughtai, N. Ahmad, H. A. Younus, A. Laypkov, F. Verpoort, *Chem. Soc. Rev.*, **2015**, *44*, 6804.
- ⁷ M. Andrzejewski, A. Katrusiak, *J. Phys. Chem. Lett.*, **2017**, *8*, 279.
- ⁸ X. Liu, W. Fu, E. Bouwman, *Chem. Commun.*, **2016**, *52*, 6926.
- ⁹ D. Wang, Q. Tan, J. Liu, Z. Liu, *Dalton Trans.*, **2016**, *45*, 18450.
- ¹⁰ L. R. Mingabudinova, V. V. Vinogradov, V. A. Milichko, E. Hey-Hawkins, A.V. Vinogradov, *Chem. Soc. Rev.*, **2016**, *45*, 5408.
- ¹¹ I. Mihad, S. Rana, A. H. Ghaleb, *Curr. Med. Chem.*, **2017**, *24*, 193.
- ¹² W. Chen, C. Wu, *Dalton Trans.*, **2018**, *47*, 2114.
- ¹³ A. C. McKinlay, R. E. Morris, P. Horcajada, G. Ferey, R. Gref, P. Couvreur, C. Serre, *Angew. Chem. Int. Ed.*, **2010**, *49*, 6260.
- ¹⁴ B. Valizadeh, T. N. Nguyen, K. C. Stylianou, *Polyhedron*, **2018**, *145*, 1.
- ¹⁵ <http://www.chemtube3d.com/solidstate/MOF-ZIF8.htm>
- ¹⁶ K. S. Park, Z. Ni, A. P. Côté, J. Y. Choi, R. Huang, F.mJ. Uribe-Romo, H. K. Chae, M. O’Keeffe, O. M. Yaghi, *PNAS*, **2006**, *27*, 10186.
- ¹⁷ <http://rcsr.anu.edu.au/nets/sod>
- ¹⁸ Z. Ni, R. I. Masel, *J. Am. Chem. Soc.* **2006**, *128*, 12394.
- ¹⁹ S. H. Jung, J. H. Lee, J. W. Yoon, C. Serre, G. Ferey, J. S. Chang, *Adv. Mater.*, **2007**, *19*, 121.
- ²⁰ P. Amo-Ochoa, G. Givaja, P. J. S. Miguel, O. Castillo, F. Zamora, *Inorg. Chem. Commun.*, **2007**, *10*, 921.
- ²¹ Y. K. Seo, G. Hundal, I. T. Jang, Y. K. Hwang, C. H. Jun, J. S. Chang, *Microporous Mesoporous Mater.*, **2009**, *119*, 331.
- ²² W. J. Son, J. Kim, W. S. Ahn, *Chem. Commun.*, **2008**, 6336.
- ²³ A. Pichon, A. Lazuen-Garay, S. L. James, *CrystEngComm*, **2006**, *8*, 211.
- ²⁴ T. Friscic, L. Fabian, *CrystEngComm*, **2009**, *11*, 743.

-
- ²⁵ K. Liang, J. J. Richardson, J. Cui, F. Caruso, C. J. Doonan, P. Falcaro, *Adv. Mater.*, **2016**, *28*, 7910.
- ²⁶ R. Riccò, W. Liang, S. Li, J. J. Gassensmith, F. Caruso, C. J. Doonan, P. Falcaro, *ACS Nano*, **2018**, *1*, 13.
- ²⁷ M. Hoopa, C. F. Waldea, R. Riccò, F. Mushtaqa, A. Terzopoulou, X. Z. Chena, A. J. deMello, C. J. Doonan, P. Falcaro, B. J. Nelson, J. Puigmartí-Luisb, S. Panéa, *Applied Materials Today*, **2018**, *11*, 13.
- ²⁸ C. Doonan, R. Riccò, K. Liang, D. Bradshaw, P. Falcaro, *Acc. Chem. Res.*, **2017**, *50*, 1423.
- ²⁹ F. Lyu, Y. Zhang, R. N. Zare, J. Ge, Z. Liu, *Nano Lett.*, **2014**, *14*, 57615.
- ³⁰ K. Liang, R. Ricco, C. M. Doherty, M. J. Styles, S. Bell, N. Kirby, S. Mudie, D. Haylock, A. J. Hill, C. J. Doonan, P. Falcaro, *Nat. Commun.*, **2015**, *6*, 1.
- ³¹ W. Liang, R. Ricco, N. K. Maddigan, R. P. Dickinson, H. Xu, Q. Li, C. J. Sumby, S. G. Bell, P. Falcaro, C. J. Doonan, *Chem. Mater.*, **2018**, *30*, 1069.
- ³² A. D. Katsenis, A. Puškarić, V. Štrukil, C. Mottillo, P. A. Julien, K. Užarević, M. H. Pham, T. O. Do, S. A. J. Kimber, P. Lazić, O. Magdysyuk, R. E. Dinnebier, I. Halasz, T. Frišćić, *Nat. Commun.*, **2015**, *6*, 6662.
- ³³ Z. Akimbekov, A. D. Katsenis, G. P. Nagabhushana, G. Ayoub, M. Arhangelskis, A. J. Morris, T. Frišćić, A. Navrotsky, *J. Am. Chem. Soc.*, **2017**, *23*, 7952.
- ³⁴ I. A. Baburin, S. Leoni, *J. Mater. Chem.*, **2012**, *22*, 10152.
- ³⁵ I. A. Baburin, S. Leoni, *CrystEngComm*, **2010**, *12*, 2809.
- ³⁶ M. Gaumet, A. Vargas, R. Gurny, F. Delie, *Eur. J. Pharm. Biopharm.*, **2008**, *69*, 1.
- ³⁷ S. Rojas, T. Devic, P. Horcajada, *Mater. Chem. B*, **2017**, *5*, 2560.
- ³⁸ V. K. La Mer, R. H. Dinegar, *J. Am. Chem. Soc.*, **1950**, *72*, 4847.
- ³⁹ M. Sindoro, N. Yanai, A. Y. Jee, S. Granick, *Acc. Chem. Res.*, **2014**, *47*, 459.
- ⁴⁰ J. Cravillon, R. Nayuk, S. Springer, A. Feldhoff, K. Huber, M. Wiebcke, *Chem. Mater.*, **2011**, *23*, 2130.
- ⁴¹ T. Enomoto, S. Ueno, E. Hosono, M. Hagiwarara, S. Fujihara, *CrystEngComm*, **2017**, *19*, 2844.
- ⁴² Y. Pan, D. Heryadi, F. Zhou, L. Zhao, G. Lestari, H. Sub, Z. Lai, *CrystEngComm*, **2011**, *13*, 6937.
- ⁴³ S. K. Nune, P. K. Thallapally, A. Dohnalkova, C. Wang, J. Liuc, G. J. Exarhosc, *Chem. Commun.*, **2010**, *46*, 4878.

-
- ⁴⁴ P. C. Tan, B. S. Ooi, A. L. Ahmad, S. C. Low, *J. Phys. Sci.*, **2017**, 28, 215.
- ⁴⁵ M. Rubio-Martinez, C. Avci-Camur, A. W. Thornton, I. Imaz, D. Maspocho, M. R. Hill, *Chem. Soc. Rev.*, **2017**, 46, 3453.
- ⁴⁶ A. Polyzoidis, T. Altenburg, M. Schwarzer, S. Loebbecke, S. Kaskel, *Chem. Eng. J.*, **2016**, 283, 971.
- ⁴⁷ O. Kolmykov, J. M. Commenge, H. Alemb, E. Girot, K. Mozet, G. Medjahdi, R. Schneider, *Mater. Des.*, **2017**, 122, 31.
- ⁴⁸ S. Watanabe, S. Ohsaki, T. Hanafusa, K. Takada, H. Tanaka, K. Mae, M. T. Miyahara, *Chem. Eng. J.*, **2017**, 313, 724.
- ⁴⁹ L. Golić, G. Branković, M. Počuča Nešić, K. Vojisavljević, A. Rečnik, N. Daneu, S. Bernik, M. Šćepanović, D. Poleti, Z. Branković, *Nanotechnology*, **2011**, 22, 395603.